

## The Analysis of Electron Densities: From Basics to Emergent Applications

Daniel Koch, Michele Pavanello,\* Xuecheng Shao, Manabu Ihara, Paul W. Ayers, Chérif F. Matta,\* Samantha Jenkins,\* and Sergei Manzhos\*



Cite This: *Chem. Rev.* 2024, 124, 12661–12737



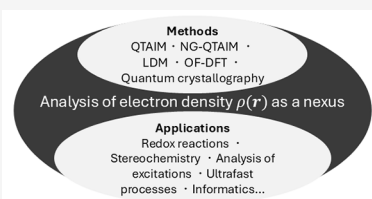
Read Online

ACCESS |

Metrics & More

Article Recommendations

**ABSTRACT:** The electron density determines all properties of a system of nuclei and electrons. It is both computable and observable. Its topology allows gaining insight into the mechanisms of bonding and other phenomena in a way that is complementary to and beyond that available from the molecular orbital picture and the formal oxidation state (FOS) formalism. The ability to derive mechanistic insight from electron density is also important with methods where orbitals are not available, such as orbital-free density functional theory (OF-DFT). While density topology-based analyses such as QTAIM (quantum theory of atoms-in-molecules) have been widely used, novel, vector-based techniques recently emerged such as next-generation (NG) QTAIM. Density-dependent quantities are also actively used in machine learning (ML)-based methods, in particular, for ML DFT functional development, including machine-learnt kinetic energy functionals. We review QTAIM and its recent extensions such as NG-QTAIM and localization-delocalization matrices (LDM) and their uses in the analysis of bonding, conformations, mechanisms of redox reactions excitations, as well as ultrafast phenomena. We review recent research showing that direct density analysis can circumvent certain pitfalls of the FOS formalism, in particular in the description of anionic redox, and of the widely used (spherically) projected density of states analysis. We discuss uses of density-based quantities for the construction of DFT functionals and prospects of applications of analyses of density topology to get mechanistic insight with OF-DFT and recently developed time-dependent OF-DFT.



### CONTENTS

1. Introduction 12662
2. The Electron Density: A Quantum Observable Accessible from Experiment 12664
3. The Quantum Theory of Atoms-in-Molecules (QTAIM)
  - 3.1. An Elementary and Brief Introduction to the Quantum Theory of Atoms-in-Molecules (QTAIM) 12667
  - 3.1.1. QTAIM and the “Observable” Electron Density 12667
  - 3.1.2. Topology and Topography of a Three-Dimensional Scalar Function 12668
  - 3.1.3. The Electron Density: From Topography to Topology 12668
  - 3.1.4. Bader’s Zero-Flux Surface as a Quantum Condition for Atoms-in-Molecules (AIMs) 12669
- 3.2. Is Energy “Equally Transferable” as the “Shape” of an Atom-in-a-Molecule? 12671
- 3.3. Bond-Paths Do Not Automatically Appear When Atoms-in-Molecules Are Congested 12673
- 3.4. Electron Localization–Delocalization Matrices (LDMs) 12675

#### 3.4.1. Complete Localization–Delocalization Molecular Graph

12677

#### 3.4.2. The Localization–Delocalization Matrix (LDM) as a Tool for Molecular Comparisons

12678

#### 3.5. QTAIM for Quantum Crystallography: The Solid State and Surfaces

12684

##### 3.5.1. Quantum Crystallography: Application to the Solid State

12684

##### 3.5.2. Quantum Crystallography: Application to Surfaces

12685

#### 4. Next Generation Quantum Theory of Atoms-in-Molecules (NG-QTAIM)

12685

##### 4.1. Evolution from Scalar QTAIM to Vector-Based Next Generation QTAIM

12685

##### 4.2. Chemical Bond Interpreted with NG-QTAIM: The Bond-Path-Framework Set B

12687

Received: April 18, 2024

Revised: September 18, 2024

Accepted: September 25, 2024

Published: November 15, 2024



4.2.1. Applications of the Bond-Path-Framework Set <i>B</i>	12688
4.3. Chemical Bond Interpreted with NG-QTAIM: The Precession <i>K</i>	12689
4.4. Applications of the Precession <i>K</i>	12689
4.4.1.1. Explaining the IR-Active Modes of Benzene	12689
4.4.1.2. Inherent Asymmetry of the $S_1$ Electronic State of Fulvene	12690
4.4.1.3. Chemical Coupling of Hydrogen Bond and Covalent Bond in Water	12690
4.5. Full Symmetry Breaking and Method of Construction of Eigenvector-Space Trajectories	12691
4.6. Eigenvector-Space-Following Trajectories	12692
4.6.1. Applications of Eigenvector-Space-Following Trajectories	12692
4.7. Eigenvector-Space-Directed Trajectories: Relevance for Experiment and Derivation	12695
4.7.1. First-Generation Eigenvector-Space-Directed Trajectories	12696
4.7.2. Second-Generation Stress Tensor-Directed Trajectory	12698
5. Applications of Electron Density-Based Analyses to the Mechanism of Redox Reactions with Anion Redox	12700
5.1. Direct Analysis of the Electron Density to Analyze the Mechanism of Redox Reactions Including Anion Redox	12701
5.2. Pros and Cons of Formal Oxidation States	12704
5.3. Density Topology versus PDOS	12706
6. Density Topology-Based Methods for Large-Scale Ab Initio Modeling with Orbital-Free DFT	12709
6.1. Density-Based Quantities for DFT Functional Construction	12709
6.2. Density-Based Analysis for OF-DFT Development and Postprocessing	12712
6.3. Toward Density-Based Analysis of Excitations	12715
7. Conclusions and Perspectives	12716
Author Information	12717
Corresponding Authors	12717
Authors	12717
Author Contributions	12718
Notes	12718
Biographies	12718
Acknowledgments	12719
Abbreviations	12719
References	12720

## 1. INTRODUCTION

Since the early work of Bader and his co-workers on the concept of atoms-in-molecules,<sup>1</sup> density-based analysis has become commonplace in the chemistry world. Prediction and rationalization of such processes as reaction mechanisms and physical properties of molecules and materials are routinely carried out by chemists via density-based analysis techniques and software.<sup>2</sup> There is something special about the electron density. The Hohenberg–Kohn theorems<sup>3,4</sup> provide us with a proof that the electron density contains all information (properties or observables) of a system of nuclei and electrons. The electron density is, in fact, the central quantity in density

functional theory (DFT), which is a formal reformulation of quantum mechanics particularly apt to the modeling of molecules and materials, i.e., the realm of chemistry and materials science.<sup>5–9</sup> Computationally amenable yet accurate DFT approaches used in applications rely on the Kohn–Sham (KS) ansatz. This introduces a unique map of the interacting system's energy, wave function, and electron density to a fictitious system of noninteracting electrons, called the KS system,<sup>9</sup> having the same electron density and electronic energy as the fully interacting system of electrons. The KS system of noninteracting electrons is described exactly by a single Slater determinant wave function made up of the so-called KS orbitals. Even though the KS orbitals and their energies belong to the fictitious KS system, they are nevertheless widely used for mechanistic analyses. A notable example is the widespread use of densities of state (DOS) for the analysis of bandgaps, mechanisms of interactions, redox reactions, etc., for which both energies and shapes (when projections on atomic states are calculated) of orbitals are used. Although this would be a formally questionable practice, there are arguments for casting the KS orbitals as objects with physical meaning.<sup>10–13</sup> The KS orbitals are thus used to compute an array of properties: for example, KS partial DOS (commonly called PDOS), energies and overlaps related to charge transfer states<sup>14–21</sup> (e.g., using Marcus theory),<sup>22</sup> as well as steady state transport<sup>23,24</sup> and spin.<sup>25–27</sup>

The topographical analysis of the electron density offers a complementary framework to commonly used wave function- or molecular orbital (MO)-based analysis techniques, a framework based on a physical observable (the electron density) that is bias-free as it avoids ascribing physical significance to a particular set of orbitals as is done in MO-analysis-based approaches. While orbitals are not devoid of physical meaning,<sup>7,13,28</sup> mechanistic analyses based on them can miss important mechanistic details, as we demonstrate in section 5. The electron density has the added advantage that it is accessible from both theory and experiment (mainly X-ray diffraction) and can serve to directly validate a computational approach.

The quantum theory of atoms-in-molecules (QTAIM) offers a framework for topographical and topological analysis of the characteristics of chemical bonding and, more recently, to understand the mechanisms of redox reactions, conformational changes, and the interplay between the electronic structure and nuclear dynamics.<sup>1,29,30</sup> While Bader atomic charges, based on integrated atomic populations over basins bounded by zero-flux surfaces, are widely used to understand charge distribution in bonding or in charge donation, it is the analysis of the topography and the associated topology of the electron density that allows obtaining mechanistic insights complementary to those based on orbitals and in some cases providing insights into phenomena where orbital-based analyses have shortcomings, as discussed in section 5.

The mechanism of bonding and of redox reactions in functional materials, for example, is still widely rationalized based on formal oxidation states (FOS), which are based on the idealization of the ionic approximation and on a simplified orbital picture derived from linear combinations of atomic states. The tacit underlying assumption that those states form a good basis set may break down in real materials with strong bonding. The mechanistic pictures constructed based on this approximation, and their shortcomings, have had wide-ranging consequences for understanding the principles of operation in,

and ultimately the design of, functional materials used in catalysis, solar cells, batteries, etc., case in point being anionic redox. Electron-density-based analysis allows a more nuanced and ultimately more realistic view of oxidation and reduction.<sup>31</sup> As a simple example, a QTAIM charge obtained by summing the negative of the atomic electron population ( $N$ ) obtained by integrating the electron density over the atomic basin and the nuclear charge is a physically sound monitor of the oxidation state of an atom supplanting the need for arbitrary rules to assign such oxidation states.<sup>31,32</sup>

Generalizations and improvements over Bader's original formulation of QTAIM<sup>1</sup> continue to appear resulting in ever more comprehensive chemical analysis and prediction tools. The theory, by defining three-dimensional (3D) bounded atomic regions, allows for the integration of any quantity over these atomic volumes. For example, a six-dimensional (6D) integration of the exchange-correlation density over one and the same basin can be shown to count the electrons which are, on average, exchanging within that basin, i.e., localized within the atom in question.<sup>33–35</sup> This is essentially what is known in QTAIM as the localization index (LI). In contrast, if one set of electronic position coordinates is integrated on basin A while a second set is integrated over basin B, then the six-dimensional integral, in this case, counts the number of electrons delocalized between A and B, the delocalization index (DI), an index that is symmetric with respect to swapping the domains of integration. An early 6D integration algorithm was introduced by Cioslowski and Liu<sup>36</sup> and later retaken by Popelier and co-workers<sup>37</sup> in their 6D algorithm used for calculating atom-pairs contributions to intra- and intermolecular Coulomb energies. Inspired by this work, and by their own admission, Blanco, Martín-Pendás, and co-workers<sup>38–40</sup> developed what is now known as the Interacting Quantum Atoms (IQA) atomic and interatomic partitioning of the total energy and their own software implementing it. A recent extension of the use of QTAIM to predict the properties in QSAR (quantitative structure to activity relationships) modeling has been the introduction of the electron localization-delocalization matrices (LDMs).<sup>41–47</sup> LDMs list the QTAIM localization indices along the diagonal and half of all delocalization indices as the off-diagonal matrix elements summarizing the electronic structure in a succinct and operational mathematical form. In this manner, an LDM summarizes the electron density distribution of the system without any reference to the orbitals used to construct the many-electron wave function. LDMs can be used to compare molecules, quantify molecular similarities, and for the empirical modeling of many of the physical and biological properties of series of compounds to predict ones with specific sought-for properties.<sup>41–47</sup> Some of these practical applications of LDM analysis are briefly revisited in this Review.

A further fundamental development of QTAIM has recently been introduced, referred to as Next Generation Quantum Theory of Atoms-in-Molecules (NG-QTAIM);<sup>48</sup> a tutorial review explains the introductory concepts.<sup>49</sup> NG-QTAIM is the first vector-based quantum chemical theory that can be used for chiral discrimination,<sup>50,51</sup> for following  $S_{N}2$  reactions,<sup>52,53</sup> for quantifying the effects of isotopomers<sup>54</sup> and of electric fields on chiral properties,<sup>55,56</sup> the dependence on the atomic weight of atomic substituents on chiral effects,<sup>57</sup> and achiral molecules.<sup>58</sup> NG-QTAIM can also provide an explanation of the *cis*-effect without using energy-based measures,<sup>59</sup> and the tools for examination of ultrafast

phenomena such as irradiation by nonionizing laser pulses.<sup>52,60</sup> NG-QTAIM provides a nonenergy-based approach to determine full symmetry-breaking, not to be confused with point or space group symmetry operations. Full symmetry-breaking within NG-QTAIM refers to the ability to map a shift of critical points in the electron density in real space to a point in the so-called U-space. This mapping is possible because one is quantifying electron dynamics as opposed to nuclear dynamics, as the latter requires determining the changes to relative energies as a function of atomic positions.<sup>49</sup> This full symmetry-breaking is required to elucidate isoenergetic and ultrafast phenomena beyond the reach of conventional quantum chemistry. This is because NG-QTAIM is uniquely able to investigate chemical-physical phenomena independent of measurable differences in geometric measures, such as atomic positions.<sup>52</sup> The consequences for the removal of the dependency on atomic positions also result in the ability to consider ultrafast phenomena that occur on the femtosecond and faster time-scales, orders of magnitude faster than time-scales relevant for atomic motion that have provided a relationship in the form of a one-to-one mapping  $\rho(\mathbf{r}) \rightarrow \psi(\mathbf{r})$ .<sup>61</sup> This mapping involved the observation of a Berry Phase, known to be highly relevant for the electronic properties of materials.<sup>62</sup> In this Review, we consider, in particular, the consequences for computational chemistry of removing reliance on scalar chemical measures with the vector-based NG-QTAIM. The NG-QTAIM interpretation of chemical bonding enables insights not accessible from scalar chemical methods into deformation anisotropy, stereochemistry, bond coupling, and polarization effects in chemical and ultrafast physical phenomena. The symmetry-breaking properties required are provided by NG-QTAIM. Current and future plans for NG-QTAIM include the use of the propagation of electron dynamics to simulate the effect of nonionizing left- and right-circularly polarized ultrafast laser pulses with controlled duration, shape, polarization, frequency content, and carrier-envelope phase, to explore a range of chemical physics phenomena using laser-induced mixtures of states. This can enable investigation into superconductivity beyond BCS (Bardeen–Cooper–Schrieffer) theory, that has proven to be unreliable,<sup>63</sup> which depends on changes to atomic positions.

Density-based methods are all the more important now given the recent advances in orbital-free (OF) DFT.<sup>64–66</sup> In OF-DFT, the total electronic energy and, generally, the electronic structure are evaluated without the explicit support of KS orbitals. OF-DFT exploits the fact that the total energy is a density functional allowing us to construct near-linear-scaling DFT algorithms. The need in conventional KS DFT to build and diagonalize matrices (e.g., to orthogonalize the KS orbitals) is completely circumvented in OF-DFT by leveraging single-particle kinetic energy functionals ( $T_s[\rho]$ ) that only depend on the electron density  $\rho$  and not on the KS orbitals. With modern implementations of OF-DFT,<sup>67–71</sup>  $10^4$ – $10^6$  atoms are routinely approached even on desktop workstations.<sup>72–76</sup> OF-DFT therefore has the potential to revolutionize materials modeling but has been held back by the lack of kinetic energy functionals (KEF) sufficiently accurate for use in chemical applications. Due to the rapid recent progress in functional development with improved applicability,<sup>77–81</sup> including machine-learning (ML)-based KEFs<sup>68,82–93</sup> and the availability of end-user codes,<sup>67–71</sup> OF-DFT appears to be on the cusp of wide deployment in applied simulations. However, the absence of orbitals in the method

puts a particular onus on density-based approaches to analyze bonding and reaction mechanisms, and, with the recent advances in time-dependent (TD) OF-DFT,<sup>67,94</sup> excitation mechanisms. Particularly important is also the role of electron density-derived quantities (which are often much the same type of quantities traditionally used in QTAIM, including, among others, gradients and Laplacians of the density) as descriptors for KEF development. Whether via ML or via traditional physics-based methods, the use of density-based descriptors is ubiquitous. The application of OF-DFT as an alternative to KS-DFT for the computation of commonly adopted density-based descriptors is considered in section 6 where we also provide a practical example.

In this work, we therefore provide an overview of real-space electron density-based analyses of bonding and mechanisms of chemical reactions and other phenomena in particular focusing on recent theoretical developments and specific applications that have emerged in recent years and have yet to be critically presented in a review. Earlier reviews covering the analysis of the electron density and of its application are available in the literature.<sup>95–99</sup>

## 2. THE ELECTRON DENSITY: A QUANTUM OBSERVABLE ACCESSIBLE FROM EXPERIMENT

According to Dirac, a quantum mechanical “observable”<sup>100</sup> must be a real (not complex) dynamical variable expressible as an expectation value of a linear Hermitian operator with a complete set of eigenstates. Bader and Zou<sup>101</sup> have shown that these conditions are satisfied by the electron density since in this case the real dynamical variable is the  $\rho(\mathbf{r})$  itself, which is the expectation value of the operator  $\hat{\rho}(\mathbf{r})$ , the eigenstates of which (the coordinate states  $|\mathbf{r}\rangle$ ) form, indeed, a complete set. This realization underlies the argument that QTAIM atomic properties, atomic charges being an example, are quantum mechanical observables and hence uniquely defined in principle.<sup>101</sup>

In his book, Dirac emphasizes that “[i]n practice it may be very awkward, or perhaps even beyond the ingenuity of the experimenter, to devise an apparatus which could measure some particular observable, but the theory always allows one to imagine that the measurement can be made.”<sup>100</sup> The electron density is a borderline case since, as argued by Bader and Zou, it is a quantum mechanical observable and is readily obtained from the many-electron wave function, and it is also accessible from elastic X-ray scattering experiment by refining it against an assumed model.<sup>102–105</sup>

The electron density can be indirectly observed experimentally, contrary to canonical or Kohn–Sham orbitals,<sup>9</sup> which are widely used for mechanistic analyses of phenomena in materials (via, in particular partial densities of states, PDOS). By “indirectly observed”, we mean that an experimental signal is determined (directly modified) by the density, although the reported density is obtained from a fit to a given assumed atomic model. This is the case for X-ray scattering, which can be done in single-crystal and powder diffraction regimes. The coherent scattering amplitude  $A(\mathbf{S})$  is the Fourier transform of the electron density:

$$A(\mathbf{S}) = \int \rho(\mathbf{r}) e^{i2\pi\mathbf{Sr}} d\mathbf{r} \quad (2.1)$$

where  $\mathbf{S}$  is the scattering vector bisecting the angle  $\theta$  between the diffracted beam and the inverted incident beam, with a magnitude  $2 \sin \theta / \lambda$ , and  $\lambda$  is the wavelength, and where the

scalar vector product is implied between quantities in bold written in immediate succession (the convention used in this article).<sup>106</sup> For crystalline materials with lattice vectors  $\mathbf{a}$ ,  $\mathbf{b}$ , and  $\mathbf{c}$ , one introduces  $\mathbf{H} = h\mathbf{a}^* + k\mathbf{b}^* + l\mathbf{c}^*$  (which we write in shorthand notation as  $\mathbf{H} \equiv hkl$ ) with integers  $h$ ,  $k$ , and  $l$  (Miller indices) and reciprocal space lattice vectors  $\mathbf{a}^*$ ,  $\mathbf{b}^*$ , and  $\mathbf{c}^*$ . The atomic scattering factor of the  $j$ th atom is then expressed via the contribution of this atom to the electron density of the unit cell, that is

$$\begin{aligned} f_j(\mathbf{H}) &= \int_{a=0}^1 \int_{b=0}^1 \int_{c=0}^1 \rho_{j(\text{unitcell})}(\mathbf{r}) e^{i2\pi\mathbf{Hr}} dV \\ &\equiv \hat{F}[\rho_{j(\text{unitcell})}](\mathbf{r}) \end{aligned} \quad (2.2)$$

where  $a$ ,  $b$ , and  $c$  are fractional coordinates and the integral is over the volume of the unit cell, and  $f_j(\mathbf{H})$  represents the  $j$ th atom's contribution to the “structure factor” (defined below in eq 2.3). As the electron density is reconstructed from the contributions of all atoms in the unit cell, contributions that are smeared by the thermal motions of the nuclei (contrary to computed densities that are typically static), one applies convolution with a probability distribution  $\delta(\mathbf{r})$  of atomic positions under thermal motion, which is typically assumed to be a Gaussian distribution centered on the equilibrium nuclear position, leading to the definition of the “structure factor” in terms of the atomic contribution as

$$F(\mathbf{H}) = \sum_j \underbrace{f'_j(\theta)}_{\text{amplitude}} \underbrace{e^{i2\pi\mathbf{Hr}}}_{\text{phase}} \underbrace{e^{-B_j \left( \frac{\sin \theta}{\lambda} \right)^2}}_{\text{temperature-dependent factor}} \quad (2.3)$$

where we now introduced the amplitude of the atomic scattering factor  $f'_j(\theta)$  that depends on the Bragg angle  $\theta$  and the phase factor  $e^{i2\pi\mathbf{Hr}}$ , as well as a temperature-dependent factor that accounts for atomic vibrations,  $\lambda$  is the X-ray wavelength, and where the temperature (Debye–Waller) factor, or the “B-factor”, is defined as

$$B_j = 8\pi^2 \langle u^2 \rangle \quad (2.4)$$

where  $\langle u^2 \rangle$  is the mean square isotropic displacement of the  $j$ th atom's coordinates averaged over all directions and over time. This corresponds to the harmonic approximation of the nuclear dynamics under Born–Oppenheimer approximation.<sup>107</sup> If the density is expressed as a sum of atomic contributions, then

$$\rho_{\text{unitcell}}(\mathbf{r}) = \sum_j \rho_j(\mathbf{r}) * \delta(\mathbf{r} - \mathbf{r}_j) \quad (2.5)$$

where “\*” stands for the convolution operator and  $\rho_j(\mathbf{r})$  is the static density. Then:

$$F(\mathbf{H}) = \sum_j \hat{F}[\rho_j(\mathbf{r})] \hat{F}[\delta(\mathbf{r} - \mathbf{r}_j)] = \sum_j f_j e^{i2\pi\mathbf{Hr}_j} T_j(\mathbf{H}) \quad (2.6)$$

where the so-called temperature factor  $T_j(\mathbf{H})$  is the Fourier transform of the probability distribution that represents the thermal motion of the  $j$ th atom, and

$$f_j = \hat{F}[\rho_j] = \int \rho_j(\mathbf{r}) e^{i2\pi\mathbf{Hr}} d\mathbf{r} \quad (2.7)$$

The analysis of experimental densities rests on the mathematical representation of  $\rho(\mathbf{r})$  in terms of atomic densities  $\rho_j(\mathbf{r})$ . Because the total density is dominated by the

contributions from core electrons often assumed to be unperturbed by bonding (which is not strictly true, see, for example, ref 108), difference densities describing the deviation from a reference density are often used to illustrate bonding effects. Traditionally, the initial guess to the crystallographic unit cell electron density is based on a spherical atoms approximation. In this approach, atoms are centered at initial guessed positions in the unit cell with overlapping spherical atomic densities obtained from theoretical calculations. These overlapping spherical atomic densities yield a “promolecular” density within the framework of the so-called independent-atom-model (IAM).<sup>109,110</sup>

$$\rho^{\text{pro}} = \sum_{i=1}^M \rho_i \quad (2.8)$$

in which  $\rho_i$  is the  $i$ th atomic spherically symmetrical density and  $\rho^{\text{pro}}$  is the approximate promolecular density. The promolecular approach has been exceedingly productive as a basis for the solution of countless X-ray structures of small-to-moderately sized molecules and generally provides accurate molecular geometries. Where the promolecular model fails is in a detailed examination of the bonding regions in the electron density between a pair or more of atomic nuclei. In these cases, a more elaborate modeling of the electron density using an aspherical model is necessary.<sup>102–104,106,111–114</sup> A widely used aspherical modeling of the electron density is the one due to Hansen and Coppens.<sup>103,104,106,114</sup> In this model, the density is split into a core treated spherically and a valence contribution treated aspherically. A structure factor in a core–valence decomposition ( $\rho(\mathbf{r}) = \rho_{\text{core}}(\mathbf{r}) + \rho_{\text{valence}}(\mathbf{r}) = \sum_j^{\text{atoms}} \rho_{j,c}(\mathbf{r}) + \sum_j^{\text{atoms}} \rho_{j,v}(\mathbf{r})$ ) can be expressed as

$$F(\mathbf{H}) = \sum_j (P_{j,c} f_{j,c} + P_{j,v} f_{j,v}) e^{i2\pi \mathbf{H} \cdot \mathbf{r}} \quad (2.9)$$

where  $P_{j,c}$  and  $P_{j,v}$  are core and valence electronic populations and  $f_{j,c}, f_{j,v}$  are normalized to one electron. The valence density of an atom is often expressed as a sum of spherical and nonspherical contributions, the latter expressed with spherical harmonics:

$$\begin{aligned} \rho_{j,\text{valence}}(\mathbf{r}) &= P_{j,v} k'^3 \rho_{j,\text{sph}}(k'r) + \sum_{l=0}^{l_{\max}} k''^3 R_l(k''r) \\ &\quad \sum_{m=-l}^l P_{lm} d_{lm}(\mathbf{r}/r) \end{aligned} \quad (2.10)$$

where the functions  $d_{lm}$  are proportional to spherical harmonics and are normalized to 2 for  $l > 0$  and to 1 for  $l = 0$ . This normalization implies that a  $P_{lm}$  value of +1 transfers one electron from the negative lobes to the positive lobes without changing the charge of the atom. Stated differently,  $P_{lm}$  does not change the net atomic charge. Here,  $k'$  and  $k''$  are empirical expansion/contraction parameters introduced to improve the accuracy of the fit. Software is available for fitting the experimental densities and to analyze chemical bonding based on experimental electron density parameters.<sup>115–118</sup> These parameters are related to atomic charges following from the rules for orbital exponents.<sup>119–121</sup> For the density around transition metal atoms, whose distribution is dominated by the preferential occupancy of d orbitals that have a relatively small overlap with ligand orbitals, the representation of eq 2.10 allows recovering d orbital populations, which can be

compared to those from ab initio calculations.<sup>122–124</sup> The Fourier transform of the representation of eq 2.9 is used to compute the structure factors. Although typically done for valence density, eq 2.10 can also be considered for core electrons if the resolution of the apparatus permits.<sup>125</sup> Resolutions (expressed as  $\sin \theta/\lambda$ , where  $\theta$  is the diffraction angle and  $\lambda$  is the X-ray wavelength, typically 0.2–0.9 Å) on the order of 2 Å<sup>-1</sup> are achievable.<sup>125–127</sup>

For the radial components  $R_l$ , Slater-type functions are typically used for the first and second row atoms:

$$R_l = Ar^{n_l} e^{-k_l \zeta r} \quad (2.11)$$

But for transition metals, Hartree–Fock solution-type radial functions were suggested to perform better.<sup>128</sup> The exponential dependence of these functions correctly accounts for the nuclear cusp. However, care must be taken comparing experimental densities described by such models to ab initio calculations, in that ab initio calculations on solids are typically done in the pseudopotential approximation correctly describing only the valence regions. Core densities need to be added separately for comparison of computed and experimental densities and for QTAIM analysis.

QTAIM studies to be performed on electron densities obtained using pseudopotentials ( $\rho_{\text{pp}}$ ) face a number of limitations. First, there are no nuclear cusps/maxima at the positions of the nuclei in  $\rho_{\text{pp}}$  since the density of the core is missing by definition. Second, a number of spurious topological features typically occur at the boundary between the replaced core and the explicitly treated electronic region. Keith and Frisch (KF)<sup>129</sup> have invented a practical method to circumvent these limitations. These authors use Douglas–Kroll–Hess two-component (DKH2) scalar-relativistic<sup>130–133</sup> all-electron DFT calculations on free neutral ground-state atoms (with a large basis set) to fit each core subshell contribution ( $\rho_{\text{ss}}$ ) to the total electron density ( $\rho_{\text{total}}$ ) separately as a linear combination of s-type Gaussian functions ( $\rho_{\text{ss}}^{\text{fit}}$ ). The missing core electron density  $\rho_{\text{total}}(\text{core})$  is then expressed as

$$\rho_{\text{total}}(\text{core}) \approx \sum_{\substack{\text{core} \\ \text{sub-shells}}} \rho_{\text{ss}}^{\text{fit}} \quad (2.12)$$

leading to the following approximate expression for the all-electron electron density:

$$\begin{aligned} \rho_{\text{total}} &= \sum_{\substack{\text{core} \\ \text{sub-shells}}} \rho_{\text{total}}(\text{core}) + \rho_{\text{pp}} \\ &\approx \sum_j \sum_{\substack{\text{core} \\ \text{sub-shells}}} \rho_{\text{ss},j}^{\text{fit}} + \rho_{\text{pp}} \end{aligned} \quad (2.13)$$

where “all PP atoms” refers to those atoms missing the core due to its replacement by a pseudopotential. Such an approximate all-electron density, in one stroke, accounts for scalar relativistic effects, is devoid of the singularity at the boundary of the missing core, and recovers the missing nuclear cusps.<sup>129,134–136</sup>

In full-potential calculations using Gaussian-type basis functions, the cusp is also obtained only approximately. The model functions of eq 2.10 may not be adequate to represent sharp features of the density distribution, and this needs to be considered when comparing the results of ab initio calculations to experimental structure factors. Because the structure factors

are estimated via Fourier transform, phase differences between experimental and calculated structure factors are an additional source of error that can result in underestimation of the deformation density.<sup>137</sup> In other words, any discrepancies should not be automatically ascribed to errors of the ab initio method. When the model is adequately parametrized (fitting of  $k$ , number of terms of the multipole expansion, and adequate thermal broadening), experimental and DFT-computed densities return very similar parameters even at the GGA level with the PBE functional commonly used in solid-state simulations (see, e.g., comparisons of different levels of refinement in refs 125 and 127). Specific choice of functional and of the Hubbard parameter typically need not significantly affect the structure factors of the ground-state density.<sup>138</sup> This is important, as one often has to rely on DFT calculations for the studies of somewhat counterintuitive phenomena such as charge self-regulation and anion redox as discussed in section 5.

To make details of bonding more prominently visible, one often reports the deformation density:

$$\Delta\rho(\mathbf{r}) = \rho(\mathbf{r}) - \rho_0(\mathbf{r}) \quad (2.14)$$

where  $\rho_0(\mathbf{r})$  is usually taken as a sum of free atom densities. Experimental densities allow computing “experimental” electrostatic potentials and fields that can also be compared to ab initio calculations. Electrostatic properties in Fourier space can be evaluated from the structure factors directly without passing through the real-space density; for example, the Fourier coefficients of the electrostatic potential are evaluated as  $F(\mathbf{H})/|\mathbf{H}|^2$ .<sup>139–142</sup>

Sometimes X-ray diffraction data are augmented with electron diffraction measurements, in that they are used instead of X-ray diffraction data at low scattering angles. The incident electrons interact with the electrostatic potential, and at small scattering angles they are more sensitive to valence-electron distribution than X-rays due to the near cancellation of the scattering from the positive nucleus and negative electron charges.<sup>143</sup> As a result, small changes in electron density lead to large changes in the scattering. This is reflected in the relation between the X-ray scattering amplitude and the electron diffraction scattering amplitude  $E(\mathbf{S})$  that can be described by the Mott formula:<sup>144</sup>

$$E(\mathbf{S}) = \frac{|e|}{16\pi^2\epsilon_0 S^2} (Z - A(\mathbf{S})) \quad (2.15)$$

where  $Z$  is the nuclear charge in atomic units (a.u.), i.e. the atomic number. The signal is obtained with TEM (transmission electron microscopy) using techniques such as convergent beam electron diffraction (CBED)<sup>145–147</sup> and parallel recording of dark-field images (PARODI).<sup>148,149</sup> As the technique is based on the TEM, it probes essentially surface layers. By combining X-ray and electron diffraction data, structure factor accuracy on the order of 0.1% is achievable.<sup>124</sup>

The experimental data often consist of a finite set of diffracted intensities that satisfy Bragg's law  $2d_{hkl} \sin \theta = n\lambda$ , each indexed by its Miller indices, which define a reciprocal space vector  $\mathbf{H} = hkl$ . In Bragg's law,  $d_{hkl}$  is interatomic planes separation,  $\theta$  represents the angle of incidence and reflection,  $\lambda$  is the wavelength of the X-ray, and  $n$  is an integer. This law specifies the condition to observe a given reflection when maximal constructive interference of scattered waves occurs.

The structure factors  $F(\mathbf{H})$  are nonobservable theoretical constructs; only their squared magnitudes are. A given reflection's intensity can be shown to be proportional to the corresponding squared structure factor:

$$I_{hkl} \propto |F_{hkl}|^2 \quad (2.16)$$

To reconstruct the crystallographic unit cell's electron density, a periodic function along the three crystal axes, it can be expanded, as any periodic function, in terms of its Fourier components. This Fourier expansion leads to the well-known expression of the density in terms of the complete set of structure factors  $\{F_{hkl}\}$ :<sup>150–154</sup>

$$\rho(\mathbf{r}) = \frac{1}{V} \sum_h \sum_k \sum_l F_{hkl} e^{-i2\pi\mathbf{H}\mathbf{r}} \quad (2.17)$$

where  $V$  is the volume of the unit cell, and here the set  $\{F_{hkl}\}$  plays the role of the Fourier expansion coefficients, each with an amplitude, a frequency, and a phase. Since observation only yields intensities, the phase information is lost irrecoverably due to the squaring in eq 2.16. This constitutes the phase problem of crystallography. The phase problem has several elegant solutions described in standard texts.<sup>150,152–154</sup> A solution to the phasing, discovered by Karle and Hauptmann, has been the basis of their 1985 Nobel Prize in Chemistry.<sup>155</sup>

The amplitude of each calculated structure factor (whether spherically or aspherically modeled),  $|F_{\text{calc},hkl}|$ , is compared iteratively to the phased structure factor determined experimentally,  $|F_{\text{exp},hkl}|$ , and then a general agreement (residual) factor is computed:

$$R_f = \frac{\sum ||F_{\text{exp}}| - |F_{\text{calc}}||}{\sum |F_{\text{exp}}|} \quad (2.18)$$

Iterative refinement is performed until  $R_f$  is minimized such that no more improvement is achieved by further recycling. The  $R_f$  is only one measure of accuracy that is commonly used to determine whether conversion has been achieved. There exist several other measures of quality of a crystallographic structural solution. Another commonly used quality measure is, for example, the weighted  $R2$  ( $wR2$ ), defined as

$$wR2 = \sqrt{\frac{\sum w(F_{\text{exp}}^2 - F_{\text{calc}}^2)^2}{\sum w(F_{\text{exp}}^2)}} \quad (2.19)$$

where “ $w$ ” are weights given to different reflections and which reflect the quality of the solution better than the original  $R_f$ . Other quality measures include, for instance,  $R_{\text{merge}}$ , which is used to quantify the internal agreement of the collected data, while  $R_{\text{free}}$  (assessed over random subsets of the data set not used in the refinement) is designed to ensure the absence of overfitting in the modeling. Each of these alternative measures of quality has its own advantages and limitations, a discussion of which is out of the scope of this Review (see refs 156 and 157).

Traditionally, the atomic scattering factors are taken to be spherically symmetric whereby promolecular densities constructed from densities of ground-state isolated atoms calculated quantum mechanically are only allowed to vary in terms of their relative spacial positions. The spherical approximation is usually sufficient to obtain molecular geometries but not for obtaining electron densities in the bonding regions between atoms. For the latter, one must go

beyond the spherical approximation and introduce, in the expression of the scattering factors, angular parameters (spherical harmonics) that are adjusted simultaneously during the refinement.<sup>102–104,111–113,158</sup> Furthermore, one can extract more than just the electron density from the experiment and obtain valid quantum mechanical one- and two-particle density matrices expressed in a given basis set.<sup>159,160</sup> These density matrices are obtained “experimentally” from the structure factors by including additional constraints of idempotency, normalization, and hermiticity during the refinement iterations in an approach termed *Quantum Crystallography* pioneered by Lou Massa, William Clinton, and Jerome Karle.<sup>161–167</sup> A more recent variant of *Quantum Crystallography* is a refinement that results in wave functions that are consistent with the experimental structure factors.<sup>168–170</sup>

Considering the uncertainties and errors in the experimental determination of the electron density and those in ab initio calculations of it, available comparisons indicate that ab initio densities, including DFT densities, are in agreement with highly accurate experimental densities, in particular those derived from combined X-ray diffraction–electron diffraction data.<sup>124,138,143,171</sup> This concerns, in particular, estimation of charges and populations around atoms, including transition metal atoms. While definitions of charges differ both conceptually and in quantitative ranges of resulting charges (see below), reported charge estimates done with similar methods on experimental and computed densities are in agreement within estimated uncertainties.<sup>124,138,143,171,172</sup> The differences on the order of 0.1e are common, and the extent of agreement is usually sufficient for the DFT density-based analysis of bonding and redox processes reviewed below.

### 3. THE QUANTUM THEORY OF ATOMS-IN-MOLECULES (QTAIM)

There exist a number of reviews of the foundations and applications of the quantum theory of atoms-in-molecules (QTAIM).<sup>1,29,30,173–177</sup> Here, we briefly summarize it and review certain aspects of this theory and its recent application, particularly as a practical tool to predict reactivity and molecular properties and in the design of new inhibitors, activators, drugs, paints, and the like. We start with generalities to lead to two new branches of modern applications of QTAIM: The first is an exposition of a new approach that uses QTAIM localization and delocalization indices, cast in matrix format, to construct what is termed the electron localization–delocalization matrix, or LDM. The LDM is a condensed description of the electronic structure integrated at the levels of atoms-in-molecules, the same “resolution” that bench-chemists use to discuss their work. LDMs of series of molecules are subjected to comparisons and statistical analyses to predict properties of useful materials. The second is a new branch of QTAIM termed “Next Generation QTAIM”, which goes beyond energetic and scalar measures by using vector fields.

To keep this Review self-contained, an elementary and short introduction to the theory will be given with the emphasis on the oft-stated maxim that the transferability of the electron density entails the transferability of the properties of Atoms-In-a-Molecule including their contributions to the total energy. This Review briefly touches also on a few examples where QTAIM is able to cut clearly in ambiguous bonding situations. The fallacy of the notion that a bond-path would arise in a promolecular density whenever the interatomic distance is less than the sum of the van der Waals radii is demonstrated with

the help of a concrete example. Finally, it is suggested to cast discussions of bonding interactions in terms of *relative stabilization (energies)* and *not in terms of “locally repulsive or locally attractive bonds”* since these descriptions invoke forces (*energy gradients*) on the nuclei, which vanish in optimized geometries by definition.

#### 3.1. An Elementary and Brief Introduction to the Quantum Theory of Atoms-in-Molecules (QTAIM)

**3.1.1. QTAIM and the “Observable” Electron Density.** The quantum theory of atoms-in-molecules (QTAIM) (refs 1, 29, 30, 178, and 179) takes the electron density, an “observable”, as its starting point. A quantum mechanical “observable” is a quantity that can be expressed in terms of a linear Hermitian operator, which when it operates on one of its eigenfunctions  $\psi$  delivers a corresponding eigenvalue in an experimental measurement or an expectation value if  $\psi$  is not an eigenfunction of the operator.<sup>100</sup> The molecular or crystal electron density satisfies this definition and, hence, is a quantum observable since it is the expectation value of the number operator as emphasized by Bader et al.<sup>101,105</sup> While not every quantum mechanical observable has a corresponding practical method to measure it, the electron density is routinely observed, albeit indirectly, in X-ray diffraction experiments, as described above.<sup>102–104,123</sup>

The electron density  $\rho(\mathbf{r})$  at a point  $\mathbf{r}$  is defined as the probability density of finding an electron, of either spins, in an infinitesimal volume around  $\mathbf{r}$  weighted by the total number of electrons ( $N$ ) and can be related to the wave function of the  $N$ -electron system as

$$\rho(\mathbf{r}) = N \sum_{\sigma=\alpha,\beta} \int \dots \int \Psi^*(\mathbf{x}_1, \dots, \mathbf{x}_N) \Psi(\mathbf{x}_1, \dots, \mathbf{x}_N) d\mathbf{r}_2 \dots d\mathbf{r}_N \quad (3.1.1.1)$$

where  $\mathbf{r}_i = (x_i, y_i, z_i)$  are the individual spacial coordinates of all  $N$  electrons,  $\mathbf{x}_i = (\mathbf{r}_i, \sigma_i)$ , and  $\sigma_i \in \{\alpha, \beta\}$  their respective spin coordinate.

The electron density of a crystallographic unit cell can be deduced from an elastic X-ray scattering experiment as a Fourier sum of structure factors, as described in section 2. Thus, the electron density is an experimentally accessible quantum mechanical “observable”, that is

$$\left[ \begin{array}{c} \text{Theory} \\ (\text{quantum mechanics}) \end{array} \right] \rightarrow \Psi(\mathbf{x}_1, \dots, \mathbf{x}_N) \rightarrow \boxed{\rho(\mathbf{r})} \leftarrow \{F(\mathbf{H})\} \leftarrow \left[ \begin{array}{c} \text{Experiment} \\ (\text{crystallography}) \end{array} \right] \quad (3.1.1.2)$$

The electron density also occupies a privileged position by virtue of the first Hohenberg–Kohn (HK-1) theorem, which stipulates that the density of a nondegenerate ground state fixes all of the properties of the system.<sup>3</sup> This existence statement lies at the foundation of density functional theory.<sup>180</sup> The theorem can be stated symbolically as:

$$\rho(\mathbf{r}) \rightarrow \left\{ \begin{array}{c} v \\ N \end{array} \right\} \rightarrow \hat{H} \rightarrow \Psi_i \rightarrow O_i[\rho(\mathbf{r})] \quad (3.1.1.3)$$

where  $v$  is the external potential,  $\hat{H}$  is the Hamiltonian, the square brackets indicate functional dependence,  $i = 0, 1, 2, 3, \dots$  for ground and excited electronic states, and  $O_i$  represents a property of the  $i$ th eigenstate obtained by applying a linear Hermitian operator to the corresponding state function.

Another important relationship connects the radial derivative of the spherically averaged electron density ( $n$ ) around a given point-nucleus  $\alpha$  to the nuclear charge. This relation is called the Kato cusp condition:<sup>181</sup>

$$Z_\alpha = -\frac{1}{2n(r_\alpha = 0)} \left. \frac{dn(r_\alpha)}{dr_\alpha} \right|_{r_\alpha=0} \quad (3.1.1.4)$$

expressed in atomic units (au), and in which  $Z_\alpha$  is the nuclear charge (which is just the atomic number in au) of atom  $\alpha$ .

Within the point-nuclei approximation (ignoring the finite nuclear size) and the frozen nuclei (Born–Oppenheimer) approximation, the total charge density ( $\rho_{\text{total}}(\mathbf{r})$ ) is the sum of the (negative) electronic charge density distribution and a Dirac-delta function-like positive charge distribution due to the nuclei. In au, the total charge density is expressed as

$$\rho_{\text{total}}(\mathbf{r}) = -\rho(\mathbf{r}) + Z_\alpha \delta(\mathbf{R}_\alpha - \mathbf{r}) \quad (3.1.1.5)$$

where  $\mathbf{R}_\alpha$  is the  $\alpha$ th nucleus position vector and  $\delta(\mathbf{R}_\alpha - \mathbf{r})$  is a Dirac delta function that has a finite value only for the set  $\{\mathbf{r} = \mathbf{R}_\alpha\}$ , i.e., when the position vector coincides with the position vector of a given nucleus. Because of Kato's condition, the total charge density and the electron density are entirely equivalent descriptions, and one determines the other uniquely.

**3.1.2. Topology and Topography of a Three-Dimensional Scalar Function.** As a prelude for the following section, we begin by reviewing briefly the closely connected, but different, concepts of topology and topography. Topography of a given  $n$ -dimensional space is a branch of descriptive mathematics, mainly applied in geography, which deals with representing and analyzing the properties, configuration, and structures of space or of the distribution of a scalar function in the space.<sup>182</sup> Three-dimensional topography involves the representation of a two-dimensional surface using an extra (property) dimension that represents the magnitude of the property at every point of the surface. A central goal of topography is to study the various features of the surface (e.g., maxima, minima, saddle points, flat regions, etc.) and their relative arrangements. It is impossible to represent graphically the topography of a three-dimensional distribution in space since this would require an extra dimension to represent the magnitude at every point. A dimensionality reduction is, hence, necessary. A three-dimensional scalar field can, for example, be reduced into a set of two-dimensional surfaces with the third being the magnitude in question or even reducing it to a line with the second dimension being the magnitude under study.

The electron density, a three-dimensional object, is often dimensionality-reduced to examine its topography in a given plane. In this case, the orthogonal axes defining the plane are augmented with a third perpendicular axis representing the value of the electron density. This very strategy is adopted in several other fields, one being statistics where the density in question consists of a set of data points.<sup>183</sup>

The representation of the density in a plane can be done using contour representation, warm-cold colors to reflect the magnitude of the density, or relief plots. One can further analyze the topography of the surface through its associated gradient vector field (which locates the critical points that, through the Hessian, are further classified according to the number of positive, negative, or null curvatures). The Laplacian (the trace of the Hessian) in the plane identifies regions of local concentration and depletion of electron

density. The gradient vector field, by locating the critical points and the unique gradient paths that link them, determines the *topology* of the surface whereby the connectivity of the various critical points in the surface is identified. The topology, hence, emerges from the gradient vector field associated with the topography of a given surface. The procedure can be repeated for as many surfaces as necessary until the full topology of the scalar field is worked out.

While topography is sensitive to deformation, topology is not. In other words, topology, unlike topography, is invariant. Thus, properties that remain invariant under continuous deformations such as stretching or bending are “topological properties”. In chemistry, a conformational change may have drastic effects on the topography of the electron density in certain planes, but the topology (the bonding pattern) remains generally unchanged (invariant). In three-dimensional spaces, topological properties include connectedness (bond-path pattern) and boundary surfaces (e.g., (internal) zero-flux surfaces or (external) van der Waals surfaces). A sphere and a cube are considered topologically equivalent in three-dimensional space because one can be deformed into the other without tearing or cutting. The same can be said of a conformational change in a molecule since the boundaries of the atoms-in-the-molecule will change and deform but without tearing or cutting, so the atoms are “topological” in the sense of changing shape without cutting and tearing, i.e., without change in topology, namely, bond-path connectivity.

**3.1.3. The Electron Density: From Topography to Topology.** The quantum theory of atoms-in-molecules (QTAIM)<sup>1,29,30,178,179</sup> begins by analyzing the three-dimensional topography of the electron density by examining its associated gradient vector field. From the topography of the electron density, the shape and boundaries of the atoms in the molecule or the crystal emerge as nonoverlapping open quantum subsystems. Such atoms, being bounded by a surface, do not overlap with each other.

The topography of the electron density is, to a large extent, governed by the Coulombic force of attraction exerted by the nuclei on the electrons. As a result, the density exhibits maxima (cusps) at the position of each nucleus according to Kato's condition expressed above (eq 3.1.1.4). Figure 1 shows a familiar topographic map of the total electron density of a Watson–Crick base pair in its main plane. The figure shows simultaneously representative isodensity lines constituting a “contour plot” of the electron density, representative lines of the gradient vector field of the electron density, and the molecular graph consisting of the set of bond-paths linking the nuclei in the base-pair. An examination of the gradient vector field lines reveals that lines in proximity to a given nucleus converge on this nucleus, suggesting a partition of space into mononuclear regions identified as Atoms-in-Molecules (AIMs). In this way, the molecular space is split into neighboring atoms without leaving any gaps. In some systems, such as lithium clusters, color F-centers, hydrated electrons, etc., there occurs maxima at other than atomic nuclei termed non-nuclear maxima (NNMs).<sup>185–195</sup> Both nuclei and NNMs act as attractors to a set of neighboring gradient vector field lines and define a bounded region of space associated with a given set of gradient vector field and bounded by a well-defined separatrix, in the first case defining atoms-in-molecules, and in the second pseudoatoms-in-molecules. The partitioning surfaces, termed the “zero-flux interatomic surfaces”, satisfy Bader's boundary condition:

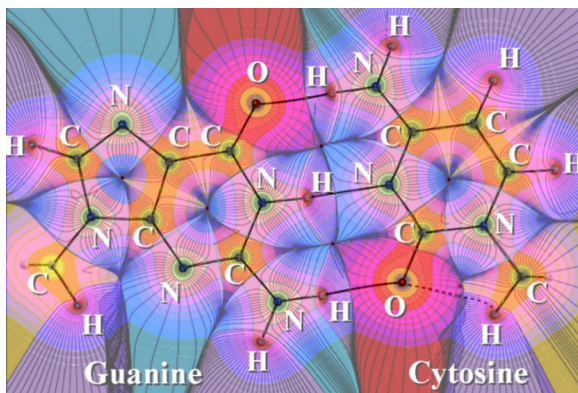


**Figure 1.** A representation of the electron density, its associated gradient vector field, and the molecular graph in the plane of a Watson–Crick nucleic acid base pair (guanine–cytosine (GC)). The isodensity contours start from the outside at 0.001 au, then  $2 \times 10^n$ ,  $4 \times 10^n$ , and  $8 \times 10^n$  with  $n = -3, -2, -1, 0, +1$ , etc. Bond-paths link certain pairs of nuclei, while the separatrices between each pair of bonded atoms denote the interatomic zero-flux surface separating them in the plane of the plot. A bond critical point (BCP) (where  $\nabla\rho(\mathbf{r}) = 0$ ) is located at the point where a given bond-path crosses its associated interatomic surface. Adapted with permission from ref 184. Copyright 2002 C. F. Matta.

$$\nabla\rho(\mathbf{r}) \cdot \mathbf{n}(\mathbf{r}) = 0, \forall \mathbf{r} \in S(\Omega, \mathbf{r}) \quad (3.1.3.1)$$

locally, where  $\mathbf{n}(\mathbf{r})$  is the normal vector to the surface.

The electron density scalar field exhibits critical points (CP), i.e., points where the three first derivatives of the density vanish (each derivative is zero and not just their sum), that is

$$\nabla\rho = \mathbf{i}\frac{d\rho}{dx} + \mathbf{j}\frac{d\rho}{dy} + \mathbf{k}\frac{d\rho}{dz} = \vec{0} \quad (3.1.3.2)$$

There are nine second derivatives, which can be cast into the “Hessian” matrix, that, after diagonalization, is

$$\Lambda = \begin{pmatrix} \frac{\partial^2\rho}{\partial x'^2} & 0 & 0 \\ 0 & \frac{\partial^2\rho}{\partial y'^2} & 0 \\ 0 & 0 & \frac{\partial^2\rho}{\partial z'^2} \end{pmatrix}_{\mathbf{r}'=\mathbf{r}_c} = \begin{pmatrix} \lambda_1 & 0 & 0 \\ 0 & \lambda_2 & 0 \\ 0 & 0 & \lambda_3 \end{pmatrix} \quad (3.1.3.3)$$

where  $\lambda_i$  is a principal curvature with respect to one of the three principal axes ( $x'$ ,  $y'$ ,  $z'$ ) aligned with (or perpendicular to) the bond-path,  $\mathbf{r}_c$  is the coordinate of the critical point in question, and where the primes denote the coordinate system aligned with the principal curvatures obtained by diagonalization of the Hessian (equivalent to a rotation of the coordinate system). The trace of the Hessian matrix, the Laplacian, is rotationally invariant and is expressed as

$$\nabla^2\rho(\mathbf{r}) = \nabla \cdot \nabla\rho(\mathbf{r}) = \frac{\partial^2\rho(\mathbf{r})}{\partial x^2} + \frac{\partial^2\rho(\mathbf{r})}{\partial y^2} + \frac{\partial^2\rho(\mathbf{r})}{\partial z^2} \quad (3.1.3.4)$$

Critical points are ranked according to their “rank” and “signature”. The rank ( $\omega$ ) is the number of nonzero curvatures and is usually 3 because CPs with  $\omega < 3$  are unstable. The algebraic sum of the signs of the curvatures is known as the signature ( $\sigma$ ), and this can be positive or negative. There occur

four types of critical points denoted by  $(\omega, \sigma)$ : (3, -3) referred to as a nuclear critical point (NCP) (a rarer occurrence are non-nuclear maxima or non-nuclear attractor (NNM/NNA), which are maxima at positions not coinciding with nuclei),<sup>185–195</sup> (3, -1) known as the bond critical point (BCP), (3, +1) called the ring critical point (RCP), and (3, +3) termed the cage critical point (CCP).

The number  $n$  and the type of critical points satisfy the Poincaré–Hopf topological relation (molecule)<sup>1</sup> or the Morse relation (crystal):<sup>103</sup>

$$n_{\text{NCP}} - n_{\text{BCP}} + n_{\text{RCP}} - n_{\text{CCP}} = \begin{cases} 1, & \text{molecule} \\ 0, & \text{crystal} \end{cases} \quad (3.1.3.5)$$

The BCP is a three-dimensional saddle point on the bond-path, a line of maximum density connecting, in space, two nuclei that are chemically bonded.

**3.1.4. Bader’s Zero-Flux Surface as a Quantum Condition for Atoms-in-Molecules (AIMs).** An Atom-in-a-Molecule (AIM) is taken as a mononuclear region of space bounded by a zero-flux surface within a molecule or a crystal. The zero-flux condition is now shown to be necessary for the identification of AIMs as open quantum subsystems with well-defined kinetic energy and unique contribution to the total molecular energy.

Leibnitz’s identity for the divergence of the product of a vector function where the vector function is taken as the gradient of a one-electron wave function ( $\psi$ ) reads:

$$\begin{aligned} \nabla^2(\psi^*\psi) &= \nabla \cdot [(\nabla\psi^*)\psi + \psi^*(\nabla\psi)] = (\nabla^2\psi^*)\psi \\ &+ \psi^*(\nabla^2\psi) + 2\nabla\psi^*\nabla\psi \end{aligned} \quad (3.1.4.1)$$

It can be rearranged as

$$-[\psi\nabla^2\psi^* + \psi^*\nabla^2\psi] = 2\nabla\psi^*\cdot\nabla\psi - \nabla^2(\psi^*\psi) \quad (3.1.4.2)$$

Substituting the one-electron function with an antisymmetrized normalized many-electron wave function  $\Psi$  followed by summing over  $N$  electrons and multiplication by fundamental constants throughout, we get (in general units):

$$\begin{aligned} -\frac{\hbar^2}{4m} \sum_{i=1}^N (\Psi\nabla_i^2\Psi^* + \Psi^*\nabla_i^2\Psi) &= \frac{\hbar^2}{2m} \sum_{i=1}^N \nabla_i\Psi^*\cdot\nabla_i\Psi \\ -\frac{\hbar^2}{4m} \sum_{i=1}^N \nabla_i^2(\Psi^*\Psi) \end{aligned} \quad (3.1.4.3)$$

where  $m$  is the rest mass of the electron and  $\hbar$  is the reduced Planck constant. Given the indistinguishability of electrons, we can write

$$\begin{aligned} -\frac{\hbar^2}{4m} N(\Psi\nabla^2\Psi^* + \Psi^*\nabla^2\Psi) &= \frac{\hbar^2}{2m} N\nabla\Psi^*\cdot\nabla\Psi \\ -\frac{\hbar^2}{4m} N\nabla^2(\Psi^*\Psi) \end{aligned} \quad (3.1.4.4)$$

Finally, integrating over all space coordinates except one and summing over the two spins gives

$$\begin{aligned} -\frac{\hbar^2}{4m} N \int d\tau' (\Psi\nabla^2\Psi^* + \Psi^*\nabla^2\Psi) &= \\ \frac{\hbar^2}{2m} N \int d\tau' \nabla\Psi^*\cdot\nabla\Psi - \frac{\hbar^2}{4m} N \int d\tau' \nabla^2(\Psi^*\Psi) \end{aligned} \quad (3.1.4.5)$$

where we introduce the notation  $\int d\tau' \equiv \sum_{\text{spins}} \int \dots \int d\mathbf{r}_2 \dots d\mathbf{r}_N$ , or

$$k(\mathbf{r}) = g(\mathbf{r}) - l(\mathbf{r}) \quad (3.1.4.6)$$

where,  $k(\mathbf{r})$  is the Schrödinger kinetic energy density,  $g(\mathbf{r})$  is the gradient kinetic energy density, and  $l(\mathbf{r})$  is the Laplacian function density.

It may seem odd to have two different definitions of the kinetic energy density in the last result. In fact, there is an infinite number of valid kinetic energy density functions that integrate over all space to yield the same expectation value of the kinetic energy. This ambiguity of the kinetic energy density is a manifestation of Heisenberg's uncertainty principle since position and momentum are incompatible (noncommuting) observables that cannot be specified simultaneously to an infinite precision, a simultaneous definition that lies at the core of any definition of the kinetic energy density (for a full discussion, see refs 196–198).

Switching the order of integration and derivative in the last term of eq 3.1.4.5 followed by the substitution of the definition of the electron density, one obtains

$$\begin{aligned} -\frac{\hbar^2}{4m} N \int d\tau' (\Psi \nabla^2 \Psi^* + \Psi^* \nabla^2 \Psi) = \\ -\frac{\hbar^2}{2m} N \int d\tau' \nabla \Psi^* \cdot \nabla \Psi - \frac{\hbar^2}{4m} \nabla^2 \rho \end{aligned} \quad (3.1.4.7)$$

If we integrate over the remaining position vector:

$$\begin{aligned} -\frac{\hbar^2}{4m} N \int_{-\infty}^{+\infty} d\mathbf{r} \left[ \int d\tau' (\Psi \nabla^2 \Psi^* + \Psi^* \nabla^2 \Psi) \right] = \\ -\frac{\hbar^2}{2m} N \int_{-\infty}^{+\infty} d\mathbf{r} \left[ \int d\tau' (\nabla \Psi^* \cdot \nabla \Psi) \right] - \frac{\hbar^2}{4m} \int_{-\infty}^{+\infty} d\mathbf{r} (\nabla \cdot \nabla \rho) \end{aligned} \quad (3.1.4.8)$$

and converting the last volume integral into an integral of the normal component crossing the surface bounding the volume (to obtain the flux through the surface) by applying Gauss' divergence theorem, we get

$$\begin{aligned} -\frac{\hbar^2}{4m} N \int_{-\infty}^{+\infty} d\mathbf{r} \left[ \int d\tau' (\Psi \nabla^2 \Psi^* + \Psi^* \nabla^2 \Psi) \right] \\ = \frac{\hbar^2}{2m} N \int_{-\infty}^{+\infty} d\mathbf{r} \left[ \int d\tau' (\nabla \Psi^* \cdot \nabla \Psi) \right] \\ - \frac{\hbar^2}{4m} \oint dS(\Omega, \mathbf{r}) [\nabla \rho \cdot \mathbf{n}(\mathbf{r})] \end{aligned} \quad (3.1.4.9)$$

Since the limits of integration in the first two integrals of eq 3.1.4.9 are at infinity, the bounding surface is at infinity as well. The integrals, in this case, result in the vanishing of the last term since at infinity the density is constant and vanishing ( $\nabla \rho(\mathbf{r}) = 0$ ). In this case, we have

$$\underbrace{-\frac{\hbar^2}{4m} N \int_{-\infty}^{+\infty} d\mathbf{r} \left[ \int d\tau' (\Psi \nabla^2 \Psi^* + \Psi^* \nabla^2 \Psi) \right]}_K = \underbrace{\frac{\hbar^2}{2m} N \int_{-\infty}^{+\infty} d\mathbf{r} \left[ \int d\tau' (\nabla \Psi^* \cdot \nabla \Psi) \right]}_G \quad (3.1.4.10)$$

or

$$K = G \equiv T \quad (3.1.4.11)$$

where  $T$  is the (unambiguous, "well-defined") kinetic energy of this system of electrons, which could be obtained by integrating either expression of the kinetic energy density over all space. If we run the integral over only an arbitrary

closed volume  $\Omega$ , the last integral in eq 3.1.4.8 does not necessarily vanish, and hence we retain that term it and write:

$$K(\Omega) = G(\Omega) - \frac{\hbar^2}{4m} \int_{\Omega} d\mathbf{r} \nabla \cdot \nabla \rho \quad (3.1.4.12)$$

which after the use of the divergence theorem gives

$$K(\Omega) = G(\Omega) - \frac{\hbar^2}{4m} \oint dS(\Omega, \mathbf{r}) [\nabla \rho \cdot \mathbf{n}(\mathbf{r})] \quad (3.1.4.13)$$

where  $\mathbf{n}(\mathbf{r})$  is the unit normal vector pointing outward of the subsystem.

A choice of the bounding surface for  $\Omega$  to satisfy Bader's local zero-flux boundary condition ensures that the last term vanishes. As a result, for such a special open system bound by a zero-flux surface, the kinetic energy is also well-defined, on par with the total system (eq 3.1.4.11). In this particular case of an open system that we call an Atom-in-a-Molecule (an AIM), one has:

$$K(\Omega) = G(\Omega) \equiv T(\Omega) \quad (3.1.4.14)$$

in complete analogy with the total system (eq 3.1.4.11).

Bader et al. first postulated<sup>199,200</sup> and later proved<sup>201–203</sup> an atomic statement of the virial theorem, i.e., that

$$T(\Omega) = -\frac{1}{2} V(\Omega) \quad (3.1.4.15)$$

leading to a simple expression for an atom's contribution to the total energy:

$$E(\Omega) = T(\Omega) + V(\Omega) = -T(\Omega) \quad (3.1.4.16)$$

decomposing the total energy of the molecule or crystallographic unit cell into a sum of atomic (virial) energies:

$$E = \sum_{\Omega} E(\Omega) \quad (3.1.4.17)$$

The superficial triviality of this result should not conceal its profundity, and that is that one can obtain the contribution of a given atom to the total energy, which includes kinetic and potential terms, classical and quantum contributions, and one- and two-electron contributions, through the sole knowledge of the (one-electron) average kinetic energy. While this result is foundational for QTAIM, it only applies for optimized geometries such as local or global minima or transition states of any order. Otherwise, one has to add to the atomic energy expression the virial of the net force on its nucleus. The sum of such atomic virial terms arising from the forces on the nuclei is, of course, independent of the choice of origin, but that origin independence is not a property of the individual atomic force virials. This origin dependence of the virial of the net forces on the nuclei invalidates the use of virial energies for an arbitrary (non-fully optimized) geometry (see ref 204 and references cited therein). An elegant workaround to this problem has been proposed by Martín Pendás et al. by partitioning the energy terms in the Hamiltonian into self- and interaction-terms, yielding an alternative energy decomposition within QTAIM but which is valid no matter what geometry is being studied. This scheme is known as the Interacting Quantum Atoms (IQA) energy decomposition.<sup>38–40,205–208</sup> As mentioned above, the roots of this work can be encountered in the work of Cioslowski and Liu<sup>36</sup> and that of Popelier and Kosov.<sup>37</sup>

Thus, IQA<sup>38–40,205–208</sup> is an atomic-interatomic energy decomposition meant as a solution to the origin dependence of the QTAIM atomic virial energies except for equilibrium structures. This origin dependence limits the use of virial energies to fully geometry-optimized structures but not, for example, to intermediate geometries on the potential energy surface. To obtain IQA energy components, space is first partitioned according to QTAIM at zero flux surfaces (eq 3.1.3.1), and then the total energy  $E$  is expressed as a sum of self- and interaction-terms as follows:

$$E = \sum_A E_{\text{self}}^A + \frac{1}{2} \sum_A \sum_{B \neq A} E_{\text{int}}^{AB} \quad (3.1.4.18)$$

An atom's so-called self-energy is written as

$$E_{\text{self}}^A = T^A + V_{\text{en}}^{AA} + V_{\text{ee}}^{AA} \quad (3.1.4.19)$$

in which the first term refers to the kinetic energy, the second to the electron–nuclear attractive energy of the electrons in  $A$  and the nucleus of  $A$ , and the third symbolizes the electron–electron repulsive energy within atom  $A$ , and where an interaction term is a sum of all of the interactions between the electrons and the nuclei of two atoms  $A$  and  $B$ , that is

$$E_{\text{int}}^{AB} = V_{\text{nn}}^{AB} + V_{\text{ne}}^{AB} + V_{\text{en}}^{AB} + V_{\text{ee}}^{AB} \quad (A \neq B) \quad (3.1.4.20)$$

where  $V_{\text{ne}}^{AB}$  is the energy of attraction of the nucleus of  $A$  with electrons in the basin of  $B$ , while  $V_{\text{en}}^{AB}$  is the energy of attraction of electrons in the basin of the  $A$  with the nucleus of  $B$ . One can hence define additive monatomic energy terms such that

$$E_{\text{add}}^A = E_{\text{self}}^A + \frac{1}{2} \sum_{B \neq A} E_{\text{int}}^{AB} \quad (3.1.4.21)$$

which sum to the total energy  $E$ , i.e.:

$$E = \sum_{i=1}^n E_{\text{add}}^{A_i} \quad (3.1.4.22)$$

In this manner, the set of additive atomic energies  $\{E_{\text{add}}^{A_i}\}$  is unique and, importantly, well-defined at any molecular geometry, whether fully optimized or not.

### 3.2. Is Energy “Equally Transferable” as the “Shape” of an Atom-in-a-Molecule?

Since the shape of an Atom-in-a-Molecule is reflected in the form of its bounding zero-flux surface and since the electron density distribution inside this surface and the shape of the surface are interdetermined,<sup>209</sup> the important result about the additivity of atomic contributions to the total energy (eq 3.1.4.17) implies that (quoting Bader from the memory): “When the density of an atom in two different systems is transferable (similar), the kinetic energy density is also transferable, and so is that atom’s contribution to the total energy.” Bader restated this observation as “the shape of an atom in real space - as determined by electron density - determines its contribution to total energy.”

The shape of an atom-in-a-molecule is reflected by its departure from spherical symmetry as can be quantifiably measured by a multipolar expansion of either its density or its electrostatic potential.

Within the Born–Oppenheimer approximation, the molecular dipole moment is the sum of the negative of the expectation value of the position operator  $\langle \hat{\mathbf{r}} \rangle$  and the position vectors of the nuclei weighted  $\mathbf{X}_A$  by their atomic numbers

(their charges in atomic units, i.e.,  $Z_A$ ). This, in au ( $|e| = 1$ ), is expressed as:

$$\begin{aligned} \boldsymbol{\mu} &= -\langle \hat{\mathbf{r}} \rangle + \sum_A \mathbf{X}_A Z_A = - \int d\tau \left[ \sum_i^N \hat{\mathbf{r}}_i \Psi^* \Psi \right] + \sum_A \mathbf{X}_A Z_A \\ &= - \int d\tau [N \mathbf{r} \Psi^* \Psi] + \sum_A \mathbf{X}_A Z_A = - \int d\mathbf{r} \mathbf{r} \rho(\mathbf{r}) \\ &\quad + \sum_A \mathbf{X}_A Z_A \end{aligned} \quad (3.2.1)$$

The molecular dipole moment can be decomposed into atomic or group contributions by, first, making the following transformation to convert the molecular coordinate system into an atom-centered system:

$$\mathbf{r} = \mathbf{r}_A + \mathbf{X}_A \quad (3.2.2)$$

where  $\mathbf{r}_A$  is relative to nucleus  $A$  at  $\mathbf{X}_A$  with charge  $Z_A$ , which when inserted into eq 3.2.1 results in

$$\boldsymbol{\mu} = \sum_A [\mathbf{M}(A) + \mathbf{X}_A q(A)] \quad (3.2.3)$$

where  $q(A)$  is the atomic monopole, i.e., the QTAIM charge of atom  $A$  obtained by integrating the electron density (to obtain the electron population of the atom ( $N(A)$ ) taken with a negative sign plus the nuclear charge, i.e.:

$$q(A) = Z_A - N(A) = Z_A - \int_A \rho(\mathbf{r}) d\mathbf{r} \quad (3.2.4)$$

In this manner, the contribution of atom  $A$  to the system’s dipole moment is a sum of two terms: an atomic dipolar polarization term ( $\mathbf{M}(A)$ ) measuring the atoms departure from spherical symmetry and a charge transfer term accounting for the flow of charge between neighboring atoms ( $\mathbf{X}_A q(A)$ ). The charge transfer terms are clearly origin-dependent since they depend on a given nucleus position vector expressed in the chosen arbitrary coordinate system. This origin dependence is lifted by the addition of a sum of terms that account for charge transfers from  $A$  to all atoms with which it shares a bond-path, leading to<sup>210–213</sup>

$$\boldsymbol{\mu} = \sum_A \left\{ \mathbf{M}(A) + \sum_{B \neq A} [\mathbf{X}^c(A|B) - \mathbf{X}_A] q(B) \right\} \equiv \sum_A \boldsymbol{\mu}(A) \quad (3.2.5)$$

where  $\boldsymbol{\mu}(A)$  is the contribution of atom  $A$  to the molecular dipole moment, defined as

$$\boldsymbol{\mu}(A) \equiv \mathbf{M}(A) + \sum_{B \neq A} [\mathbf{X}^c(A|B) - \mathbf{X}_A] q(B) \quad (3.2.6)$$

and where  $\mathbf{X}^c(A|B)$  is the position vector of the BCP on the interatomic surface between atom  $A$  and atom (or group)  $B$ ,  $S(A|B)$ .

A more general expression for  $\boldsymbol{\mu}(A)$  that is a function of  $A$  only, independent of the charge on its bonded neighbors (which would be problematic to determine in infinite periodic systems such as a crystal), can be obtained using Maxwell’s equation expressing the electrostatic Gauss’ Law.<sup>184,212</sup> Thus, we can replace the charge of each neighbor by the flux in the electrostatic field  $\mathbf{E}(\mathbf{r})$  due to the charge enclosed within  $A$  through the zero-flux surface shared with that neighbor. In differential form and in au (in which the electric constant  $k_{\text{elec}} = 1/(4\pi\epsilon_0) = 1$ ), this Maxwell’s equation is expressed as:

$$\nabla \cdot \mathbf{E}(\mathbf{r}) = 4\pi\rho_{\text{total}}(\mathbf{r}) \quad (3.2.7)$$

where  $\rho_{\text{total}}$  is the sum of the continuous charge density distribution of the electrons with a negative sign and the nuclear point-like positive charge (eq 3.1.1.5) (where the symbol X (instead of R) is used here to denote nuclear coordinates). On integration over a volume  $\Omega$ , we get:

$$\int_A d\mathbf{r} \nabla \cdot \mathbf{E}(\mathbf{r}) = 4\pi \int_A d\mathbf{r} \rho_{\text{total}}(\mathbf{r}) = 4\pi \left[ Z_A - \int_A d\mathbf{r} \rho(\mathbf{r}) \right] \\ = 4\pi q(A) \quad (3.2.8)$$

which is the well-known integrated form of Gauss's Law applied to atom A.

The divergence theorem can be used to convert the volume integral on the L.H.S. of eq 3.2.8 into a surface integral over the bounding surface, that is:

$$\oint dS(A) \mathbf{n}(\mathbf{r}) \cdot \mathbf{E}(\mathbf{r}) = 4\pi q(A) \quad (3.2.9)$$

which, in words, is simply a statement of Maxwell's equation that says that the flux in the electric field  $\mathbf{E}(\mathbf{r})$  through the Gaussian surface surrounding a given volume ( $S(A)$ ) is equal to the net charge enclosed by the volume up to a constant that depends on the choice of units. An elegant computational implementation of Gauss' electric law for atoms-in-molecules has been developed by Popelier some time ago.<sup>214</sup>

In addition to any external van der Waals surface for exposed atoms, the surface bounding an Atom-in-a-Molecule internally,  $S(A)$ , is generally a union of several interatomic zero-flux surfaces  $S(A|B)$ , i.e.:

$$S(A) = \bigcup_i S(A|B_i) \quad (3.2.10)$$

where  $B_i$  denotes the  $i$ th atom, which is bonded to A, and where the vertical bar symbolizes the zero-flux surface between any of these atomic pairs, and because of the electrical neutrality constraint, that requires that

$$q(A) = - \sum_{B \neq A} q(B) \quad (3.2.11)$$

Then  $q(A)$  can be re-expressed as:

$$q(A) = 4\pi \sum_{B \neq A} \oint dS(A|B; \mathbf{r}) \mathbf{n}(\mathbf{r}) \cdot \mathbf{E}(\mathbf{r}) \quad (3.2.12)$$

which is equivalent to

$$q(A) = - \sum_{B \neq A} Q(A|B) = \sum_{B \neq A} Q(B|A) \quad (3.2.13)$$

where  $Q$  refers to the (*signed*) integral of the normal component of the electric field through a given surface (that is, the electric flux through the surface). From the above considerations, the first equality of eq 3.2.5 can be re-expressed as

$$\boldsymbol{\mu} = \sum_A \left\{ \mathbf{M}(A) + \sum_{B \neq A} [\mathbf{X}^c(A|B) - \mathbf{X}_A] \right. \\ \times \left. \left[ -\frac{1}{4\pi} \oint dS(A|B; \mathbf{r}_s) \mathbf{E}(\mathbf{r}) \cdot \mathbf{n}(\mathbf{r})_B \right] \right\} \quad (3.2.14)$$

or

$$\boldsymbol{\mu} = \sum_A \boldsymbol{\mu}(A) \quad (3.2.15)$$

with the final expression of an atomic contribution to the molecular dipole moment given by

$$\boldsymbol{\mu}(A) \equiv \mathbf{M}(A) + \sum_{B \neq A} [\mathbf{X}^c(A|B) - \mathbf{X}_A] \\ \times \left[ -\frac{1}{4\pi} \oint dS(A|B; \mathbf{r}_s) \mathbf{E}(\mathbf{r}) \cdot \mathbf{n}(\mathbf{r})_B \right] \quad (3.2.16)$$

In summary, an atom contributes to the molecular dipole moment  $\boldsymbol{\mu}$  through an atomic polarization dipolar term arising from the noncoincidence of the center of electronic charge in the atom with the nucleus ( $\mathbf{M}(A)$ ) and a sum of dipolar terms arising from the flux in the electric field through each shared interatomic surface with a bonded neighbor referenced to the position vector of nucleus A. The latter is the charge transfer term.

If we are dealing with a (finite) molecule, one can use either expression (the one in terms of direct charge transfers (eq 3.2.5) or the one that involves the electric flux (eq 3.2.16)) to obtain an atomic contribution to the total dipole moment. However, for infinite (usually periodic) systems, whether one-, two-, or three-dimensional, we must use the latter, that is, eq 3.2.16, because charge transfer through any interatomic surface between A and infinity can only be calculated in this manner.

Combining and simplifying the notation of eqs 3.2.14–3.2.16, we write this result as

$$\boldsymbol{\mu} = \sum_A \boldsymbol{\mu}(A) = \sum_A \left\{ \mathbf{M}(A) + \sum_{B \neq A} [\mathbf{X}^c(A|B) - \mathbf{X}_A] Q(A|B) \right\} \quad (3.2.17)$$

in which  $Q(A|B)$  symbolizes the surface integral including  $(-1/4\pi)$ , with the normal vector on the surface directed from B to A, and hence

$$q(B) = Q(A|B) = -Q(B|A) \quad (3.2.18)$$

leading to

$$q(A) = \sum_{B \neq A} Q(B|A) \quad (3.2.19)$$

Summing pairs of terms associated with one and the same surface, such as  $Q(A|B)$  and  $Q(B|A)$ , yields  $(\mathbf{X}_A - \mathbf{X}_B) Q(B|A)$ , useful in the calculation of group or unit cell contributions to the overall dipole moment or polarization. The calculation of atomic and/or group contributions to the molecular dipole moment or crystallographic dielectric polarization has been implemented in the program FRAGDIP,<sup>184,211,215</sup> which has been superseded as an option by the comprehensive QTAIM analysis software AIMAll.<sup>216</sup>

An example is given below illustrating the parallel transferability of the energy and the contribution to the dipole moment following ref 211. Consider a set of linear polyacetals capped with hydrogens with the general formula  $\text{H}|\text{CH}_2\text{O}|_\text{H}$  where the vertical bars represent the interatomic surfaces bounding the repeating group. The  $|\text{CH}_2\text{O}|$  group can be thought of as a unit cell in a one-dimensional periodic system. The electron density map, the gradient vector field of the electron density, the gradient kinetic energy density, and the potential energy density (virial field) for a central portion of  $\text{H}|\text{CH}_2\text{O}|_\text{H}$  are displayed in Figure 2 along with overlays of the

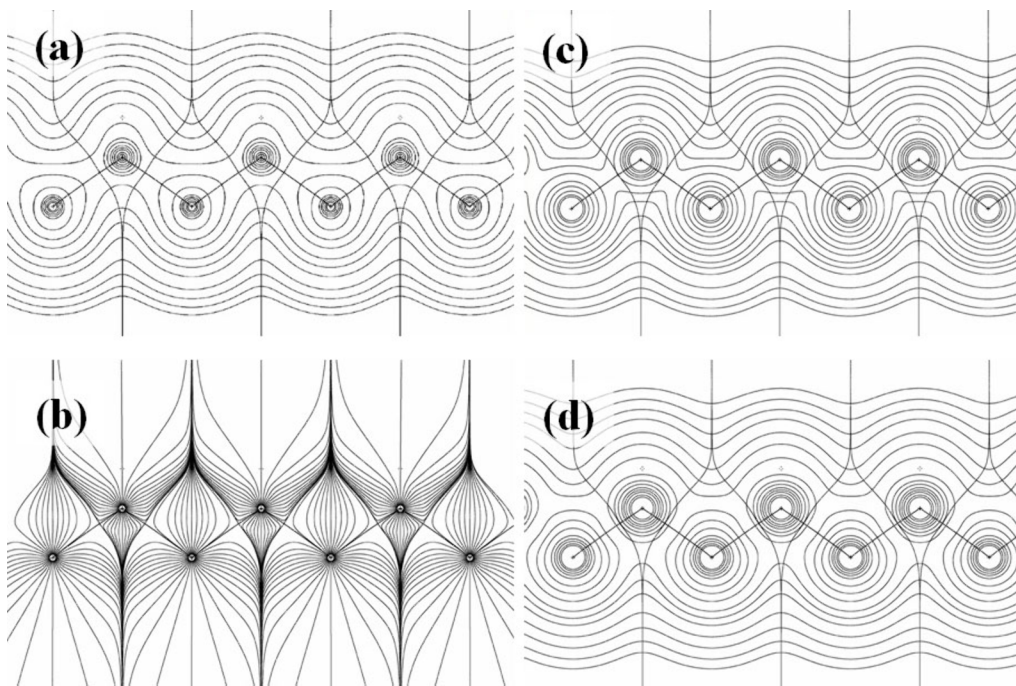


**Figure 2.** (a) Electron density contour map for the central part of  $\text{H}|\text{CH}_2\text{O}|_8\text{H}$  with overlays from the interatomic surfaces and bond-paths. (b) The gradient vector field associated with the electron density. (c) The gradient kinetic energy density. (d) The potential energy density (virial field). Adapted with permission from ref 211. Copyright 2001 Wiley Periodicals, LLC.

**Table 1. Transferability of Cell Properties in Linear  $\text{H}|\text{CH}_2\text{O}|_n\text{H}$** <sup>a</sup>

system <sup>b</sup>	cell	q(cell)	M(cell)	μ(cell)	E(cell)	v(cell) <sup>c</sup>
$n = 4$	2	-0.00980	1.19868	0.56488	-113.881152	228.32
	3	-0.00923	1.20837	0.55883	-113.881330	227.89
$n = 6$	3	0.00120	1.21491	0.56181	-113.881344	227.31
	4	0.00156	1.21585	0.56155	-113.881380	227.36
$n = 8$	4	0.00259	1.21698	0.56370	-113.881561	227.23
	5	0.00267	1.21734	0.56377	-113.881522	227.30
$n = 21$	11	-0.00344	1.21570		-113.879348	228.18
	12	-0.00257	1.21448		-113.879662	227.87
average		-0.00213	1.21279	0.56242	-113.880912	227.68
std dev		0.00476	0.00594	0.00198	0.000825	0.41

<sup>a</sup>Values in au. Reproduced with permission from ref 211. Copyright 2001 Wiley Periodicals, LLC. <sup>b</sup> $n$  is the number of cells denoted by the vertical bars in  $\text{H}|\text{CH}_2\text{O}|_n\text{H}$ , and the cell numbering starts at the methyl end of the system. <sup>c</sup>Volume integrated to the 0.001 au isodensity envelope.

interatomic surfaces and bond-paths in the plane of the drawing.

The charge, group contribution to the dipole moment, volume, and energy of a  $|\text{CH}_2\text{O}|$  group all exhibit rapid convergence as we move away from the extremities. Since the system is electrically neutral, so should be its composing unit cells. This electrical neutrality is also quickly reached as can be seen from Table 1. Even for a system with as little as  $n = 4$  repeat units, the two interior cells have, each, a net charge of only 0.01 au. The table lists the properties of the two internal cells of chains with  $n = 4, 6, 8$ , and 21 units, and in all cases the deviations from electrical neutrality are negligible.

While we know of no mathematical proof that the transferability of the properties of the group's electron density is accompanied by the transferability of its energy contribution to the total energy, Table 1 and Figure 2 show the plausibility of this assertion numerically at least for the studied systems. The transferability of the atomic dipolar contributions, related

to the form of the atom (its departure from spherical symmetry), also parallel the transferability of the energies.

That being said, such "generalized transferability", as we may call it, is not as surprising in the light of Walter Kohn's concept of the "near-sightedness of the density matrix".<sup>217–219</sup> As emphasized by Bader et al., this generalized transferability of atomic and group properties underpins empirical additivity schemes epitomized by those of Benson et al.<sup>47,220–225</sup>

### 3.3. Bond-Paths Do Not Automatically Appear When Atoms-in-Molecules Are Congested

Generally, the molecular graph is homeomorphic with the chemical structure. Occasionally, however, inconsistencies are found between the bond-path-based molecular graph and the conventional chemical structure. It is occasionally asserted that bond-paths appear wherever two atoms occur in a crowded system such that their interatomic distance is less than the sum of their van der Waals radii. While this proposition may, superficially, be reasonable, it is untrue. In the Popperian

sense,<sup>226</sup> one counter example suffices to falsify it, and such an example is now briefly discussed.<sup>227</sup>

In 1998, an article by Tomaszewski et al.<sup>228</sup> suggested the observation of an extraordinary agostic bond between an  $sp^3$  carbon atom and a transition metal atom based on spatial proximity. The organometallic complex, subject of this study, is redrawn in Figure 3. From the distances indicated in the figure,

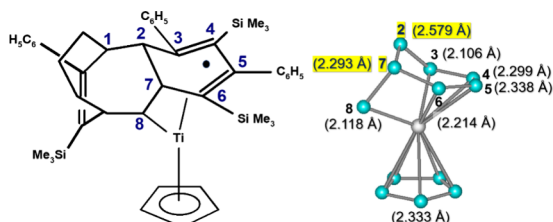


**Figure 3.** (Left) The structure of the titanium organometallic complex redrawn after Tomaszewski et al.<sup>228</sup> along with their atom numbering scheme. (Right) A ball-and-stick representation of the Ti atom (gray) and its immediate surrounding carbons (blue) after the omission of hydrogen atoms for clarity. The carbon atoms are labeled by their respective X-ray crystallographic distance from the Ti (in Å). All distances have experimental uncertainties of 0.006 Å except for the Ti–C2 and Ti–C7 distances, which have uncertainties of 0.007 Å. C2 and C7 (highlighted) are  $sp^3$  carbons with distances from the Ti atom suggestive of a fifth (agostic) bond for each of these two saturated carbon atoms.

atom C7 is closer to the central Ti atom than C4:  $d(\text{Ti–C7}) = 2.293(7)$  Å <  $d(\text{Ti–C4}) = 2.299(6)$  Å; meanwhile, only C4 is formally bonded to the transition metal. Further, the Ti–C7 distance is significantly shorter than the distance of the Ti to any of the five carbons of the adjacent cyclopentadienyl ring (with an average Ti–C distance  $\approx 2.333$  Å). Another close contact that is not formally connected by a “chemical bond” is the one between the Ti atom and C2, which are separated by 2.579(7) Å, still considerably smaller than the sum of the van der Waals radii of Ti and of C (ca. 2.2 and 1.7 Å, respectively<sup>229</sup>). From these observations, it was concluded that C2 and C7 are bonded agostically to the Ti atom.

These extraordinary claims were scrutinized from the perspective of the electron density distribution and its underlying structure by Bader and Matta.<sup>227</sup> The electron density of a model of the region surrounding the metal was obtained using Hartree–Fock and BLYP-DFT calculations in conjunction with a polarized basis set augmented with diffuse functions (6-31+G\* for C and H and a 14s 11p 6d basis contracted to [10s 8p 3d] triple- $\zeta$  valence basis set for the Ti) at the experimental geometry after optimizing only the positions of the hydrogen atoms but leaving all non-hydrogen atoms at their experimental geometry.<sup>227</sup>

The QTAIM results consistently lacked any indications of unusual (or even incipient) bonding between either C2 or C7 and the Ti atom. No bond-paths were found to link these carbons and the central metal. Comparatively low values of the delocalization indices (DIs) were found to connect these two carbons and the central Ti (the DIs, which measure the total exchange-correlation between two atoms, are defined and discussed in section 3.4). The low DI and the absence of bond-path are consistent with the concept that “bond-paths are privileged exchange channels”.<sup>230</sup> The DIs of Ti with C3, 4, 5, 6, and 8 are, respectively, 0.14, 0.14, 0.11, 0.24, and 0.33, while with C2 and C7 they are an order of magnitude lower (0.03

and 0.06 electrons, respectively). It may seem surprising that Ti–C4 ( $d = 2.299(6)$  Å) exhibits a DI of  $0.14 e^-$ , while the shorter Ti–C7 ( $d = 2.293(7)$  Å) is characterized by a DI of only  $0.06 e^-$ . Further, there are none of the hallmarks of any incipient bonding interaction that appears in the form of the Laplacian of the electron density pointing from either C2 or C7 toward the central Ti atom.<sup>227</sup>

An earlier theoretical study of the nature of the agostic bonding of the type C–H···Ti in three cationic Ti-complexes, conducted at the Hartree–Fock, DFT-BLYP, and MP2 levels of theory, demonstrates that agostic bonding is a distinct type of bonding on its own right and not an extension of the hydrogen-bonding interaction.<sup>231</sup> In fact, the hydrogen in question behaves in an opposite manner to the behavior of the acidic hydrogen in a typical hydrogen bond. In this paper, Popelier and Logothetis summarize the characteristics of an agostic bond into seven features that must coexist:<sup>231</sup> (1) the presence of a bond-path and its associated bond critical point and interatomic surface, (2) an electron density at the bond critical point of between 0.04–0.05 au, (3) a Laplacian of the density at the bond critical point in the range 0.15–0.25 au, (4) an increased electron population (slightly negative net charge on the hydrogen atom), (5) an energetic stabilization of the hydrogen, (6) an increase of dipolar polarization of the hydrogen, and (7) a slight increase in atomic volume of the hydrogen. The work of Popelier and Logothetis has been extended by Tognetti and Joubert et al. by considering a much larger data set of organometallic complexes and proposing to classify agosticity into four subtypes according to the bond-path and bond critical point properties including the use of kinetic energy densities in the classification.<sup>232,233</sup> While neither Popelier and Logothetis nor Tognetti and Joubert et al. consider the DIs in their analysis, the fact that none of the three first criteria of Popelier and Logothetis apply to the interactions claimed to be agostic on the basis of their geometric proximity by Tomaszewski et al.<sup>228</sup> is aligned to the conclusion of Bader and Matta negating the presence of such bonding in the organometallic compound of Figure 3.

These negative results falsify claims that closeness in space is enough to guarantee the appearance of a bond-path and that promolecular densities are capable of reproducing the bond-path structure of the full electron density. While closeness in space is no guarantee for the presence of chemical bonding, it is neither a sufficient condition for a so-called “repulsive” interaction when the classical picture suggests “steric repulsion”. This leads to an initially heated debate regarding the nature of some hydrogen···hydrogen (H···H) closed-shell interactions in congested systems.<sup>234</sup> Such H···H bond-paths appear, for example, in several polycyclic aromatic hydrocarbons (PAHs) and in planar biphenyl transition-state structure.<sup>234</sup> Such bond-paths were previously observed by Cioslowski and Mixon and described as “non-bonded interactions”.<sup>235</sup> An examination of the virial energies of the hydrogen atoms in these systems reveals that the hydrogen atoms involved in an H···H interaction are more stable than other hydrogen atoms in the system.

The initial controversy arose from the confusion of the description “locally stabilizing interaction” with a globally stabilizing one. Not all locally stabilizing interactions necessarily lead to global stabilization. In fact, the local stabilization of the H···H bonding in planar biphenyl is overshadowed by the destabilization of other atoms in the molecule (mainly the two *ipso*-carbon atoms) leading the

molecule to twist in its global minimum geometry. In planar biphenyl, each of the two pairs of *ortho*-hydrogens shares a bond (and virial) path and are more stable than the average of the rest of the hydrogens by ca. 8 kcal/mol per atom, imparting a total lowering of 32 kcal/mol to the energy of the system. To accommodate the bulk of the four coplanar H atoms in planar biphenyl, the two bonded *ipso*-carbons are slightly further apart than in the twisted minimum geometry. This elongation reduces the stabilizing interaction between the electrons in the basin of one *ipso*-carbon and the nucleus of the other. The net result is an overall rise in the virial energies of the two *ipso*-carbons, which together destabilize planar biphenyl by 44 kcal/mol with respect to the twisted conformer. Taking the lead energetic differences between the planar and the minimum conformers, we have approximately  $-38 + 44 \approx 6$  kcal/mol (which is in the ballpark order of magnitude of the actual energy barrier that is around 3 kcal/mol). To sum, the barrier to rotation of biphenyl is primarily driven by the four *ortho*-hydrogens (which favor the planar conformer) and the two *ipso*-carbons (which favor the twisted conformer exceeding the effect of the *ortho*-hydrogens).<sup>204,234,236,237</sup>

The reader must have noted that the discussion above has been couched in a language using energies and not forces (energy derivatives). At an optimized geometry, whether a minimum or a transition state, there are no net pairwise attractive or repulsive interactions between the atoms in the molecule since the net forces on nuclei are zero. It is thus meaningless to refer to the H···H interaction as repulsive or attractive at an optimized geometry since “attraction” and “repulsion” refer to a force (i.e., to an energy derivative), while it is meaningful to discuss relative energies (relative stabilities) whether global or local in a region within the molecule or crystal.

Popelier et al.<sup>238</sup> use a method termed the “Relative Energy Gradient (REG)”<sup>239</sup> to evaluate the changes in the Interacting Quantum Atoms (IQA)<sup>38–40</sup> energy components associated with the rotational deformation of the biphenyl C–C nuclear skeleton. The authors state the problem as “which subset of terms can be shown, by computation, to be responsible for the energy barriers.”<sup>238</sup> According to their REG analysis, the bond critical point between the two pairs of *ortho*-hydrogens in planar biphenyl is not indicative of a “repulsive interaction”. Instead, this analysis attributes the barrier to a “destabilization” of the four *ortho*-hydrogens mitigated by a weak covalent bonding formation between them. This partial cancellation reduces the role of *ortho*-hydrogens in the emergence of the barrier, which is, instead, played by the *ortho*-carbon atoms. The rotational barrier of biphenyl, in this approach, stems primarily from the energies of the two *ipso*-carbons, which, in the perpendicular conformation, are insufficiently stabilized by the exchange energy contributions.<sup>238</sup>

Cukrowski et al. define a method termed FALDI-ED (Fragment, Atomic, Localized, Delocalized and Interatomic – Electron Density (decomposition scheme))<sup>240–247</sup> by which the electron density at any point is decomposed into one- and two-center contributions, each of which, in their turn, can be integrated over atomic basins. In doing so, this decomposition expresses the electron density at any point as a sum of atomic contributions. There exists an alternative way to obtain atomic contributions at an arbitrary molecular point due to Gatti and Bader termed the source function (interested readers may consult refs 248–256). A FALDI decomposition can be applied at special points in the electron density scalar field, e.g.,

bond critical points. Further, if the density at the bond critical point for the FALDI analysis is further split based on the MO contributions to bonding (nonbonding and antibonding densities), one can gain insight into the nature of the bonding. The FALDI electron density decomposition indicates that hydrogen–hydrogen (H···H) interactions in biphenyl are characterized by a complex interplay of bonding and nonbonding (or even antibonding) components. According to the FALDI approach, most electron density in the H···H bonding can be traced to a strong overlap of *ortho* C–H  $\sigma$ -bonds and electrons delocalized between the phenyl rings and *ortho*-carbons and their hydrogens. In this manner, the CH···HC interaction reflects long-range electron delocalization over the entire biphenyl molecule with *meta*-carbons having a significant contribution to the bonding (more than the *para*-carbons and the hydrogens of the rings). The early debates sparked by this work<sup>237–261</sup> appear to have now subsided in favor of the locally stabilizing nature of this interaction.<sup>236,237,262–271</sup> A take-home message from this discussion is that language is important. While it is meaningful to refer to stabilizing and destabilizing interactions in an optimized geometry, it is totally devoid of sense to single out a given interaction as attractive or repulsive in such a stationary point on the potential energy hypersurface.

### 3.4. Electron Localization–Delocalization Matrices (LDMs)

Electron localization–delocalization matrices (LDMs) are mathematical constructs meant to capture molecular electron distributions.<sup>41–47</sup> An LDM is constructed from the QTAIM localization indices (localized electron population within atomic basins) along the diagonal and 1/2 of the delocalization indices (1/2 of the number of electrons shared between every pair of atoms) as off-diagonal elements. This section follows closely the exposition in the recent book on the subject.<sup>41</sup>

The spinless one- and two-body reduced density matrices (RDMs) are defined as<sup>272–276</sup>

$$\gamma_1(\mathbf{r}_1, \mathbf{r}'_1) = N \sum_{\sigma_1=\alpha,\beta} \sum_{\sigma_2=\alpha,\beta} \dots \sum_{\sigma_N=\alpha,\beta} \int \dots \int \Psi^*(\mathbf{r}'_1, \sigma_1; \mathbf{x}_2; \dots; \mathbf{x}_N) \times \Psi(\mathbf{r}_1, \sigma_1; \mathbf{x}_2; \dots; \mathbf{x}_N) d\mathbf{r}_2 \dots d\mathbf{r}_N \quad (3.4.1)$$

and

$$\Gamma_2(\mathbf{r}_1, \mathbf{r}_2; \mathbf{r}'_1, \mathbf{r}'_2) = \frac{N(N-1)}{2} \sum_{\sigma_1=\alpha,\beta} \sum_{\sigma_2=\alpha,\beta} \dots \sum_{\sigma_N=\alpha,\beta} \int \dots \int \Psi^*(\mathbf{r}'_1, \sigma_1; \mathbf{r}'_2, \sigma_2; \mathbf{x}_3; \dots; \mathbf{x}_N) \times \Psi(\mathbf{r}_1, \sigma_1; \mathbf{r}_2, \sigma_2; \mathbf{x}_3; \dots; \mathbf{x}_N) d\mathbf{r}_3 \dots d\mathbf{r}_N \quad (3.4.2)$$

where the normalization of the one-particle density matrix delivers the number of electrons and that of the two-particle density matrix the number of unique pairs of electrons. The latter can also be normalized to  $N(N-1)$  (without the division by 2), which counts the number of nondistinct electron pairs. The diagonal elements of these RDMS are, respectively, the density:

$$\rho(\mathbf{r}) = \gamma_1(\mathbf{r}, \mathbf{r}) \quad (3.4.3)$$

and the pair density:

$$\rho_2(\mathbf{r}_1, \mathbf{r}_2) = \Gamma_2(\mathbf{r}_1, \mathbf{r}_2; \mathbf{r}_1, \mathbf{r}_2) \quad (3.4.4)$$

The (spinless) pair density is defined as the probability of finding an electron in an infinitesimal volume at  $\mathbf{r}_1$  when another is in such a volume at  $\mathbf{r}_2$  regardless of their respective spins. Since electrons with opposite spins are distinguishable, the initial sums over spins can be omitted in the expression of the corresponding spin, leading to the expression for the spin-density matrices as:

$$\gamma_1^{\sigma_1}(\mathbf{r}_1, \mathbf{r}'_1) = N_{\sigma_1} \sum_{\sigma_2=\alpha, \beta} \dots \sum_{\sigma_N=\alpha, \beta} \int \dots \int \Psi^*(\mathbf{r}'_1, \sigma_1; \mathbf{x}_2; \dots; \mathbf{x}_N) \times \Psi(\mathbf{r}_1, \sigma_1; \mathbf{x}_2; \dots; \mathbf{x}_N) d\mathbf{r}_2 \dots d\mathbf{r}_N \quad (3.4.5)$$

and

$$\Gamma_2^{\sigma_1 \sigma_2}(\mathbf{r}_1, \mathbf{r}_2; \mathbf{r}'_1, \mathbf{r}'_2) = \frac{N_{\sigma_1}(N_{\sigma_2} - \delta_{\sigma_1 \sigma_2})}{2} \sum_{\sigma_3=\alpha, \beta} \dots \sum_{\sigma_N=\alpha, \beta} \int \dots \int \Psi^*(\mathbf{r}'_1, \sigma_1; \mathbf{r}'_2, \sigma_2; \mathbf{x}_3; \dots; \mathbf{x}_N) \times \Psi(\mathbf{r}_1, \sigma_1; \mathbf{r}_2, \sigma_2; \mathbf{x}_3; \dots; \mathbf{x}_N) d\mathbf{r}_3 \dots d\mathbf{r}_N \quad (3.4.6)$$

where, in the last (same spin) expression, the normalization differs from the corresponding opposite spin (eq 3.4.2). Similar to the spinless case, here the separate spin electron densities and pair densities are the diagonals of the corresponding RDMs, respectively:

$$\rho^\sigma(\mathbf{r}) = \gamma_1^\sigma(\mathbf{r}, \mathbf{r}) \quad (3.4.7)$$

and

$$\rho_2^{\sigma_1 \sigma_2}(\mathbf{r}_1, \mathbf{r}_2) = 2\Gamma_2^{\sigma_1 \sigma_2}(\mathbf{r}_1, \mathbf{r}_2; \mathbf{r}_1, \mathbf{r}_2) \quad (3.4.8)$$

For a Slater determinant, the RDMs are expressed as

$$\gamma^{\sigma_1 \sigma_2}(\mathbf{r}, \mathbf{r}') = \delta_{\sigma_1 \sigma_2} \sum_j n_j \psi_j(\mathbf{r}, \sigma_1) \psi_j^*(\mathbf{r}', \sigma_2) \quad (3.4.9)$$

and

$$\Gamma_2^{\sigma_1 \sigma_2}(\mathbf{r}_1, \mathbf{r}_2; \mathbf{r}'_1, \mathbf{r}'_2) = \frac{1}{2} \begin{vmatrix} \gamma^{\sigma_1 \sigma_1}(\mathbf{r}_1, \mathbf{r}'_1) & \gamma^{\sigma_1 \sigma_2}(\mathbf{r}_1, \mathbf{r}'_2) \\ \gamma^{\sigma_2 \sigma_1}(\mathbf{r}_2, \mathbf{r}'_1) & \gamma^{\sigma_2 \sigma_2}(\mathbf{r}_2, \mathbf{r}'_2) \end{vmatrix} \quad (3.4.10)$$

Can one express the pair density in terms of the simple one-electron density? At the Hartree–Fock level, the answer would be “yes” for opposite spin electrons since no correlation exists among them. In this case, the pair density is the product of the opposite uncorrelated spin densities:

$$\rho^{\alpha\beta}(\mathbf{r}_1, \mathbf{r}_2) = \rho^\alpha(\mathbf{r}_1) \rho^\beta(\mathbf{r}_2) \quad (3.4.11)$$

but this will not work for same-spin electrons. In the latter case, the simple product:

$$\rho^{\sigma\sigma}(\mathbf{r}_1, \mathbf{r}_2) = \rho^\sigma(\mathbf{r}_1) \rho^\sigma(\mathbf{r}_2) \quad (3.4.12)$$

yields a pair density which normalizes to  $(N^\sigma)^2$  which is incorrect and which should be  $N^\sigma(N^\sigma - 1)$ . This is called a “self-interaction error”, which arises since each  $\sigma$ -spin electron interacts with the  $N^\sigma - 1$  other electrons of its same spin. To renormalize this expression, a six-dimensional hole correlation function,  $h$ , is introduced as

$$\rho^{\sigma\sigma}(\mathbf{r}_1, \mathbf{r}_2) = \rho^\sigma(\mathbf{r}_1) \rho^\sigma(\mathbf{r}_2) + \rho^\sigma(\mathbf{r}_1) \rho^\sigma(\mathbf{r}_2) h^{\sigma\sigma}(\mathbf{r}_1, \mathbf{r}_2) \quad (3.4.13)$$

But since Fermi correlation prohibits the same spin electron to coincide in space and time, which is expressed as  $h^{\sigma\sigma}(\mathbf{r}, \mathbf{r}) = -1$ , this leads to the normalization of the hole as:

$$\int \rho^\sigma(\mathbf{r}_2) h^{\sigma\sigma}(\mathbf{r}_1, \mathbf{r}_2) d\mathbf{r}_2 = -1 \quad (3.4.14)$$

In the case of a Slater determinant, the hole is expressed explicitly as

$$\begin{aligned} h^{\sigma\sigma}(\mathbf{r}_1, \mathbf{r}_2) &= \frac{|\gamma^{\sigma\sigma}(\mathbf{r}_1, \mathbf{r}_2)|^2}{\rho^\sigma(\mathbf{r}_1) \rho^\sigma(\mathbf{r}_2)} \\ &= \frac{\sum_{j,k} n_j n_k \psi_j(\mathbf{r}_1, \sigma) \psi_j^*(\mathbf{r}_2, \sigma) \psi_k(\mathbf{r}_1, \sigma) \psi_k^*(\mathbf{r}_2, \sigma)}{\sum_{j,k} n_j n_k \psi_j(\mathbf{r}_1, \sigma) \psi_j^*(\mathbf{r}_1, \sigma) \psi_k(\mathbf{r}_2, \sigma) \psi_k^*(\mathbf{r}_2, \sigma)} \end{aligned} \quad (3.4.15)$$

Electrons have a higher propensity to form localized  $\alpha\beta$  pairs in electronic structure models, which ignore dynamic Coulombic correlation. The pairing occurs as an electron tends to minimize its average separation from the positive nuclei and maximize its separation from other electrons. Meanwhile, the Pauli principle prohibits the proximity of same-spin electrons, enhancing the probability for opposite-spin electrons to come closer to one another forming an  $\alpha\beta$  pair. Since this pair consists of one electron of each spin, additional electrons of either spin are excluded from the vicinity, and we have a localized pair of electrons.

The total Fermi or exchange correlation of electrons of spin  $\sigma$  (which could be either  $\alpha$  or  $\beta$ ) within a volume  $\Omega$  is obtained from

$$\begin{aligned} F^\sigma(\infty, \infty) &= \int_\infty d\mathbf{r}_1 \int_\infty d\mathbf{r}_2 \rho^\sigma(\mathbf{r}_2) \rho^\sigma(\mathbf{r}_1) h^{\sigma\sigma}(\mathbf{r}_1, \mathbf{r}_2) \\ &= -N^\sigma \end{aligned} \quad (3.4.16)$$

that is, the negative of the  $\sigma$ -electrons population of the system, e.g., of the molecule. If instead of integrating over all space, now we integrate over a part of the entire space, e.g., over an Atom-in-a-Molecule ( $\Omega$ ), the integral will generally yield a number, which is smaller than the total  $\sigma$ -electrons population of the atom since the electrons in  $\Omega$  are exchanging (delocalized) with other atoms in the molecule, i.e.:

$$\begin{aligned} |F^\sigma(\Omega, \Omega)| &= \left| \int_\Omega d\mathbf{r}_1 \int_\Omega d\mathbf{r}_2 \rho^\sigma(\mathbf{r}_2) \rho^\sigma(\mathbf{r}_1) h^{\sigma\sigma}(\mathbf{r}_1, \mathbf{r}_2) \right| \\ &\leq N^\sigma(\Omega) \end{aligned} \quad (3.4.17)$$

where  $N^\sigma$  is  $\sigma$ -electron population of basin  $\Omega$ . The equality in eq 3.4.17 holds at the (unreachable) limit where electrons are totally localized within  $\Omega$ .

Bader et al. take the total Fermi correlation in an atom  $\Omega$  as the definition of an electron localization index (LI, or  $\Lambda(\Omega)$ ) since it provides a count of those electrons that exchange within that basin.<sup>33</sup> At the limit of complete electron localization,  $|F^\sigma(\Omega, \Omega)|$  approaches the number of  $\sigma$ -electrons in  $\Omega$ , and thus, in general:

$$\Lambda(\Omega) = |F^\alpha(\Omega, \Omega)| + |F^\beta(\Omega, \Omega)| < N(\Omega) \quad (3.4.18)$$

Bader and co-workers also define an electron delocalization index [DI,  $\delta(\Omega, \Omega')$ ] as a count of the number of electrons shared between two atoms  $\Omega$  and  $\Omega'$ <sup>33</sup> using both spin Fermi correlations, where:

$$\begin{aligned} F^\sigma(\Omega, \Omega') &= \int_{\Omega} d\mathbf{r}_1 \int_{\Omega'} d\mathbf{r}_2 \rho^\sigma(\mathbf{r}_2) \rho^\sigma(\mathbf{r}_1) h^{\sigma\sigma}(\mathbf{r}_1, \mathbf{r}_2) \\ &= \int_{\Omega'} d\mathbf{r}_1 \int_{\Omega} d\mathbf{r}_2 \rho^\sigma(\mathbf{r}_2) \rho^\sigma(\mathbf{r}_1) h^{\sigma\sigma}(\mathbf{r}_1, \mathbf{r}_2) = F^\sigma(\Omega', \Omega) \end{aligned} \quad (3.4.19)$$

where the volume integrals are over  $\Omega$  and  $\Omega'$ , respectively, and where the integral is symmetric upon relabeling  $\Omega \leftrightarrow \Omega'$ , and if we sum over both spins ( $F \equiv F^\alpha + F^\beta$ ), we obtain  $F(\Omega, \Omega') = F(\Omega', \Omega)$ . That leads to Bader's delocalization index defined as

$$\delta(\Omega, \Omega') = 2|F^\alpha(\Omega, \Omega')| + 2|F^\beta(\Omega, \Omega')| \quad (3.4.20)$$

which, for a closed-shell molecule, reduces to

$$\delta(\Omega, \Omega') = 4|F^\sigma(\Omega, \Omega')| \quad (3.4.21)$$

The delocalization index is usually highest at the HF level of theory because the Coulombic correlation increases the effective average separation of electrons. Thus, the DI between two nitrogen atoms in the ground state of  $N_2$  is 3.04 at the Hartree–Fock level of theory and goes down to 2.22 at the CISD level.<sup>33,277</sup> If Kohn–Sham orbitals are used as a practical tool to calculate DIs, this observation is no longer universal. Generally, DIs exhibit high magnitudes between nonpolar covalently bonded atoms, and the magnitude of the DI reflects the bond order in these cases. In closed-shell interactions (ionic, hydrogen bonding, etc.), the DI may reach values as low as approaching zero. In her Ph.D. Thesis, Bader's former student Maggie Austen derived an equation relating  $\delta(\Omega, \Omega')$  and the charge transfer in closed-shell diatomics ( $|q(\Omega)|$ ):

$$\delta(\Omega, \Omega') = p - \frac{|q(\Omega)|^2}{p} \quad (3.4.22)$$

where  $p$  is the number of electron pairs available in the valence shell.

Two prototypical ionic and covalent nonpolar small molecules include LiF and methane. In LiF a DI of only ca.  $0.18 e^-$  indicates a low level of electron sharing between the two basins, while in  $CH_4$  the bonded (C–H) DI is ca.  $0.98 e^-$ . In methane, the DI between any pair of hydrogens is ca.  $0.04 e^-$ . In LiF, the atomic electron populations  $N(\Omega)$  are only marginally larger than the LIs since there is very little exchange between the two atomic basins:  $N(Li) = 2.07 > \Lambda(Li) = 1.98$ ,  $N(F) = 9.94 > \Lambda(F) = 9.85$ . In contrast, in methane, the atomic populations are significantly larger than the LIs:  $N(C) = 6.01 > \Lambda(C) = 4.04$ , and  $N(H) = 1.00 > \Lambda(H) = 0.44$ . Atomic charges in LiF indicate ionic bonding with a near complete charge transfer of one electronic charge (in au):  $q(Li) = +0.94$ ,  $q(F) = -0.94$ . In methane, there is almost no charge transfer between its constituent atoms:  $q(C) = +0.20$  and  $q(H) = -0.05$  (based on restricted Hartree–Fock calculations using a 6-311++G(3df, 2pd) basis set with self-consistent virial scaling (SCVS)).<sup>278,279</sup>

One can anticipate that LIs and DIs are not independent. A strongly localized electron population is unavailable for delocalization and vice versa. One may envisage a sort of a conservation principle by which the more the electrons of a basin are delocalized with other basins, the less they are localized within that basin and vice versa. This is expressed mathematically by what we term the Bader summation rule:

$$N(\Omega_i) = \Lambda(\Omega_i) + \frac{1}{2} \sum_{j \neq i}^n \delta(\Omega_i, \Omega_j) \quad (3.4.23)$$

where  $n$  is the number of atoms in the molecule. Since the electron population of an Atom-in-a-Molecule can be obtained from the integral of the electron density, Bader's rule can be expanded as

$$N(\Omega_i) = \Lambda(\Omega_i) + \frac{1}{2} \sum_{j \neq i}^n \delta(\Omega_i, \Omega_j) = \int_{\Omega_i} \rho(\mathbf{r}) d\mathbf{r} \quad (3.4.24)$$

where the sum of the LI of atom  $\Omega_i$  and the sum of half of its DIs is equal to its total electron population  $N(\Omega_i)$ .

**3.4.1. Complete Localization–Delocalization Molecular Graph.** The chemical graph theory (CGT)<sup>280–289</sup> is concerned with the mathematical representation of conventional molecular graphs, often in the form of some form of topological (connectivity) matrices. This theory extracts mathematical invariants, i.e., properties that are independent of the particular atom labeling used to construct the matrix, and then uses these invariants in interpretative work or in the construction of predictive quantitative structure to activity (or property) relationships (QSAR/QSPR) models. CGT assigns bonding inferred from traditional chemical knowledge and/or intuition. While the bond-path is determined by the three-dimensional topography of the electron density, it is a dichotomous bonding indicator (“all-or-none”). The strength and nature of bonding are captured in the so-called “bond properties” whether evaluated at the bond critical point, or integrated over the bond-path, over the interatomic surface, or over the volumes of the bonded atoms.

QTAIM also defines a set of continuous descriptors of bonding that are important when small geometrical changes lead to abrupt (catastrophic) changes in the bond-path graph, while properties such as the energy or the electron delocalization change gradually including near the points of sudden change in the molecular graph structure. To illustrate the gradual change in DIs as a function of a geometrical parameter, Figure 4 shows the evolution of the H···H DI in biphenyl as a function of the angle between its ring planes. The H···H bond-paths between the *ortho*-hydrogen atoms persist

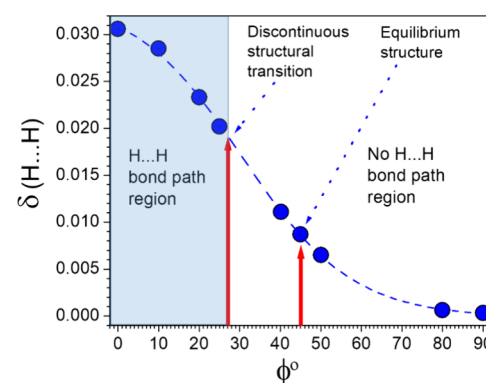


**Figure 4.** Discontinuous H···H bond-paths description in biphenyl splitting the plot in two regions, the shaded one whereby the two H···H bond-paths persist and the clear region without them contrasted with the continuous evolution of the DI between a pair of hydrogen atoms involved in an H···H bonding as a function of the rotation angle of the two ring planes.

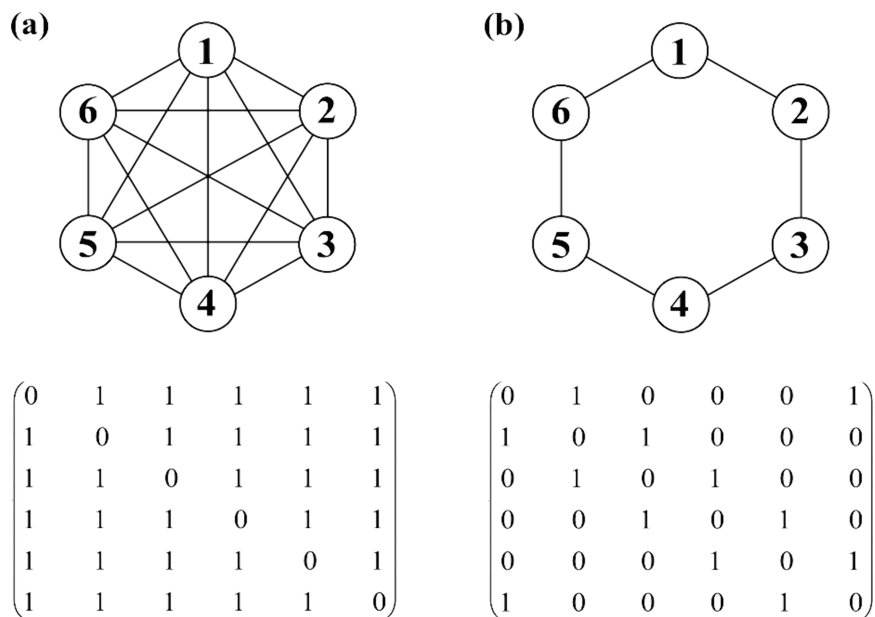


**Figure 5.** (a) An example of a complete graph and a corresponding topological connectivity matrix. (b) An example of an incomplete graph of the same system and one of its possible matrix representatives.

from the planar transition state up to approximately an angle of  $26^\circ$  where an abrupt change in structure occurs annihilating the H··H bond-paths and all of their topological associates (interatomic surfaces and ring critical points), yet the curve showing the evolution of the DI does not exhibit such an abrupt change.

A delocalization index (DI,  $\delta(\Omega, \Omega')$ ), defined above, exists between any pair of atoms  $\Omega$  and  $\Omega'$  in the molecule, bonded or not. Meanwhile, as we have seen in the previous section, theory also defines a localization index for every atom in the system ( $\text{LI}, \Lambda(\Omega)$ ).<sup>33,34,290,291</sup> These two sets of indices can be arranged in a matrix format to represent a complete and “fuzzy” molecular graph of the system in which an edge links every pair of atoms in the molecule. The matrix representation of this graph has been introduced in the literature as the electron localization–delocalization matrix (LDM).<sup>41,47</sup> Generally, a molecular graph is an incomplete graph meaning that not all pairs of vertices are joined by edges. In contrast, a complete graph is one in which every pair of vertices is connected by an edge. Figure 5 provides an example of a complete and incomplete graph along with their respective matrix representatives where 0/1 denotes the absence/presence of an edge (a bond) linking the given pair of vertices (atoms). Only graphs of diatomics are, by necessity, complete. All other molecular graphs are, in general, incomplete. However, if now the graph is defined not on the basis of the presence/absence of bonding (according to, say, the dichotomous presence/absence of a bond-path) but on the basis of continuous measure such as the DIs, then the (DI) molecular graph is “complete” by construction.

**3.4.2. The Localization–Delocalization Matrix (LDM) as a Tool for Molecular Comparisons.** The localization–delocalization matrix (LDM), also named the  $\zeta$ -matrix, is constructed such as the  $i$ th row or column contains  $1/2$  of the DIs between the atom labeling the row/column and all other atoms in the molecule. The diagonal elements of this matrix consist of the localization indices. Clearly, the LDM is a square symmetric matrix with dimensions  $n \times n$ , where  $n$  is the

number of atoms in the molecule. Symbolically, the LDM of a molecule is expressed as<sup>41,47</sup>

$$\text{LDM} \equiv \zeta \equiv \left[ \begin{array}{cccccc} \Lambda(\Omega_1) & \delta(\Omega_1, \Omega_2)/2 & \cdots & \delta(\Omega_1, \Omega_n)/2 \\ \delta(\Omega_2, \Omega_1)/2 & \Lambda(\Omega_2) & \cdots & \delta(\Omega_2, \Omega_n)/2 \\ \vdots & \vdots & \ddots & \vdots \\ \delta(\Omega_n, \Omega_1)/2 & \delta(\Omega_n, \Omega_2)/2 & \cdots & \Lambda(\Omega_n) \end{array} \right]_{n \times n} = N(\Omega_1) \sum_{i=1}^n N(\Omega_i) = N$$

$$\sum_{\text{column}} = N(\Omega_1) = N(\Omega_2) = \cdots = N(\Omega_n) \quad \text{tr}(\zeta) = N_{\text{loc}}$$

$$\sum_{i=1}^n N(\Omega_i) = N$$
(3.4.2.1)

The definition of the LDM above embodies Bader summation rule since the sum of any column or row is equal  $N(\Omega_i)$  (eq 3.4.24). Because the LDM contains information on atomic electron populations, it also contains information about atomic charges (eq 3.4.24). The LDM decomposes the total molecular electron population into a localized population ( $N_{\text{loc}}$ ) residing within atomic basins and represented by the trace of the LDM and a delocalized population ( $N_{\text{deloc}}$ ) shared between all pairs of atoms in the molecule.<sup>41,47</sup>

$$N = \sum_{i=1}^n N(\Omega_i) = \sum_{i=1}^n \Lambda(\Omega_i) + \frac{1}{2} \sum_{i=1}^n \sum_{j \neq i}^n \delta(\Omega_i, \Omega_j)$$

$$= N_{\text{loc}} + N_{\text{deloc}}$$
(3.4.2.2)

where

$$N_{\text{loc}} \equiv \sum_{i=1}^n \Lambda(\Omega_i)$$
(3.4.2.3)

and

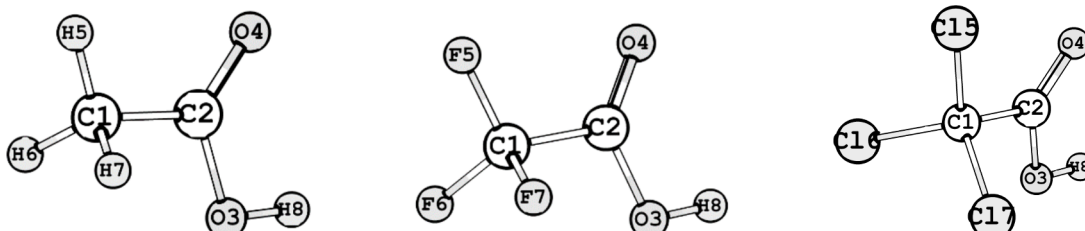
$$N_{\text{deloc}} \equiv \frac{1}{2} \sum_{i=1}^n \sum_{j \neq i}^n \delta(\Omega_i, \Omega_j) = N - \text{tr}(\zeta) = N - N_{\text{loc}}$$
(3.4.2.4)

When a pair of molecules have the same number of atoms or a common skeleton, their matrices can be compared directly. But

**Table 2.** LDMs of Acetic Acid ( $\text{CH}_3\text{COOH}$ ), Trifluoroacetic Acid ( $\text{CF}_3\text{COOH}$ ), and Trichloroacetic Acid ( $\text{CCl}_3\text{COOH}$ )<sup>a,b</sup>

$\text{CH}_3\text{COOH}$	C1	C2	O3	O4	H5	H6	H7	H8	SUM
C1	3.981	0.470	0.048	0.055	0.477	0.473	0.473	0.005	5.982
C2	0.470	2.849	0.438	0.664	0.018	0.022	0.023	0.006	4.491
O3	0.048	0.438	8.108	0.152	0.006	0.007	0.007	0.321	9.088
O4	0.055	0.664	0.152	8.237	0.009	0.011	0.011	0.010	9.149
H5	0.477	0.018	0.006	0.009	<b>0.410</b>	0.017	0.017	0.001	0.956
H6	0.473	0.022	0.007	0.011	0.017	<b>0.410</b>	0.018	0.000	0.958
H7	0.473	0.023	0.007	0.011	0.017	0.018	<b>0.410</b>	0.000	0.958
H8	0.005	0.006	0.321	0.010	0.001	0.000	0.000	0.076	0.420
SUM	5.982	4.491	9.088	9.149	0.956	0.958	0.958	0.420	32.000
$\text{CF}_3\text{COOH}$	C1	C2	O3	O4	F5	F6	F7	H8	SUM
C1	2.723	0.388	0.037	0.049	0.362	0.361	0.361	0.005	4.287
C2	0.388	2.748	0.451	0.680	0.032	0.033	0.033	0.006	4.370
O3	0.037	0.451	8.081	0.154	0.006	0.016	0.016	0.309	9.071
O4	0.049	0.680	0.154	8.156	0.025	0.010	0.010	0.008	9.093
F5	0.362	0.032	0.006	0.025	<b>8.999</b>	0.086	0.085	0.001	9.596
F6	0.361	0.033	0.016	0.010	0.086	<b>9.000</b>	0.085	0.001	9.592
F7	0.361	0.033	0.016	0.010	0.085	0.085	<b>9.000</b>	0.001	9.592
H8	0.005	0.006	0.309	0.008	0.001	0.001	0.001	0.070	0.399
SUM	4.287	4.370	9.071	9.093	9.596	9.592	9.592	0.399	56.000
$\text{CCl}_3\text{COOH}$	C1	C2	O3	O4	Cl5	Cl6	Cl7	H8	SUM
C1	3.604	0.416	0.042	0.055	0.542	0.527	0.527	0.005	5.718
C2	0.416	2.736	0.446	0.673	0.028	0.033	0.033	0.006	4.371
O3	0.042	0.446	8.068	0.151	0.008	0.028	0.028	0.310	9.082
O4	0.055	0.673	0.151	8.148	0.041	0.016	0.016	0.008	9.106
Cl5	0.542	0.028	0.008	0.041	<b>16.305</b>	0.084	0.084	0.001	17.093
Cl6	0.527	0.033	0.028	0.016	0.084	<b>16.342</b>	0.084	0.001	17.115
Cl7	0.527	0.033	0.028	0.016	0.084	0.084	<b>16.342</b>	0.001	17.115
H8	0.005	0.006	0.310	0.008	0.001	0.001	0.001	0.070	0.400
SUM	5.718	4.371	9.082	9.106	17.093	17.115	17.115	0.400	80.000

<sup>a</sup>The LIIs of the atoms attached to the methyl carbon are indicated in bold. <sup>b</sup>For the Atomic Labeling Scheme and Optimized Geometries see Figure 6.

**Figure 6.** Optimized geometries and atomic labeling scheme of, left to right,  $\text{CH}_3\text{COOH}$ ,  $\text{CF}_3\text{COOH}$ , and  $\text{CCl}_3\text{COOH}$ .

when the molecular matrices to be compared differ in sizes, molecular comparison is not as straightforward.

Even in the simplest of cases, when the matrices have equal sizes, comparing two matrices is not uniquely defined. An intuitive measure of the dissimilarity of two matrices is a Euclidean-like distance between them whereby the longer is the distance the less similar they are. If the distance is zero, the matrices (and the molecules they represent) are identical. Provided the two molecules contain the same number of atoms (and hence their LDM representatives are of equal sizes), one can calculate the Frobenius norm of the difference matrix as

$$d(\mathbf{A}, \mathbf{B}) \equiv \|\mathbf{A} - \mathbf{B}\| \equiv \sqrt{\sum_{i,j} |\alpha_{ij} - \beta_{ij}|^2} \quad (3.4.2.5)$$

where  $\alpha_{ij}$  and  $\beta_{ij}$  are corresponding elements in the LDMs  $\mathbf{A}$  and  $\mathbf{B}$ , respectively. Ismat Sumar has written a Python

program, AIMLDM,<sup>44</sup> that automates the extraction of the LIIs and DIIs from the output of AIMAll<sup>216</sup> and then calculates the Frobenius distance matrix between the LDMs set and extracts from each LDM matrix invariants that can also be used in modeling studies.

An important problem with any matrix representative of a molecular topology is the existence of  $n!$  ways of labeling a group of  $n$ -atoms. Hence, unless the molecules in the set are all derivatives of the same basic structure that allows a consistent labeling, one must extract matrix invariants from the LDMs before any meaningful comparison can be performed. These invariants may include the characteristic polynomial, eigenvalues, eigenvectors, trace, determinant, etc. Since LDMs are real and symmetric, they are diagonalizable into a matrix  $\mathbf{D}$  by a similarity transformation, i.e., by an operation represented by

$$\mathbf{P}^{-1} \zeta \mathbf{P} = \mathbf{D} \quad (3.4.2.6)$$

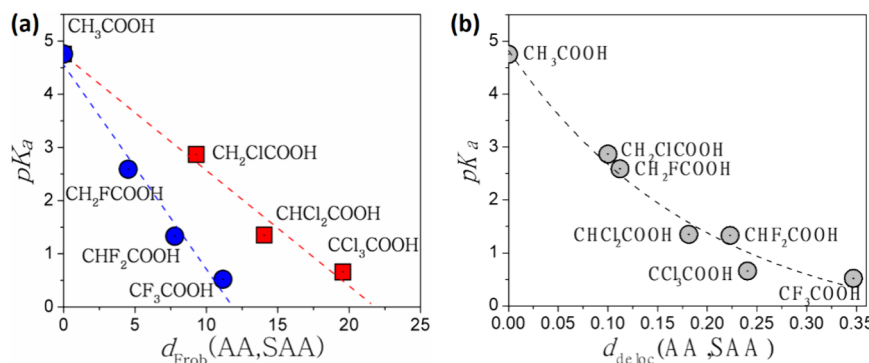


**Figure 7.** (a) Frobenius distance between LDMs of substituted acetic acids (SAA) and the unsubstituted acetic acid (AA) versus experimental  $pK_a$ 's. (b) Frobenius distances of the localization-suppressed LDMs (delocalization matrices (DMs)).

A comparison of the eigenvalues of the set of  $\mathbf{D}$  matrices can then be achieved in a meaningful and consistent manner as discussed below with the help of two example cases, where we also illustrate the application of PCA (principal component analysis) and of the concept of superatoms to LDM.

**3.4.2.1. Case 1: Molecular Sizes Are Equal and/or a Consistent Numbering Can Be Assigned.** As a first example, the LDMs of acetic acid ( $\text{CH}_3\text{COOH}$ ) and its trifluoro ( $\text{CF}_3\text{COOH}$ ) and trichloro derivatives are listed in Table 2. The structures and numbering schemes of these molecules are shown in Figure 6. These are extreme members of a set of seven progressively substituted acetic acids with the general formula  $\text{CH}_a\text{X}_b\text{COOH}$ , where  $\text{X} = \text{F or Cl}$ ,  $a = 0, 1, 2, 3$ , and  $b = 3 - a$ . To construct a QSAR model for the prediction of the  $pK_a$ 's of this series of compounds, a Frobenius distance criterion for molecular dissimilarity can be used directly since all molecules in the set have a common skeleton and the same LDM size.<sup>45</sup>

The LDM modeling requires a reference molecule from which the distance can be taken. We can take the parent (unsubstituted) acetic acid (AA) as a reference, but any member of the molecular set would do. Experience suggests that one chooses a compound at either extreme of the property to be modeled (the  $pK_a$  in this case). Figure 7a compares the experimental  $pK_a$ 's against the LDM distances of the substituted acetic acids (X-SAA,  $\text{X} = \text{F or Cl}$ ) from unsubstituted acetic acid (AA). It is found that the Frobenius distance and the  $pK_a$  can be fitted to linear relations, one for  $\text{X} = \text{F}$  and one for  $\text{X} = \text{Cl}$ :

$$\begin{aligned} pK_a(\text{F-SAA}) &= 4.5511 - 0.3840 d(\text{AA}, \text{F-SAA}) \\ (r^2 &= 0.9793, \text{ STD} = 0.3256, n = 4) \end{aligned} \quad (3.4.2.1.1)$$

and

$$\begin{aligned} pK_a(\text{Cl-SAA}) &= 4.73954 - 0.2173 d(\text{AA}, \text{Cl-SAA}) \\ (r^2 &= 0.9834, \text{ STD} = 0.2872, n = 4) \end{aligned} \quad (3.4.2.1.2)$$

In this case, the LDM modeling is able to discriminate between the two sets of substituted acids, the one with  $\text{X} = \text{F}$  and that with  $\text{X} = \text{Cl}$ , each with its own linear regression equation. This is so since the Frobenius distances are dominated by the large localization indices of the chlorine atom. To reduce this size-effect, one can suppress the diagonal elements to extract the “localization-suppressed LDM” or,

simply, the “delocalization matrix (DM)”. A similar analysis using the distances between the delocalization matrices ( $d_{\text{de loc}}(\text{AA}, \text{SAA})$ ) yields a single relation between the  $pK_a$  and the Frobenius distances of all seven compounds (displayed graphically in Figure 7b):

$$\begin{aligned} pK_a(\text{SAA}) &\approx -0.588 + 5.415 \times \exp[-5.066 \times d_{\text{de loc}}(\text{AA}, \text{SAA})] \\ (r^2 &= 0.979, n = 7) \end{aligned} \quad (3.4.2.1.3)$$

**3.4.2.2. Case 2: Molecular Sizes Are Different.** Suppose we would like to compare the members of a homologous series such as the aliphatic hydrocarbon series: methane ( $\text{CH}_4$ ), ethane ( $\text{CH}_3\text{CH}_3$ ), propane ( $\text{CH}_3\text{CH}_2\text{CH}_3$ ), and butane ( $\text{CH}_3(\text{CH}_2)_2\text{CH}_3$ ). Since the LDMs have different sizes in this case, the Frobenius distance is not defined. An algorithm has been proposed to deal with this common situation and consists of comparing the eigenvalues of the LDMs up to the size of the smallest matrix in the set. These steps can be summarized using an illustrative example of the series of aliphatic hydrocarbons limiting the series to only the two first members, namely, methane and ethane, for simplicity (but the same steps can be applied to any number of members in the series in the same manner):

(1) Calculate the LDMs of the compounds in the series at an appropriate level of theory.

(2) Obtain the eigenvalues of the LDM representing the smallest compound in the series (the compound with the least number of atoms) and arrange them in ascending order, say, as a column vector. Thus, for methane (5 atoms), we have

$$\zeta_{\text{CH}_4} = \text{H}_3 \begin{pmatrix} \text{C}1 & \text{H}2 & \text{H}3 & \text{H}4 & \text{H}5 \\ 0.4040 & 0.492 & 0.492 & 0.492 & 0.492 \\ 0.492 & 0.444 & 0.021 & 0.021 & 0.021 \\ 0.492 & 0.021 & 0.444 & 0.021 & 0.021 \\ 0.492 & 0.021 & 0.021 & 0.444 & 0.021 \\ 0.492 & 0.021 & 0.021 & 0.021 & 0.444 \end{pmatrix}_{5 \times 5} \rightarrow \lambda_{\text{CH}_4} = \begin{pmatrix} 0.251 \\ 0.423 \\ 0.423 \\ 0.423 \\ 4.295 \end{pmatrix}_{5 \times 1} \quad (3.4.2.2.1)$$

(3) Pad the vector constructed from these eigenvalues to make it equal in size as that of the largest molecule in the set (ethane (8 atoms)). The “augmented eigenvalue vector” of methane is then:

$$\lambda_{\text{CH}_4} = \begin{bmatrix} 0.251 \\ 0.423 \\ 0.423 \\ 0.423 \\ 4.295 \end{bmatrix}_{5 \times 1} \rightarrow \lambda'_{\text{CH}_4} = \begin{bmatrix} 0.000 \\ 0.000 \\ 0.000 \\ 0.251 \\ 0.423 \\ 0.423 \\ 0.423 \\ 4.295 \end{bmatrix}_{8 \times 1} \quad (3.4.2.2.2)$$

(4) Repeat step 2 for every molecule except for the largest one (ethane).

(5) Obtain the eigenvalues of the LDM of the largest molecule (ethane):

$$\zeta_{\text{C}_2\text{H}_6} = \begin{array}{ccccccccc} & \text{C1} & \text{H2} & \text{C3} & \text{H4} & \text{H5} & \text{H6} & \text{H7} & \text{H8} \\ \text{C1} & 3.941 & 0.483 & 0.505 & 0.483 & 0.483 & 0.022 & 0.022 & 0.022 \\ \text{H2} & 0.483 & 0.456 & 0.022 & 0.021 & 0.021 & 0.007 & 0.002 & 0.002 \\ \text{C3} & 0.505 & 0.022 & 3.941 & 0.022 & 0.022 & 0.483 & 0.483 & 0.483 \\ \text{H4} & 0.483 & 0.021 & 0.022 & 0.456 & 0.021 & 0.002 & 0.007 & 0.002 \\ \text{H5} & 0.483 & 0.021 & 0.022 & 0.021 & 0.456 & 0.002 & 0.002 & 0.007 \\ \text{H6} & 0.022 & 0.007 & 0.483 & 0.002 & 0.002 & 0.456 & 0.021 & 0.021 \\ \text{H7} & 0.022 & 0.002 & 0.483 & 0.007 & 0.002 & 0.021 & 0.456 & 0.021 \\ \text{H8} & 0.022 & 0.002 & 0.483 & 0.002 & 0.007 & 0.021 & 0.021 & 0.456 \end{array} \sum \begin{array}{c} 5.961 \\ 1.013 \\ 5.961 \\ 1.013 \\ 1.013 \\ 1.013 \\ 1.013 \\ 1.013 \\ 18.000 \end{array} \quad (3.4.2.2.3)$$

which yields the  $\lambda$ -vector:

$$\lambda_{\text{C}_2\text{H}_6} = \begin{bmatrix} 0.284 \\ 0.323 \\ 0.430 \\ 0.430 \\ 0.440 \\ 0.440 \\ 3.638 \\ 4.632 \end{bmatrix}_{8 \times 1} \quad (3.4.2.2.4)$$

(6) Compute the Frobenius distance between the vectors constructed of the sorted eigenvalues that are now made to be equal in size.

Following this algorithm, the  $\log P$  of aliphatic hydrocarbons  $\text{C}_n\text{H}_{2n+2}$  with  $1 \leq n \leq 4$ , i.e., up to butane, can be fitted to the following regression equation (displayed in Figure 8):

$$\log P \approx 1.0092 + 0.2898 \times d_{\text{Frob}}(\text{CH}_4, \text{C}_n\text{H}_{2n+2}) \quad (r^2 = 0.973, n = 4) \quad (3.4.2.2.5)$$

The distances between the augmented eigenvalue vectors are  $d(\text{C}_2\text{H}_6, \text{CH}_4) = 3.29$ ,  $d(\text{C}_3\text{H}_8, \text{C}_2\text{H}_6) = 3.04$ , and  $d(\text{C}_4\text{H}_{10}, \text{C}_3\text{H}_8) = 2.92$ . There is a trend in these values that approaches an additive group contribution of  $\approx 3$ . This trend parallels the known fixed increments of a methylene group to the  $\log P$ , which converges quickly to about 0.52  $\log P$  units:  $[\log P(\text{C}_2\text{H}_6) - \log P(\text{CH}_4)] = 0.72$ ,  $[\log P(\text{C}_3\text{H}_8) - \log P(\text{C}_2\text{H}_6)] = 0.55$ , and  $[\log P(\text{C}_4\text{H}_{10}) - \log P(\text{C}_3\text{H}_8)] = 0.53$ . The sharp rise from methane to ethane (when the first "substituent" is added) is unsurprising since the first added substituent is not a methylene group ( $-\text{CH}_2-$ ) but, rather, a methyl group ( $-\text{CH}_3$ ). Clearly, the  $\log P$  is an extensive molecular property that is easily predicted by several methods including, for example, using Carbó(-Dorca) molecular similarity measures.<sup>292–296</sup> It is an example of a simple extensive property that could be predicted from an electronic

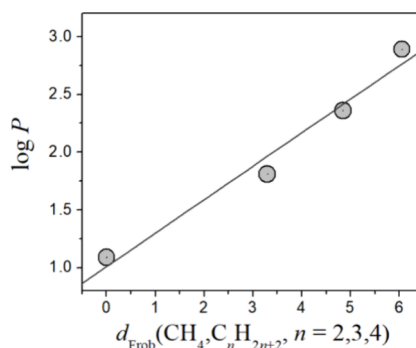


Figure 8.  $\log P$ 's fitted to the Frobenius distance between the augmented eigenvalue vectors of the first four aliphatic alkanes.

similarity matricial measure such as the Frobenius distance between the members of a homologous series.

Cook devised an alternative approach. He applies Principal Component Analysis (PCA) to the LDMs to extract the invariants, which he then compares as a basis for his QSAR modeling.<sup>41,42</sup> In this manner, an LDM is just an  $n$ -dimensional data set from which an  $n \times n$  covariance matrix is extracted and the eigenvalues evaluated. The eigenvalues with the largest magnitudes, common with the smallest molecule in the set, are saved and compared. The PCA analysis of the LDMs yields robust predictive modeling of corrosion inhibitors' efficiency and the discovery of the active species of three stress corrosion cracking inhibitors containing sulphydryl groups (R-SH). The modeling with these three inhibitors taken as monomers makes them outliers; yet when the LDMs of their oxidized form (R-S-S-R) are used the predicted activities fit the regression line perfectly.<sup>41,42</sup> This PCA applied to mosquito repellents can be used to classify odorants and uncover certain aspects of their modes of action.<sup>41,42</sup> LDM-PC analysis has also been shown to be useful in predicting acetylcholine esterase enzyme inhibitors' ability to slow the progression of Alzheimer's Disease.<sup>41</sup> It has also been shown capable to predict the efficiency of bioremediation in eliminating organophosphorus environmental toxicants and chemical warfare agents.<sup>41</sup>

Another approach suited for series with a clearly identifiable "common skeleton" with different substituents, which are not necessarily made of the same number of atoms, is now described. In such cases, the entire substituent can be condensed in a "composite multi-nuclear superatom", which considers the entire group as a single entity with one entry in the LDM, and hence equalizing the sizes of all LDMs of the series. As an example of how this may be achieved, we review an application to substituted benzoic acids.<sup>41,45</sup> The common skeleton for the series of substituted *para*-substituted benzoic acids is presented in Figure 9. Any member of this series can be viewed as being composed of an "active center" responsible for the  $pK_a$  (the carboxylic group) perturbed by a substituent S attached to the common skeleton (the substituent is numbered as 15 at position C8 of the ring).

All LDMs of this series of compound are made equal in size by condensing the substituent atoms as a "superatom" called S (for substituent). The localization index of the superatom counts all the electrons localized within its composing atoms (the sum of their LIs) in addition to the number of electrons delocalized within the group itself. Thus, the superatom localization index of S is expressed as<sup>45</sup>



spectrum of activity. In this example, both the  $pK_a$ 's and the UV  $\lambda_{\max}$  of these compounds are modeled, and since the extremes of activity are not coinciding, they are modeled separately taking *p*-nitrobenzoic acid as a reference for the  $pK_a$  modeling [ $pK_a(\text{BANO}_2) = 3.44$ ] since it is the most acidic in the series and, for  $\lambda_{\max}$ , unsubstituted benzoic acid since it has the shortest  $\lambda_{\max}(\text{BA}) = 230 \text{ nm}$ .

The squared Pearson linear correlation coefficients ( $r^2$ ) for  $pK_a$  and  $\lambda_{\max}$  are collected in Table 3. From the table,  $pK_a$  is

**Table 3.** Squared Pearson Linear Regression Coefficients ( $r^2$ ) between  $pK_a$  and  $\lambda_{\max}$ , respectively, and the Frobenius Distances between LDMs<sup>a</sup>

property	<i>n</i>	LDM		
		full	–COOH	–OH
$pK_a^b$	14	0.159	0.970	0.973
$\lambda_{\max} (\text{nm})^c$	8	0.445	0.972	0.931

<sup>a</sup>The LDMs of the super-atom substituted benzoic acids are  $15 \times 15$ , while those for a sub-graph of the active center only include the atoms of the active center; that is, they are  $4 \times 4$  for the –COOH group and  $2 \times 2$  for the –OH group. Data from ref 45. <sup>b</sup>Reference is *p*-nitrobenzoic acid,  $pK_a(\text{BA}-\text{NO}_2) = 3.44$ . <sup>c</sup>Reference is unsubstituted benzoic acid,  $\lambda_{\max}(\text{BA}) = 230 \text{ nm}$ .

best fit to Frobenius distances between subgraph matrices of the center of activity (the –COOH group, or the proton donor (–OH) group), while using the graphs of the entire molecules results in considerably lower correlation coefficients. This may be desirable since an automation of a search using sets of randomly constructed subgraphs can deliver, in principle, an automatic procedure to “detect” the center responsible for the sought-for activity. The idea of an algorithm for the automatic detection of an active center similar to the one mentioned here has been described by Popelier et al.<sup>297–302</sup> These workers use bond critical point data to construct a mathematical space whereby Euclidian distances measure molecular similarity. Popelier et al. show that incorporating properties of bonds beyond the “active center” diminishes statistical correlations. This observation parallels the situation outlined here, where correlations using partial-LDMs (of the active center) are weakened by the inclusion of extraneous atoms outside the active group.

The plot on the left of Figure 10 correlates  $pK_a$  with the Frobenius distances of the full matrices indicating no clear trends, while the plot on the right uncovers a strong (linear)

correlation obtained when submatrices of the “active site” are singled out by the analysis.

An illustration of the predictive power of this approach is a correction to an entry in the *CRC Handbook of Chemistry and Physics*.<sup>303</sup> The *CRC Handbook* lists, as a  $pK_a$  for *p*-dimethylaminobenzoic acid (*p*-DMABA), a value of 6.03;<sup>303</sup> meanwhile, the LDM predicts a  $pK_a$  of 5.04 for this compound.<sup>45</sup> The latter LDM-model value agrees well with the primary literature, which gives a  $pK_a$  of 5.03, and is also in agreement with a prediction based on Hammett  $\sigma$ -constants, which yields a  $pK_a$  of 4.85.<sup>304</sup> It appears likely that the *CRC Handbook* has made a typographical error regarding the  $pK_a$  of this compound.

Finally, the primary UV  $\lambda_{\max}$  of the (protonated) benzoic acid, the parent compound, is 230 nm.<sup>305–307</sup> It is known that substituents at the *p*-position shift the maximum of this band bathochromically whether S is electron-donating or withdrawing.<sup>305</sup> For eight compounds with known spectra, the 230 nm bands modeled against the Frobenius distances taking only the chromophore (–COOH) subgraph into consideration yield high  $r^2$  values (Table 3). The correlation between the Frobenius distances taken between the –COOH subgraph matrices and  $\lambda_{\max}$  can be fitted to<sup>45</sup>

$$\lambda_{\max} = 222.50 + 3.4171 \times 10^3 \times d_{\text{LDM}}^{[\text{COOH}]}(\text{BA}, \text{BAS})$$

$$[r^2 = 0.973, q^2 = 0.944, \text{St. Err.} = 5.74, n = 8]$$

(3.4.2.2.8)

where  $q^2$  is the cross-validated leave-one-out correlation coefficient, a relation illustrated graphically in Figure 11. The closeness of  $q^2$  and  $r^2$  measures the predictivity of the model, which, in this case, has a quality and strength that exceeds a Hammett  $\sigma$ -constants-based model.<sup>45</sup>

We mention, in passing, that the energetic decomposition by way of Interacting Quantum Atoms (IQA),<sup>38–40,205–208</sup> whereby the electron density is first partitioned according to QTAIM followed by the calculation of the atomic averages of various atomic contributions to energy, can be used to define an “energetic analogue” of the LDM. This is so since IQA self- and interaction-energetic terms satisfy a summation rule that is identical in form to the Bader summation rule of LIs and DIs (compare eqs 3.1.4.18 and 3.4.23). In this fashion, an additive atomic energy,  $E_{\text{add}}^A$ , is the analogue of the corresponding atomic population ( $N(\Omega)$ ), a self-energy,  $E_{\text{self}}^A$ , corresponds to the localization index ( $\Lambda(\Omega)$ ), and an interaction energy,  $E_{\text{int}}^{AB}$ , plays the role of a corresponding delocalization index ( $\delta(\Omega, \Omega')$ ). Because of this formal identity, IQA energies can be used to construct a corresponding matrix of an identical form as its

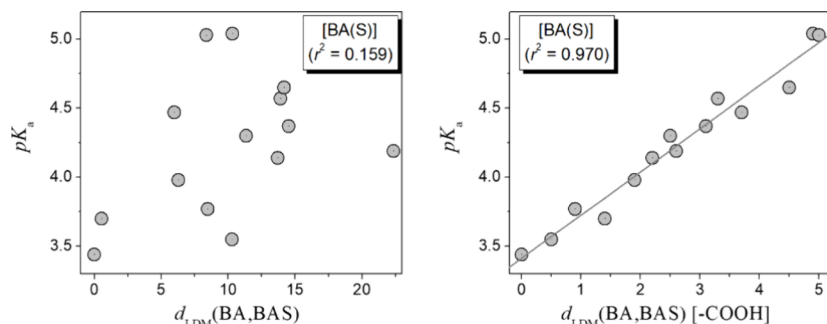


**Figure 10.** (Left) Frobenius distances between full LDMs against  $pK_a$ . (Right) Corresponding Frobenius distances of only the subgraph of the activity center (acidity) against  $pK_a$ .

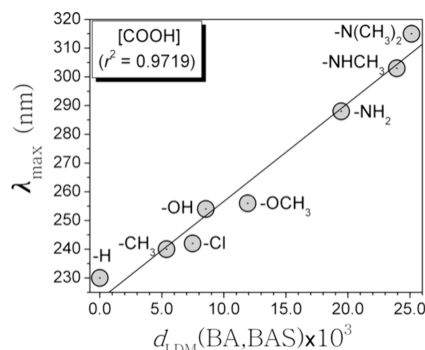


**Figure 11.** Correlation of  $\lambda_{\text{max}}$  and the Frobenius distances of the subgraph  $-\text{COOH}$  matrices, which contain the presumed chromophore for the substituted benzoic acid 230 nm band.

corresponding LDM, a matrix that one can term the Interacting Quantum Atoms Matrix (IQAM) or the “ $\eta$ -matrix” expressed explicitly:

$$\begin{aligned} \eta &\equiv \left[ \begin{array}{cccc} E_{\text{self}}^{A_1} & E_{\text{int}}^{A_1 A_2}/2 & \cdots & E_{\text{int}}^{A_1 A_n}/2 \\ E_{\text{int}}^{A_2 A_1}/2 & E_{\text{self}}^{A_2} & \cdots & E_{\text{int}}^{A_2 A_n}/2 \\ \vdots & \vdots & \ddots & \vdots \\ E_{\text{int}}^{A_n A_1}/2 & E_{\text{int}}^{A_n A_2}/2 & \cdots & E_{\text{self}}^{A_n} \end{array} \right]_{n \times n} = E_{\text{add}}^{A_n} \sum_{i=1}^n E_{\text{add}}^{A_i} = E \\ \sum_{\text{col.}} &= E_{\text{add}}^{A_1} = E_{\text{add}}^{A_2} = \cdots = E_{\text{add}}^{A_n} \quad \text{tr}(\eta) = E_{\text{self}}^{\text{total}} \\ &\sum_{i=1}^n E_{\text{add}}^{A_i} = E \end{aligned} \quad (3.4.2.2.9)$$

The IQA matrices have never been used as molecular descriptors, which could be work for future investigations.

### 3.5. QTAIM for Quantum Crystallography: The Solid State and Surfaces

Quantum crystallography<sup>161–170,308–310</sup> is a subfield of crystallography consisting of a combination of quantum mechanics and X-ray diffraction data with the goal of obtaining accurate and precise crystal structure and electron density information. Quantum crystallography involves incorporating quantum mechanical mathematical structure into X-ray diffraction data refinements to provide a representation of total electronic structure beyond the simple electron density normally obtained from standard X-ray crystallography. This includes obtaining one- and two-electron density *matrices* (not just electron densities) and/or wavefunctions which are consistent with both the requirements of quantum mechanics such as *N*-representability and/or the minimization of the energy simultaneously with fitting the observed (phased) structure factors. In this section, we overview the tools for the extraction of charge density distributions for use with QTAIM, either from calculations or from experiment, for use with the solid state or surfaces, that are usually modeled using periodic boundary conditions.

Tsirelson and co-workers have recently developed software for orbital-free quantum crystallography based on multipole experimental electron-density parameters that allows extraction of the chemical-bonding information previously unavailable for X-ray single-crystal diffraction analysis.<sup>118</sup> In addition, Tsirelson and co-workers have used orbital-free quantum crystallography in partnership with experiments and extracted

charge density distributions to provide novel insights into hydrogen-bonding features.<sup>311,312</sup> See section 6 for details of the orbital-free method.

Gatti and co-workers provided overviews into QTAIM use in crystals including software developments.<sup>313,314</sup> Gatti also provided contributions to the extraction of chemical information from experimental electron densities using the source function mentioned above.<sup>250,253</sup> Otero-dela-Roza also created software to robustly locate critical points on grids obtained from calculation.<sup>315</sup> Crespo and co-workers developed the Interacting Quantum Atoms (IQA) method for crystals that provides a real space energy decomposition of the energy of crystals in which all energy components are physically meaningful.<sup>316</sup>

#### 3.5.1. Quantum Crystallography: Application to the Solid State.

Quantum crystallography has widespread applications in the analysis of intermolecular bonding interactions and materials including crystal engineering, semiconductors, and pharmaceuticals that we will now highlight. Understanding of the mechanical properties of crystals, including hardness/softness, elasticity, and brittleness, is central for the realization of practical applications of crystalline materials for crystal engineering, e.g., piezoelectric properties and the creation of better alloys. Differences in the mechanical properties of crystals are explained by the anisotropy of the crystal structure that results in varying responses, i.e., resistance to applied external stresses dependent on the direction of application. A reasonable assumption made is that the macroscopic response of the equilibrium-state crystal to the directed external stress is determined by the integrated response of all interatomic interactions that are mostly aligned along the direction of the applied stress. The response of each specific interaction is associated with the changes to the electron density distribution between bonded atoms. Therefore, it is important to reveal the quantitative parameters such as the quantum pressure that can describe the response of the specific crystal structure regions to external stress correctly.

Early QTAIM investigations of the bonding in solid molecular chlorine were undertaken by Bader and co-workers.<sup>317</sup> Tsirelson used the quantum pressure to quantify the response of a specific crystal structure region to external stress, including external compression<sup>318</sup> in the crystal continuum using electronic charge density distributions derived from calculation.<sup>319–321</sup> Further applications explored by Tsirelson and co-workers included the determination of piezoelectric properties and high-pressure phase transitions.<sup>322</sup> Relationships were established between the changes in microscopic quantum pressure of the electronic continuum and the macroscopic compressibility, piezoelectric properties, geometries, and energies of the hydrogen bonds in the crystal structure of  $\beta$ -glycine. Compression of  $\beta$ -glycine crystals subject to external hydrostatic pressure resulted in a change in the internal quantum pressure in the intermolecular space and along a pair of weak noncovalent hydrogen bonds that comprised the two branches of a bifurcated hydrogen bond.<sup>322</sup> Tsirelson also used electronic charge density distributions derived from X-ray diffraction experiment.<sup>323,324</sup>

Luaña, Costales, Martín Pendás, and co-workers have extensively investigated alkali halide perovskites<sup>325–328</sup> in addition to the properties of crystals under mechanical strain,<sup>329</sup> and the topological<sup>330</sup> and chemical properties of crystals.<sup>331</sup>

An early example of the application of QTAIM to semiconductors was provided by Jenkins who introduced a QTAIM metallicity measure, i.e., in real space, to explain the origins of the problematic high conductivity known to exist in thin silicon oxide layers. This QTAIM metallicity measure was used for the discovery of metallic interactions (Si1–Si2) found connecting the layers of an SnO-type relaxed SiO structure that explained the unexpectedly high conductivity.<sup>332</sup> Recently, Bouafia and co-workers investigated the bonding properties of a new narrow-gap semiconductor YPdAs half-Heusler compound with significant properties for the semiconductor industry that include a narrow-band gap, polar bonding, and high melting temperature that allows for use in optoelectronics, photovoltaics, and thermoelectric applications.<sup>333</sup>

Eberhart and co-workers created a “bond bundle” approach within QTAIM partitioning of open systems into the thinnest chemically meaningful volumes bounded by zero-flux surfaces.<sup>334</sup> In particular, the space around a molecule was found to be decomposable into bonding, nonbonding, or lone pair volumes. Eberhart later used his “bond bundle” approach for materials applications including the design of better alloys.<sup>335</sup>

Characteristic of molecular crystals is the presence of both strong intramolecular bonds and generally weak intermolecular bonds as well as contacts where there are exchanges of chemical character between bonding types. Water ice is an example of such a molecular crystal where exchanges of chemical character are present that influence bond strengths; see section 4.4.1.3 for further details.

The basis of crystal engineering of cocrystals, useful for the pharmaceutical industry, concerns weak and/or strained intermolecular interactions, especially hydrogen bonds, utilized to design supramolecular synthons “gluing” together the constituent molecules without perturbing their covalent bonds to avoid modifying the bulk properties of the molecular solid-state system.<sup>336–338</sup> An example of the use for pharmaceuticals is provided by Ahmed and co-workers who explored the mechanism of the cocrystal growth of a 2:2 nicotinic acid:gallic acid (NAGA)-3H<sub>2</sub>O cocrystal. A QTAIM analysis was performed using electronic charge densities distributions obtained from high-resolution X-ray diffraction data using a Hansen and Coppens multipolar formalism.<sup>339</sup> Another example of the relevance of QTAIM for the pharmaceutical industry was provided by Gatti, who used QTAIM to consider the urea crystal and the 3,4-bis-(dimethylamino)-3-cyclobutene-1,2-dione (DMACB) crystal.<sup>340,341</sup> Answers were provided to issues such as the effect of packing effects on intramolecular bonds and groups, the size of the enhancement of the molecular dipole on crystallization, as well as dependencies of the global molecular volume contraction on crystallization.

**3.5.2. Quantum Crystallography: Application to Surfaces.** Experimental techniques are available for qualifying the geometrical atomic reconstructions occurring at the surfaces of semiconductors. Accurate electronic charge density distributions of surfaces are much less easily obtained from experiment<sup>342,343</sup> than from ab initio periodic calculations of model surfaces. Ab initio periodic calculations analyzed by Srivastava generally reproduced observed geometrical atomic distortions to a reasonable degree and provided a satisfactory description of the electronic structure and the electronic charge density distribution at the surface.<sup>344</sup> QTAIM analysis of ab initio wave functions by Gatti and co-workers provided quantitative insight into the relationships between geometrical

atomic reconstructions, electronic relaxations, and bonding.<sup>345</sup> In particular, Gatti and co-workers demonstrated that use of QTAIM provided insights into the details of the bonding of surface atoms during modification by surface reconstructions as well as the propagation of changes in perturbations to the surface in terms of their effect on the adsorption process.

Tsirelson and co-workers recently demonstrated for doped graphene how the details of tetrel bonds and other non-covalent interactions can be physically justified at the level of electron pair (de)localization.<sup>346</sup>

#### 4. NEXT GENERATION QUANTUM THEORY OF ATOMS-IN-MOLECULES (NG-QTAIM)

The vector-based analysis of the electron density of molecules and materials constitutes a crucial tool for understanding phenomena beyond the scope of scalar-based considerations no matter how accurately the associated energies are calculated. In sections 2, 3, and 5, the main lines of research that enabled information to be extracted from the scalar analysis of the electron density are provided. Section 6 discusses the usefulness of density-based quantities and analysis in OF-DFT simulations and OF-DFT method development. In this section, we will demonstrate the usefulness of vector-based density-based quantities, by providing numerous examples along with the NG-QTAIM method development that includes the historical context.

##### 4.1. Evolution from Scalar QTAIM to Vector-Based Next Generation QTAIM

The necessary background on (scalar) QTAIM theory is provided in section 3. In this section, the historical context that led to the creation of Next Generation (NG)-QTAIM<sup>347,348</sup> is outlined. A tutorial review of NG-QTAIM is available.<sup>49</sup> NG-QTAIM is a vector-based, as opposed to scalar-based, quantum chemical theory. A fundamental quantum chemical concept in scalar QTAIM is the ellipticity  $\varepsilon$ , which is defined as  $\varepsilon = \lambda_1/\lambda_2 - 1$ , where  $\lambda_1$  and  $\lambda_2$  correspond to the eigenvalues of the Hessian of  $\rho(r_b)$ , and which is commonly used to determine the presence of single bond ( $\varepsilon \leq 0.1$ ) and double bond ( $\varepsilon \geq 0.25$ ) character. The accumulation of the total electronic charge density distribution  $\rho(r_b)$  is quantified by the  $e_1$  and  $e_2$  eigenvector directions that are perpendicular to the bond-path at a Bond Critical Point (BCP) and the ellipticity  $\varepsilon$  with  $|\nabla\rho_b(r_b)| = 0$  with  $\lambda_1$  and  $\lambda_2 < 0$  and  $\lambda_3 > 0$ , at position  $r_b$ . The shortest and longest axes of the ellipse-shaped cross-section distribution of  $\rho(r)$  are associated with the  $\lambda_1$  and  $\lambda_2$  eigenvalues of the Hessian of  $\rho(r_b)$ , respectively; see Figure 12a. The  $e_2$  eigenvector of the Hessian of  $\rho(r_b)$  corresponds to the most preferred “easy” direction of accumulation of the  $\rho(r_b)$  distribution and hence determines the “easy” direction of bond displacement.<sup>349</sup> When a molecular structure is subjected to a slight perturbation, the direction of shift of the displaced electrons was found to align with that of the atoms;<sup>350</sup> this was later confirmed.<sup>351,352</sup>

The evolution of vector-based NG-QTAIM from (scalar) QTAIM required the understanding that the linear sum of the Hessian of  $\rho(r_b)$  “easy” ( $e_2$ ) and “hard” ( $e_1$ ) directions of  $\rho(r_b)$  accumulation at a BCP correlated with the directions of low frequency rotation phonon modes;<sup>353</sup> see Figure 12a. The development toward NG-QTAIM was then enabled by comparison and quantification of the projected phonon density of states (PPDOS) of the zone-center modes of vibration of

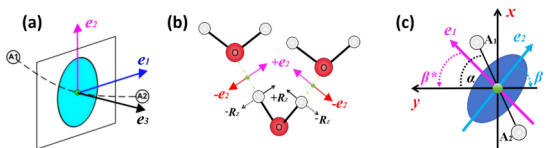


**Figure 12.** (a) Sketches of the ( $e_2$ ) “easy” most preferred and ( $e_1$ ) “hard” least preferred eigenvectors of the Hessian of  $\rho(r)$  along with the ( $e_3$ ) eigenvectors of the bonded atoms A1–A2 BCP (green circle) for values of the ellipticity  $\epsilon > 1$  and an ellipse shaped cross-section (pale-blue ellipse) of the  $\rho(r)$  distribution. (b) The  $\pm e_2$  eigenvectors of the H–O hydrogen-bond BCPs of cubic ice Ic are represented by green spheres with the associated directions of the rotation ( $\pm R_z$ ) projections with the H–O hydrogen-bond-paths denoted by yellow dashed lines. Reproduced with permission from ref 52. Copyright 2022 Wiley. (c) The extents of the semimajor and semiminor axes are indicated by the lengths of the blue ellipse and represent the  $\lambda_2$  and  $\lambda_1$  eigenvalues, respectively. The mechanical torsion angle of the methylene group in fulvene is indicated by the  $\alpha$  angle. The corresponding “easy” and “hard” responses are denoted by the angles  $\beta$  and  $\beta^*$ , respectively.

cubic ice (Ic) with the “easy” ( $e_2$ ) and “hard” ( $e_1$ ) eigenvectors; see Figure 12b.

The  $R_z$  rotation component is the most significant contribution of PPDOS, associated with a water molecule in cubic Ice Ic, at the bottom of the rotation band since the  $R_z$  phonon mode possesses the largest component of angular momentum.

The Hessian of the  $\rho(r_b)$  “hard” ( $e_1$ ) eigenvector, i.e., the least preferred direction, corresponds almost entirely to the  $R_x$  rotation direction; see Table 4. The “easy” ( $e_2$ ) eigenvector, i.e., the most preferred direction, demonstrates clearly that the  $R_z$  rotation contribution is almost entirely associated with the  $e_2$  “easy” eigenvector: this is demonstrated by a comparison of the directions associated with  $\pm R_z$  and  $\pm e_2$ ; see Figure 12. The linear combination ( $a e_1 + b e_2$ ) very closely matches the corresponding PPDOS.

The top of the stretching band ( $3174.60\text{ cm}^{-1}$ ) is dominated by the symmetric-stretch (ss) mode corresponding to the sigma O–H bond of the water molecule. The  $e_3$  direction corresponding to the O–H  $\sigma$  bond BCP bond-path direction closely aligns with the symmetric-stretch (ss) phonon vibrational mode. The correspondence between the PPDOS entries in Table 4 and Table 5 and the ( $a e_1 + b e_2$ ) in Table 5 is not perfect because contributions of the PPDOS are calculated from the locations of the hydrogen atoms in contrast to the eigenvectors that instead use positions of the H–O hydrogen-bond BCPs.

Combining the dynamic and static properties of cubic ice Ic demonstrated a strong need for the role of the Hessian of  $\rho(r_b)$  eigenvectors in providing a deeper understanding of the connection between  $\rho(r_b)$  and dynamic properties. The

creation of the bond-path-framework<sup>354</sup> was a result of the realization that there is an absence of alignment of the motion of the  $\rho(r_b)$  and associated atoms for a chemical bond subjected to a torsional distortion during the progression of the bond torsion. Subsequently, it was found that at the BCP the  $e_1$  and  $e_2$  eigenvectors can each align to and lose alignment with the containing nuclear skeleton. This finding provided a nonenergy-based understanding of the contribution of H–H bonding in the topological stability of biphenyl.<sup>355</sup> There is therefore a direct physics-based link between the ellipticity  $\epsilon$  and bond-path torsion angle  $\alpha$  since the torsion BCP attains a minimum value during a bond-path torsion since  $\lambda_2 \approx \lambda_1$ ; see Figure 12c. A more advanced quantification of the bond torsion process was developed, based on the  $e_1$  and  $e_2$  eigenvectors, referred to as the response angle  $\beta$ <sup>356–360</sup> of  $\rho(r_b)$ : note that a stress tensor  $\sigma(r)$  response angle  $\beta_\sigma$  is defined as  $\beta_\sigma = \arccos(e_{1\sigma} \cdot y)$  where  $e_{1\sigma}$  defines the “easy” direction for the stress tensor  $\sigma(r)$ , i.e., the most preferred direction of motion of  $\rho(r_b)$ , and  $y$  is a reference vector of unit length directed along the  $y$ -axis of the global Cartesian coordinate frame where the global frame  $z$ -axis is aligned with the  $e_3$  eigenvector (see Figure 12).

The response angle  $\beta$  of  $\rho(r_b)$ , for the Hessian of  $\rho(r)$ , is dependent on the nature of the deformation of the nuclear skeleton or on electronic states. The “easy” response angle  $\beta$  and “hard” response angle  $\beta^*$  are determined by the Hessian of  $\rho(r)$  eigenvectors  $e_2$  and  $e_1$ , respectively, of the bond torsion BCP projected onto the  $x$ - $y$  plane: these are provided along with the ellipticity  $\epsilon$  in Figure 12c. The response angle  $\beta$  is defined as

$$\beta = \arccos(e_2 \cdot y) \quad (4.1.1)$$

and

$$\beta^* = \arccos(e_1 \cdot y) \quad (4.1.2)$$

The bond-path-framework was also used for the quantification of the asymmetry of the 11-cis retinal bond-torsion potential energy surface (PES) in addition to that of the conical intersection (CI), i.e., to partition the derived properties of the ground state ( $S_0$ ) and first excited state ( $S_1$ ).<sup>361</sup>

The construction of the QTAIM interpretation of the Ramachandran plot provided a unique nonenergy-based representation of closed-shell BCPs (H–H, H–O, and H–O) as well as shared-shell BCPs.<sup>356</sup>

The Hessian of  $\rho(r_b)$  eigenvectors  $\{e_1, e_2, e_3\}$  of the torsioned bond’s BCP were later discovered not to rotate in alignment with the atoms comprising the rotated group.<sup>354</sup> This discovery led to the concept of the bond-path-framework set  $B$ ; see section 4.2. Scalar QTAIM can only magnify  $\rho(r)$ -derived scalar properties from the Hessian of  $\rho(r)$  due to the

**Table 4.** Contributions from the Top ( $1143.17\text{ cm}^{-1}$ ) and Bottom ( $579.62\text{ cm}^{-1}$ ) of the Rotation Band, Respectively, Stretching Band ( $3174.60\text{ cm}^{-1}$ ), and Translation Band to the Projected Phonon Density of States (PPDOS) for Cubic Ice Ic from the Symmetric-Stretch (ss), Anti-symmetric Stretch (as), Bend (b), Rotation ( $R_x$ ), ( $R_y$ ), and ( $R_z$ ), and Translation ( $T_x$ ), ( $T_y$ ), and ( $T_z$ ) for Frequencies ( $\omega$ )

$\omega, \text{cm}^{-1}$	stretching			rotation			translation		
	ss	as	b	$R_x$	$R_y$	$R_z$	$T_x$	$T_y$	$T_z$
579.62	0.0000	0.0000	0.0000	0.1994	0.0000	0.7394	0.0350	0.0000	0.0261
1143.17	0.0000	0.0000	0.0000	0.0000	1.0000	0.0000	0.0000	0.0000	0.0000
3174.60	0.9962	0.0007	0.0030	0.0000	0.0000	0.0000	0.0000	0.0000	0.0000

**Table 5. Comparison of the Hessian of  $\rho(r_b)$  ( $e_1$ ) “Hard” and ( $e_2$ ) “Easy” Eigenvector Directions Corresponding to the H–O Hydrogen Bonds with the Calculated PPDOS of Cubic Ice Ic<sup>a</sup>**

direction	stretching			rotation			translation		
	ss	as	b	$R_x$	$R_y$	$R_z$	$T_x$	$T_y$	$T_z$
$e_1$	0.0000	0.0000	0.0000	0.8880	0.0000	0.0000	0.0560	0.0000	0.0560
$e_2$	0.0000	0.0011	0.0000	0.0000	0.0000	0.9624	0.0182	0.0000	0.0182
( $ae_1+be_2$ )	0.0000	0.0008	0.0000	0.1994	0.0000	0.7394	0.0266	0.0000	0.0266
$e_3$	1.0000	0.0000	0.0000	0.0000	0.0000	0.0000	0.0000	0.0000	0.0000

<sup>a</sup>The projection of the  $e_3$  eigenvector along the bond-path enables comparison with the bond stretching (ss) vibration. Parabolic fit  $y = ax^2 + b$  coefficients  $a = 0.2246$  and  $b = 0.7680$  were used. The  $R_x$  and  $R_z$  rotation band PPDOS results are provided in Table 4.

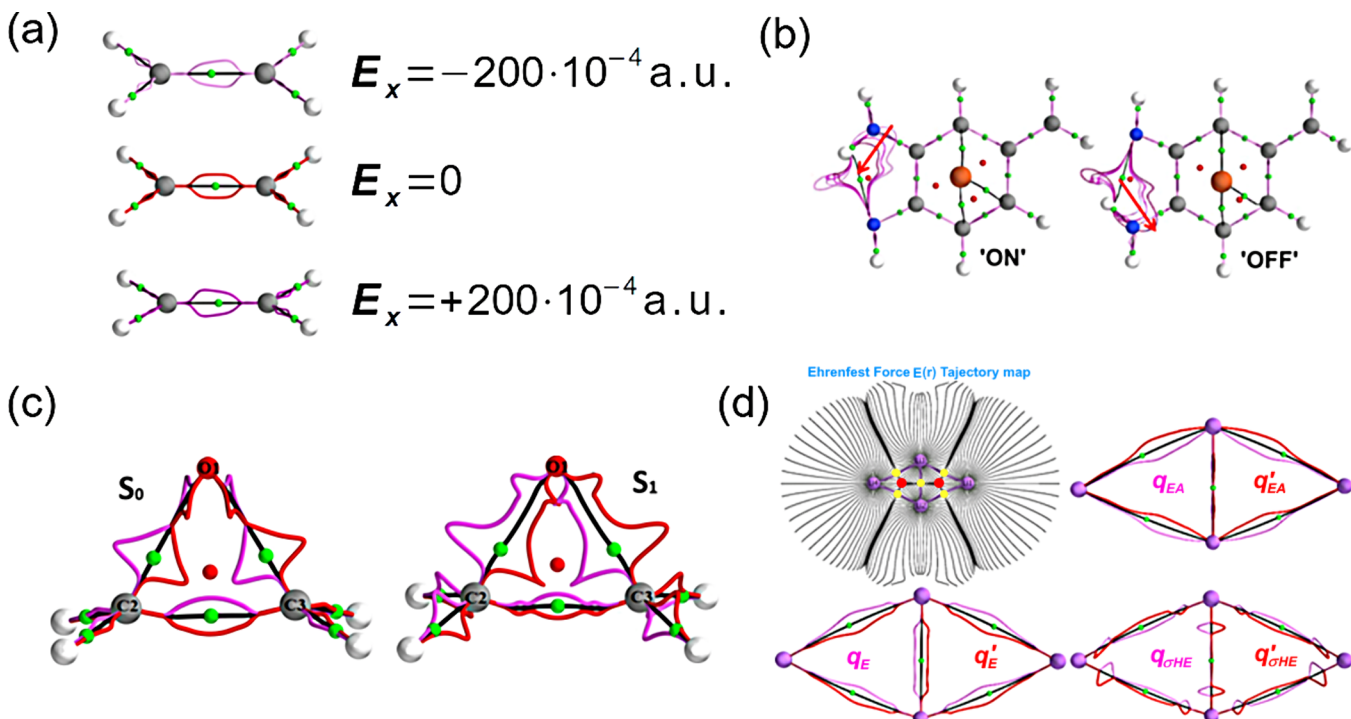


**Figure 13.** (a) Effect of an electric ( $E$ )-field on the ethene  $\{q, q'\}$  path-packets where the  $+E_x$  is applied along the C1  $\rightarrow$  C2 BCP-bond-path. Reproduced with permission from ref 386. Copyright 2020 Wiley. (b) A quinone-analogue switch is used for the “ON” and “OFF” position of the switches with the associated molecular graphs and  $\{q, q'\}$  path-packets. Reproduced with permission from ref 387. Copyright 2019 Wiley. (c) The oxirane molecular graph for the twisted  $\{q_0(\text{magenta}), q'_0(\text{red})\}$  and planar  $\{q_1(\text{blue}), q'_1(\text{cyan})\}$  path-packets for the  $S_0$  and  $S_1$  electronic states for the C3–O1 BCP ring-opening bond-path. Reproduced with permission from ref 52. Copyright 2022 Wiley. (d) The Ehrenfest force  $E(r)$  trajectory map for  $\text{Li}_4$ , where red and yellow red circles indicate the ring critical points (RCPs) and bond critical points (BCPs), respectively. Moving counterclockwise,  $\{q_{EA}, q'_{EA}\}$  path-packets are shown superimposed on the Ehrenfest force  $E(r)$  molecular graph, using the Ehrenfest force  $E(r)$  ellipticity  $\epsilon_{EA} = (|\lambda_{1E}|/|\lambda_{2E}|) - 1$ . The  $\{q_E, q'_E\}$  and  $\{q_{\sigma HE}, q'_{\sigma HE}\}$  path-packets are constructed with the Hessian of  $\rho(r)$  and the stress tensor ellipticity  $\epsilon_{\sigma H} = |\lambda_{1\sigma}|/|\lambda_{2\sigma}| - 1$  superimposed on the  $E(r)$  molecular graph.

absence of full symmetry-breaking properties. This shortfall is addressed by construction of the eigenvector-space-trajectory  $T_i(s)$ ;  $i = \{\text{stress tensor } (\sigma(r)), \text{ QTAIM } (\rho), \text{ Ehrenfest force } E(r)\}$ ; see section 4.5.

#### 4.2. Chemical Bond Interpreted with NG-QTAIM: The Bond-Path-Framework Set $B$

The chemical bond interpreted by NG-QTAIM, i.e., the bond-path-framework set  $B$ , is far closer in spirit to the profound work of Tachibana et al.<sup>362–366</sup> than is scalar QTAIM. Tachibana used the “spindle structure” to quantify covalent bonding. Significant levels of bond migration can result in topological catastrophes of molecular structures that occur during chemical reactions.<sup>1,367–371</sup>

The bond-path-framework set  $B$  enables a quantification and visualization of the degree of the chemical character of a bond for the full length of the bond-path and not just at the location

of the BCP. This has therefore enabled a more complete understanding of reaction mechanisms.<sup>372–388</sup>

The bond-path-framework set<sup>52</sup>  $B = \{(q, q'), (p, p'), r\}$  comprises 3-D strands or linkages, the  $\{q, q'\}$  and  $\{p, p'\}$  path-packets and includes the conventional QTAIM bond-path  $r$  for a given electronic state; see eqs 4.2.1–4.2.4. The bond-path-framework set  $B$  can currently use the Hessian of  $\rho(r)$ , stress tensor<sup>389,390</sup>  $\sigma(r)$  and Ehrenfest force  $E(r)$  Hessian;<sup>384</sup> other future partitioning schemes of  $\rho(r)$  are also possible. Note, Bader’s definition<sup>389,390</sup> of the stress tensor  $\sigma(r)$  is used here because it provides a direct physics-based explanation related to the lowest-frequency normal modes associated with structural rearrangement<sup>352,391,392</sup> and is determined by the Ehrenfest force  $E(r)$  using the virial theorem. In each case, the  $\{q, q'\}$  and  $\{p, p'\}$  path-packets can be transplanted between the Ehrenfest Force  $E(r)$  and Hessian of  $\rho(r)$  partitioning

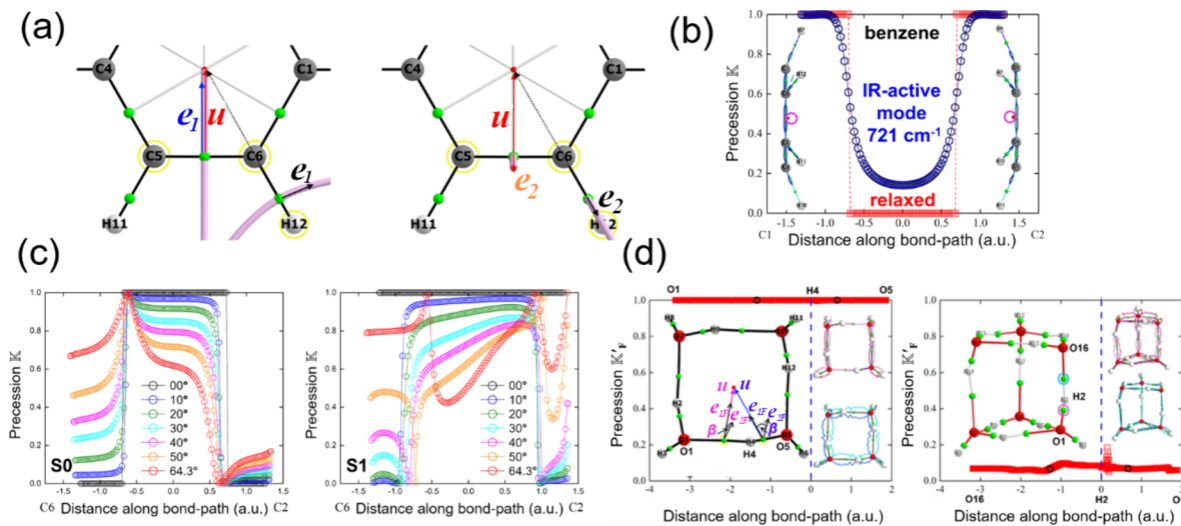


**Figure 14.** (a) The path-packet precession  $K\{p, p'\}$  (left panel) and  $K'\{q, q'\}$  (right panel) constructions are shown for the C6–H12 BCP and C5–C6 BCP for the molecular graph of benzene. The  $u$  (red arrow) denotes a unit vector along the BCP → RCP path. The pale magenta line denotes the interatomic surface paths (IAS) that originate at a BCP. Reproduced with permission from ref 400. Copyright 2021 Wiley. (b) The precessions  $K$  for the benzene IR-active mode at  $721.57 \text{ cm}^{-1}$  along the C–C BCP bond-paths, BCPs are located at a distance = 0.0 au along the bond-path, while RCPs are indicated in magenta (circled). Red spheres and green spheres indicate locations of ring critical points (RCPs) and bond critical points (BCPs), respectively. Reproduced with permission from ref 400. Copyright 2021 Wiley. (c) Variations of the precession  $K$  of fulvene along the C2–C6 BCP torsion bond-path for the  $S_0$  (left panel) and  $S_1$  (right panel) states with the bond torsion angle  $\theta = 0.0^\circ$  (Franck–Condon point) to  $\theta = 64.3^\circ$  (conical intersection CI). Reproduced with permission from ref 393. Copyright 2021 Elsevier. (d) Construction of the  $K'_E$  ( $u, e_{1E}, e_{2E}$ , and  $\beta$ ) for the Ehrenfest force  $E(r)$ : the “easy” ( $e_{2E}\{q_E(\text{magenta}), q'_E(\text{red})\}$  and  $\{p_E(\text{blue}), p'_E(\text{cyan})\}$ ) “hard” ( $e_{1E}$ ) directions of  $\rho(r)$  for the strongly coupled O5–H4 covalent-bond BCP and H4–O1 hydrogen-bond BCP ((H<sub>2</sub>O)<sub>4</sub>, left panel). The strongly coupled O1–H2 covalent-bond BCP and H2–O16 hydrogen-bond BCP in (H<sub>2</sub>O)<sub>6</sub> are shown in the right panel. Reproduced with permission from ref 401. Copyright 2021 Elsevier.

schemes.<sup>384</sup> In addition, multiple excited states may be considered where each excited state  $n$  will produce unique pairs of  $\{q_n, q'_n\}$  and  $\{p_n, p'_n\}$  path-packets.<sup>52361,372–387,393–400</sup>

The ellipticity  $\epsilon$ , see Figure 12, is used as the scaling factor, motivated by the utility of the chemical and physics-based insights it provides is used for the construction of the  $\{q, q'\}$  and  $\{p, p'\}$  path-packets, where  $r$  is derived using the  $e_3$  eigenvector:

$$\mathbf{q}_i = \mathbf{r}_i + \epsilon_i \mathbf{e}_{2,i} \quad (4.2.1)$$

$$\mathbf{q}'_i = \mathbf{r}_i - \epsilon_i \mathbf{e}_{2,i} \quad (4.2.2)$$

$$\mathbf{p}_i = \mathbf{r}_i + \epsilon_i \mathbf{e}_{1,i} \quad (4.2.3)$$

$$\mathbf{p}'_i = \mathbf{r}_i - \epsilon_i \mathbf{e}_{1,i} \quad (4.2.4)$$

The term  $\{q, q'\}$  “path-packet” was inspired by the resemblance to the “orbital-like” shape that a pair of  $q$ - and  $q'$ -paths possess on the bond-path of a molecular graph.<sup>384</sup>

The vectors  $\mathbf{q}_i$  and  $\mathbf{p}_i$  are constructed from  $n$  points  $\mathbf{r}_i$  located along the bond-path  $r$  using the  $\mathbf{e}_{2,i}$  and  $\mathbf{e}_{1,i}$  eigenvectors, respectively, scaled by  $\epsilon_i$ , defined as the ellipticity at  $\mathbf{r}_i$ . The path-packets traced out by the tips of these  $\mathbf{q}_i$  and  $\mathbf{p}_i$  vectors define the paths  $p$  and  $q$ ; see eqs 4.2.1–4.2.4.

The well-known benzene molecule is used with the familiar topology feature of the single ring critical point (RCP) at the center of the molecule to quantify the degree of wrapping, or precession of the  $\{p, p'\}$  path-packet about a bond-path; see Figure 13.

**4.2.1. Applications of the Bond-Path-Framework Set B.** NG-QTAIM enables consideration of the Ehrenfest force  $E(r)$ <sup>401</sup> and physical and chemical effects of electric ( $E$ )-fields on molecular devices<sup>386,387</sup> and on reactivity,<sup>402–406</sup> which are

outside of the scope of scalar QTAIM. The oxirane ring-opening reaction<sup>376</sup> was demonstrated to be hindered by the presence of twisted  $\{q_0, q'_0\}$  and facilitated by planar  $\{q_1, q'_1\}$  path-packets for the  $S_0$  and  $S_1$  electronic states, respectively; see Figure 13c.

NG-QTAIM was used to highlight the disadvantages of relying on mathematical modeling of the molecular modes of vibrations that includes the use of normal mode coordinate analysis and symmetry assignments<sup>407</sup> and assumptions of stick-like bonds.

**4.2.1.1. Improving Switch Function and Scoring Molecular Wires with Electric Fields.** The ability to screen molecules, particularly those that contain C=C double bonds that are a common structural motif in molecular electronic devices, is essential for the design of efficient “wires” linking molecular building blocks. This more direct screening process is possible because the reaction to the applied electric ( $E$ )-field can be directly visualized and quantified, on a bond-by-bond basis, guided by the “easy” ( $e_2$ ) most preferred directions of accumulation of  $\rho(\mathbf{r})$ . Therefore, the 3-D bond-path-framework set  $B$  is constructed to determine the effects of the electric field, e.g., of the ethene molecule.<sup>386</sup> Notice the morphology of the  $\{q, q'\}$  path-packets depends on the applied  $E$ -field direction; see Figure 13a.

This finding built upon previous work also using the  $\{q, q'\}$  path-packets where the “ON” and “OFF” functions of an azophenine switch were visualized in terms of the measured effects of the applied external  $E$ -field.<sup>387,388,408</sup> This is demonstrated by examination of the red arrows, for the “ON” and “OFF” position of the switches, that highlight the effect on the  $\{q, q'\}$  path-packets of increasing the magnitude of the  $E$ -field; see Figure 13b.

**4.2.1.2. Photochemistry of Ring-Opening Reactions of Oxirane.** The photodecomposition pathways of the oxirane molecule were analyzed in partnership with multireference density functional calculations.<sup>376</sup> The tendency to complete the ring-opening reaction and to continue on to the dissociation products was found to be dependent on the type of the S<sub>1</sub>/S<sub>0</sub> conical intersection (CI) traversed by the reaction path. Traversing through a planar intersection geometry resulted in a restoration of the ring geometry, while traversing a conical intersection with twisted (−CH<sub>2</sub>) geometry led directly to the ring-opening dissociation products. The origin of this difference was explained using the bond-path-framework set *B*. The ability of the photoexcitation to facilitate the reaction was demonstrated by the presence of the twisted and planar bond-path-framework *B* for the S<sub>0</sub> and S<sub>1</sub> electronic states, respectively; see Figure 13c.

**4.2.1.3. Effects of the Removal of Non-nuclear Attractors from Neutral Lithium Clusters.** Earlier, non-nuclear attractors (NNAs) were discovered to be persistent features in the  $\nabla\rho(\mathbf{r})$  that could be detected with the Hessian of  $\rho(\mathbf{r})$  partitioning but not with the more “compact” Ehrenfest force  $E(\mathbf{r})$  partitioning scheme.<sup>192,409</sup> The true nature of the stress tensor  $\sigma(\mathbf{r})$ , free from the confines of the Hessian of  $\rho(\mathbf{r})$  partitioning, was determined using the Hessian of  $\rho(\mathbf{r})$  bond-path-framework *B* and compared with the Ehrenfest force  $E(\mathbf{r})$  bond-path-framework *B<sub>E</sub>*; see Figure 13d. Evidence of NNA character was found in the form of localized peaks in the path-packets created with the stress tensor  $\sigma(\mathbf{r})$  eigenvectors on both the Ehrenfest force  $E(\mathbf{r})$  and the Hessian of  $\rho(\mathbf{r})$  molecular graphs.

When stretching or compression distortions applied are sufficient to remove the NNA from Li<sub>2</sub>, this resulted in increased topological instability, which was discovered by the unexpected torsion of the Li<sub>2</sub>, the stress tensor  $\sigma(\mathbf{r})$  bond-path-framework set *B<sub>σ</sub>* on the Hessian of the  $\rho(\mathbf{r})$  molecular graph. This demonstrated the topologically stabilizing influence that NNAs have on the sparse distribution of  $\rho(\mathbf{r})$  of neutral Li<sub>2</sub> clusters.

#### 4.3. Chemical Bond Interpreted with NG-QTAIM: The Precession *K*

For the benzene molecule, under normal conditions, the reference direction *u* is typically defined as the BCP → RCP path along the *e*<sub>1</sub> eigenvector, see Figure 14, i.e., the most difficult direction of bond deformation of the benzene C–C bonds. The {*p*, *p'*} path-packet typically “wraps” around the bond-path. The extent of this phenomenon can be quantified by defining the so-called precession *K*:<sup>393,400</sup>

$$K = 1 - \cos^2 \alpha \quad (4.3.1)$$

where

$$\cos \alpha = \mathbf{e}_1 \cdot \mathbf{u} \quad (4.3.2)$$

and thus  $0 \leq K \leq 1$ . Note, the existence of an RCP is not required, only the existence of a fixed reference direction *u*, to calculate the precession *K*. We consider the extreme values of the precession *K*, using  $\alpha$  defined by eq 4.3.2. We obtain a value of *K* = 0 for the maximum alignment of the *e*<sub>1</sub> eigenvector, the least preferred “hard” direction, with a reference direction *u*. The other extreme, *K* = 1, corresponds to the minimum degree of alignment of *u* with the *e*<sub>1</sub> eigenvector. *K* = 0 and *K* = 1 define bond-paths with the lowest and highest bond-path-flexibility tendencies, respectively. Consistent with this, and specific to benzene, *K* = 0 and

*K* = 1 also correspond to the lowest and highest so-called IR-responsivity<sup>400</sup> tendencies, respectively. Generally there is a “spectrum” of bond types, from rigid bond, i.e., shared-shell BCP character *K* = 0, to flexible bond, i.e., closed-shell character *K* = 1, characteristic of sigma bonds and hydrogen bonding, respectively.

The precession *K* is calculated starting at the BCP, sampling the *e*<sub>1</sub> eigenvectors in both (−*e*<sub>3</sub>) and (+*e*<sub>3</sub>) directions along the bond-path toward the atoms at the ends of the bond-path. The reference direction *u* is chosen to align parallel to the ±*e*<sub>1</sub> eigenvector and is used to construct the {*p*, *p'*} path-packet, which corresponds to minimum bond-path rigidity. The precession *K* enables the chemical bond character to be quantified along the full length of a bond-path.

For the precession *K'* of the {*q*, *q'*} path-packet, defined using the *e*<sub>2</sub> eigenvector, about the bond-path,  $\beta = (\pi/2 - \alpha)$  and  $\alpha$  is defined by eq 4.3.2, see Figure 14a, the expression *K'*:

$$K' = 1 - \cos^2 \beta \quad (4.3.3)$$

where

$$\cos \beta = \mathbf{e}_2 \cdot \mathbf{u} \quad (4.3.4)$$

$$\beta = \left( \frac{\pi}{2} - \alpha \right) \quad (4.3.5)$$

Thus,  $0 \leq K' \leq 1$ , where *K'* = 0 corresponds to a maximum possible degree of facile, i.e., easily distorted, character and *K'* = 1 corresponds to the minimum possible degree of facile character; see eqs 4.3.3–4.3.5. In particular, for benzene, *K*' = 0 and *K'* = 1 also correspond to the lowest and highest tendencies, respectively, toward non-IR-responsivity. The *K* and *K'* are not always trivial converses of each because the C–H BCP bond-path may be shifted out of the benzene molecule plane; therefore, it is necessary to also calculate *K'*.

#### 4.4. Applications of the Precession *K*

NG-QTAIM provides new insights into deformation anisotropy phenomena<sup>372–388</sup> including the mechanisms of reaction pathways<sup>376</sup> that use bond coupling with the Ehrenfest force *E*( $\mathbf{r}$ ),<sup>401</sup> outside of the scope of scalar QTAIM. The precession *K* that used the {*p*, *p'*} path-packets was demonstrated for cycl[3.3.3]azine<sup>399</sup> for nonionizing ultrafast laser pulse induced polarization effects that were only found with the laser that included the detection of “mixed” bond types, that were also not apparent using scalar QTAIM. In this case, the precession *K* corresponds to the precession of the path-packet during laser-induced electron dynamics, although it is a useful quantity also in static situations.

##### 4.4.1.1. Explaining the IR-Active Modes of Benzene.

An investigation quantified the tendencies toward maximum and minimum IR-responsivity and the IR-nonresponsivity of the four IR-active modes of benzene, mode 5, mode 14, mode 21, and mode 28. The outcome of the investigation was that for the C–C BCP bond-paths, the lowest frequency IR-active mode 721.57 cm<sup>−1</sup> (mode 5) was the only mode to display a precession *K* profile plot with a harmonic form; see Figure 14b. This provided consistency with the finding that mode 5 is the only benzene IR-active mode where the molecular graph is nonplanar: because of the flexing of the C–H BCP bond-paths above and below the plane of the benzene C<sub>6</sub> ring with the corresponding change in position, i.e., above or below, of the RCP relative to the plane of the C<sub>6</sub> ring. The minimum IR-responsivity (*K* = 0.0) for the entire C–C BCP bond-path

**Table 6.** Fulvene Precessions  $K(S_0, S_1)$  ( $\text{CI}_{\text{tor}}$ ) for the C2–C6 BCP Torsion Bond-Path, Partial Bond-Path Lengths  $\Delta(\text{C}-\text{BCP}) = \Delta A$ , along with  $\Delta(\text{BCP}-\text{C}) = \Delta B$  Including the Relative Geometric Bond-Lengths  $\Delta(\text{GBL})$  and Relative Bond-Path Lengths  $\Delta(\text{BPL})^a$

$S_0$			$S_1$		
$(\Delta A, \Delta B)$	$\Delta \text{BPL}(\Delta \text{GBL})$	$\Delta Q_0$	$(\Delta A, \Delta B)$	$\Delta \text{BPL}(\Delta \text{GBL})$	$\Delta Q_1$
(0.086, 0.045)	0.131(0.131)	-0.130	$\theta = 10.0^\circ$	(0.050, 0.081)	0.131(0.131)
(0.056, 0.081)	0.137(0.137)	-0.120	$\theta = 20.0^\circ$	(0.051, 0.086)	0.137(0.137)
(0.060, 0.088)	0.148(0.148)	-0.110	$\theta = 30.0^\circ$	(0.053, 0.095)	0.148(0.148)
(0.064, 0.095)	0.159(0.159)	-0.100	$\theta = 40.0^\circ$	(0.054, 0.105)	0.159(0.159)
(0.067, 0.105)	0.173(0.173)	-0.080	$\theta = 50.0^\circ$	(0.051, 0.121)	0.173(0.173)
(0.077, 0.143)	0.220(0.220)	-0.010	$(\text{CI}) \theta = 64.3^\circ$	(0.049, 0.172)	0.220(0.220)
					-0.549

<sup>a</sup> $\Delta Q_0$  and  $\Delta Q_1$  denote the relative integrated areas under the  $K(S_0, S_1)$  plots for the ground  $S_0$  and first excited  $S_1$  states, respectively. Atomic units (au) are used throughout. Reproduced with permission from ref 393. Copyright 2021 Elsevier.

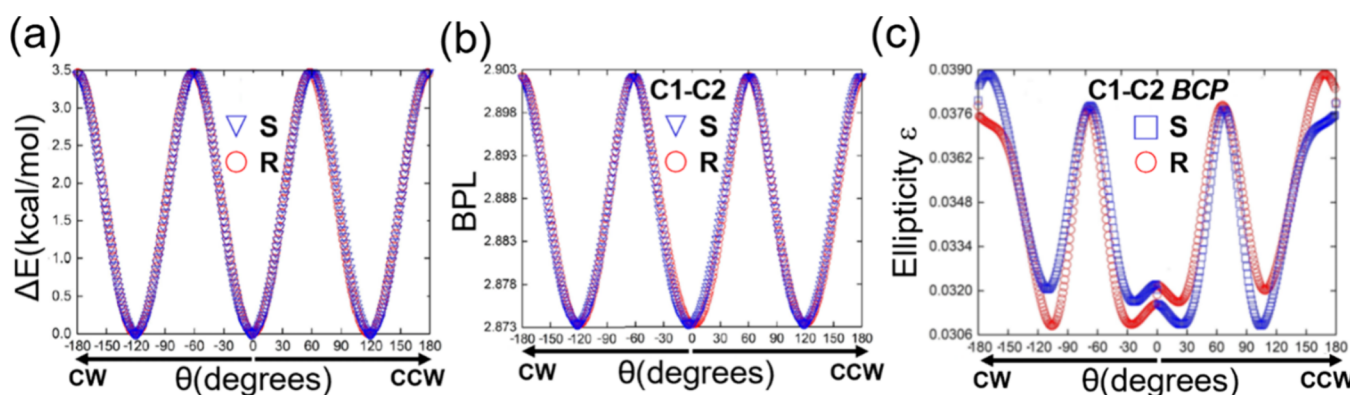


**Figure 15.** (a) Variations with applied torsion angle  $\theta$  of the relative energy  $\Delta E$  for the rotation isomers of the R and S stereoisomers of lactic acid for the applied clockwise (CW) ( $-180.0^\circ \leq \theta \leq 0.0^\circ$ ) and counterclockwise (CCW) ( $0.0^\circ \leq \theta \leq 180.0^\circ$ ) torsion distortions. (b) Variations of the C1–C2 BCP torsion bond-path length (BPL), where C1 denotes the chiral carbon atom. (c) The corresponding variations of the ellipticity  $\epsilon$  with torsion angle  $\theta$  for the C1–C2 torsion BCP. Reproduced with permission from ref 51. Copyright 2019 Elsevier.

profile is associated with the highest frequency IR-active mode  $3298.32 \text{ cm}^{-1}$  (mode 28). The C–H  $K$  profiles generally possess maximum IR-responsivity ( $K = 1.0$ ) for the entire bond-path profile. This use of  $K$  can accommodate the NNAs,<sup>192,384</sup> which occur for a C–C BCP bond-path in mode 21 ( $1573.93 \text{ cm}^{-1}$ ) along the mirror plane, during the vibration associated with mode 21. The presence of an NNA in mode 21 resulted in C–C BCP bond-path  $K$  profiles that are very similar to the corresponding  $K$  profiles of relaxed benzene, demonstrating the stabilization effect of the NNA; see the red  $K$  profile in Figure 14b.

**4.4.1.2. Inherent Asymmetry of the  $S_1$  Electronic State of Fulvene.** The tendency for both bond-path rigidity and bond-path flexibility<sup>393</sup> occurring during the course of the fulvene double bond isomerization for both the ground state  $S_0$  and the first excited  $S_1$  electronic state was quantified, building on earlier work.<sup>354,372,373,394</sup> The maximum values of the bond-path-rigidity and bond-path-flexibility were defined by values of  $K = 0$  and  $K = 1$ , respectively. The  $S_1$  state at the bond torsion angle  $\theta = 0.0^\circ$  was found to uniquely possess the maximum possible value of  $K = 1$ , along the entire bond-path. At the conical intersection, however, the value of  $K$  for the  $S_1$  state drops lower than that for the  $S_0$  state, indicating that the photoexcitation facilitated the torsion; see Figure 14c. We define  $\Delta Q_0$  and  $\Delta Q_1$  as the relative integrated areas under the  $K(S_0, S_1)$  plots for the ground  $S_0$  and first excited  $S_1$  states, respectively, and  $\Delta A = \Delta(\text{C}-\text{BCP})$ ,  $\Delta B = \Delta(\text{BCP}-\text{C})$  as the linear separation between the BCP and respective C atoms. The relative areas of  $\Delta Q_0$  associated with the precession  $K$

plots for the  $S_0$  state, for the torsion C2–C6 BCP bond-paths, were found to increase monotonically as the torsion coordinate  $\theta$  increased; see Table 6. This correlation, however, between  $\Delta Q_1$  and  $\Delta B$  is not found to be present for the  $S_1$  state. This caused unpredictable variations in the bond-path rigidity for the  $S_1$  state due to the asymmetry for the  $S_1$  state in agreement with earlier work.<sup>373</sup>

**4.4.1.3. Chemical Coupling of Hydrogen Bond and Covalent Bond in Water.** Much earlier, a scalar QTAIM investigation with one of the current authors discovered H–O hydrogen bond BCPs with values of  $H(r_b) < 0$  in ice Ih indicating covalent character<sup>410</sup> and hence determined the presence of coupling between the H–O hydrogen bonds and O–H covalent (sigma) bonds in confirmation of X-ray diffraction work of E. D. Isaacs.<sup>411</sup> The Ehrenfest force  $E(r)$  partitioning was employed to explain why variations in the chemical coupling in the  $(\text{H}_2\text{O})_4$  cyclic and  $(\text{H}_2\text{O})_6$  compact water cluster morphologies resulted in weaker H–O hydrogen-bonds in the  $(\text{H}_2\text{O})_6$  compared with the  $(\text{H}_2\text{O})_4$ <sup>412</sup> water cluster. This investigation was undertaken by quantifying the electron momentum transfer that occurs between an O–H covalent bond and H–O hydrogen bond and that share a hydrogen atom. As a consequence, the ability of the Ehrenfest force  $E(r)$  to quantify the vector (directional)<sup>385,409</sup> aspects of cooperativity of H–O hydrogen bonding was demonstrated: this was not possible using the Hessian of  $\rho(r)$ ; see Figure 14d.

#### 4.5. Full Symmetry Breaking and Method of Construction of Eigenvector-Space Trajectories

The ability to consider iso-energetic phenomena is possible due to attainment of full symmetry-breaking. This is achieved by the removal of the constraint that systems under comparison possess measurable differences in molecular geometries. A simple example demonstrating full symmetry-breaking, within the context of NG-QTAIM, is provided by quantifying the effect of an applied electric (*E*)-field on the C1–C2 BCP of the ethene molecule;<sup>386</sup> see section 4.2.1.1. The C1–C2 BCP shifts along the C1–C2 BCP bond-path in response to an electric (*E*)-field applied parallel/antiparallel to the C1–C2 BCP bond-path. This is despite the C1 and C2 atoms not measurably shifting in response to the applied electric (*E*)-field. In contrast, the C1–C2 BCP readily shifts along the C1–C2 BCP bond-path. This is due to the valence electrons associated with the C1–C2 BCP being very much lighter and more responsive than are the nuclei of the C1 and C2 atoms. Iso-energetic phenomena for an entire molecule have been successfully quantified by constructing the eigenvector-space-trajectories  $T_i(s)$ ;  $i = \{\sigma, \rho, E\}$  using the stress tensor  $\sigma(r)$  with eigenvectors  $\{\pm e_{1\sigma}, \pm e_{2\sigma}, \pm e_{3\sigma}\}$ , Hessian of  $\rho(r)$  with eigenvectors  $\{\pm e_1, \pm e_2, \pm e_3\}$ , and the Ehrenfest Force  $E(r)$  with eigenvectors  $\{\pm e_{1E}, \pm e_{2E}, \pm e_{3E}\}$ . In the future, additional partitioning schemes of  $\rho(r)$  could also be implemented.

All scalar measures lack full symmetry-breaking, including the molecular geometry, relative energy  $\Delta E$  (see Figure 15a), and the (scalar) QTAIM measures, e.g., stiffness  $S$ , bond-path length (BPL), stress tensor stiffness  $S_\sigma$ , and local total energy density  $H(r_b)$ ; see Figure 15b. This lack of full symmetry-breaking was demonstrated for the *S* and *R* stereoisomers of lactic acid earlier<sup>50</sup> for the torsion bond subjected to a bond-torsion  $-180.0^\circ \leq \theta \leq 180.0^\circ$  in the vicinity of the chiral carbon. Partial symmetry-breaking is apparent in the variation of the ellipticity  $\epsilon$ , a scalar; however, it cannot distinguish the ellipticity  $\epsilon$  values of the *S* and *R* stereoisomers for the complete set of values of the torsion angle  $\theta$ , e.g.,  $\theta = 0.0^\circ$ ; see Figure 15c.

The stress tensor  $\sigma(r)$ , Hessian of  $\rho(r)$ , and Ehrenfest force  $E(r)$  eigenvectors defining the associated coordinate frames were used as a reference to construct the  $U_\sigma$ -space,  $U_\rho$ -space, or  $U_E$ -space,<sup>52</sup> respectively, that enable full-symmetry-breaking. The  $U_\sigma$ -space,  $U_\rho$ -space, or  $U_E$ -space are created by the sets of three orthogonal eigenvectors: stress tensor  $\sigma(r)$  with eigenvectors  $\{\pm e_{1\sigma}, \pm e_{2\sigma}, \pm e_{3\sigma}\}$ , Hessian of  $\rho(r)$  with eigenvectors  $\{\pm e_1, \pm e_2, \pm e_3\}$ , and the Ehrenfest force  $E(r)$  with eigenvectors  $\{\pm e_{1E}, \pm e_{2E}, \pm e_{3E}\}$ , respectively. They track the real space shift  $dr$  of a BCP. In doing so, we map the shift  $dr$  to a point in the  $U_\sigma$ -space,  $U_\rho$ -space, or  $U_E$ -space, to enable the full-symmetry-breaking. The frame of reference is usually selected to correspond to the geometry associated with the minimum energy. The  $T_\sigma(s)$ ,  $T_\rho(s)$ , and  $T_E(s)$  trajectories are defined as an ordered sets of points with a sequence parameter  $s$ . The coordinates are constructed using the  $\sigma$ ,  $\rho$ , or  $E$  eigenvectors and associated with each of the points on the  $T_i(s)$  for a given BCP and are calculated by determining the shift vector  $dr = r_b(s) - r_b(s-1)$ ,  $s > 0$  of the location  $r_b$  of the BCP, between the previous step  $(s-1)$  and the current step  $(s)$ . Each BCP shift vector  $dr$  is therefore projected onto the  $\sigma$ ,  $\rho$ , or  $E$  eigenvectors and then mapped to a point for use in the construction of, e.g., the stress tensor-directed trajectory  $T_\sigma(s)$ :  $\{(e_{1\sigma} \cdot dr), (e_{2\sigma} \cdot dr), (e_{3\sigma} \cdot dr)\}$  in sequence to form the  $T_\sigma(s)$ .

This method of construction of the  $T_i(s)$  is used as the basis for the two main types of  $T_i(s)$ : the eigenvector-space-following trajectories  $T_{iF}(s)$  and the eigenvector-space-directed trajectories  $T_{iD}(s)$ . Note the use of subscripts “F” and “D” to denote “following” and “directed”, respectively, and also that the subscript “E” is used for the Ehrenfest force  $E(r)$  to avoid confusion with the “F” corresponding to the eigenvector-space-following trajectories  $T_{iF}(s)$ . Both the following  $T_{iF}(s)$  and the directed  $T_{iD}(s)$  trajectories are generated by the passage created by BCP motion in  $U_i$ -space.

The coordinates associated with each of the points on the  $T_F(s)$  or  $T_D(s)$  trajectory are calculated by evaluating the components of the BCP shift vector  $dr = r_b(s) - r_b(s-1)$ ,  $s > 0$ , where  $r_b$  (dark green) indicates the location of the BCP, from the previous step sequence number  $s-1$  located at  $r_b(s-1)$  (light green) to the current step sequence number  $s$ ; see Figure 16. Every BCP shift vector  $dr$  is projected onto the

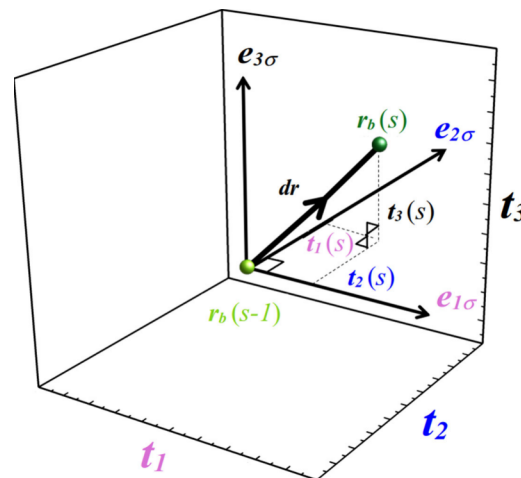


**Figure 16.** A schematic of the basic construction of the eigenvector-following trajectory  $T_F(s)$  and eigenvector-directed trajectory  $T_D(s)$ . The BCP shift vector  $dr$  between a position  $r_b(s-1)$  (light green) with step sequence number  $(s-1)$  and the position  $r_b(s)$  (dark green) with step sequence number  $(s)$  is projected onto the mutually orthogonal  $e_{1\sigma}$ ,  $e_{2\sigma}$ , and  $e_{3\sigma}$  unit eigenvectors, which are used to construct the mutually orthogonal  $t_1$ ,  $t_2$ , and  $t_3$  axes as described in the main text. The start and end positions of the BCP are denoted by the light green and dark green spheres respectively. Note the  $t_1(s)$ ,  $t_2(s)$ , and  $t_3(s)$  components associated with this BCP shift vector  $dr$  for the step sequence number  $s$ .

mutually orthogonal unit eigenvectors: e.g., for the construction of the stress tensor  $T_{\sigma F}(s)$  or  $T_{\sigma D}(s)$ , these are  $e_{1\sigma}$ ,  $e_{2\sigma}$  and  $e_{3\sigma}$  using a vector dot product denoted by “.” and thus mapped to a point  $\{(e_{1\sigma} \cdot dr), (e_{2\sigma} \cdot dr), (e_{3\sigma} \cdot dr)\}$ . For simplicity, we display these projections onto mutually orthogonal axes as  $\{(e_{1\sigma} \cdot dr), (e_{2\sigma} \cdot dr), (e_{3\sigma} \cdot dr)\} = \{t_1, t_2, t_3\}$ , where  $t_1 = e_{1\sigma} \cdot dr$ ,  $t_2 = e_{2\sigma} \cdot dr$ , and  $t_3 = e_{3\sigma} \cdot dr$ ; see Figure 16. Note, the  $t_1(s)$ ,  $t_2(s)$ , and  $t_3(s)$  are components parallel to each of the  $t_1$ ,  $t_2$ , and  $t_3$  axes, respectively.

Examples of eigenvector-space-following trajectories  $T_{iF}(s)$ <sup>358,395,408,413–418</sup> include normal mode behaviors such as isotopic effects,<sup>413</sup> prediction of inward-conrotatory or outward-conrotatory ring-opening (competitive) reaction pathways consistent with experiment,<sup>358,419</sup> the functioning of molecular switches,<sup>408</sup> the flip rearrangement of the water molecule within a pentamer<sup>416</sup> and molecular rotary motors that track nonadiabatic dynamics-trajectories through a conical

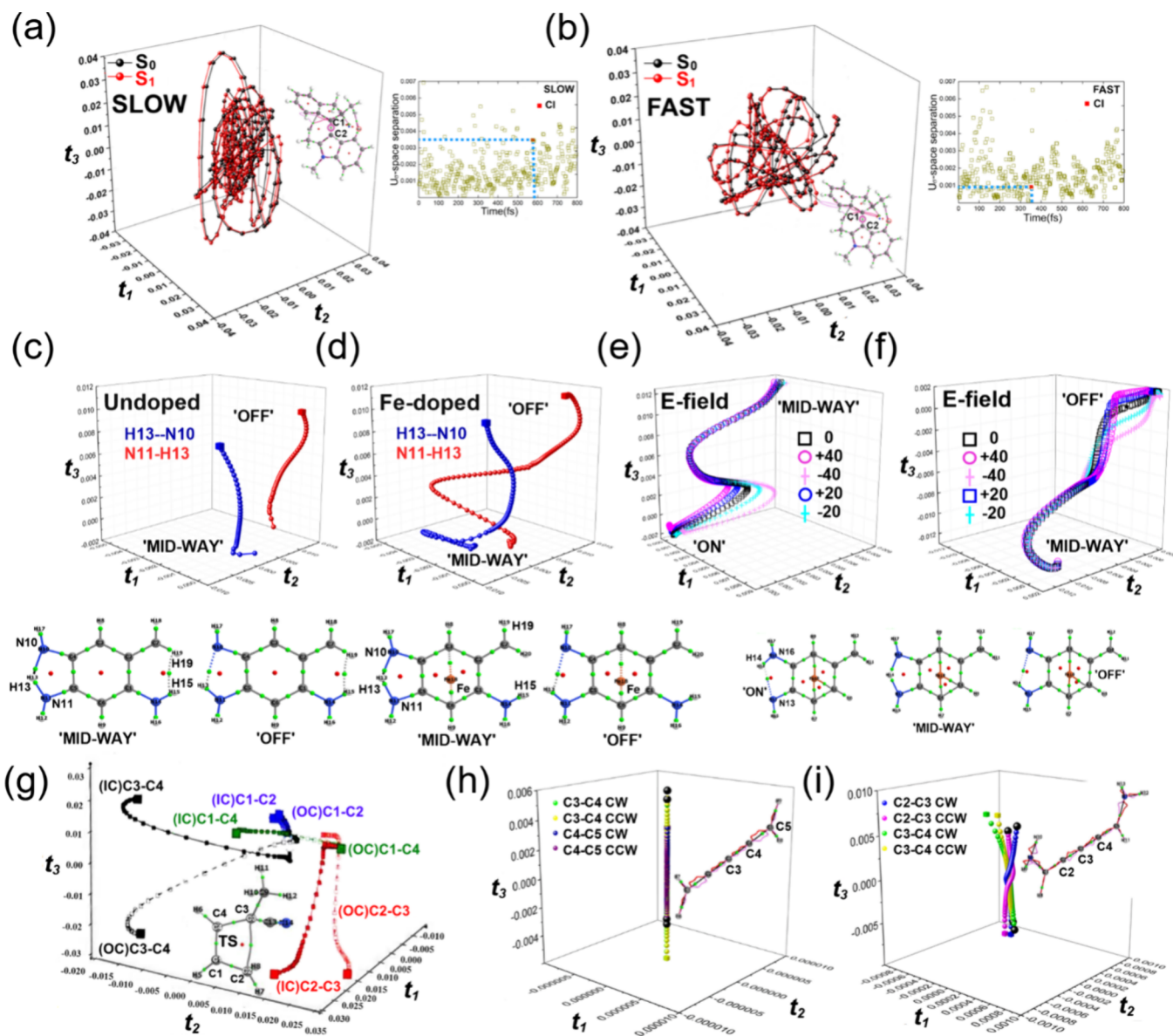


**Figure 17.** Stress tensor-following trajectory  $T_{\sigma F}(s)$  for the (a) slow and (b) fast nonadiabatic dynamics-trajectories corresponding to the axial bond C1–C2 BCP in the F-N.A.I.B.P molecular-rotary motor prior to passage through the CI for the  $S_0$  and  $S_1$  electronic states. Reproduced with permission from ref 395. Copyright 2020 Wiley. The inset molecular graphs display the associated  $U_{\sigma}$ -space  $S_0$  and  $S_1$  separations at the CI (red square). The  $T_{\sigma F}(s)$  for a benzoquinone-like molecule displaying the hydrogen transfer tautomerization with (c) no Fe dopant and (d) Fe dopant for the switch set to the “MID-WAY” and “OFF” positions, where the H15–H19 contact is shown on the molecular graph at the “MID-WAY” position. Reproduced with permission from ref 387. Copyright 2019 Elsevier. Reproduced with permission from ref 388. Copyright 2019 Wiley. The  $T_{\sigma F}(s)$  of a quinone-analogue molecule in the (e) “MID-WAY” and (f) “OFF” position of the switches with an applied electric  $E$ -field, units of  $10^{-4}$  au, with molecular graphs indicating the “ON”, “MID-WAY”, and “OFF” position of the switches. (g) The  $T_{\sigma F}(s)$  of the competitive ring-opening reaction of 1-cyano-1-methylcyclobutene for both inward conrotatory (IC) and outward conrotatory (OC) pathways where the inset molecular graph corresponds to the transition state. Reproduced with permission from ref 358. Copyright 2016 Wiley. Linear morphologies of the  $T_{\sigma F}(s)$  of the (h) [4]cumulene conformation and (i) the twisted morphology (+)S(−) conformations of S-1,5-diamino-[4]cumulene with inset molecular graphs with numbered carbon atoms. Reproduced with permission from ref 414. Copyright 2022 Wiley.

intersection (CI)<sup>395</sup> and the Ehrenfest Force  $E(r)$ ;<sup>415</sup> see the eigenvector-space-following trajectories  $T_{iF}(s)$  in section 4.6.1.

Iso-energetic phenomena relating to stereochemistry have also been examined, including chiral discrimination,<sup>50,51</sup> following  $S_N2$  reactions,<sup>52,53</sup> the effects of isotopomers<sup>54</sup> and electric fields,<sup>55,56</sup> the dependence on the atomic weight of atomic substituents of chiral effects<sup>57</sup> and achiral molecules,<sup>58</sup> and an explanation of the *cis*-effect without using energy-based measures.<sup>59</sup> These phenomena all use the eigenvector-space-directed trajectories  $T_{iD}(s)$  construction in section 4.7.

#### 4.6. Eigenvector-Space-Following Trajectories

The eigenvector-space-following trajectories  $T_{iF}(s)$ ;  $i = \{\sigma, \rho, E\}$  are created by following the motion of the BCPs of interest: the basic method for construction of the eigenvector-space-following trajectories  $T_{iF}(s)$  is explained in section 4.5. A selection of five contrasting types of chemical environments is focused on in more detail in the following five subsections.

**4.6.1. Applications of Eigenvector-Space-Following Trajectories.** Examples of the application of the eigenvector-space-following trajectories  $T_{iF}(s)$  include: molecular devices

**Table 7.** Stress Tensor-Following Trajectory  $T_{\sigma F}(s)$ , of the C1–C2 Axial BCP in the F-N.A.I.B.P Motor Corresponding to the ( $S_1$ ) Reaction Pathways for Hop Events Occurring at the Conical Intersections (CI) for Both Slow and Fast Dynamics-Trajectories<sup>a</sup>

time <sup>CI</sup>	$T_{\sigma F}(s)^{CI}$				$U_{\sigma}$
	$I_{\sigma}^{CI}_{S0}$	$I_{\sigma}^{CI}_{S1}$	$L_{\sigma}^{CI}_{S0}$	$L_{\sigma}^{CI}_{S1}$	
352	3.387	3.405	0.948	0.964	fast
					$\{(−0.0042), (0.0184), (−0.0009)\}$
574	5.341	5.342	1.626	1.642	slow
					$\{(0.0198), (0.0033), (0.0138)\}$

<sup>a</sup>Time<sup>CI</sup> corresponds to the duration (femtoseconds (fs)) of both the slow and the fast dynamics-trajectories to each of their respective  $T_{\sigma F}(s)^{CI}$ , with the corresponding stress tensor-following trajectory space  $U_{\sigma}$ -space separation  $L_{\sigma}^{CI}_{S0}, L_{\sigma}^{CI}_{S1}$ , real space separation  $I_{\sigma}^{CI}_{S0}, I_{\sigma}^{CI}_{S1}$ , and location in  $U_{\sigma}$  space  $\{t_1, t_2, t_3\}^{CI}_{S0}$  and  $\{t_1, t_2, t_3\}^{CI}_{S1}$  for the  $S_1$  and  $S_0$  states, respectively. Atomic units (au) are used throughout. Reproduced with permission from ref 395. Copyright 2020 Wiley.

including rotary motors<sup>395</sup> and switches,<sup>396,408</sup> the prediction of ring-opening reactions<sup>358,415,419</sup> and normal mode behaviors of benzene<sup>418</sup> and of water with isotopic effects that used oppositely directed Hessian of  $\rho(r)$  trajectories  $T_{\rho D}(s)$ .<sup>413</sup> Other examples are to predict the outcome of the flip rearrangements of the water pentamer<sup>416</sup> and H–O hydrogen bond and O–H covalent (sigma) bond coupling effects in the water pentamer,<sup>417</sup> as well as cumulenes,<sup>414</sup> predicting ring-opening reactions and inclusion of the use of the Ehrenfest force  $E(r)$ .<sup>415</sup>

A selection of five applications are chosen from the above topics of eigenvector-space-following  $T_{\sigma F}(s)$  to examine in more detail; see Figure 17: nonadiabatic dynamics-trajectories through a conical intersection (CI)<sup>395</sup> for functioning of molecular-rotary motors, the effects of the application of an electric ( $E$ )-field and photoexcitation on the functioning of switches,<sup>408,387</sup> competitive conrotatory (inward or outward) reaction pathways consistent with experiment<sup>358,419</sup> and the presence of the twisted morphology of the  $T_{\sigma F}(s)$  of cumulenes.<sup>414</sup>

**4.6.1.1. Understanding Efficient Functioning of F-N.A.I.B.P Molecular-Rotary Motors.** A chiroptical molecular motor 3-[*(2S*)-2-fluoro-2-methyl-1-indanylidene]-1-methyl-2-methylin-dole (F-N.A.I.B.P) with ideal stereocontrol using a modified light-driven unidirectional molecular rotor<sup>420</sup> was earlier presented by Feringa and co-workers; see Figure 17a and b. The control of excited-state properties such as the maintenance of full ( $360^\circ$ ) unidirectional and non“jittery” torsion motion is a vital step toward the goal of attaining very efficient controllable molecular-rotary motors.

The presence of both slow and fast categories of dynamics-trajectories<sup>421</sup> was demonstrated using NAMD (nonadiabatic molecular dynamics) simulations of modified (chemically) molecular motors of the F-N.A.I.B.P molecular-rotary motor. Scalar QTAIM earlier demonstrated, for a selection of dynamics-trajectory for the (F-N.A.I.B.P) molecular motor<sup>421</sup> blades, that the torsional motor motion was controlled by very strongly coupled “sticky” intramolecular F–H closed-shell BCPs and bond-paths linking atoms of the stator and rotor blades.<sup>422</sup> “Sticky” intramolecular bonds impeded free torsion about the axial bond (the C1–C2 BCP); in particular, the “sticky” F–H closed-shell BCPs only exist for the slow dynamics-trajectory, where the F–H closed-shell BCP bond “stickiness” was caused by a significant level of covalent character in the F–H closed-shell BCPs, from values of  $H(r_b) < 0$ .

The F-N.A.I.B.P motor was reexamined with NG-QTAIM to quantify rotary motor function that followed fast and slow

nonadiabatic dynamics-trajectories across a CI.<sup>395</sup> The stress tensor-following trajectories  $T_{\sigma F}(s)$  associated with the  $S_0$  and  $S_1$  electronic states were discovered to occupy unique locations in  $U_{\sigma}$ -space at the CI.

The shorter extent of the  $T_{\sigma F}(s)$  along the  $t_3$  axis for the FAST nuclear dynamics versus the SLOW nuclear dynamics-trajectory indicated greater efficiency for the axial rotation motion around the C1–C2 axial bond (BCP).<sup>395</sup> This was found to be a new measure for visualization and quantification of the degree of axial bond torsion purity associated with the F-N.A.I.B.P rotary motor.<sup>395</sup>

The presence of variations in the measured NG-QTAIM properties of the  $S_1$  and  $S_0$  electronic states at the CI of the F-N.A.I.B.P molecular-rotary motor was caused by the effective use of full symmetry-breaking in  $U_{\sigma}$ -space<sup>50</sup> that created separations in the measured NG-QTAIM properties associated with the  $S_1$  compared with the  $S_0$  state; see Figure 17a and b and Table 7.

The morphology of the  $T_{\sigma F}(s)$  was found to be relatively isotropic for the fast dynamics-trajectory with near equally spaced  $T_{\sigma F}(s)$  steps with a small  $t_{3,max} = (e_3 \cdot dr)_{max}$  component corresponding to motion along the C1–C2 BCP axial bond-path. The magnitude, large or small, of the  $t_{3,max}$  component was found to be due to the presence or absence of “sticky” ( $H(r_b) < 0$ ) closed-shell BCPs that connect the stator and rotor portions of the motor and therefore provides a measure of the low or high operational efficiency of the molecular-rotary motor. This is explained by the fact that in the limit of a 100% efficient molecular-rotary motor comprising pure axial bond-path torsion, then significant motion along the length of the C1–C2 BCP axial bond-path would not be present.

**4.6.1.2. Understanding “ON” and “OFF” Switch Functioning.** The stress tensor-following  $T_{\sigma F}(s)$  was applied to a proposed molecular switch with hydrogen atom transfer tautomerization in a benzoquinone-like molecule in the presence and absence of a coordinated iron atom, i.e., an Fe-dopant. This was undertaken to gain insight into the switch functioning that was not otherwise available with all energy-based approaches. Insight into, for instance, switch function failure, will remove the trial-and-error basis on which design and choice of molecular electronics candidate components can be based.

The lack of Fe-dopant atom resulted in an impairment of the switch “OFF” function mechanism and with the creation of an H–H closed-shell BCPs that demonstrated an electron-deficient and therefore strained bonding environment; see Figure 17c. Consequently, the undoped quinone switch did not reach the “OFF” position of the switch due to the N10–

**Table 8.** Real Space-Following Trajectory  $T_{\sigma F}(s)$  Lengths  $l$  for the BCP Shifts Occurring for the H14–N13 BCP/N13–H14 BCP and N16–H14 BCP/H14–N16 BCP for the (“ON”, “OFF”) Switch Directions<sup>a</sup>

	BCP				
	-40	-20	0	+20	+40
H14–N13/N13–H14	(0.784, 0.783)	(0.701, 0.836)	(0.654, 0.891)	(0.617, 0.930)	(0.591, 0.955)
N16–H14/H14–N16	(1.129, 0.485)	(1.087, 0.510)	(1.054, 0.533)	(1.025, 0.554)	(1.006, 0.577)

<sup>a</sup>Values of the applied  $E$ -field = 0,  $\pm 20 \times 10^{-4}$ , and  $\pm 40 \times 10^{-4}$  au. Shared-shell BCPs and closed-shell BCPs are denoted by the notations “–” and “–”, respectively. Atomic units are used throughout. Reproduced with permission from ref 387. Copyright 2019 Wiley.

H13 BCP and N11–H13 BCP remaining close to the “MID-WAY” quinone position of the switch. This was demonstrated by the absence of the associated  $T_{\sigma F}(s)$  in the  $e_{1\sigma}$  direction, i.e., the “easy” direction. This resulted in an unstable “OFF” position of the switch, which renders the undoped quinone switch unsuitable for use in electronic circuits. This was corrected by the substitution of an Fe-dopant in the switch that facilitated the full and topologically stable “OFF” position of the switch. This is explainable by the very significant sliding motion of the H13–N10 BCP and the N11–H13 BCP in the “easy” ( $e_{1\sigma}$ ) direction in  $U_\sigma$  space.

The reversal of a homogeneous external electric field on a candidate molecular switch using a quinone-analogue molecule was demonstrated to improve the “OFF” functioning; see Figure 17f. NG-QTAIM was also used to understand why the performance of the switch depended on the  $\pm E$ -field direction in the process of the H14 atom destabilization that participated in the hydrogen atom transfer tautomerization process. Larger (+) $E$ -field values improved the “OFF” switch function that enabled the H14 atom transfer tautomerization to occur with greater readiness by the destabilization of the H14–N16 closed-shell BCP bond-path that exists from the “MID-WAY” to the “OFF” position of the switch. Larger (−) $E$ -field values improved the “ON” switch function by destabilizing the H14–N13 closed-shell BCP that exists for the “MID-WAY” and the “ON” position of the switch. Reversal of the electric  $E$ -field improved the “ON” functioning of the switch, from the “MID-WAY” position of the switch that corresponds to the tautomerization energy barrier: this insight was previously inaccessible. The real-space-following trajectory  $T_{\sigma F}(s)$  lengths  $l$  for the “OFF” switch direction of the H14–N16 BCP were demonstrated to increase with increase in the (+) $E$ -field and decrease with increase in the (−) $E$ -field values; see Table 8. Relative energy  $\Delta E$  plots cannot provide insight into the switch mechanism due to their inability to quantify variations in chemical behavior induced by the passage of the H14 atom along the extent of the participating H–O hydrogen bond in the tautomerization process; see Figure 15.

**4.6.1.3. Predicting the Products of Competitive Ring-Opening Reactions.** Prior to NG-QTAIM, quantum chemistry theories could neither provide explanations nor predict the electronic reorganization occurring as a result of the torquoselectivity of a ring-opening reaction. In addition, they did not include the directional chemical character inherent in the reaction pathway, except for very high symmetry cases. The Woodward–Hoffmann rules use the conservation of orbital symmetry as their basis and have long been used to investigate the torquoselectivity of a ring-opening reaction.<sup>423,424</sup> The torquoselectivity is a category of stereoselectivity that depends on the direction of the reaction pathway. The torquoselectivity<sup>425</sup> is defined as the preference for the transition state inward conrotatory (T.S.I.C) or transition state outward conrotatory (T.S.O.C) rotation of substituent species in

electrocyclic reactions. NG-QTAIM was demonstrated to quantify and distinguish clearly the transition states associated with the inward and outward conrotations of competitive ring-opening reactions of 3-(trifluoromethyl) cyclobut-1-ene and 1-cyano-1-methylcyclobutene; see Figure 17g. The competitive case is known to be the hardest test for any theory that analyzes torquoselectivity. The NG-QTAIM directional properties of both the T.S.I.C and the T.S.O.C ring-opening reactions were determined by calculating the stress tensor-directed trajectory  $T_{\sigma F}(s)$  with length  $l$  in real space. Larger  $l$  values correlated well with the lowest density functional theory (DFT)-evaluated total energy barriers. The  $l$  values were generally larger (7 of 8) for T.S.I.C compared with T.S.O.C for the forward (*f*) reaction pathway. Therefore, the real space length  $l$  provided consistency with experiment for competitive reactions: the T.S.I.C reaction pathway is energetically preferred by −1.76 kcal/mol; see Table 9.

**Table 9.** NG-QTAIM Real Space Lengths ( $l$ ) in au of the Ring-Opening T.S.I.C and T.S.O.C Pathways for the Forward (*f*) Direction Corresponding to the IRC of 1-Cyano-1-methylcyclobutene<sup>a</sup>

	T.S.I.C	T.S.O.C
C3–C4 $f$	2.6396	2.1010
C1–C4 $f$	0.4920	0.4609
C2–C3 $f$	0.2980	0.3425
C1–C2 $f$	0.0866	0.0804
C13–N14 $f$	7.8767	6.7040
C3–C9 $f$	5.6734	3.7664
C13–C3 $f$	5.5260	4.4632
C2–H8 $f$	1.3176	0.8620

<sup>a</sup>Reproduced with permission from ref 358. Copyright 2016 Wiley.

**4.6.1.4. Twisted Stress Tensor-Directed Trajectories  $T_{\sigma D}(s)$  of  $\alpha,\omega$ -Disubstituted [4]Cumulenes.** The concepts of helical character and chirality in  $U_\sigma$ -space were explored using NG-QTAIM, instead of orbitals, for the  $\alpha,\omega$ -disubstituted [4]-cumulenes as the end groups were torsioned.<sup>414</sup> The stress tensor-directed trajectory  $T_{\sigma D}(s)$  provided the quantification of both the nature and the degree of the chiral and helical character in  $U_\sigma$ -space. The S-1,S-dimethyl-[4]cumulene was found to comprise insignificant chiral character but significant axiality (helicity), which resulted in a (weakly) helical morphology of the associated  $T_{\sigma D}(s)$ . The (−)S(−), (+)S(−), and (+)S(+) S-1,S-diamino-[4] cumulene conformations contained very significant chiral and helical character. This resulted in significant helix-like morphologies of the associated  $T_{\sigma D}(s)$ . The consequences for the  $T_{\sigma D}(s)$  in quantifying the chiral and helical character in these molecules for future experiments was discussed. The morphologies of the [4] cumulene  $T_{\sigma D}(s)$  and (+)S(−) S-1,S-diamino-[4]cumulene conformations  $T_{\sigma D}(s)$  were found to be linear and twisted,

respectively; see Figure 17*h* and *i*. The chirality in  $U_\sigma$ -space is explored in detail within the context of NG-QTAIM in section 4.7.

#### 4.7. Eigenvector-Space-Directed Trajectories: Relevance for Experiment and Derivation

A chiral molecule is defined as possessing at least one chiral center, and the Cahn–Ingold–Prelog (CIP) priority rules are employed to assign the (*R/S*) chiral configurations without calculation;<sup>426,427</sup> recently, these rules have been updated.<sup>428</sup> The CIP rules are widely used throughout the chemical sciences and rely on the molecular geometries of *S* and *R* stereoisomers possessing mirror image geometries. The CIP rules, therefore, cannot be used for the classification of the chirality of achiral species. Quack considered the subject of biomolecular homochirality as a candidate “chemical signature” of life;<sup>429</sup> from a very extensive theoretical investigation, no clear correlation between energy differences and *L* or *R* handedness of a given chiral molecule was found, that would be expected in an *L*-amino acid dominant world. The origin of chirality as being due to helix character of stereoisomers was proposed as early as 1851 by Fresnel.<sup>430</sup> Later this effect was examined by optical experiment and referred to as circular dichroism<sup>431</sup> and is in agreement with theories of optical activity that correlate the inherent helix(helical) identities with directions left (*S*) or right (*R*) of rotation of the incident circularly polarized light.<sup>432–434</sup> Wang much later provided a proposal of a “helix theory” for the chirality of molecules and realized that neither steric hindrance alone nor molecular geometries<sup>435</sup> provided the evidence for this helical character. Wang referred to the correlation between chiral and helix-(helical) characteristics as the “chirality-helicity equivalence”, which was later investigated with NG-QTAIM. The requirement for an improved understanding of the consequences of charge density  $\rho(r)$  redistribution was later found in experiments on neutral chiral molecules.<sup>436</sup> These experiments utilized the coherent helical motion of bound electrons in agreement with the NG-QTAIM derived helix-shaped directed trajectories  $T_{\sigma D}(s)$  uncovered by previous work.<sup>50</sup> The details of the charge density  $\rho(r)$  redistribution occurring in chiral molecules rather than spatial effects<sup>437</sup> were recently demonstrated as being responsible for enantiospecific preferences in the orientation of electron spins in agreement with the proposed “chirality-helicity equivalence” of Wang.<sup>435</sup> This is also in agreement with theoretical investigations<sup>438</sup> that discovered the interdependence of steric-electronic factors were more complicated than can be revealed by sole consideration of molecular geometries, e.g., the helical electronic transitions occurring for spiroconjugated (cumulene) molecules.<sup>414,439</sup>

Full symmetry-breaking<sup>440</sup> is needed to induce helical character, not to be confused with helical molecular geometries, associated with chirality. Full symmetry-breaking is achieved by creating a set of rotation isomers by applying a pair of Cartesian torsions  $0.0^\circ \leq \theta \leq 180.0^\circ$  counterclockwise (CCW) and  $-180.0^\circ \leq \theta \leq 0^\circ$  clockwise (CW), for the *S* and *R* stereoisomers; see Figure 18a. The stress tensor trajectories  $T_{\sigma D}(s)$  consequently reveal the intrinsic helical character required to enable the location of the chirality-helicity. A demonstration of the full symmetry-breaking properties inherent to the  $T_{\sigma D}(s)$  is uncovered by inspection of the gap at  $\theta = 0.0^\circ$  between the  $T_{\sigma D}(s)$  for the CCW (*S* stereoisomer) and CW (*R* stereoisomer) bond torsions of lactic acid. This

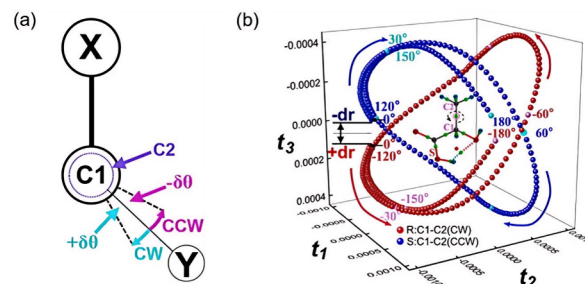


**Figure 18.** (a) Definitions of the dihedral angles  $\theta$  using the clockwise (CW) and counterclockwise (CCW) directions of bond torsion where the X–C1–C2–Y atoms are placed in sequence away from the viewing plane that is perpendicular to the C1–C2 bond-path direction; note, atom X is closest to the viewer and at the “12 o’clock” position. The C2–Y bond rotating in a CCW direction in the viewing plane corresponds to a negative shift ( $-\delta\theta$ ) in the dihedral angle  $\theta$ . Conversely, C2–Y rotating in a CW direction in the viewing plane corresponds to a positive shift ( $+\delta\theta$ ) in the dihedral angle  $\theta$ . Reproduced with permission from ref 56 under Creative Commons license. (b) The stress tensor-directed trajectory  $T_{\sigma D}(s)$  of the *R* (red) and *S* (blue) stereoisomers ( $\theta = 0.0^\circ$ ) for the torsional C1–C2 bond critical point (BCP) for CW and CCW bond torsions display a full symmetry-breaking shift ( $2\ dr$ ). The *S* stereoisomer molecular graph (inset) with the associated ring critical point (RCP) and C1–C2 torsional BCP are shown as the undecorated red and green spheres, respectively. The maximum stress tensor-directed trajectory projections  $T_{\sigma D}(s)_{\max} = \{t_{1\max}, t_{2\max}, t_{3\max}\} = \{(e_{1\sigma} \cdot dr)_{\max}, (e_{2\sigma} \cdot dr)_{\max}, (e_{3\sigma} \cdot dr)_{\max}\}$ , where the  $dr$  denote the BCP shift vectors. Reproduced with permission from ref 50. Copyright 2019 American Chemical Society.

gap at  $\theta = 0.0^\circ$  is due to the presence of the associated BCP shift vectors  $+dr$  and  $-dr$  having opposite directions; see Figure 18b. For example, consider a CCW bond torsion starting at  $\theta = 0.0^\circ$  with a finite BCP shift  $+dr = \{+0.0001, 0.000, 0.000\}$ , with the associated CW BCP shift vector  $-dr \approx \{-0.0001, 0.000, 0.000\}$ , yielding a  $U_\sigma$ -space separation of  $2\ dr$ .

A bond that can torsion freely, usually a C–C bond that is associated with the chiral carbon atom, is subjected to a pair of geometric torsion distortions: CCW and CW. This procedure is used to create the stress tensor-directed trajectory  $T_{\sigma D}(s)$  that results in a full symmetry-breaking perturbation to calculate the NG-QTAIM stereoisomer  $S_\sigma$  or  $R_\sigma$  classifications independently of using the CIP priority rules; note the subscript “ $\sigma$ ” that denotes use of the  $T_{\sigma D}(s)$ . The stress tensor-directed trajectory  $T_{\sigma D}(s)$  is generated by constraining a pair of bond-torsions  $0.0^\circ \leq \theta \leq 180.0^\circ$  (CCW) and  $-180.0^\circ \leq \theta \leq 0^\circ$  (CW) that yields a sequence of points that tracks subsequent induced motion of the BCP. The CCW and CW directions of bond torsion represent a pair of left-handed ( $S_\sigma$ ) and right-handed ( $R_\sigma$ ) directions of bond torsion, respectively. This mapping of CCW (left-handed) and CW (right-handed) is in agreement with circular dichroism optical experiments that provide refractive indices for left-handed (*S*) and right-handed (*R*) directions of circularly polarized light.

The maximum stress tensor-directed trajectory projections  $T_{\sigma D}(s)_{\max} = \{t_{1\max}, t_{2\max}, t_{3\max}\}$  are used to define the dimensions of a “bounding box” that surround a  $T_{\sigma D}(s)$  that are used in the calculation of the chirality  $C_\sigma$ , bond-flexing  $F_\sigma$  and bond-axiality  $B_\sigma$ . Note, the subscript “max” comprising  $T_{\sigma D}(s)_{\max}$  corresponds to the difference between the minimum and maximum values of the projection of the BCP shift  $dr$  vector onto  $e_{1\sigma}$ ,  $e_{2\sigma}$  or  $e_{3\sigma}$  along all of the stress tensor-directed

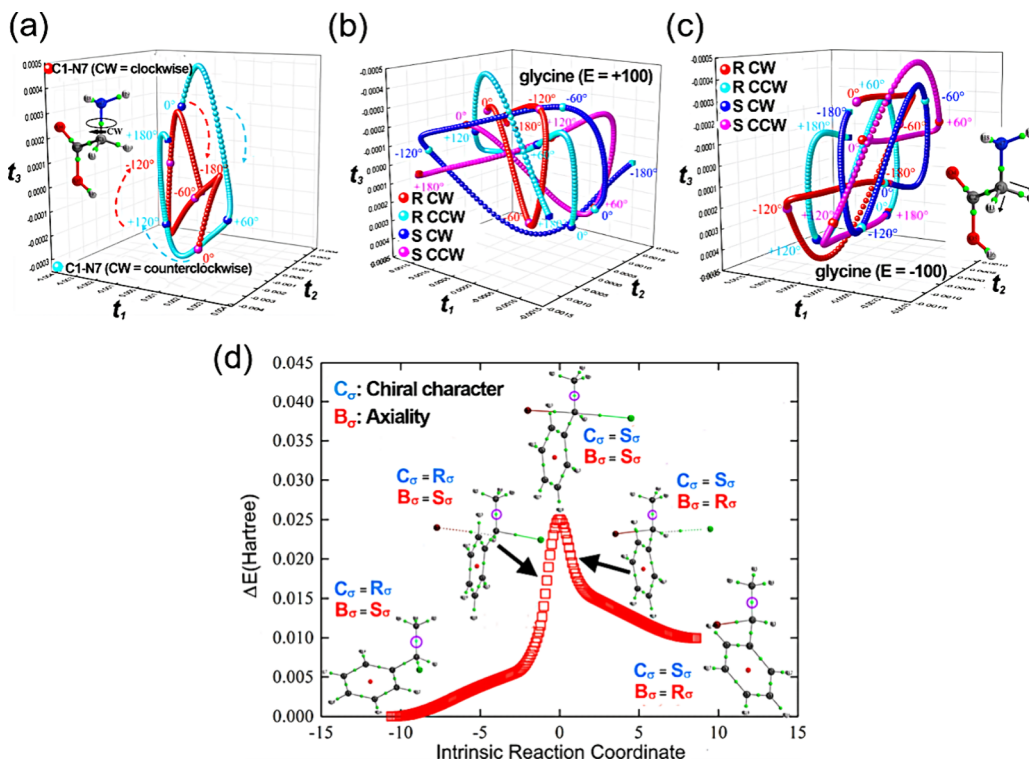


**Figure 19.** (a) The stress tensor-directed trajectories  $T_{\sigma D}(s)$  of the C1–N7 BCP torsion bond-path of glycine for the clockwise (CW) ( $-180.0^\circ \leq \theta \leq 0.0^\circ$ ) and counterclockwise (CCW) ( $0^\circ \leq \theta \leq 180.0^\circ$ ) rotation directions with the CW bond torsion direction displayed. (b) Corresponding results for the  $T_{\sigma D}(s)$  for the applied electric ( $E$ )-field =  $+100 \times 10^{-4}$  au. (c) Corresponding  $T_{\sigma D}(s)$  for the applied  $E$ -field =  $+100 \times 10^{-4}$  au, where the black arrow of the inset indicates the  $+E$ -field direction: for easier comparison, equally scaled axes are used for all  $E$ -field values, and further details are provided in Figure 6. Reproduced with permission from ref 55. Copyright 2021 Wiley. (d) The relative energy  $\Delta E$  profile of the  $S_2N_2$  reaction of the Br<sup>-</sup> attack on (R)-1-chloro-1-phenylethane (reactant) resulting in (S)-1-bromo-1-phenylethane (product) along with the transition state are shown with the chirality  $C_\sigma$  and axiality  $B_\sigma$  assignments superimposed. Reproduced with permission from ref 53. Copyright 2021 Wiley.

trajectory  $T_{\sigma D}(s)$ . It should be noted that the stress tensor eigenvector  $e_{1\sigma}$  is associated with the direction where the BCP electrons are subject to the greatest compressive forces,<sup>366</sup> therefore,  $e_{1\sigma}$  corresponds to the (“easy”) most preferred direction for the BCP electrons to be displaced when the BCP is torsioned. The  $e_{2\sigma}$  and  $e_{3\sigma}$  correspond to the directions that are associated with the lowest compressive forces and tensile forces on the BCP electrons, respectively.

The chirality  $C_\sigma$  is generated from the BCP (bond-twist) shift in the plane perpendicular to  $e_{3\sigma}$  (defines the bond-path) and is calculated as the difference in the maximum  $T_{\sigma D}(s)$  projections,  $t_1 = e_{1\sigma} \cdot dr$  (the scalar “dot” product of the stress tensor  $e_{1\sigma}$  eigenvector and the BCP shift vector  $dr$ ) of the  $T_{\sigma D}(s)$  values between the CCW and CW bond torsions:

$$C_\sigma = [(e_{1\sigma} \cdot dr)_{\text{max}}]_{\text{CCW}} - [(e_{1\sigma} \cdot dr)_{\text{max}}]_{\text{CW}} \quad (4.7.1)$$

The bond-flexing  $F_\sigma$  is associated with the least preferred direction corresponding to the  $e_{2\sigma}$  stress tensor  $\sigma(\mathbf{r})$  eigenvector and is generated from  $t_2 = e_{2\sigma} \cdot dr$ . The bond-flexing  $F_\sigma$  was earlier used for determining the chiral effects induced by applying an electric E-field to glycine:<sup>55</sup>

$$F_\sigma = [(e_{2\sigma} \cdot dr)_{\text{max}}]_{\text{CCW}} - [(e_{2\sigma} \cdot dr)_{\text{max}}]_{\text{CW}} \quad (4.7.2)$$

The axiality  $B_\sigma$  is generated from axial BCP sliding and defined by  $t_3 = e_{3\sigma} \cdot dr$ , where the BCP sliding is defined as the shift of the BCP position along the associated bond-path:

$$B_\sigma = [(e_{3\sigma} \cdot dr)_{\text{max}}]_{\text{CCW}} - [(e_{3\sigma} \cdot dr)_{\text{max}}]_{\text{CW}} \quad (4.7.3)$$

The axiality  $B_\sigma$  is used to quantify the resultant extent of the axial BCP displacement along the associated bond-path<sup>413</sup> in reaction to the applied CCW and CW bond torsions.

The  $S_\sigma$  or  $R_\sigma$  assignments for the chirality  $C_\sigma$ , bond-flexing  $F_\sigma$ , and axiality  $B_\sigma$  are determined by the sign (+) or (-) of eqs 4.7.1–4.7.3. The  $S_\sigma$  character is specified for  $C_\sigma > 0$ ,  $F_\sigma > 0$ , or  $B_\sigma > 0$  and the  $R_\sigma$  character for  $C_\sigma < 0$ ,  $F_\sigma < 0$ , or  $B_\sigma < 0$ ; the subscript “ $\sigma$ ” indicates that  $S_\sigma$  and  $R_\sigma$  are calculated using the stress tensor-directed trajectory  $T_{\sigma D}(s)$ .

Helical characteristics derived from the  $\rho(r_b)$  of the C1–C2 torsion BCP are found in the form of both a nonaxial component perpendicular to the bond-path and an axial component that is parallel to the bond-path; notice the helical shaped  $T_{\sigma D}(s)$  in Figure 18. Helical shaped  $T_{\sigma D}(s)$  also may occur for achiral molecules that transform to chiral molecules in the presence of suitable atomic substitution. This was earlier found for both ethane and singly halogen substituted ethane where each possess associated helical shaped  $T_{\sigma D}(s)$ ; see Figure 20a. The chirality-helicity function  $C_{\text{helicity}}$  is then calculated from the simple numerical product of the circular ( $C_\sigma$ ) and axial ( $B_\sigma$ ) displacements and is used to quantify the resulting torsional BCP displacement:

$$C_{\text{helicity}} = (\text{chirality } C_\sigma) \times (\text{axiality } B_\sigma) = C_\sigma B_\sigma \quad (4.7.4)$$

The chirality-helicity function  $C_{\text{helicity}}$  provides a chirality measure for chiral discrimination in agreement with photoexcitation circular dichroism experiments.

**4.7.1. First-Generation Eigenvector-Space-Directed Trajectories.** The first-generation<sup>50,51</sup> eigenvector-space-

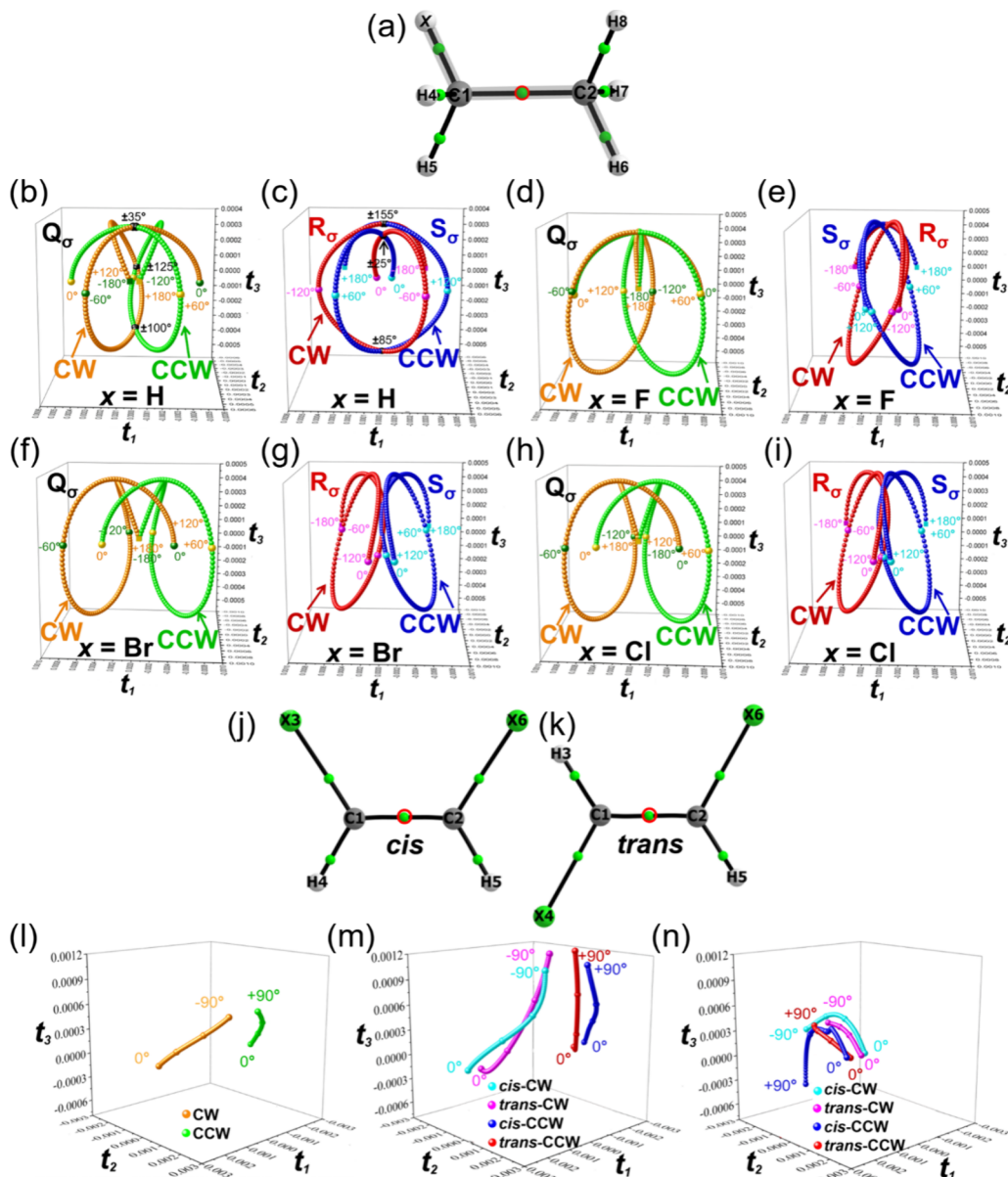


**Figure 20.** (a) Molecular graph for ethane and the singly halogen substituted ethane molecule with  $x = \text{F, Cl, Br}$  with  $x$  bonded to the C1 atom. Reproduced with permission from refs 57 and 58. Copyright 2022 Elsevier. (b–i) Clockwise: in order of increasing halogen atomic weight, the stress tensor-directed trajectory  $T_{\sigma D}(s)$  corresponding to  $x = \text{H}$  (b, c),  $\text{F}$  (d, e),  $\text{Cl}$  (h, i),  $\text{Br}$  (f, g), for the  $Q_\sigma$  isomer in  $U_\sigma$ -space (b, d, f, h) and  $R_\sigma$  and  $S_\sigma$  stereoisomers in  $U_\sigma$ -space (c, e, g, i). The molecular graphs of the doubly halogen substituted ethene and the (j) *cis*- and (k) *trans*-isomers for ethene for  $X = \text{F, Cl}$ . The  $T_{\sigma D}(s)$  of (l) ethene and the (m) *cis*- and (n) *trans*-isomers for  $\text{Cl}_2$ -ethene and (n)  $\text{F}_2$ -ethene: notice the markers at 90° intervals. See Figure 18 for further details. Reproduced with permission from ref 59 under Creative Common license.

directed  $T_{iD}(s)$  and refinements<sup>52,54,55</sup> used only one dihedral angle. First-generation directed  $T_{iD}(s)$  values were found able to differentiate<sup>50</sup> the *S* and *R* stereoisomers in agreement with the naming schemes of optical experiments. The inability of scalar QTAIM<sup>1</sup> for use in distinguishing *S* and *R* stereoisomers was also demonstrated.

The stress tensor  $\sigma(r)$  eigenvectors are often used for the eigenvector-space directed trajectories due to the superior performance in chiral discrimination.<sup>51</sup> The first-generation directed  $T_{\sigma D}(s)$  were in addition used to find helical-shaped  $T_{\sigma D}(s)$  that provided evidence of the unknown “chirality-helicity equivalence”, although this was not initially determined; see Figure 18b. This enabled the  $C_{\text{helicity}}$  for a pair of chiral and achiral  $\text{S}_{\text{N}}2$  reactions to be tracked,<sup>53</sup> in addition to the effects of isotopomers<sup>54</sup> and electric fields.<sup>55,56</sup>

**4.7.1.1. Proportionate Effects of Glycine to a Homogeneous Electric Field.** Using first-generation stress tensor-directed trajectories  $T_{\sigma D}(s)$ , the  $S_\sigma$  stereoisomer was located in glycine, an achiral molecule; see Figure 19a. The formation of *S* and *R* geometric stereoisomers was induced by an applied homogeneous electric  $E$ -field along the pair of C–H bonds bonded to the chiral carbon atom that induced full symmetry-breaking; see Figure 19b and c. The resulting proportionate effects of the nonstructurally distorting electric  $E$ -field on the chirality  $C_\sigma$  in  $U_\sigma$ -space, indicated control of chirality  $C_\sigma$  and as well use of  $C_\sigma$  as a molecular similarity measure. The measure of bond-strain, the bond-flexing  $F_\sigma$  was a factor of 3 higher or lower dependent on the direction of the applied electric  $E$ -field compared to the absence of an applied electric

**Table 10.** Ethane C1–C2 BCP Distortion Sets  $\{C_\sigma F_\sigma B_\sigma\}$ , Sum  $\sum \{C_\sigma F_\sigma B_\sigma\}$ , and the Chirality-Helicity Function  $C_{\text{helicity}} = (\text{Chirality } C_\sigma) \times (\text{Axiality } B_\sigma) = C_\sigma B_\sigma$  and Total Chirality  $C_\sigma$  and  $B_\sigma$  Assignments That Are Denoted by  $[C_\sigma B_\sigma]$ <sup>a</sup>

isomer	$\{C_\sigma F_\sigma B_\sigma\}$	$C_{\text{helicity}}$	$[C_\sigma B_\sigma]$
D <sub>3126</sub>	{−0.00010[R <sub>σ</sub> ], 0.00003[S <sub>σ</sub> ], −0.000003[R <sub>σ</sub> ]}	0	[Q <sub>σ</sub> ]
D <sub>4128</sub>	{−0.00010[R <sub>σ</sub> ], 0.00003[S <sub>σ</sub> ], −0.000003[R <sub>σ</sub> ]}	−0.0003	[R <sub>σ</sub> R <sub>σ</sub> ]
D <sub>5127</sub>	{0.29096[S <sub>σ</sub> ], 0.12635[S <sub>σ</sub> ], 0.00099[S <sub>σ</sub> ]}	0.0003	[S <sub>σ</sub> S <sub>σ</sub> ]
$\sum \{C_\sigma F_\sigma B_\sigma\}$		$\sum C_{\text{helicity}}$	
{−0.00024[R <sub>σ</sub> ], −0.00006[R <sub>σ</sub> ], 0.000047[S <sub>σ</sub> ]}		0	[Q <sub>σ</sub> ]

<sup>a</sup>The four-digit sequence (left column) refers to the atom numbering used in the dihedral angles (D<sub>3126</sub> = H3–C1–C2–H6, D<sub>4128</sub> = H4–C1–C2–H8, and D<sub>5127</sub> = H5–C1–C2–H7) used in the construction of the stress tensor following trajectories  $T_{\sigma D}(s)$ ; see Figure 19. The null-isomer Q<sub>σ</sub> chirality assignment is used for values of  $\sum C_{\text{helicity}} = 0$ . Reproduced with permission from ref 58. Copyright 2022 Elsevier.

E-field. Values of the bond-axiality  $B_\sigma$  were not affected by the application of the electric E-field.

**4.7.1.2. Chiral Properties of S<sub>N</sub>2 Reactions Tracked.** The theoretical foundations necessary to predict the results of photoexcitation circular dichroism experiments<sup>43b</sup> where the helical motion of bound electrons is utilized have been provided. This work builds on recent work that was able to locate, but not quantify, the missing “chirality-helicity equivalence” in lactic acid and alanine,<sup>50</sup> because previously only chiral discrimination was considered and not the helicity that quantifies the axial displacement of the BCP sliding along the extent of the bond-path; see Figure 19d.

The ability to determine the degree of chiral character of all reaction species during S<sub>N</sub>2 and other reactions will provide new insights to inform stereocontrol of chiral reaction species. For both a chiral and an achiral S<sub>N</sub>2 reaction, the “chirality-helicity equivalence” was quantified using the chirality-helicity function  $C_{\text{helicity}}$ . For the chiral S<sub>N</sub>2 reaction, agreement was found with optical experiment results that were used to label the S and R stereoisomers. For each of the achiral S<sub>N</sub>2 and chiral S<sub>N</sub>2 reactions, two intermediate structures were tracked along with the transition state, on the IRC path. Both reactions undergo a Walden inversion, where the chirality assignment (S or R) is inverted from the reactant to the product. The first-generation stress tensor-directed trajectory  $T_{\sigma D}(s)$  was found to be more useful for tracking the S<sub>N</sub>2 reaction than second-generation  $T_{\sigma D}(s)$ , which may lead to a complete cancellation of the components of  $C_\sigma$  and  $B_\sigma$  leading to zero values of the  $C_{\text{helicity}}$ .

**4.7.2. Second-Generation Stress Tensor-Directed Trajectory.** The second-generation stress tensor-directed trajectory  $T_{\sigma D}(s)$ <sup>56–59</sup> uses all possible sets of atoms that define the bond torsion dihedral angle in their construction, e.g., for ethane: {(H5–C1–C2–H6, H5–C1–C2–H7, H5–C1–C2–H8), (H4–C1–C2–H6, H4–C1–C2–H7, H4–C1–C2–H8), (H3–C1–C2–H6, H3–C1–C2–H7, H3–C1–C2–H8)}; see Figure 20a. Further advances in stereochemistry included quantification of the degree of achiral character,<sup>56–58</sup> mixed achiral character, and the dependency of chirality on the atomic weight of substituents as well a nonenergy-based explanation of the “cis-effect”.<sup>59</sup>

**4.7.2.1. Explanation of the Dominance of Steric Effects over Hyper-conjugation in Ethane.** NG-QTAIM chirality measures<sup>58</sup> were used to provide nonenergy-based insights into why steric effects are generally considered more important<sup>441</sup> than hyper-conjugation<sup>442</sup> in explaining the “staggered” configuration of the relaxed ethane molecule.

The idea that steric effects dominate hyper-conjugation is corroborated within the NG-QTAIM formalism. This was undertaken by relating steric effects to the presence of chirality

$C_\sigma$  and hyper-conjugation to the compression/expansion of the C–C nuclear skeleton, i.e., the C–C bond-axiality  $B_\sigma$ . Steric effects were, however, demonstrated to be a significant factor in explaining the “staggered” geometry of ethane by the presence of very large values of the chirality  $C_\sigma$  for the D<sub>4128</sub> and D<sub>5127</sub> isomers that indicated the presence of an asymmetry in the CCW versus CW bond torsions for the C1–C2 BCP, therefore relating to steric effects in  $U_\sigma$ -space.<sup>58</sup> The values of the chirality  $C_\sigma$  for the D<sub>4128</sub> and D<sub>5127</sub> isomers were found to possess equal magnitudes but opposite signs. This finding is in agreement with the presence of equal and opposite bond torsions of the ethane CH<sub>3</sub> groups located in a “staggered” configuration either side of the C1–C2 BCP torsion bond-path. The values of the chirality  $C_\sigma$  for the D<sub>4128</sub> and D<sub>5127</sub> isomers are 2 orders of magnitude greater than the associated values of the bond-axiality  $B_\sigma$ . Therefore, NG-QTAIM was found to indicate that steric effects ( $C_\sigma$ ) dominate over hyperconjugation ( $B_\sigma$ ).

The processes of using all nine possible dihedral angles for the construction of the  $T_{\sigma D}(s)$  resulted in three symmetry-inequivalent  $T_{\sigma D}(s)$  representing the Q<sub>σ</sub> isomer S<sub>σ</sub> and R<sub>σ</sub> stereoisomers. Variations in the values of the ethane C1–C2 BCP ellipticity  $\epsilon$  for the CW and CCW bond torsions displayed mirror symmetry at  $\theta = 0.0^\circ$  for the D<sub>3126</sub> isomer, which was found to possess a chirality  $C_\sigma$  assignment Q<sub>σ</sub>. The Q<sub>σ</sub> isomer, a newly discovered “null-isomer”, identified ethane as achiral in  $U_\sigma$ -space since the value of the chirality-helicity function  $C_{\text{helicity}} = 0$ ; see Figure 20a–i and Table 10.

**4.7.2.2. Factors Influencing the Chiral Properties of Substituted Ethane.** The effect of the chiral properties of doubly and singly halogen ( $x = F, Cl, Br$ ) substituted ethane was investigated with NG-QTAIM.<sup>57</sup> While all of the singly halogen substituted ethane molecules are overall achiral in  $U_\sigma$ -space, because of the presence of the Q<sub>σ</sub> (null) isomer, a strong dependency on the atomic weight of the halogen substituent was discovered. This dependency on the halogen substituent ( $x = H, F, Cl, Br$ ) atomic weight is apparent both in ethane and in singly halogen substituted ethane where each pair of the CCW and CW  $T_{\sigma D}(s)$  appear further apart with increasing substituent atomic weight ( $x = H, F, Cl, Br$ ) for the Q<sub>σ</sub> isomers and S<sub>σ</sub>, R<sub>σ</sub> stereoisomers; see Table 11.

This dependency on the halogen substituent ( $x = H, F, Cl, Br$ ) atomic weight was not apparent by visual inspection of the derived values of the  $T_{\sigma D}(s)$  for the doubly halogen (Cl,F), (Br,Cl), (Br,F) substituted ethane molecules. The S<sub>σ</sub> and R<sub>σ</sub> chirality  $C_\sigma$  assignments of the doubly halogen substituted ethane molecules demonstrated agreement with the CIP rules. In addition, a mixture of S<sub>σ</sub> and R<sub>σ</sub> chirality  $C_\sigma$  assignments for each of the S and R geometric stereoisomers was uncovered. The highest mixing of both the S<sub>σ</sub> and the R<sub>σ</sub> chirality  $C_\sigma$

**Table 11.** Single Halogen Atom Substituted Ethane C1–C2 BCP  $U_\sigma$ -Space Distortion Sets Sum of All Nine Isomers Generated by Using the Dihedral Angles  $\sum C_\sigma F_\sigma B_\sigma$  and the Summing over the Nine Isomers  $\sum C_{\text{helicity}}$ , Where the  $C_{\text{helicity}} = (\text{Chirality } C_\sigma) \times (\text{Axiality } B_\sigma) = C_\sigma B_\sigma$ <sup>a</sup>

substituted	$\sum \{C_\sigma F_\sigma B_\sigma\}$	$\sum C_{\text{helicity}}$	$[C_\sigma B_\sigma]$
F-ethane	$\{-0.00001[R_\sigma], -0.0029[R_\sigma], -0.00003[R_\sigma]\}$	0	$Q_\sigma$
Cl-ethane	$\{0.0010[S_\sigma], 0.0012 [S_\sigma], 0.000006[S_\sigma]\}$	0	$Q_\sigma$
Br-ethane	$\{0.00005[S_\sigma], -0.0009[R_\sigma], 0.000006[S_\sigma]\}$	0	$Q_\sigma$

<sup>a</sup>The null-isomer  $Q_\sigma$  classification is used when the  $\sum C_{\text{helicity}} = 0$ . Reproduced with permission from ref 57. Copyright 2022 Elsevier.

assignments for the doubly halogen substituted ethane was discovered for the F substituent atom, and this corresponded to the highest achiral behavior in  $U_\sigma$ -space and hence lowest chiral character. Both the F–Br-ethane and the Br–F-ethane possess the lowest chiral character  $\sum_{S\sigma} \{C_\sigma\} / \sum_{R\sigma} \{C_\sigma\} \approx 2$ . The doubly halogen substituted ethane with the lowest mixed chirality in  $U_\sigma$ -space was found to be Cl–Br-ethane, where  $\sum_{S\sigma} \{C_\sigma\} / \sum_{R\sigma} \{C_\sigma\} \approx 12$ , i.e., corresponding to the highest degree of chiral character.

**4.7.2.3. Why the *cis*-Effect Is the Exception Rather than the Rule for Ethene and Diazene.** The *cis*-effect, known to exist for doubly halogen substituted (F, Cl) ethene and diazene, was recently explored,<sup>59</sup> using unsubstituted ethene as a control; see Figure 20j and k. It was found that  $C_2X_2$  and  $N_2X_2$  ( $X = F, Cl$ ) display the *cis*-effect within NG-QTAIM, consistent with existing experiment data, and predicts that  $N_2X_2$  ( $X = Cl$ ), for which experiment data are not present, displays the *cis*-effect. A physics-based explanation of the *cis*-effect was provided by observing that it is harder to bend ( $F_\sigma$ ) than to twist ( $T_\sigma$ ) the C1–C2 BCP bond-path and N1–N2 BCP bond-path. The *cis*-isomer more readily undergoes bond-bending ( $F_\sigma$ ) and the *trans*-isomer more readily undergoes bond-twist ( $T_\sigma$ ) due to the atomic weight of the substituents; see Figure 20l–n.

Differences in the readiness of the *cis*- and *trans*-isomers to distort are explained by the bond-bend ( $F_\sigma$ ) and bond-twist ( $T_\sigma$ ) constructions used to sample the least (“hard”) preferred  $e_{2\sigma}$  and most (“easy”) preferred  $e_{1\sigma}$  directions of the  $\rho(r)$  distribution, respectively. Therefore, the *cis*-effect was independently discovered to be the exception and not the rule. This discovery is consistent with the energy-based understanding using steric effects and relative energetic stabilities of *cis*- and *trans*-isomers. This is also in agreement with the earlier NG-QTAIM associations of chiral character with steric effects for ethane; see section 4.7.2.1 and Table 12.

**4.7.2.4. Inducing Achiral Character in a Chiral Molecule Using an Applied Electric Field.** The effects of an external homogeneous electric ( $E$ )-field on the *S* and *R* geometric stereoisomers of the alanine molecule were found to be consistent with the CIP priority rules and earlier investigations using first-generation stress tensor-directed trajectories  $T_{\sigma D}(s)$ .<sup>56</sup> The occurrence of up to a 7% mixture of the  $S_\sigma$  and  $R_\sigma$  chirality  $C_\sigma$  assignments for the application of the electric field indicated the occurrence of up to 7% achiral character. For  $E = 0$ , 2% achiral character was detected. There was also a lack of mixing of the  $S_\sigma$  and  $R_\sigma$  chirality  $C_\sigma$  assignments, i.e.,  $C_{\text{mixing}} = 0.0$  for  $E = \pm 25 \times 10^{-4}$  au with the positive (+ $E$ ) field along the C3 → O10 BCP bond-path. This indicated for  $E = \pm 25 \times 10^{-4}$  au that the alanine molecule

**Table 12.**  $U_\sigma$ -Space Summations  $\sum \{\text{Bond-Twist } T_\sigma, \text{ Bond-Flexing } F_\sigma\}$  of the Bond Torsion C1–C2 BCP of Pure Ethene and the *cis*- and *trans*-Isomers of Doubly-Halogen Substituted Ethene with the Corresponding Results for Diazene<sup>a</sup>

	$\sum \{T_\sigma, F_\sigma\}$	
H <sub>2</sub> -ethene	{0.00483[S <sub>σ</sub> ], 0.00030[S <sub>σ</sub> ]}	
<i>cis</i> -		<i>trans</i> -
F <sub>2</sub> -ethene	{-0.01138[R <sub>σ</sub> ], -0.00493[R <sub>σ</sub> ]}	{-0.01710[R <sub>σ</sub> ], 0.00043[S <sub>σ</sub> ]}
Cl <sub>2</sub> -ethene	{-0.24833[R <sub>σ</sub> ], 1.06578[S <sub>σ</sub> ]}	{-0.40417[R <sub>σ</sub> ], 0.19351[S <sub>σ</sub> ]}
	$\sum \{T_\sigma, F_\sigma\}$	
H <sub>2</sub> -diazene	{0.00812[S <sub>σ</sub> ], 0.00016[S <sub>σ</sub> ]}	{-0.00176[R <sub>σ</sub> ], {0.00070[S <sub>σ</sub> ]}}
F <sub>2</sub> -diazene	{-0.01077[R <sub>σ</sub> ], -0.00886[R <sub>σ</sub> ]}	{0.00023[S <sub>σ</sub> ], {0.00014[S <sub>σ</sub> ]}}
Cl <sub>2</sub> -diazene	{0.00020[S <sub>σ</sub> ], 0.00672[S <sub>σ</sub> ]}	{-0.00022[R <sub>σ</sub> ], {-0.00402[R <sub>σ</sub> ]}}

<sup>a</sup>See Figure 20. Reproduced with permission from ref 59 under Creative Common license.

possessed less achiral character compared without the electric  $E$ -field. The presence of the  $E$ -field approximately doubled the magnitude of  $C_{\text{helicity}}$  because of very strong interactions of the  $E$ -field with the bond torsion BCP. The  $E$ -field reduced the degree of bond-flexing  $F_\sigma$  associated with bond strain in all cases, indicating a protective effect.

We can summarize as follows:

- The bond-path-framework set  $B$  quantifies the full spectrum of bonding types by including the mixture of single, double, or ionic bond character, etc., along the length of a bond-path and has enabled a more complete understanding of reaction mechanisms, including photochemistry. The  $B$  can be used with the stress tensor  $\sigma(r)$  formalism, the Ehrenfest force  $E(r)$ , and the Hessian of  $\rho(r)$  partitioning schemes, and in future additional  $\rho(r)$  partitioning schemes.
- The precession  $K$  has proved useful for bond coupling phenomena, photochemistry and polarization effects, as well as detecting asymmetry of the excited states with the Ehrenfest force  $E(r)$  and Hessian of  $\rho(r)$  partitioning schemes and could in the future be used with alternative partitioning of  $\rho(r)$  schemes.
- Both the eigenvector-space-following trajectory  $T_{\text{IF}}(s)$  and the eigenvector-space-directed  $T_{\text{ID}}(s)$  track the most/least preferred direction of electronic  $\rho(r)$  motion and accumulation in the 3-D  $U_\sigma$ -space of the Ehrenfest force  $E(r)$  and Hessian of  $\rho(r)$  partitioning schemes. In the future, additional  $\rho(r)$  partitioning schemes could also be used.
- The eigenvector-space-following trajectories  $T_{\text{IF}}(s)$  are useful for inherently noisy dynamics-trajectories because they remove requirements for the presence of correlations that are present for 2-D plots.
- First- and second-generation eigenvector-space-directed trajectories  $T_{\text{ID}}(s)$  identify *S* and *R* stereoisomers without using the CIP rules.
- Second-generation directed trajectories  $T_{\text{ID}}(s)$  are additive and yield a new isomer type, the “null-isomer”  $Q_\sigma$ , for formally achiral molecules as well as quantifying chiral mixing and achiral character.

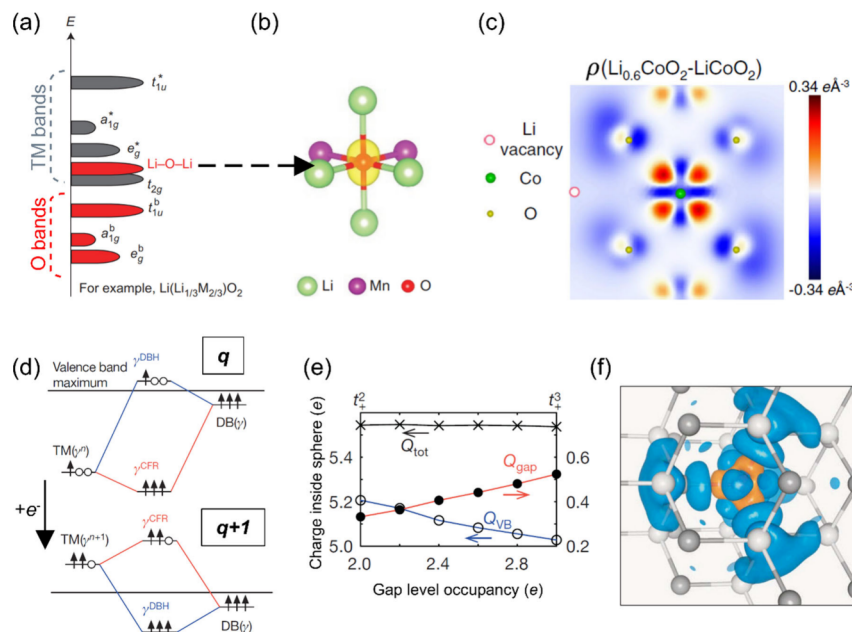


**Figure 21.** (a) Electronic structure schematic of a Li-excess material like  $\text{Li}_2\text{MnO}_3$  with a high-lying Li–O–Li O p state above hybridized O and low-energy transition metal (TM) states. (b) Charge density isosurface of an orphaned O 2p orbital (yellow) in the Li-excess material  $\text{Li}_2\text{MnO}_3$ . Reproduced with permission from ref 484. Copyright 2016 Springer Nature. (c) Electron density difference maps of  $\text{Li}_{18}\text{Co}_{30}\text{O}_{60}$  minus  $\text{Li}_{30}\text{Co}_{30}\text{O}_{60}$  simulation cells in the (144) plane. The red color region and blue color region represent an increase and decrease in electron density, respectively. Reprinted with permission from ref 499 under Creative Commons Attribution 4.0 International License (<http://creativecommons.org/licenses/by/4.0/>). (d) Energy-level diagrams for TM–host interactions with a system charge  $q$  and  $q + 1$ . The free-TM-atom orbital with irreducible representation  $\gamma$  (left-hand side) interacts with a host dangling bond level with the same representation (right-hand side), forming two hybrid levels (center), namely the crystal field resonance level  $\gamma^{\text{CFR}}$  and a dangling bond hybrid level  $\gamma^{\text{DBH}}$ . (e) Integrated charge inside the transition metal-centered sphere in GaAs:Mn depending on gap-level occupancy. The total charge  $Q_{\text{tot}}$  is decomposed into contributions from gap-level charge  $Q_{\text{gap}}$  (red) and from TM charge inside the valence band  $Q_{\text{VB}}$  (blue). (f) Charge density difference between charge  $-1$  and charge-neutral states for GaAs:Mn. Cations and anions are shown as white and gray spheres, respectively. The blue and red isosurfaces, respectively, correspond to charge densities of  $0.003$  and  $-0.003$  e Å<sup>-3</sup>. Upon adding an electron, the blue and red isosurfaces, respectively, represent an increase and a decrease in the total charge density. Reproduced with permission from ref 502. Copyright 2008 Springer Nature.

- Both the first- and the second-generation directed trajectories  $T_{iD}(s)$  share the limitation of requiring bond torsions to be performed in the vicinity of a “chiral” carbon, since this will displace portions of the molecule relative to each other.

NG-QTAIM is a work in progress. Suggestions and references to our recent work on the implementation of a third-generation  $T_i(s)$  that do not require bond torsions are provided in the overall conclusions of this contribution.

## 5. APPLICATIONS OF ELECTRON DENSITY-BASED ANALYSES TO THE MECHANISM OF REDOX REACTIONS WITH ANION REDOX

The previous sections outlined different aspects of the QTAIM, how it relates to a broad range of chemical phenomena, and how it can be used to establish a mechanistic understanding of these phenomena based on the analysis of electron density features. In the more than three decades since the publication of the seminal monograph of Bader,<sup>1</sup> QTAIM has been utilized widely in chemistry and materials science and has proven itself as a powerful instrument for the analysis and fundamental understanding of chemical properties and reactions. Density-derived atomic charges are particularly often utilized in first-principles studies of processes involving redox reactions in the solid state, most notably for reactions in catalysis<sup>443–446</sup> and energy storage.<sup>447–450</sup> Here, we will focus in more depth on the utility of a density-based framework for the analysis of redox reactions and gaining of mechanistic

understanding of phenomena in multiple electrochemical technologies including fuel cells, batteries, electrocatalysis, etc. Specifically, we consider the description of anion redox, which is particularly important in metal ion batteries and which is challenging with the MO-based Ansatz but appears naturally with the density-based Ansatz.

The investigation of metal ion battery (MIB) electrode materials exhibiting anion redox has become a major direction for the advancement toward rechargeable electrochemical cells with higher energy density since this effect was first described nearly a decade ago.<sup>451,452</sup> Insertion-type electrodes in which working metal ions are intercalated into interstitial positions of the host material in a solid solution-like mechanism are currently the primary choice for secondary batteries<sup>453</sup> due to the high degree of reversibility of these types of reactions and the cycling stability of the involved electrode materials compared to cells with conversion- or alloying-type electrodes. Most investigated MIB electrode materials consist of transition metal compounds due to the more positive redox potential of transition metal ion redox couples compared to working metal couples like  $\text{Li}/\text{Li}^+$ ,  $\text{Na}/\text{Na}^+$ , or  $\text{K}/\text{K}^+$  while lying within the stability window of common MIB electrolytes.<sup>454</sup> In addition, transition metal compounds exhibit a rich redox chemistry and often form crystal structures with a high interstitial site density. Commercial cathodes for Li-ion batteries, for example, are predominantly layered compounds with an  $\alpha\text{-NaFeO}_2$  structure like  $\text{Li}_{1-x}\text{CoO}_2$ , which facilitates an easy Li ion insertion into vacant octahedral sites and a rapid multidirec-

tional ionic diffusion between them.<sup>455</sup> In conventional electrode materials, the insertion or extraction of the working metal ions is accompanied by a respective reduction or oxidation of the transition metal center. Therefore, one theoretical limit to the amount of reversibly transferred charge during battery operation is the range of oxidation states that the transition metal can assume in the metalated structure. In most cases, it does not exceed one electron per transition metal ion, since larger changes are often accompanied by a change in either the preferred coordination number of the transition metal cation, its coordination geometry, or the most stable connectivity of the coordination polyhedra, which all lower the thermodynamic stability of strongly reduced/oxidized host structures.<sup>456</sup> Because of this, an extension of the electron transfer process during cycling onto the anionic species bears the promise to alleviate the traditionally limited capacity of transition metal compound electrodes and enable higher energy densities compared to electrodes without anionic redox. In order to occur, this type of reaction requires the presence of anionic hole states in the charged material, which are occupied during discharge. For oxygen redox, the most common form of anionic redox, this entails the formation of partially or fully oxidized oxide anions with oxidation states less negative than the element's most stable  $-2$  state. While anion redox was found even in conventional layered transition metal oxide cathode materials at high states of charge,<sup>457–461</sup> the most prominent representatives for these types of electrodes are alkali-rich layered transition metal oxides,<sup>462–470</sup> alkali-poor transition metal oxides,<sup>471–474</sup> or disordered rocksalt oxides.<sup>475–483</sup> These structures all can be understood as stoichiometric transition metal oxides in stable oxidation states in which some of the transition metal ions are substituted by lower-valent main group metal cations. For oxygen to partake in the redox process, furthermore, labile anionic states at high energies are necessary as was determined in a theoretical study on Li-excess materials by Seo et al.<sup>484</sup> The occurrence of such orphan orbitals was attributed to the excess of Li in oxygen coordination polyhedra, where linear Li–O–Li structural motifs give rise to unhybridized O p orbitals with higher energy compared to the ones partially hybridized with transition metal states, as shown schematically in Figure 21a and b. This concept was subsequently extended to any similar M–O–M configuration in which M is not a transition metal,<sup>485</sup> for example, in alkali-poor transition metal oxides, which averts p–d hybridization and causes the appearance of orphaned high-energy O p states. In the presence of such labile O states, the transfer of electrons during the charge exceeds the theoretical limit for the transition metal centers alone based on FOS and is assigned to the participation of the anions in the redox process. Besides localized holes on single oxygen centers, the formation of peroxy-like O–O dimers states has been reported as a result of oxygen redox activity as well, and even the reversible formation of molecular O<sub>2</sub> has been proposed as a model for oxygen redox activity.<sup>485–491</sup> Recently, delocalized  $\pi$  orbitals from hybridization of transition metal d and O p states were suggested as the cause for the observed excess capacity in Li-rich cathode materials rather than an atomic site-specific redox process.<sup>492</sup> Overall, the mechanism by which the half-cell reactions in this material class take place remains the subject of debate and continues to draw significant attention.

While anionic redox materials exhibit an anomalously large discharge capacity, their practical application has been obstructed by their voltage hysteresis, voltage fading, and a

low first-cycle Coulombic efficiency, possible reasons for which include a sluggish oxygen redox process, irreversible structural transformations, the emergence of other redox couples, or the loss of oxygen by molecular O<sub>2</sub> evolution.<sup>482,483</sup> To eliminate these shortcomings of anionic redox materials and to tailor their properties to suit an application in MIBs, a solid fundamental understanding of this process is necessary first. While some mechanistic aspects of anion redox are widely accepted, others still require further investigation in order to rationally design such materials. Lately, QTAIM has received growing attention in the analysis of this process based on theoretically and experimentally obtained electron densities.<sup>493–501</sup> While any assignment of atomic charges in any compound with more than one interacting atomic center is by default arbitrary, different ways of defining atomic charges reflect different aspects of the interaction and bonding between atoms, which is important to take into account when using them to rationalize redox reactions. The analysis of real-space charge distributions results in a distinct mechanistic picture from one based on electronic states, capable of providing additional understanding of redox processes in materials with a formal anionic redox as will be discussed in more detail in the following subsections.

### 5.1. Direct Analysis of the Electron Density to Analyze the Mechanism of Redox Reactions Including Anion Redox

In a recent work, Shang et al. combined quantitative convergent-beam electron diffraction and synchrotron powder X-ray diffraction to quantify transition metal and oxygen orbital populations in Li<sub>1-x</sub>CoO<sub>2</sub>, a commercially deployed Li-ion battery cathode material with conventional transition metal redox capability.<sup>499</sup> They were able to obtain the material's electron density via multipole expansion of the experimental structure factors. QTAIM was then applied to analyze electron densities at different stages of lithiation using the bond critical point between Co and O where a positive Laplacian of the density as well as a large value of the density itself suggest a closed-shell covalent interaction between these atoms rather than an ionic one.<sup>104</sup> Using the deformation densities for Li<sub>1-x</sub>CoO<sub>2</sub> (charge density difference of the refined density relative to a superposition of the isolated neutral atoms, cf., eq 2.2), the shapes of the t<sub>2g</sub> and e<sub>g</sub> states formed by Co 3d orbitals in the octahedral field of the oxide ions could be identified, with orbital lobes along or between the Co–O bonding axes, respectively. With decreasing Li content, not only the changes in density distribution around the Co centers became less pronounced compared to the atom, indicating a less preferential charge accumulation in the t<sub>2g</sub> states, but the deformation density also decreased around the oxygen centers, implying additional changes in the charge distribution around the anionic species. The reported orbital populations calculated from the multipole expansion suggest that, while the Co 3d population remains approximately constant or even increases with decreasing Li content, the population of O 2p states decreases. From additional DFT+U calculations, it could be confirmed that upon removal of Li from the structure, electron density accumulates in regions oriented along the Co–O axes (e<sub>g</sub> orbitals), while the electron-depleted regions are located around the O nuclei as well as between the Co–O bond directions (t<sub>2g</sub> orbitals) as can be seen in the density difference map in Figure 21c. The observation that Li removal (and hence oxidation of the material) actually increases the e<sub>g</sub> population while introducing t<sub>2g</sub> and O 2p hole states does not

correspond to what would be commonly expected when assuming fully ionic bonding where oxidation is solely ascribed to electron loss from transition metal d states. This effect was attributed to a rehybridization of Co 3d and O 2p orbitals, where upon Li extraction from  $\text{LiCoO}_2$  (and therefore an electron extraction), the O 2p contribution to the emptying antibonding states inside the band gap increases, whereas Co 3d contributions increase for the low-lying bonding levels within the material's valence band. This charge feedback mechanism results in the observed net loss of charge around the oxygen and a slight net gain around the transition metal centers. Based on their electron density topology analysis, the authors conclude that the performance of oxide electrode materials upon cycling can be influenced by adapting the chemical bonds between transition metals and oxygen, since the latter was found to play a significant role in the lithiation reaction via the real-space ligand-to-metal charge transfer through bonds with covalent character as identified by QTAIM.

Interestingly, these findings are a direct experimental observation of an effect, which was theoretically described for  $\text{Li}_{1-x}\text{CoO}_2$  more than two decades prior by Wolverton and Zunger.<sup>503</sup> They computed charge density differences for the full and partial delithiation of  $\text{LiCoO}_2$  where a charge accumulation along the Co–O axis and loss in between was found in accordance to what was later also described by Shang et al.<sup>499</sup> They explained this finding as the result of a “self-regulating response” of the transition metal to changes in electron population of the  $\text{CoO}_2$  host material. This description was in turn based on earlier theoretical works on transition metal impurities in semiconducting host materials<sup>504–508</sup> where the integrated charge density around the transition metal stays nearly constant upon varying total charge of the system. Electronic structure analysis revealed a charge displacement between the antibonding defect gap states and bonding valence band (VB) states through enhanced transition metal contributions to the former and decreasing contributions to the latter upon the injection of additional electrons into the system. While these early electronic structure studies used model systems like 3d transition metal-doped Si, GaP, or InP, the computed shift of d orbital population and a redistribution of charge density between the transition metal and the ligand upon the change of the total charge in the system are in agreement with the observed participation of oxygen in the  $\text{Li}_{1-x}\text{CoO}_2$  redox reaction during cycling. Based on these early works, Raebiger et al. proposed a mechanistic explanation for the spatial redistribution of charge density around transition metal ions, which is schematically shown in Figure 21d.<sup>502</sup> the relative energy of a transition metal electronic state will increase upon addition of electrons to the system relative to an anion dangling bond level with the same irreducible representation in the symmetry of the coordination polyhedron. While for the uncharged system, the low-lying bonding combination of the transition metal and the dangling bond orbital will therefore carry predominantly transition metal character, denoted as crystal-field resonance state, and the high-lying antibonding orbital mostly anionic character, denoted as dangling bond hybrid state, this situation inverts upon the injection of an additional electron into the system due to the now higher energy of the transition metal relative to the anionic dangling bond level. The authors corroborated this mechanism by integrating the charge density in a sphere with a radius of 1.3 Å around transition metal dopant atoms (Co, Fe,

Mn, and Cr) in  $\text{MgO}$ ,  $\text{GaAs}$ , and  $\text{Cu}_2\text{O}$  while varying the number of electrons of system via charge doping. An additional differentiation by low-lying VB and high-lying gap contributions revealed that the total integrated transition metal charge does not vary significantly upon an increase in total electron number due to a decreasing contribution of VB state charge, which is compensating the growing gap state charge as shown in Figure 21e for Mn-doped  $\text{GaAs}$ . Charge density difference maps like the one shown in Figure 21f further confirm that the regions with electron loss are located along the transition metal–ligand bonds, while electron gain is calculated in the antibonding regions in between. These results are in accordance with the mechanism proposed by the authors, previous theoretical literature, and also with the recent real-space charge measurement in  $\text{Li}_{1-x}\text{CoO}_2$ . While the last one is the first experimental density analysis directly confirming the charge self-regulation mechanism, there had been prior indirect evidence for a mostly unchanged real-space charge around transition metal cations during redox reactions from experimental data.

Wolczanski introduced the charge distribution via reporters (CDVR) method, which allows one to assess the atomic charge state of the central ion in a transition metal complex based on the infrared frequency shift of certain charge-reporting ligands.<sup>509</sup> One such transition metal ligand, carbon monoxide, is well-established to have varying C–O stretching frequencies in different complexes ranging from ~1500 to ~2300 cm<sup>-1</sup>, which is commonly explained by a covalent overlap of transition metal d and CO  $\pi^*$  orbitals.<sup>510,511</sup> The occupation of these states destabilizes the C–O bond by populating antibonding ligand orbitals and reduces the vibrational frequencies of the ligand stretching modes, while the oxidation state of the ligands formally remains zero. Surveying experimental literature, atomic charges were determined for transition metal centers in different carbonyl complexes in ref 509 based on the reported C–O stretch frequencies; i.e., the lower is the reported frequency, the larger is the charge transfer from the transition metal to the ligands. The relationship between CO frequencies and ligand charge was computed via a calibration curve obtained from the reported frequencies of iron carbonyls with different charges and numbers of ligands, where the Fe central ion was assumed to have a constant +2 atomic charge across all considered complex ions despite its changing oxidation state. Under this assumption, a strong linear correlation between computed CO charge and vibrational frequencies was found as shown in Figure 22a. While the number of data points is small from the statistical point of view, the trend is compelling. While this specific choice for iron was in principle arbitrary, the established charges for other transition metals still allow one to draw conclusions about their magnitude and changes relative to this reference. The assignment of a stable low atomic charge on iron carbonyls was also supported by additional Mulliken and natural bond orbital calculations from first-principles within ref 509 and by QTAIM charges based on DFT results in a later work by other authors,<sup>512</sup> the latter reporting that while atomic charges on Fe stay indeed nearly constant with varying oxidation states, the computed charge states for Fe were actually computed closer to +1 than +2. Calculated Fe-complex QTAIM charges are shown for comparison in Figure 22b. Based on the CDVR approach, it was found that other transition metal charges also do not vary significantly for the same element and only exhibit slight variations across the periodic table. Average transition

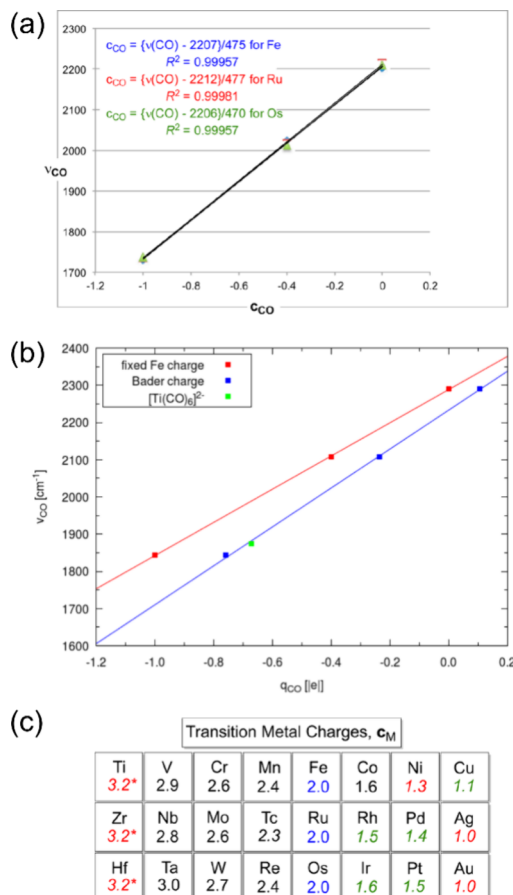


**Figure 22.** (a) Plots of  $[M(CO)_6]^{2-}$ ,  $M(CO)_5$ , and  $[M(CO)_4]^{2-}$  charges ( $M = Fe$  (blue), Ru (red), Os (green)) as a function of CO stretching frequencies,  $\nu_{CO}$ , based on a constant metal atomic charge of +2. Reprinted with permission from ref 509. Copyright 2017 American Chemical Society. (b) Computed average vibrational frequencies of the C–O stretch in  $[Fe(CO)_4]^{2-}$ ,  $Fe(CO)_5$ , and  $[Fe(CO)_6]^{2-}$  against an assumed fixed cation atomic charge of +2 (red color) or calculated QTAIM charges from DFT (blue). Reprinted with permission from ref 512 under Creative Commons Attribution 3.0 license (<https://creativecommons.org/licenses/by/3.0/>). (c) Transition elements and charges,  $c_M$ , relative to  $c_{Fe} = +2.0$ , derived from the CDVR approach. Charge numbers in green italics are derived from limited sets of data, and those in red italics are generated from single points, i.e., single  $M(CO)_x^n$  species. The charges given to group 4 (\*) are based on the trend in the table. For details, see ref 509 from which the figure was reprinted with permission. Copyright 2017 American Chemical Society.

metal charges obtained this way are shown in Figure 22c. These findings support the proposed charge self-regulation mechanism and further indicate that there are only minor differences in the behavior of different transition metals as all of them exhibit mostly constant, relatively low atomic charges independent of their (formal) oxidation state. QTAIM charges, which are based on the electron density topology and are predominantly based on charge densities obtained from first-principles, have commonly predicted these low, weakly varying atomic charges of transition metals in a wide range of other types of transition metal compounds as well.<sup>32,496,S12–S14</sup> For instance, Bader (i.e., QTAIM) charges calculated for  $TiO_2$  suggest only a charge loss of around 2.3 e per Ti basin, while DIs of approximately 0.5 per Ti–O bond indicate a pronounced covalent character of these bonds.<sup>S12</sup> Contrary

to the commonly chosen description of titanium dioxide as ionic compound, these pronounced covalent contributions, which can be quantified, for example, with the help of DIs, are enabling the charge self-regulation through delocalized orbitals with significant transition metal d contributions. The crucial role of d orbitals in the stabilization of charge density around transition metal centers was also studied theoretically for various carbonyl complexes in which the CO red shift became more pronounced when purposefully removing d functions from the basis set, which led to increasingly positive Bader charges on the metals while shifting charge density into the ligand basins.<sup>S13</sup>

These computed QTAIM charges substantiate that the charge stability on transition metals is indeed expected to cause a significant real-space charge contribution from anionic species in any type of redox activity involving transition metal compounds and is a common phenomenon not only confined to the cases discussed above.

Based on these findings, suggesting that anions also participate heavily via real-space charge transfer for conventional formal cationic redox materials, naturally the question arises how anionic and cationic redox can actually be distinguished from a real-space charge density transfer perspective versus the commonly used orbital-based (spectral) approach. Koch and Manzhos investigated the changes in the electron densities of  $Li_2MnO_3$ , a typical Li-excess cathode material displaying oxygen redox, as well as of its isostructural analogues  $Li_2CrO_3$  and  $Li_2VO_3$ , which both retain a high-lying d population at the Fermi level and hence constitute conventional cationic redox materials, upon the removal of Li from first principles.<sup>496</sup> They found, as would be expected, a significant loss of real-space charge density around oxygen centers between  $Li_2MnO_3$  and  $LiMnO_3$  as shown in Figure 23a. However, a very similar picture was also found for the cation redox materials  $Li_2CrO_3$  as well as  $Li_2VO_3$  shown in Figure 23b and c, with a clearly visible charge density loss around O and the previously described gain and loss regions around the transition metal due to the charge self-regulation mechanism. From QTAIM charges, a loss of 0.15, 0.03, and 0.08 e was found for the V, Cr, and Mn ions, while the O centers in the corresponding compounds lost on average 0.25, 0.29, and 0.32 e, respectively. Due to their weakly bound 2s electrons resulting in highly ionic bonds, the Li atoms are computed to be almost fully ionized and hence can be ignored in the analysis. These findings suggest that the oxygen ions bear the main load of the real-space charge loss upon delithiation for all investigated compounds, irrespective of formal cationic or anionic redox. While the charge density reduction around oxygen is indeed the highest for  $Li_2MnO_3$ , comparison between various oxides of V, Cr, and Mn across different oxidation states in ref 496 showed that these subtle differences are the result of an increasing charge density retention around the transition metals within a row of the periodic table. The computed transition metal QTAIM charges in V, Cr, and Mn oxides versus their formal oxidation states are shown in Figure 23d where with the increasing atomic number of the transition metal species the slope of the curve decreases. This can be explained by the increasing ionization energies,<sup>S15</sup> which lead to more covalent bonds between transition metal and oxygen and a more pronounced charge self-regulation effect. This is also in agreement with the trends among the CDVR charges in Figure 22c, where the average transition metal charges increase from left to right within the d block.

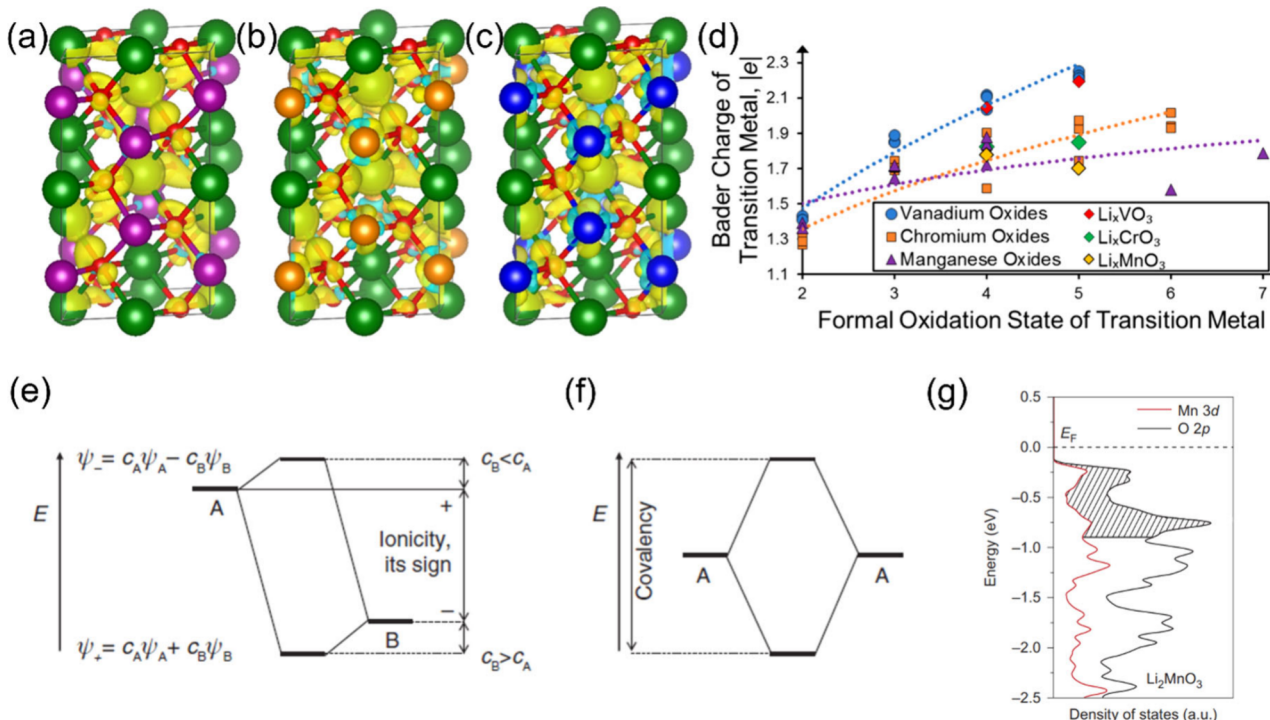


**Figure 23.** Charge density difference between (a)  $\text{Li}_2\text{MnO}_3$  and  $\text{LiMnO}_3$ , (b)  $\text{Li}_2\text{CrO}_3$  and  $\text{LiCrO}_3$ , as well as (c)  $\text{Li}_2\text{VO}_3$  and  $\text{LiVO}_3$  (view in [001] direction). Yellow isosurfaces indicate positive regions, light blue negative ones; isovalue of  $0.01 \text{ e} \text{ \AA}^{-3}$ . Li atoms are represented by green, Mn by purple, Cr by orange, V by blue, and O by red spheres. (d) Computed QTAIM charges for different vanadium (blue circles), chromium (orange squares), and manganese oxides (purple triangles) depending on oxidation states. QTAIM charges for the Li-excess compounds  $\text{LiVO}_3/\text{Li}_2\text{VO}_3$  (red diamonds),  $\text{LiCrO}_3/\text{Li}_2\text{CrO}_3$  (green diamonds), and  $\text{LiMnO}_3/\text{Li}_2\text{MnO}_3$  (yellow diamonds) are included for comparison. Least-squares fit power functions (dotted lines) are included for a better visibility of the trends. Reprinted with permission from ref 496. Copyright 2020 American Chemical Society. (e) Essential scheme for ionic approximation based on contribution to the bonding MO with mixing coefficients  $c_A$  and  $c_B$  referring to the AOs  $\psi_A$  and  $\psi_B$  in an LCAO-MO approach for a heteronuclear bond; in (f) a homonuclear bond, the electrons are distributed evenly between the two atoms. Reprinted with permission from ref 516. Copyright 2016 IUPAC and De Gruyter. (g) PDOS of the O 2p orbitals (black) and Mn 3d orbitals (red) in the Li-excess material  $\text{Li}_2\text{MnO}_3$  where the shaded region denotes redox-active states. Reproduced with permission from ref 484. Copyright 2016 Springer Nature.

On the first glance, the substantial electron density changes around anions in all transition metal compounds and not only the ones which exhibit oxygen redox activity, which was first established qualitatively and later substantiated by QTAIM, seemingly contradict the well-established understanding of transition metal redox chemistry. However, cationic and anionic reduction and oxidation reactions are established through the species' oxidation states, not their atomic charges, which are based on the assignment of electronic states to different species and have no direct conceptual relation to the real-space charge density distribution within a compound.

### 5.2. Pros and Cons of Formal Oxidation States

During the operation of any MIB, a certain number of electrons is transferred between anode and cathode, with an oxidation reaction taking place in the former and a reduction in the latter, implying the change of oxidation states in the electrochemically active compounds in both half cells. In their most recent recommendation from 2016, the International Union of Pure and Applied Chemistry (IUPAC) provides a normative definition for oxidation state as the atom's charge after ionic approximation of its heteronuclear bonds.<sup>516</sup> Atomic charge in this context is the virtual ionic charge relative to the neutral atom, and ionic approximation is the assignment of all electrons of a bonding orbital to the atom with the largest contribution to this orbital. In practice, electrons are most commonly assigned based on the electronegativities of the

atoms participating in the respective bond with the more electronegative partner receiving all its electrons (and an equal split in the case of homonuclear bonds). The IUPAC recommendation also outlines two general algorithms to establish oxidation states in molecular and periodic systems based on bonds or bond orders and electronegativity, and while they allow the ad hoc determination of oxidation states for simple cases, numerous ambiguous cases remain, which require additional measurements or computations to establish its correct value.<sup>516</sup> Among such cases are the oxidation states in materials exhibiting anionic redox activity, which cannot be easily inferred. Applying the above definition of oxidation states more stringently, the assignment of electronic states can be based on the largest LCAO (linear combination of atomic orbitals) coefficients of bonding molecular orbitals. This is schematically shown in Figure 23e for the simple case of a diatomic heteronuclear bond between two atomic sites A and B with one orbital per site. Upon their interaction, two MOs are formed as linear combinations of A- and B-site orbitals with LCAO coefficients  $c_A$  and  $c_B$ . All electrons of the MO closer in energy to the atomic orbital (AO) on A with  $c_A > c_B$  are then assigned to site A, and the ones in the MO closer to the AO on B with  $c_B > c_A$  to site B accordingly. In the case of homonuclear bonds like the one shown in Figure 23f, the electrons of the bonding orbital are shared evenly between both atoms. However, such qualitative MO schemes and LCAO coefficient

relations can only be constructed directly for the simplest cases and require additional input from quantum chemical calculations for more complex systems.<sup>517</sup> Furthermore, homonuclear bonds are not always as regular as implied in Figure 23f, and their equivalent splitting requirement complicates the assignment in delocalized states with homonuclear contributions from different centers with varying coefficients.

From electronic structure calculations, anionic redox is in practice identified via an atomic-site and orbital projected density of states (PDOS)<sup>518–522</sup> and the changes in state occupancies during working metal extraction or insertion as shown on the example of the Li-excess material  $\text{Li}_2\text{MnO}_3$  in Figure 23g where O p-dominated electronic states are participating in the charge–discharge process.<sup>484</sup> The dominant contributions to the involved states indicate whether cationic or anionic redox takes place, in accordance with the oxidation state formalism. Experimentally, redox-active species are commonly identified spectroscopically, most notably via X-ray photoelectron spectroscopy (XPS), soft X-ray absorption spectroscopy (sXAS), and resonant inelastic X-ray scattering (RIXS).<sup>471,523–528</sup> While an XPS O 1s feature around 531 eV has been commonly ascribed to a peroxide-like state in anion redox electrode materials, XPS has the drawback of being a surface-sensitive technique with a recent study suggesting that this signal might originate from the cathode–electrolyte interface and not be indicative of bulk anion redox.<sup>529</sup> K-edge sXAS and RIXS, on the other hand, can achieve sufficient penetration depth to probe bulk electronic excitations into unoccupied O 2p states of reduced oxygen centers, which lie in the known energy range for peroxide states and  $\text{O}_2$ . Thus, the sXAS peak around 531 eV has been utilized as evidence for oxidized oxygen species, although the O K-edge spectrum was reported to primarily provide information about the O p–TM d hybridization in the compound and its changes during the reaction rather than an O-redox specific spectroscopic signature.<sup>526,530</sup> The RIXS fluorescence emission feature around 524 eV, on the other hand, has been identified as the localized O hole state fingerprint region and is regarded as solid spectroscopic evidence of O redox activity.<sup>531,532</sup> It should be noted, however, that any measured electronic transition always corresponds to an excitation of the total wave function of the compound and not to element- or site-specific orbital contributions, which are not physical observables. Probing electronic structure from electronic spectroscopy therefore always relies on a comparison with reference systems with established oxidation states providing the necessary context for its interpretation in an element- and site-specific manner.<sup>31</sup> Since reduction and oxidation reactions are defined by changes in oxidation states, which are not observables, but are measured by electronic spectroscopy, which measures observables, difficulties in translating the latter into the former are expected to occur the more the oxidation state picture deviates from reality for a compound as the lines between localized ionic and delocalized hybridized states blur with increasingly covalent bonding.

Nevertheless, despite not necessarily reflecting the charge density distribution between neighboring cations and anions with their generally noninteger real-space charges, the oxidation state formalism is a useful electron counting method assigning whole electrons to atoms in molecules and solids. While the notion of oxidation states predates the advent of quantum mechanics, they remain widely used in electro-

chemistry, spectroscopy, and in general for the rationalization of physical properties of materials.<sup>533</sup> They have been applied as a descriptor, a parameter in chemical nomenclature, a variable for the tabulation or plotting of certain parameters (e.g., effective atomic radii, bond-valence coefficients, or standard reduction potentials), as a value related to transition metal d orbital occupations in compounds (as established via spectroscopic or spin-sensitive methods), and as a formalized basis for balancing redox equations.<sup>534</sup> As it is explicitly stated in the IUPAC technical report on the oxidation state issue,<sup>534</sup> an oxidation state is not the charge on an atom and is not related to the valence charge density surrounding a nucleus, but rather a formal charge obtained from an integer electron counting scheme. Similarly, any of the numerous existing population analysis methods, which are based on either the partitioning of charge density into atomic domains (including QTAIM charges), the projection onto basis functions, or the fitting of the electrostatic potential, will only coincide with the assigned oxidation state of an atom in a compound in rare cases, although general qualitative trends like the sign of the ionic approximation agree more consistently between population analyses and oxidation state formalism. Specifically, QTAIM atomic charges approach the value of oxidation states (within a small margin) only in systems with a high degree of ionicity, while in the case of more covalent compounds with stronger hybridization between atomic wave functions, for example, in transition metal compounds, atomic and formal charges diverge more significantly. While this is duly acknowledged in the latest IUPAC technical report on oxidation states,<sup>534</sup> previous definitions of the oxidation state formalism had been less rigorous. For example, a previous definition, which could be found in the IUPAC Compendium of Chemical Terminology, was relying on a set of general rules including the preferential oxidation states of elements like hydrogen, oxygen, alkali metals, or halides, providing more vaguely defined boundaries in which oxidation states could be determined.<sup>535</sup> Such a lack of rigor in its definition is not only problematic due to possible ambiguities in the actual value of oxidation states determined as a result, but also more generally due to a lack of a clear understanding of what the meaning of these formal charges is, where they originate from, and what their limitations are. This confusion has perhaps contributed to the repeated discussion of the physical meaning of both oxidation states and density-based atomic charges, in chemical literature, as if one were an approximation of the other. In light of the charge self-regulation mechanism reported by Raebiger et al.<sup>502</sup> in 2008, Resta commented in a viewpoint on its implications for the oxidation state formalism,<sup>536</sup> stating that “charge transfers associated with changes in oxidation states have often been considered as a first approximation to the physical, ionic charge of a transition-metal atom, with covalent hybridization accounting for just a small correction to it” and that in reality oxidation states and static atomic charges are not related. This led them to the conclusion that oxidation state-dependent ionic radii and X-ray spectroscopy signatures of transition metals need to be re-evaluated in terms of hybridization with the anion instead of formal ionic charge. In an essay published shortly thereafter, Jansen and Wedig pointed out the heuristic nature of oxidation states and that their correlation with many real properties justifies its use also for the description of bonding in transition metal compounds and that the oxidation state concept does not claim any connection to real ionic charges by its definition.<sup>537</sup> However,

the authors continue to conclude that it is meaningful to correlate atomic charges and oxidation states, referencing examples of unusual transition metal oxidation states, which are qualitatively matched by QTAIM charges. They further challenged the conclusions obtained by Raebiger et al. by questioning the arbitrary radius for charge integration of 1.3 Å, noting that the results can vary depending on the chosen cutoff value, and the assignment of the transition metal oxidation states due to the delocalized nature of the involved states. In their rebuttal, Raebiger, Resta, and others replied to the criticisms by providing an extended charge accumulation plot for Cr in MgO and GaAs, demonstrating that the observed charge self-regulation is not a fluke due to a specific reservoir radius choice, as well as pointing out that all oxidation states were determined in accordance with the standard oxidation state definition.<sup>538</sup> Raebiger et al. also examined the question whether oxidation states themselves are predictive or rather postdictive, arriving at the conclusion that a priori assigned oxidation states are often incapable of predicting the correct electronic structure of transition metal compounds and require additional insights, which then allow for a correct labeling within the oxidation state formalism. They also pointed out that the usefulness of oxidation states is often demonstrated based on models, which are constructed using this same oxidation state formalism. Lastly, they provided a list of specific examples of compounds in which oxidation states could only be assigned a posteriori after performing electronic structure calculations. With the latest IUPAC oxidation state definition, debates like the one summarized here have mostly been defused since a less ambiguous definition of oxidation states has been provided, and it has been clearly acknowledged that oxidation states are indeed not an expression for real charges and not conceptually related to QTAIM. The necessity of additional data, experimental or theoretical, for the determination of oxidation states in complex cases is recognized, and the associated IUPAC technical report also includes a comprehensive discussion of examples, including cases of ambiguous oxidation states.<sup>534</sup> Nevertheless, arguments similar to the ones in the representative exchange highlighted here continue to echo in literature. More recently, Walsh et al., referencing a work by Koch and Manzhos in which they analyzed the charge distribution around Ti in TiO<sub>2</sub> from first-principles using QTAIM and questioned the perceived meaning of the element's +4 oxidation state as a descriptor of the mechanism of redox reactions (reminiscent of Raebiger, Resta, and others' arguments about the tacit association of oxidation state and physical charge),<sup>32</sup> pointed out the degree of arbitrariness in the way the electron density is partitioned into QTAIM basins (similar to the criticism of Jansen and Wedig concerning charge integration cutoffs) and provided examples for the utility of oxidation states and their derivation from experimental data.<sup>539</sup> The same authors provided later a comprehensive discussion on formal oxidation states and atomic charges in a dedicated article, concluding that the oxidation state formalism will remain central to the description of the interaction between atoms in molecules or solids, although modern sophisticated theoretical methods may uncover challenges to these inherently simple investigative tools.<sup>533</sup> Even more recently, Norman and Pringle published a perspective "in defence of oxidation states"<sup>540</sup> responding to criticisms of the use of oxidation states in organic chemistry in light of reported advantages of the covalent bond classification

method in molecular systems, bringing to mind analogous discussions for the solid state.

These types of discussions are likely to keep reappearing in future literature for the reason alone that formal and atomic charges are both expressed using a similar notation and share semantic similarities in their discussion, which invites comparison between them. Likewise, the important role of oxidation states in the rationalization of chemical processes will probably continue to be questioned relative to other models. However, understanding oxidation states and real-space density analyses like QTAIM as mutually supportive rather than competing concepts<sup>540</sup> and as purpose-oriented tools with varying degrees of physical meaningfulness depending on the problem at hand has the potential to enhance the understanding of chemical processes, or as it was succinctly put in a review by Zhao et al.: "Chemical bonding models are not right or wrong, they are more or less useful."<sup>541</sup>

Therefore, the attention that was placed on anionic activity in materials exhibiting anionic redox needs to be understood as a peculiarity of the oxidation state formalism. Outside of it, no elemental redox activity can be defined in the sense of changing oxidation states anyway, and depending on the model chosen, the anionic contributions to the electrochemical reaction taking place might play only a secondary role for compounds classified as anionic redox materials. Similarly, it has to be understood that experimental electronic structure fingerprints from, e.g., XPS, sXAS, or RIXS can be interpreted within different models, not only the oxidation state formalism. Within the latter, spectroscopic signatures are assigned based on comparison with elemental ones in simple compounds in which oxidation states can be defined without additional experimental confirmation. Nothing prohibits the analysis of the same results within a different model as was advocated by Resta,<sup>536</sup> for example, QTAIM. Within the QTAIM model, there is no qualitative difference in the charge transfer to or from the oxygen centers in oxygen redox materials compared to transition metal redox ones upon electrochemical reaction (due to the effect of charge self-regulation). However, oxygen redox materials show a different electrochemical behavior than materials classified as cationically redox-active, which suggests that there might be some other distinctive property of these materials within the QTAIM model, which is yet to be identified. While the rationalization of electrochemical reactions is traditionally heavily reliant on the oxidation state formalism, QTAIM and QTAIM-derived charges offer an alternative point of view for the interpretation of redox processes in materials exhibiting anionic redox. Shifting focus away from the anion and anionic contributions to electronic states (e.g., the effect of the O binding environment, Li–O–Li motifs, charge delocalization, etc.) toward a density topology-based picture might allow for a better understanding of how to influence the electrochemical properties of such materials for the next generation of MIBs and other applications.

### 5.3. Density Topology versus PDOS

The real-space charge fluctuations around the anions in transition metal compounds upon removal or addition of electrons do by themselves not constitute anionic redox activity, since the ionic approximation neither accounts for the covalent character of bonding in these compounds nor the extensive rehybridization in their occupied states with changing number of electrons in the system, resulting in unchanged anionic oxidation states unless anion-dominated electronic

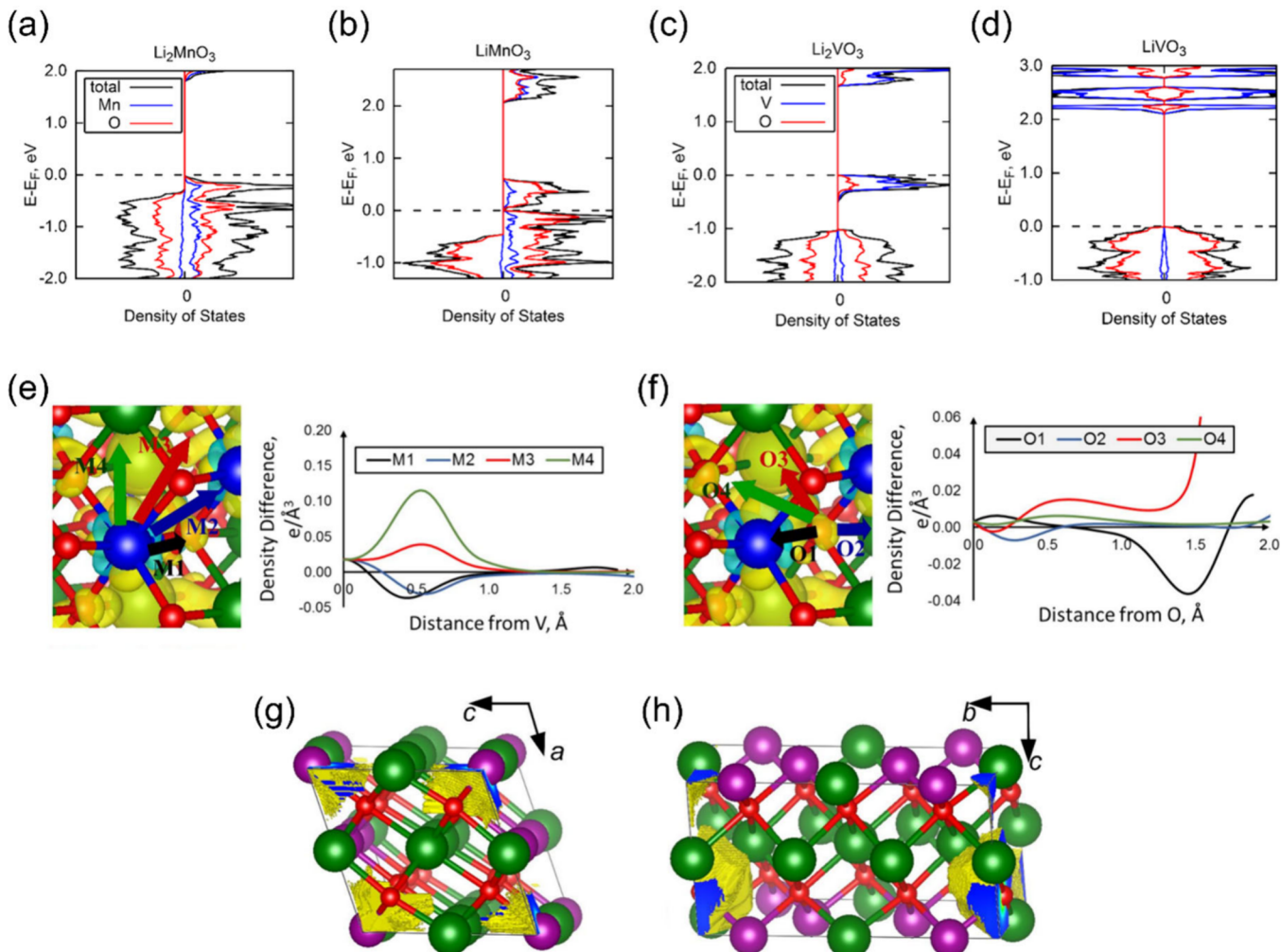


**Figure 24.** (a) Total (black) and species-projected (transition metals in blue; oxygen in red) densities of states of  $\text{Li}_2\text{MnO}_3$ , (b)  $\text{LiMnO}_3$ , (c)  $\text{Li}_2\text{VO}_3$ , and (d)  $\text{LiVO}_3$ . The energies ( $E$ ) are relative to the Fermi level ( $E_F$ ). (e) Density difference line profiles in  $\text{Li}_2\text{VO}_3$  for different directions, starting from a vanadium, or (f) oxygen center. (g) Shape of the QTAIM domains of the transition metal and (h) oxygen in  $\text{Li}_2\text{MnO}_3$ . The domain is shown in yellow (surface) or blue (cuts), while manganese, oxygen, and lithium centers are represented by purple, red, and green spheres, respectively. Reprinted with permission from ref 496. Copyright 2020 American Chemical Society.

states are involved in the reaction. The determination of oxidation states often relies on first-principles computations, but calculating them directly from electronic structure data remains challenging. While for simple cases (such as  $\text{Li}^+$ ) the approach is straightforward, the IUPAC definition introduces several pitfalls for a reliable oxidation state deduction from first-principles: (i) One-electron wave functions are not unique to a certain density. Within DFT, the workhorse of computational chemistry, the unitary transformation of orbitals leads to a new set of orbitals, which do not change the total density and hence energy of the system, a property that is, for example, exploited to construct localized orbitals.<sup>542–545</sup> In certain cases, such different localization schemes could hence lead to a conflicting oxidation state assignment based on LCAO coefficients. (ii) Acceptor–donor bonding cannot be identified directly from LCAO coefficients and demands more involved calculations.<sup>546</sup> (iii) The requirement to evenly split homonuclear bonds adds complexity to the oxidation state definition, which requires additional analysis beyond the magnitude of LCAO coefficients for delocalized states that involve, for example, additional heteronuclear centers.

Different attempts beyond population analysis methods have been suggested to establish oxidation states in agreement with the IUPAC definition, and while they have been demonstrated to correctly identify oxidation states in various types of compounds,<sup>547–550</sup> their transferability remains limited and a rigorous quantum mechanical definition of oxidation states is still lacking. Furthermore, in the solid state, plane-wave basis sets are often employed for electronic structure calculations, which are not atom-centered like most basis sets used for molecular systems. Therefore, some sort of projection of electronic states onto localized functions associated with site  $\alpha$ , angular momentum  $l$ , and magnetic quantum number  $m$  is necessary to quantify the site- and AO-specific contributions to energy bands in extended systems. For the analysis of oxygen redox activity, PDOS ( $g_{alm}$ ) plots are most commonly used, which can be calculated via

$$g_{alm}(\varepsilon) = \sum_{nk} |\langle Y_{lm}^\alpha | \varphi_{nk} \rangle|^2 \delta(\varepsilon - \varepsilon_{nk}) \quad (5.3.1)$$

where the sum runs over all  $k$  vectors (Brillouin zone sampling)  $k$ , and  $\varepsilon$  are the energies of the electronic states  $\varphi$ , which are projected onto the localized function (spherical

harmonic)  $Y$ . The delta function is in practice often replaced by a narrow Gaussian function due to the finite number of  $k$  points sampled in electronic structure calculations. In ref 496, Koch and Manzhos computed the element-resolved PDOS of the anion redox material  $\text{Li}_2\text{MnO}_3$  as well as the cation redox material  $\text{Li}_2\text{VO}_3$  before and after Li extraction as shown in Figure 24a–d using spherical harmonics as projector functions, which is a common choice in plane-wave codes. The resolution into elements is computed from eq 5.3.1 by summing over all  $l$ ,  $m$ , and  $\alpha$  of sites of the same element. It can be seen that for  $\text{Li}_2\text{MnO}_3$ , the electron loss is indeed confined to states that have majority O character (cf., Figure 24a and b), while for  $\text{Li}_2\text{VO}_3$  the redox activity takes place within V states (cf., Figure 24c and d). Such an identification of anionic redox based on PDOS changes is common practice in literature covering this class of materials. According to the charge self-regulation mechanism presented in section 5.1, the increasing V d population in  $\text{Li}_2\text{VO}_3$  compared to  $\text{LiVO}_3$  would be associated with a decreasing participation of the transition metal in lower-lying states. However, it is difficult to assess such changes from plots like in Figure 24a–d, and they are not commonly considered in PDOS analyses. In order to quantify the shifting transition metal and oxygen contributions, atomic populations  $\rho_\alpha$  can be obtained by integrating eq 5.3.1 up to the Fermi level, weighting each state by its occupation number  $f_{nk}$  and summing over all  $m$  and  $l$  contributions as<sup>552</sup>

$$\rho_\alpha = \frac{1}{N_k} \sum_{nk} f_{nk} \sum_{lm} |\langle Y_{lm}^\alpha | \varphi_{nk} \rangle|^2 \quad (5.3.2)$$

with the number of  $k$  points  $N_k$ . The changes in these atomic populations (or in the partial charges obtained by subtracting  $\rho_\alpha$  from the number of electrons of atom  $\alpha$ ) should indicate the magnitude of changes in the valence DOS contributions from different elements. A detailed evaluation of these populations, however, did not show any negative charge feedback mechanism between transition metal and oxygen during the oxidation of  $\text{Li}_2\text{VO}_3$ . Since the functions  $Y$  are localized, they are commonly confined to a sphere with a defined cutoff radius whose choice can influence the magnitude of the computed atomic populations, but different radii for  $Y$  were not found to recover the charge self-regulation effect, which was clearly seen from QTAIM charges in ref 496. Closer inspection of the compound's electron density difference between charged and discharged states revealed that the addition of electrons to  $\text{LiVO}_3$  leads to charge density gains in diffuse O orbitals along the O–Li axis as well as V contributions between the V–O bonding axes (in agreement with the mechanism outlined in section 5.1), while electron density loss occurs along the V–O bond close to the cation. This can be seen from the charge density profiles in different directions around V and O in the electron density difference of  $\text{Li}_2\text{VO}_3$  shown in Figure 24e and f, respectively. The transition metal centers exhibit a concave QTAIM domain, while the anionic ones have a rather convex shape as shown in Figure 24g and h. The volume of both TM and oxygen basins increases upon oxidation due to cell volume changes and by expansion into empty Li interstitial sites. Besides this expansion, the basin shapes can also adjust to other changes in the electron density distribution around the TM and O centers, which is particularly important for capturing the shift between different d populations on the TM centers due to charge self-regulation. This anisotropy in the atomic domains

is insufficiently taken into account by the spherical projector domains, which are commonly used for the construction of the PDOS in plane-wave codes, and they either neglect the charge density gain region of oxygen (small domain radii) or cut into the charge self-regulation region of the transition metal (large radii) canceling out the changes around the O centers through the overlap with transition metal-near d density (cf., Figure 24e and f). The resulting PDOS plots hence do not show the significant rehybridization and changing oxygen contributions expected also for cationic redox where it is clearly seen from the QTAIM charges. These findings exemplify the systematic errors that can occur in the analysis of the redox mechanism via atomic state projections and are a probable reason why the participation of anionic states in formally cationic redox processes has been rarely acknowledged in literature, since the bulk of electronic structure calculations in the solid state is conducted using plane-wave bases suffering from the drawbacks of the PDOS construction described in ref 496. For localized-basis codes, the choice of function to project upon is more straightforward, and, for example, a Mulliken-type analysis can be performed using the overlap matrix of the atom-centered basis functions, their LCAO coefficients, and the orbital occupations to establish atomic populations. However, such basis-projected population analyses suffer from limitations of their own,<sup>553</sup> most importantly the question of how to divide the overlap population between atoms. Within the QTAIM, the atomic basins do not overlap and are not subjected to geometrical restrictions, which permits identifying and ascribing asymmetric atomic charge density changes to the corresponding nuclei.

The notion of anionic redox activity itself inherently necessitates defining atomic contributions to electron transfer processes, which is always arbitrary and not one approach by itself can provide a complete picture, but they rather need to be chosen in a purpose-oriented way. Understanding anionic redox strictly within the bounds of the oxidation state formalism, i.e., within the classification of electronic states as anionic or cationic, can result in shortcomings due to the limitations of the model or the (theoretical or experimental) methods employed, which influence our interpretation of the process. Anionic redox is a comparatively young and actively researched field; hence our understanding of the underlying mechanism in these materials is expected to evolve in the foreseeable future. The above examples showcase how density-based descriptors can complement our understanding of redox reactions established from oxidation states as the defining metric and their supporting projection-based atomic population analyses based on electronic structure calculations. Specific advantages of QTAIM are the direct quantification of charges of and charge transfer in between atomic sites based on an observable property, namely electron density, without the need for comparison with reference compounds or the additional analysis of ab initio one-electron states. It can further alleviate ambiguities connected to the analysis of these states, which arise from the way orbital contributions are computed. Other than for oxidation states, the same level of insight can in principle be obtained from the analysis of experimental and ab initio results, the latter of which remain essential for the discussion of the anionic redox mechanism in literature due to the often difficult transfer of experimental characterization into the oxidation state picture. It remains unclear how and if a QTAIM-based theoretical model will further contribute to the deepened understanding of oxygen

redox in particular and which merit it might have compared to our current understanding of the process in the end, but the insights obtained so far are a striking example of the potential of QTAIM for the conceptual understanding of chemistry in the future.

## 6. DENSITY TOPOLOGY-BASED METHODS FOR LARGE-SCALE AB INITIO MODELING WITH ORBITAL-FREE DFT

The analysis of the electron density of molecules and materials constitutes a crucial tool for understanding bonding, reactivity, and generally yields an overall picture of a molecular system that goes much beyond the mere partial atomic charges. In sections 2–5, we have discussed the main avenues of research that allow one to extract information from the electron density and density-derived quantities. In section 5, we have demonstrated how density-based analyses can be advantageous over orbital-based analyses for gaining mechanistic insights. The literature overviewed in section 5 concerned itself with the analysis of DFT densities obtained with Kohn–Sham DFT (in which the density is in fact obtained from KS orbitals) with which orbital-based analyses (such as PDOS) are also available but may suffer from shortcomings. Quantum crystallography overviewed in section 3.5 concerns itself with the analysis of experimental electron densities probed directly by diffraction experiments. It is an orbital-free (OF) method for the analysis of the densities, and the name “orbital-free quantum crystallography” has now established itself.<sup>118,554,555</sup> One can also compute the density ab initio in an orbital-free way with orbital-free DFT (OF-DFT).<sup>64</sup> Naturally, density-based approaches are demanded to get mechanistic insight post an OF-DFT calculation absent orbitals, or to build extensions of OF-DFT such as calculations of excitations with time-dependent OF-DFT.<sup>67,94,556</sup> Density-derived quantities similar to those used in orbital-free quantum crystallography (including reduced density gradient, Thomas–Fermi, von Weizsäcker, and Pauli potentials and energy densities, etc.) are also used in the development of the OF-DFT method, in particular for the development of kinetic energy functionals, which are key to OF-DFT. The synergy of the fields of QTAIM and its extensions and of OF-DFT is natural and is expected to be increasingly important going forward. In this section, we discuss the usefulness of density-based quantities for OF-DFT method development and analysis post OF-DFT simulations.

### 6.1. Density-Based Quantities for DFT Functional Construction

In OF-DFT, the electron density,  $\rho(\mathbf{r})$ , is the central quantity in the sense that it is the central variational function. Namely, the ground state density,  $\rho_0(\mathbf{r})$ , is given by

$$\rho_0(\mathbf{r}) = \arg \min_{\rho} \left\{ E[\rho] - \mu \left[ \int \rho(\mathbf{r}) \, d\mathbf{r} - N_{\text{el}} \right] \right\} \quad (6.1.1)$$

where  $N_{\text{el}}$  is the number of electrons in the system (imposed with a constraint in the usual Lagrangian formalism). The issue at hand for OF-DFT is the need to approximate the kinetic energy functional (KEF), as it is a central component of the energy functional:

$$E[\rho] = T_s[\rho] + E_H[\rho] + E_{\text{xc}}[\rho] + \int v_{\text{ext}}(\mathbf{r}) \rho(\mathbf{r}) \, d\mathbf{r} \quad (6.1.2)$$

where  $E_H[\rho]$  is the classical electron–electron Coulomb repulsion,  $E_{\text{xc}}[\rho]$  is the so-called exchange correlation functional,<sup>9</sup> and  $v_{\text{ext}}(\mathbf{r})$  is the external potential, which is usually only given by the attractive electron–nuclear potential.  $T_s[\rho]$  is the kinetic energy. While we can prove that there must be a functional dependence of  $T_s$  on the electron density, such dependency is explicitly unknown. It is, however, known implicitly via the solution of the associated KS equations. Kohn–Sham DFT allows using the noninteracting kinetic energy functional:

$$T_s[\{\psi_i\}] = -\frac{1}{2} \int d\mathbf{r} \sum_{i=1}^{N_{\text{el}}} \psi_i^*(\mathbf{r}) \nabla^2 \psi_i(\mathbf{r}) \quad (6.1.3)$$

where  $\psi_i$  are Kohn–Sham single-electron orbitals (solutions of the Kohn–Sham equation  $-\frac{1}{2} \nabla^2 \psi_i(\mathbf{r}) + v_{\text{eff}}(\mathbf{r}) \psi_i(\mathbf{r}) = \epsilon_i \psi_i(\mathbf{r})$ ), the sum is over all occupied states, and the integration is over the entire support of the orbitals. We ignore spin and partial occupancies without loss of generality of the present discussion. In the case of a periodic system, one also has to integrate over the Brillouin zone, which increases the computational cost. Solving such equations would require diagonalization of the KS Hamiltonian and, generally, is a computationally intensive algorithm (near-cubically scaling in the general case). The major determinant of accuracy is then the exchange-correlation functional of the density  $E_{\text{xc}}[\rho]$ . The XC potential  $v_{\text{xc}}(\mathbf{r}) = \frac{\delta E_{\text{xc}}[\rho]}{\delta \rho(\mathbf{r})}$  enters the effective potential ( $v_{\text{eff}}(\mathbf{r})$ ) of the Kohn–Sham equation and makes sure that the density derived from the solutions of the Kohn–Sham equation,  $\rho_{\text{KS}}(\mathbf{r}) = \sum_{i=1}^{N_{\text{el}}} |\psi_i(\mathbf{r})|^2$ , matches the true electron density.

The XC functionals proposed to date do not allow improving the accuracy of DFT simulations in a controlled manner by choosing convergence parameters in the same way as can be done, for example, by increasing the size of the basis set or of a discretization grid (for quadrature or finite difference approximations, respectively). Instead, one chooses from different approximations which have advantages and disadvantages when used for different purposes. Those approximations utilize purely density dependent quantities including different functions (such as different powers) and orders of derivatives of  $\rho(\mathbf{r})$ . Widely used LDA and GGA type functionals depend on density-dependent quantities such as  $\rho^{4/3}(\mathbf{r})$  (exchange term of LDA), powers and logarithm of  $\rho^{-1/3}(\mathbf{r})$  (correlation of the homogeneous electron gas),<sup>180</sup> density gradient  $\nabla \rho(\mathbf{r})$ , or its dimensionless form  $\nabla \rho / \rho^{4/3}$  (GGA functionals). Such functionals have been constructed as formulas of various and often nontrivial degrees of complexity and containing various empirical parameters and functions,<sup>557–560</sup> which are introduced and modified based on chemical intuition to achieve certain properties (e.g., compare PW1,<sup>560</sup> PBE,<sup>558,561</sup> and PBEsol<sup>559</sup> functionals).<sup>557–560</sup>

The promise of OF-DFT is to rid the model of the computationally intensive steps associated with the solution of the KS equation and exploit directly eq 6.1.2 utilizing KEFs approximations for  $T_s[\rho]$  as functionals of density-dependent quantities only (i.e., without recourse to orbitals) that allow swift evaluation in a number of operations that ideally grows linearly with the system size.<sup>73</sup> OF-DFT can use existing XC functional approximations that have proven themselves as “good enough” for use in various applications of KS DFT,

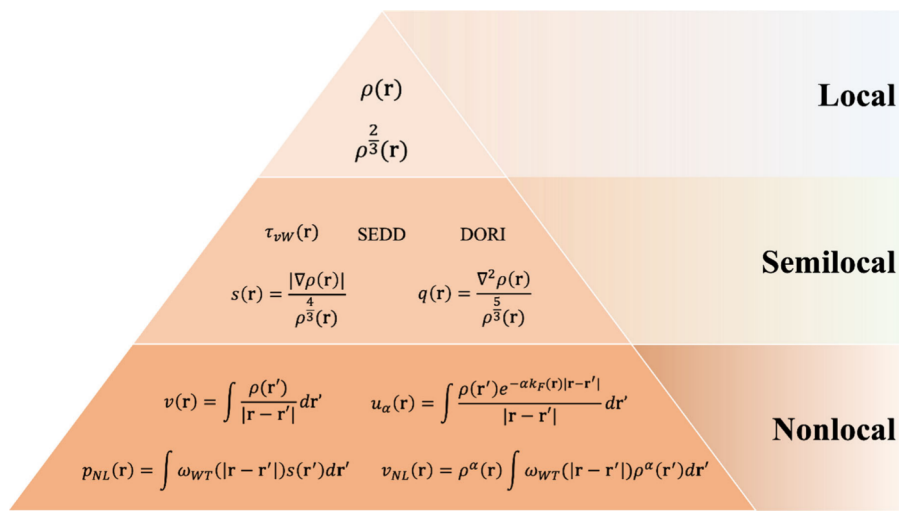


**Figure 25.** Commonly adopted orbital-free density-based descriptors. These include the single exponential decay detector (SEDD)<sup>614</sup> and the density overlap regions indicator (DORI).<sup>615</sup> In the formulas,  $k_F(r) = (3\pi^2\rho(r))^{1/3}$ ,  $\omega_{WT}(|r - r'|)$  is the Wang–Teter kernel function,<sup>569</sup> and  $\tau_{vW}(r)$  is the von Weizsäcker KEDF energy density.

although in the absence of a universal XC functional, different XC models are used in different applications (such as hybrid functionals in molecular modeling or GGA functionals in solid state modeling or range-separated hybrid functionals for charge-transfer excitations, etc.). The major determinant of the accuracy of OF-DFT is then the KEF approximation. In principle, a KEF can also be made to capture, effectively and approximately, any remaining XC contributions not captured by the KS kinetic energy, by, for example, fitting it to observables (such as structural parameters and properties of materials or molecules). A number of KEF approximations have been derived with the help of chemical intuition and various conditions such as the scaling relations<sup>562</sup> (see a recent review<sup>64</sup> for an overview).

Similar to XC functionals, semilocal (GGA-like) functionals have been proposed for the KEF.<sup>80,81,563–565</sup> In the semilocal approach, one models the KED (kinetic energy density)  $\tau[\rho](r)$ , and the corresponding KEF is

$$T_s[\rho] = \int \tau[\rho](r) dr \quad (6.1.4)$$

where one typically strives to match  $\tau[\rho](r) = \tau_{KS}(r) = \sum_i -\frac{1}{2}\psi_i(r)\nabla^2\psi_i(r)$  or  $\tau[\rho](r) = \tau_+(r) = \sum_i \frac{1}{2}\nabla\psi_i(r)\cdot\nabla\psi_i(r)$ , where  $\tau_{KS}[\rho](r)$  and  $\tau_+(r)$  are Kohn–Sham KED and its positively definite version<sup>82–84,563,566</sup> (both integrating to the same kinetic energy). To summarize:

$$\tau_+(r) = \frac{1}{2} \sum_{i=1}^{N_{el}} |\nabla\psi_i(r)|^2 = \tau_{KS}(r) + \frac{1}{4}\nabla^2\rho(r) \quad (6.1.5)$$

The semilocal approach for KEFs is naturally apt to achieve near-linear scaling. The nonlocal KEF functionals are typically written in the form<sup>79,567–571</sup>

$$T_s[\rho] = T_{TF}[\rho] + T_{vW}[\rho] + T_{NL}[\rho] \quad (6.1.6)$$

where  $T_{TF}[\rho] = \frac{3}{10}(3\pi^2)^{2/3} \int \rho^{5/3}(r) dr$  is the Thomas–Fermi (TF) kinetic energy<sup>572</sup> and  $T_{vW}[\rho] = \frac{1}{8} \int \frac{|\nabla\rho(r)|^2}{\rho(r)} dr$  is the von Weizsäcker (vW) kinetic energy.<sup>573</sup> The nonlocal term  $T_{NL}[\rho]$  is usually expressed as

$$T_{NL}[\rho] = \iint \rho^\alpha(r)\omega(r, r')\rho^\beta(r') dr dr' \quad (6.1.7)$$

which in general results in a  $n \log(n)$  scaling.

Unfortunately, KEF approximations proposed to date are not accurate enough for their wide use in materials science applications for which KS DFT is deemed to be sufficiently accurate. As of today, existing KEF approximations are sufficiently accurate for use in real-life applications for light metals.<sup>574–581</sup> Progress is being made with monoelemental or alloy type inorganic semiconductors, for which nonlocal functionals are able to model structures and some of the properties.<sup>78,79</sup> For molecules<sup>582,583</sup> and materials containing d- and f-block elements including metals and ceramics such as practically important oxides and metals used for catalysis, fuel cells, batteries, etc., existing models are insufficient.<sup>584,585</sup> Even though avenues of KEF research based on machine learning (vide infra) and mixed density-orbital methods<sup>586,587</sup> are actively pursued, the lack of accurate KEF for some classes of systems represents a severe bottleneck in computational materials modeling. This is because OF-DFT is the large-scale ab initio method par excellence that achieves both good scaling and low prefactors (contrary to order-N KS DFT approaches<sup>588–591</sup> that suffer from large prefactors even with improved scaling), whereby systems with tens of thousands of atoms are computable on a desktop computer, with millions of atoms routinely computable with access to supercomputers.<sup>72,574</sup>

This in turn would allow routine large-scale ab initio modeling for systems up to and beyond  $10^6$  atoms, thus enabling direct ab initio modeling of genuinely large-scale systems and phenomena such as nanostructures, including plasmonic nanostructures,<sup>592,593</sup> and heterostructures, melting, plasticity, and in general dislocation- and microstructure-driven properties,<sup>574,594–599</sup> disordered systems, etc.<sup>74,76,574,575,600–603</sup> Large-scale phenomena are typically modeled with force fields, which, due to the simplified models of interactions in force fields, have limited descriptive and predictive power and by construction do not provide access to electronic properties and the mechanistic insight provided by DFT. Even when electronic structure and properties are not of interest, direct modeling of large systems with OF-DFT could provide an

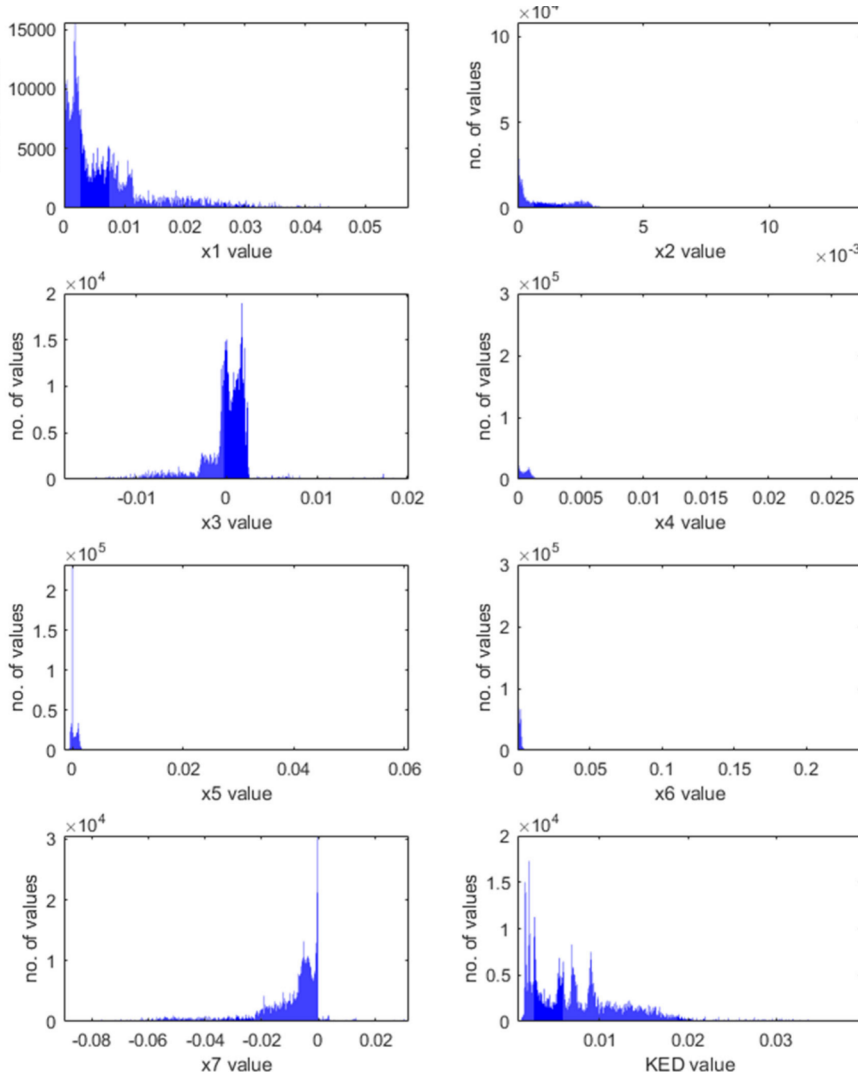


**Figure 26.** Histograms (500 bins) of density-dependent features and of the Kohn–Sham kinetic energy density computed on a Fourier grid of a plane wave basis using Kohn–Sham DFT simulations of Li, Si, and Al (combined in one data set), used in ref 93 to machine learn the KED. The features  $x_1, \dots, x_7$  are elements of the vector  $\mathbf{x} = (\tau_{\text{TF}}, \tau_{\text{TF}}p, \tau_{\text{TF}}q, \tau_{\text{TF}}p^2, \tau_{\text{TF}}pq, \tau_{\text{TF}}q^2, \rho v_{\text{eff}})$ .

independent, ab initio, view and validation, free of the assumptions embedded in force fields.<sup>604</sup>

An enticing proposition is to outsource the construction of the functional, whether XC functional or KEF functional, to a computer. With the advent of end-use friendly machine learning (ML) algorithms available in many publicly accessible environments (Python, Matlab, Octave, and others), and with easily accessible CPU and RAM resources necessary to process electron density-based data (which can easily necessitate working with gigabyte-sized arrays) and large nonlinear optimization problems, this has been increasingly feasible. General-purpose ML methods such as neural networks<sup>605</sup> or kernel regression methods (kernel ridge regression, KRR,<sup>606</sup> or Gaussian process regression, GPR<sup>607</sup>) allow their applications by quantum chemists<sup>608</sup> to the functional construction problem without requiring extensive training in computer or data sciences. Recently, ML has been increasingly used for the construction of KEFs, in particular semilocal KEFs,<sup>68,82–93</sup> as well as learning the density-to-potential bijective map.<sup>92,609,610</sup>

The success of machine learning in general and of machine learning of functionals in particular stands and falls on the choice of descriptors. The descriptors are typically derivatives

and powers of the density (as we focus on density-based methods, we do not consider here methods that also feed into an ML algorithm structural information directly besides any density-dependent quantities,<sup>83,611</sup> which can be thought of as hybrids between OF-DFT and energy surfaces as explicit functions of geometry). In Figure 25, we list some of the semilocal and nonlocal descriptors commonly used.<sup>82,86,92,93,612,613</sup> Even though all of the listed density-based descriptors are directly obtained from the electron density, they highlight different aspects of the electronic system. Going back to Bader, the gradient and the Laplacian of the electron density hold useful information.<sup>370</sup> For example, when the Laplacian (or the reduced (scaled) Laplacian  $q(r)$ , see below) is positive/negative, it denotes regions of depletion/accumulation of the electron density. These regions are particularly evident when visualizing shell structures of atoms and chemical bonds (single and multiple bonds). In particular, Bader drew a parallel between the lumps of  $-\nabla^2\rho(r)$  with the Lewis electron pair model in Gillespie's VSEPR (valence shell electron pair repulsion) theory for explaining and predicting molecular geometries<sup>370</sup> as well as reactivity. For example, maxima of  $-\nabla^2\rho(r)$  indicate charge

compression regions and thus locations of potential electrophilic attack.

Higher order derivatives of the density have also been used, in particular terms of the fourth-order gradient expansion:<sup>86,87,93,564,616</sup>

$$\tau_{\text{GE4}} = \tau_{\text{TF}} \left( 1 + \frac{5}{27} p + \frac{20}{9} q + \frac{8}{81} q^2 - \frac{1}{9} p q + \frac{8}{243} p^2 \right) \quad (6.1.8)$$

where  $\tau_{\text{TF}}$  is the Thomas–Fermi KED,  $p = \frac{|\nabla \rho|^2}{4(3\pi^2)^{2/3}\rho^{8/3}}$  is the scaled squared gradient, and  $q = \frac{\nabla^2 \rho}{4(3\pi^2)^{2/3}\rho^{5/3}}$  is the scaled Laplacian of the density. Manzhos and co-workers demonstrated that it is in principle possible to reproduce KS KED of metals (on the example of Li, Al, and Mg), semiconductors (on the example of Si), and molecules (on the example of H<sub>2</sub>O and benzene) when using the terms of the fourth-order gradient expansion as inputs to a neural network.<sup>86</sup> A neural network was also able to learn the KS KED of several materials simultaneously, providing a degree of portability of a KEDF model. It was found that the optimal NN architecture is intrinsically related to the data aspect of the ML problem. While small single hidden layer NNs were able to learn the KS KED of individual materials, learning it for several materials simultaneously required a deep NN; this was related to very uneven distributions of the density-dependent features (descriptors or inputs of the ML algorithm) as well as of the KS KED itself.<sup>86</sup> The data aspect of ML from or of density-dependent quantities remains understudied. This aspect is important, as one has to work with highly unevenly distributed data. An example of distributions of the terms of the fourth-order gradient expansion and of the KS KED for a data set used in ref 93 combining samples of these quantities from respective crystal unit cells of Li, Si, and Al is shown in Figure 26. In ref 87, it was shown that the product of the density and KS effective potential  $\rho\nu_{\text{eff}}$  is a useful input feature when machine learning the KED, as it is responsible for a significant fraction of the variance of the KED (via  $\tau_{\text{KS}}(\mathbf{r}) + \nu_{\text{eff}}(\mathbf{r})\rho(\mathbf{r}) = \sum_i e_i |\psi_i(\mathbf{r})|^2$ ). This quantity can be constructed from the density without recourse to the orbitals unless orbital-dependent, i.e., hybrid or meta-GGA,<sup>617</sup> XC functionals are used (which then naturally would not be in an OF-DFT simulation). The very uneven distribution of this quantity is also shown in Figure 26. The uneven nature of data distribution complicates sampling. This is a serious issue in ML of KED, which is data-intensive, as density-dependent quantities need to be sampled in real space (for a given geometry) as well as in configuration space (i.e., for different geometries). Data sets with more than 10<sup>6</sup> instances easily arise, which may be difficult to handle with ML algorithms;<sup>618</sup> efficient sampling is therefore important. In some cases, the data distribution issue can be palliated by simple smoothing, as was shown in ref 93. In ref 87, a histogram equalization-like approach was explored for dealing with the uneven distributions, with limited improvement. In ref 619, it was shown that one can work with spatial averages of the density-dependent features and the KED when machine-learning the KEF for large sets of materials and that this is advantageous compared to using integrated quantities. Using the terms of the fourth-order gradient expansion and  $\rho\nu_{\text{eff}}$  as ML features, it was possible to reproduce, with a GPR model, the energy-volume dependence proxied by the quantity:

$$B' = V_0^2 \frac{d^2 E}{dV^2} \approx \frac{E(V_0 - \Delta V) - 2E(V_0) + E(V_0 + \Delta V)}{(\Delta V/V_0)^2} \quad (6.1.9)$$

where  $V_0$  is the equilibrium volume of the simulation cell and  $E$  is the total energy, to within a couple % compared to KS DFT, simultaneously for Li, Al, and Si.<sup>87,93</sup>

## 6.2. Density-Based Analysis for OF-DFT Development and Postprocessing

Density analysis is perhaps the single most important task of an OF-DFT modeler and developer. But the scope of density analysis transcends OF-DFT. Whether one develops exchange-correlation functionals for improved KS-DFT simulations<sup>620–622</sup> or noninteracting kinetic energy density functionals for improved OF-DFT simulations,<sup>64,623</sup> the assessment of the quality of the electron density is a core metric.<sup>624–626</sup>

Since the early days of KEF development, the analysis of the electron density has guided development, pointing out important features, first and foremost, atomic shells and Friedel oscillations.<sup>627</sup> Ballinger and March in 1954<sup>628</sup> showed that a many-electron system confined in a harmonic oscillator potential exhibits characteristic oscillations of the electron density profile; see Figure 27. Disregarding the curves due to

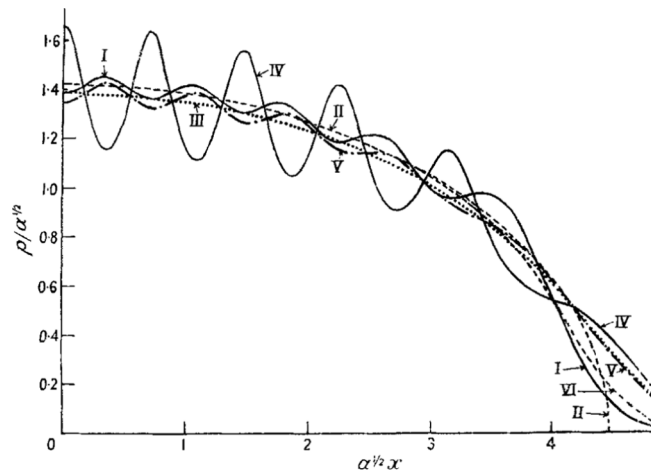


**Figure 27.** Electron density profile of a system of 20 noninteracting electrons in the one-dimensional quantum harmonic oscillator (the first 10 energy levels are occupied).  $\alpha = \frac{4\pi^2 m \nu_0}{h}$ ,  $m$  is the electron mass,  $\nu_0$  is the classical frequency of the oscillator, and  $x$  is the spatial displacement from the bottom of the well. Curve I, analytical solution; II, Thomas–Fermi model; III–V, Plaskett model; and VI, von Weizsäcker model. Reproduced with permission from ref 628. Copyright 1954 IOP Publishing.

the Plaskett model (which does not yield a unique solution), the figure shows that both Thomas–Fermi (TF) and von Weizsäcker's (vW) KEDFs cannot reproduce the pseudoatom's shell structure, a result that would be very clearly discussed a decade later by Yonei and Tomishima.<sup>629</sup>

Electron density profiles also showed that TF was not suitable for evaluating dipole moments of molecules, such as CH<sub>4</sub>. Figure 2 of ref 630 clearly shows the electron density decaying much too slowly away from the methane molecule. Later, Teller formally showed that the TF KEDF should never be applied to molecular systems as no bonding is to be expected.<sup>631</sup>

Many new research directions for KEF development have been explored since the early days of quantum chemistry. These include GGA,<sup>632,633</sup> Laplacian-level functionals,<sup>564,634–637</sup> and nonlocal functionals.<sup>77–79,569,638,639</sup> The assessment of these functionals has almost always relied on the KEF's ability to reproduce the electron density of the reference KS-DFT calculation. A most notable achievement came in 1985 when the CAT functional (a nonlocal KEF)<sup>567</sup> reproduced the density oscillation off of a jellium surface. That result showed, as hinted by Hohenberg and Kohn,<sup>3</sup> that it is possible to encode the correct density response in a nonlocal KEF. Various nonlocal KEFs followed. We refer to a recent review on this subject for additional details.<sup>64</sup>

More recently, it was shown that nonlocal KEFs could deliver qualitatively correct electron density of nonmagnetic materials and of diatomic compounds of Si, Al, and P.<sup>583</sup> See, for example, Figure 28 showing a qualitative agreement

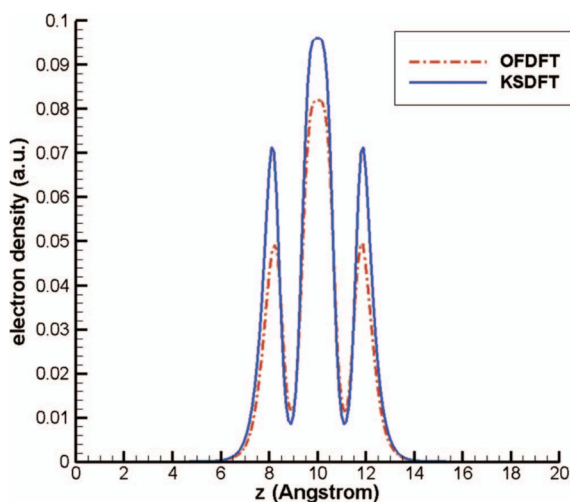


**Figure 28.** Electron density profile along the  $\text{Si}_2$  bond axis. More details are available in the original work by Xia et al.<sup>641</sup> Reproduced with permission from ref 641. Copyright 2012 American Institute of Physics.

between the KS-DFT and OF-DFT densities for  $\text{Si}_2$ . Blatant failures in qualitatively predicting electron densities by approximate KEFs were also reported. For example, for sodium–aluminum hydride,  $\text{NaAlH}_3$ ,<sup>640</sup> the problem was ascribed to the incorrect electron density around the hydrogen atoms due to the too approximate nature of the KEFs employed in that work, WGC.<sup>638</sup> WGC was shown to be inappropriate for highly inhomogeneous systems<sup>582</sup> due to a

numerically ill-behaved Taylor expansion that likely affected the predictions for the hydride.

An inspection of Figure 28 hints that a Laplacian calculated with the OF-DFT density should be qualitatively similar to the one calculated by the reference KS-DFT calculation. Such an agreeable behavior was achieved thanks to the employment of nonlocal KEFs with density-dependent kernel. Even though WGC also has a density dependence, its numerical instability (*vide supra*) makes it inapplicable to molecular systems. Nonlocal KEFs of more recent formulation encode the density dependence in a numerically stable way,<sup>77–79</sup> and it is, therefore, not surprising that they can deliver qualitatively correct electron densities. We reiterate this concept in this section by showcasing some density-based descriptors for the benzoic acid molecule that highlight bonding character and reactivity: Laplacian, Fukui functions ( $f_-$  and  $f_+$ ), and the linear response function ( $\chi$ ), all derived from OF-DFT simulations.

The methods used for the presented examples are as follows. Pseudopotentials for C, H, and O were obtained according to a recipe of recent formulation.<sup>642</sup> In short, the local part of the GBRV ultrasoft pseudopotentials<sup>643</sup> was augmented in the atomic core region by a spherical term that minimizes the density difference between the OF-DFT (using the simple TF +  $\lambda$ vW KEDF<sup>629</sup> with  $\lambda = 0.2$  for ease of optimization) and KS-DFT for the closed-shell diatomics  $\text{H}_2$ ,  $\text{O}_2$ , and  $\text{C}_2$ . To produce quality electron densities, we use the nonlocal functional with density dependent kernel LMGP-G<sup>77</sup> throughout. We use the LDA exchange-correlation functional.<sup>644</sup> The electron density from KS-DFT with GBRV pseudopotentials and the difference of the OF-DFT densities from the KS density for benzoic acid are shown in Figure 29. The figure clearly indicates that OF-DFT with optimal atomic pseudopotentials can qualitatively reproduce the KS-DFT electron density.

Fukui functions describe the electron density in a frontier orbital.<sup>645,646</sup> There are two Fukui functions,  $f_-(\mathbf{r}) = \frac{(\rho_N(\mathbf{r}) - \rho_{N-\epsilon}(\mathbf{r}))}{\epsilon}$  and  $f_+(\mathbf{r}) = \frac{(\rho_{N+\epsilon}(\mathbf{r}) - \rho_N(\mathbf{r}))}{\epsilon}$ , which represent removing and adding an electron to the system, respectively. And  $\epsilon$  is a small, fractionary number of electrons. In this work, we choose  $\epsilon = 0.1$ .

The response function,  $\chi$ , was evaluated by employing Gaussian perturbation potentials,  $\delta v_I(r) = \frac{V_0}{(2\pi\sigma^2)^{\frac{3}{2}}} e^{-\frac{|r-R_I|^2}{2\sigma^2}}$  centered at the position of each atom,  $\{R_I\}$ . The variance of the Gaussian was chosen to be small,  $\sigma = 0.3$  bohr, and the strength of the potential was chosen to be  $V_0 = 0.1$  hartree atomic units. The same Gaussian function (voided of the  $V_0$

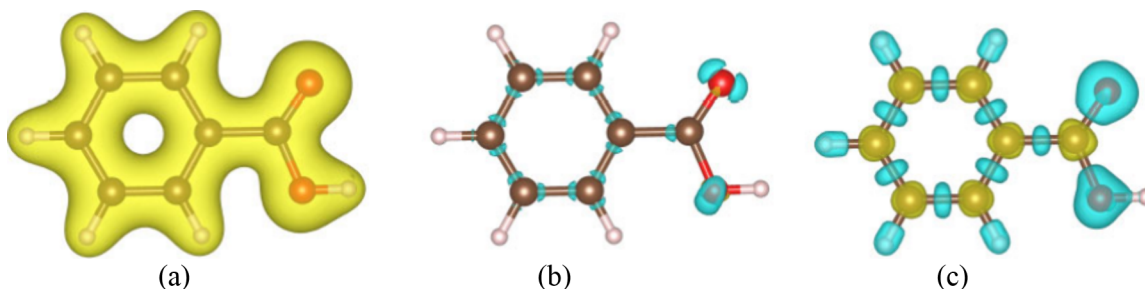


**Figure 29.** Electron density of benzoic acid. (a) KS-DFT. The density difference between OF-DFT and KS-DFT is shown in (b) for OF-DFT using optimized pseudopotentials, and in (c) for OF-DFT using only the local part of the chosen KS-DFT pseudopotential. An isosurface value of  $\pm 0.4$  au is used throughout.

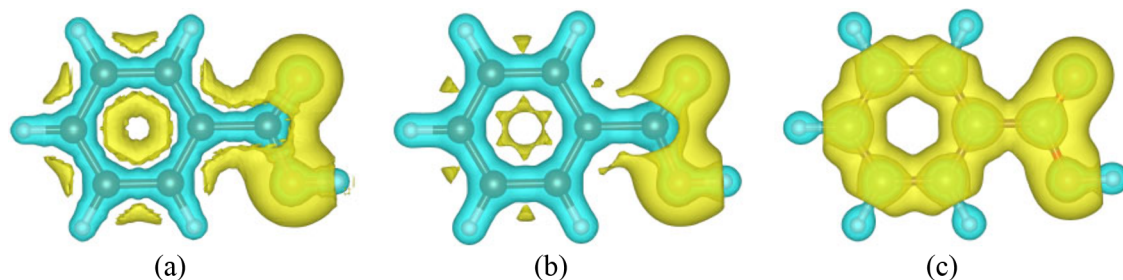


**Figure 30.** Laplacian of the electron density for (a) KS-DFT, (b) OF-DFT, and (c) OF-DFT only with the local part of the chosen KS-DFT pseudopotential. An isosurface value of  $\pm 1.2$  au is used throughout.

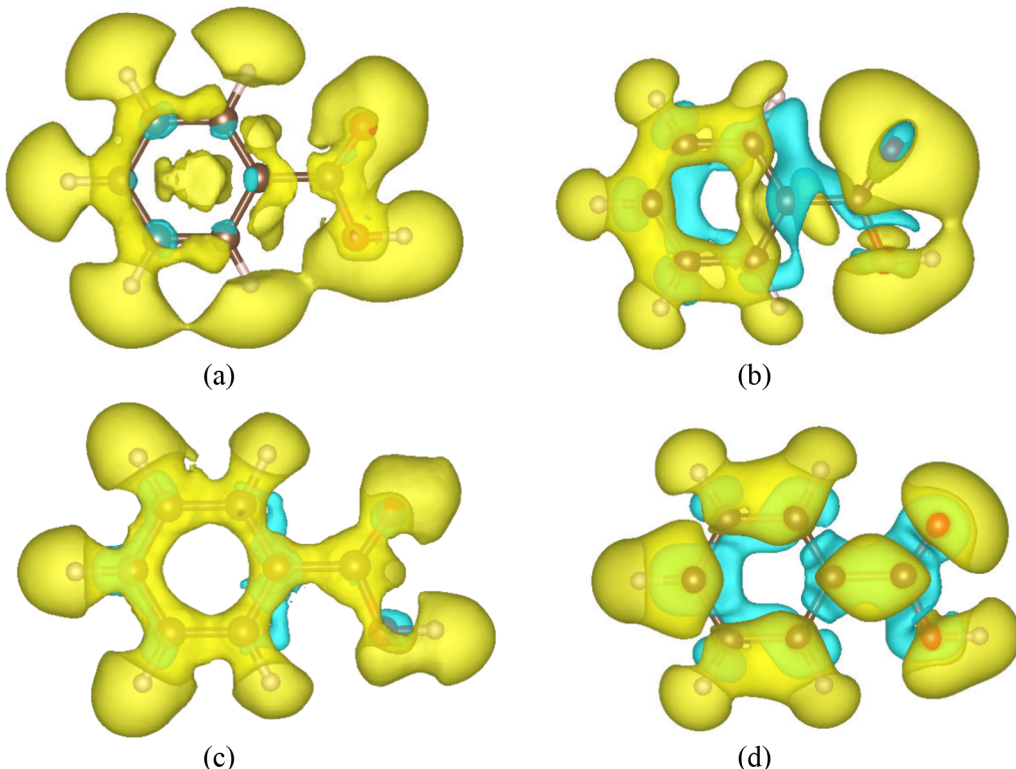


**Figure 31.** The “lesser” Fukui function  $f_-$  computed by (a) OF-DFT and (b) KS-DFT. The “greater” Fukui function  $f_+$  computed by (c) OF-DFT and (d) KS-DFT. An isosurface value of  $\pm 0.006$  au is used throughout.

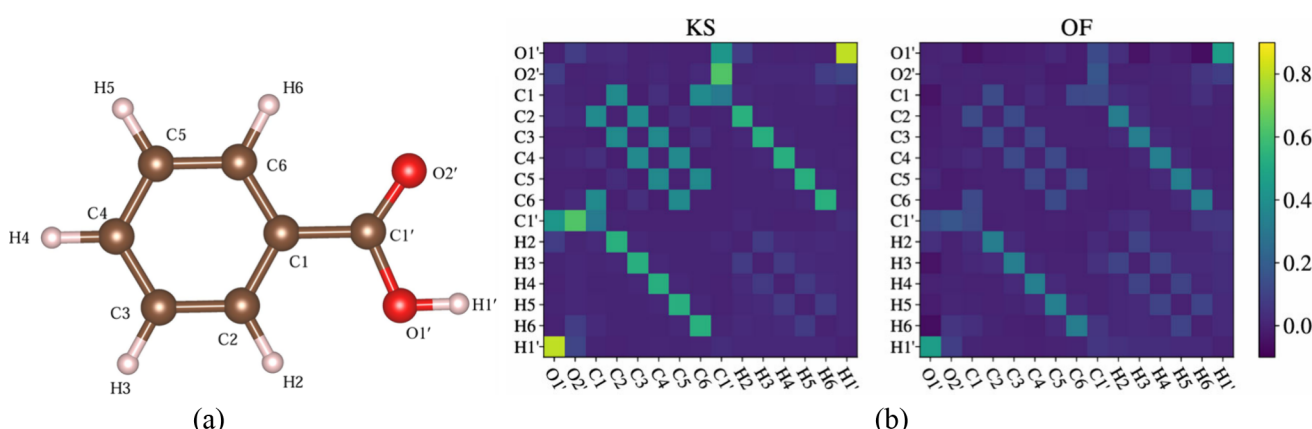


**Figure 32.** (a) The geometry of the benzoic molecule with labeled atoms. (b) The response function,  $\chi$ , matrix computed by KS-DFT (labeled KS) and OF-DFT (labeled OF).

factor) was used as population analysis function to determine the response charge of all other atoms.

The Laplacian of benzoic acid in Figure 30 shows that OF-DFT is indeed capable of reproducing the most important

features of the electron density in comparison with KS-DFT (compare panel (a) with panel (b) of the figure). Specifically, the  $\sigma$  bonding characterized by a cylindrical density featuring negative Laplacian is clearly visible (blue features in the figure). Also, the  $\pi$  bonding in the molecule is almost completely recovered by OF-DFT as one can see the features of positive Laplacian (yellow) in panel (a) qualitatively finding their counterpart in panel (b). As was clearly and convincingly discussed in previous literature,<sup>577,647–649</sup> using the local part of a KS-DFT pseudopotential in OF-DFT simulations leads to very approximate (qualitatively incorrect) results. See panel (c) of Figure 30.

The lesser and greater Fukui functions for benzoic acid are plotted in Figure 31. Fukui functions probe the character of the frontier orbitals as the lesser/greater Fukui function relates to the orbital density of the HOMO/LUMO. Expectations that OF-DFT will deliver quality Fukui functions need to be curbed as practical approximations of the OF-DFT energy functional have no knowledge of KS orbitals. With this in mind, we compare OF with KS, that is, panels (a) with (b) and (c) with (d) of Figure 31, to find for  $f_-$  some differences inside the phenyl ring. However, the general qualitative features, e.g., crossing from phenyl to carbonyl moieties, are recovered by OF-DFT. Not surprisingly, the comparison for  $f_+$  is of much lower quality. This is not unexpected as it relates to the previously discussed concept that OF-DFT has no knowledge of the KS orbitals,<sup>556,650</sup> particularly the virtual orbitals.

Finally, we discuss OF-DFT calculations of response functions,  $\chi$ . Panel (b) of Figure 32 clearly shows that OF-DFT qualitatively reproduces the response function of the benchmark KS-DFT simulation. This is essentially a reproduction of the result by Moldabekov et al.<sup>651</sup> regarding the capability of nonlocal KEFs to reproduce the adiabatic density response. A similar result has been also provided independently for the adiabatic response of time-dependent OF-DFT by Jiang et al.<sup>94</sup> This shows that even though the KS response function appears to be strongly orbital-dependent, its effect can be semiquantitatively approached by a orbital-free functional, which only depends on the electron density, albeit needing to be nonlocal in character.<sup>652</sup>

We stress that a very different picture is found when considering the specifically nonadiabatic response to frequency-dependent perturbations.<sup>556,650</sup> However, the study of the nonadiabatic response in orbital-free TD-DFT simulations lies beyond the scope of this Review.

### 6.3. Toward Density-Based Analysis of Excitations

Kohn–Sham TD-DFT is the most frequently adopted method for modeling excited states (e.g., via the Casida formalism of linear response TD-DFT<sup>653,654</sup>) or for modeling systems out of equilibrium (e.g., via the real-time formulation<sup>655</sup>). A straightforward product of TD-DFT in the Casida formalism is transition densities, which can be analyzed similarly to how one would analyze the ground-state density matrix (i.e., finding representations that optimize some physical conditions, such as the natural transition orbitals<sup>656</sup> and the many other methods that have surfaced in the past two decades<sup>657</sup>). Linear response TD-DFT can also produce electron densities,<sup>658</sup> which can then be analyzed analogously to ground-state densities.<sup>659</sup>

While DFT was originally developed as a ground-state theory, theorems indicate that employing TD-DFT techniques is not a requirement. In fact, the ground-state functional can capture excited states as stationary points with respect to the

electron density.<sup>660</sup> Recent formal work<sup>661</sup> has reinforced this concept utilizing, rather than the density, the density matrix as the fundamental variable (or equivalently the potential or the noninteracting wave function) and reevaluated methods, such as delta-SCF<sup>662–664</sup> and similar methods,<sup>665,666</sup> as resting on rigorous grounds. In addition, it had previously been shown that local minima of the Hartree–Fock energy functional can describe excited states,<sup>667,668</sup> and with accuracy of excitation energy competitive with that of more costly methods.<sup>669</sup> Exploitation of local minima of the energy functional typically involves magnetic systems and generally systems where the electronic structure symmetry can be broken.<sup>670</sup> Even as the potential of minima of the ground-state functional for the description of excited states is established based on KS DFT, it is particularly attractive for OF-DFT where it is in principle applicable straightforwardly with appropriately chosen functionals.

As an example, we discuss the work of Koch et al.<sup>671</sup> who investigated local minima of the DFT+U energy functional when modeling different phases of VO<sub>2</sub>, a material known to exhibit a metal-to-insulator transition at 68 °C between a low-temperature semiconducting monoclinic (M) ground state and a high-temperature metallic rutile (R) phase.<sup>672</sup> Such a transition is notoriously difficult to model by DFT<sup>673–675</sup> (in part due to a small difference in energy between the phases, which is at the limit of DFT accuracy). However, its importance for a range of applications such as smart windows, sensors, and batteries<sup>676–680</sup> makes it a very important and interesting problem for the modeler and the DFT developer. Other phases of VO<sub>2</sub> in that energy range were also reported that can be induced, in particular, by photoexcitation (such as a metallic metastable M phase).<sup>681</sup> Koch et al.<sup>671</sup> found that the relative first-principles energies of the semiconducting M phase, the metallic metastable M phase, and the metallic ground-state R phase, which correspond to different local minima, are in good agreement with previous experimental findings on the thermal and photoexcitation of semiconducting vanadium dioxide leading to a transition into a metallic phase.<sup>681,682</sup> The local minima of the energy functional were achieved by exploring different initial local vanadium d state occupations with a U value appropriately chosen as the smallest value enabling local minima in both M and R phases.

Using the local minima, whether those of DFT+U or of Hartree–Fock,<sup>667–669</sup> as appropriate approximations for excited states is, however, expected to be viable only if those excited states have no pronounced multiconfigurational character, i.e., if they are reasonably well representable by the corresponding local occupation.<sup>683</sup> This suggests that multiple density minima with the DFT+U, or other density-based approaches such as OF-DFT, can also potentially be used to model excitations in other systems at much lower computational cost compared to, e.g., time-dependent DFT. This could be especially promising in the solid state where TD-DFT is not easy to apply, and the commonly used dipole approximation is known to be of limited accuracy.<sup>684</sup> The electron density associated with stationary points of the ground-state energy functional could also be helpful to describe allotropes where energy differences between phases are small enough to be problematic for DFT accuracy, which includes, other than vanadia, technologically relevant materials such as tin.<sup>685,686</sup>

Moving back to TD-DFT methods, in recent years, there has been substantial progress in the development of orbital-free

DFT for excited states. In particular, optical spectra and nonequilibrium electron dynamics have been the focus of several authors. In time-dependent OF-DFT, an OF-DFT extension of the Runge–Gross theorem<sup>687–689</sup> is exploited to provide rigorous footing to the use of the time-dependent OF-DFT Schrödinger-like equation for propagating the electron density in time. The main difference between the time-dependent KS-DFT equations and the OF-DFT counterparts has to do with the inclusion in OF-DFT of the time-dependent Pauli potential. Such a potential was shown to necessarily be extremely nonadiabatic in character<sup>650,688</sup> (i.e., it depends strongly on the frequency or on the electron density at past times). The advent of time-dependent OF-DFT for plasmonics,<sup>592,690–694</sup> optical spectra,<sup>67,94,556</sup> and nonequilibrium electron dynamics<sup>689</sup> calls for the application of density-based descriptors to the time-dependent OF-DFT density. While the general rules that govern these descriptors do not generally apply to nonequilibrium states (for which ad hoc descriptors are usually developed based on the time-dependent electron density), the so-called Casida formalism for obtaining electronic excited states and their properties<sup>654,695</sup> applied to OF-DFT,<sup>556</sup> would provide the same type of information (e.g., transition densities) as a conventional TD-DFT simulation.<sup>556,696</sup>

## 7. CONCLUSIONS AND PERSPECTIVES

We reviewed methods for the analysis of the electron density and their uses to understand the mechanisms of bonding and other phenomena in molecules and solids. As electron density is both experimentally observable as well as in principle computable with all electronic-structure methods (wave function-based, DFT-based methods, as well as semiempirical and valence bond methods<sup>697–703</sup>), it in principle allows direct validation of computational methods and thereby validation of the insights derived from the analyses of the density, which are most often performed on computed densities.

Some of the density-based techniques are well-known and form the field of QTAIM (quantum theory of atoms-in-molecules). Particular density-based quantities such as Bader atomic charges are widely used in applications and have demonstrated certain advantages over other approaches, for example, reflecting better the true charge or oxidation/reduction state (e.g., full ionization of alkali atoms in ionic compounds) than orbital coefficients-based methods (such as Mulliken charges). Analysis of other QTAIM quantities such as various critical points (bond critical point, ring critical point, cage critical point) of the density topology provides insight into the bonding mechanism. QTAIM localization and delocalization indices (LI, DI) inform about charge sharing between atoms and can be used to analyze bonding, in particular bonds with different degrees of ionicity and changes in bonding during redox reactions, in finer details than the pre-quantum chemistry picture based on atomic valence and integer electron counting. They are obtained by 6D integrations of the exchange-correlation density. Direct analysis of the electron density allows analyzing the type of bonding (e.g., degree of ionicity) in a relatively straightforward, basis set-independent procedure and avoiding the complexities of orbital-based approaches.<sup>704</sup>

Further insight can be gained from localization–delocalization matrices (LDM) that list as their elements the number of electrons localized or shared/delocalized within a molecule or a complex. LDMs are constructed from the QTAIM

localization and delocalization indices. A recent book has appeared<sup>41</sup> where numerous predictive applications of these matrices are discussed, and which are briefly touched upon in this Review. These matrices can be used as an electronic molecular descriptor to quantify molecular similarity. Since LDMs are real symmetric matrices, they are diagonalizable, a procedure often required to compare molecules that have different numbers of atoms or atomic skeletons that cannot be numbered in a consistent manner across a series of compounds. Among the practical applications of LDM analysis are the prediction of corrosion inhibitors' activities (and even illuminating their mechanism of action by pinpointing the active corrosion inhibitor's molecular species), mosquito repellency, enzyme inhibition activities, bioremediation of environmental toxicants, and several physicochemical properties of molecular substances. LDMs have also elegant summation properties since the sum of any row or column of these symmetric matrices yields the number of electrons associated, on average, with a given atom in the molecule, viz., its electron population. The elegance of these matrices is such that it suggests that their full potential is yet to be actualized.

QTAIM quantities such as critical points or localization–delocalization indices form what can be called “scalar” QTAIM. We considered the consequences of going beyond the reliance on scalars and instead using vector-based Next Generation Quantum Theory of Atoms-in-Molecules (NG-QTAIM) for computational chemistry. NG-QTAIM is useful for providing the first nonenergy-based approach to elucidate molecular mechanisms and isoenergetic and ultrafast phenomena beyond the reach of conventional quantum chemistry. The interpretation of the chemical bond using NG-QTAIM enabled insights not accessible from scalar methods into deformation anisotropy, bond coupling, and polarization effects in chemical and physics-based phenomena. Full symmetry-breaking is required to elucidate molecular mechanisms and isoenergetic and ultrafast phenomena beyond the reach of conventional quantum chemistry. The full symmetry-breaking properties required are provided by NG-QTAIM and are computed using the Quantvec software<sup>705</sup> developed by some of us. Current work is underway using third-generation eigenvector trajectories  $T_i(s)$  that no longer use bond torsions in their construction and are universally referred to as eigenvector-space-following trajectories  $T_{iF}(s)$ . Instead, these torsion-free  $T_{iF}(s)$  are generated by BCP motion induced by the propagation of electron dynamics. The electron dynamics can be simulated by the effect of nonionizing ultrafast laser pulses with controlled shape, duration, frequency content, and polarization to enable control of switches, molecular devices, or effects in the solid state, e.g., relating to superconductivity, employing a laser-induced mix of electronic states. This can be undertaken without disturbing the nuclear coordinates<sup>706</sup> including the use of lasers as probes.<sup>60</sup> In particular, eigenvector-space-following trajectories  $T_{iF}(s)$  can be constructed using simulations of ultrafast laser pulses with varying intensities to “reverse-engineer” the  $\rho(\mathbf{r})$  distribution at the subfemtosecond or lower time scales. The  $T_{iF}(s)$  have recently been used for the discovery of one-to-one mapping between the carrier envelope phase angle (CEP)  $\phi$  and the  $T_{iF}(s)$ ,<sup>61</sup> thus providing an insight into the previously unknown relationship  $\rho(\mathbf{r}) \rightarrow \psi(\mathbf{r})$  in the form of a Berry Phase, i.e., a rigid rotation of the  $T_{iF}(s)$ . The reverse mapping  $\psi(\mathbf{r}) \rightarrow \rho(\mathbf{r})$  is already established<sup>707,708</sup> using scalar quantum chemical theories. Further avenues currently being explored include the

use of ultrafast nonionizing laser irradiation for superconductivity.

Mechanistic insights derived from the analysis of the electron density are in principle free from the biases and limitations of molecular orbital-based analysis. This is important in particular for the modeling of molecules, materials, and phenomena for which wave function-based methods are impractical, and DFT is then the only practical way of doing electronic structure calculations, that is to say for the vast majority of practically important situations. When orbitals are available, i.e., when Kohn–Sham DFT is feasible, density-based analyses offer a complementary framework, which is more apt to shed light on certain phenomena. Examples were given in this Review of how direct analysis of the electron density topology in all its complexity (exemplified e.g. in the nonspherical shape of attractors) naturally captures anion redox whose extent tends to be either underestimated in an orbital-based picture (e.g., when relying on spherical projector based PDOS) or outright missed (when relying on formal oxidation states that are themselves a result of an orbital-based construction). Density-based analysis naturally accounts for the charge self-regulation phenomenon,<sup>502</sup> whereby Bader charges that are smaller than FOSs and relatively stable for different FOSs of the same element in different compounds (e.g., transition metal oxides), far from being artifacts of the analysis, reflect charge self-regulation.

The need for density-based analyses is obvious when orbitals are unavailable. This is the case, in particular, with orbital-free DFT (OF-DFT), where analysis of bonding and of mechanisms, including reaction and excitation mechanisms, has to be done without recourse to orbitals. OF-DFT is enjoying renewed attention, in particular, due to the promise of machine learning and in general data-driven methods in the construction of kinetic energy functionals that have been the Achilles heel of the method that otherwise has the potential to revolutionize computational materials science by enabling routine direct ab initio modeling at much more realistic length scales than Kohn–Sham DFT. Recent progress in kinetic energy functional (KEF) construction as well as in other issues that have been holding back the use of OF-DFT in applications (local pseudopotentials or excitations with time-dependent OF-DFT) make it in the realm of possibilities that use of OF-DFT will be growing fast in the next decade. This puts an onus on density-based analysis frameworks. Machine-learned (ML) functionals (KEFs for OF-DFT but also exchange-correlation functionals for Kohn–Sham DFT) often use QTAIM-like density-derived quantities as inputs. While up to second-order derivatives of the density are typically used in QTAIM, higher order (such as the terms of the fourth-order gradient expansion) terms as well as other density-based quantities (such as  $\rho v_{\text{eff}}$ ) are useful descriptors for ML KEFs. The data aspect of this application is important, as, especially when machine-learning kinetic energy density functionals, one is bound to work with very large data sets and very unevenly distributed data. We demonstrated that OF-DFT derived densities and density-dependent quantities can reproduce key features of the true density with current KEF approximations even for cases where OF-DFT is deemed to be not yet application-ready for molecules. The research reviewed here also indicated that local minima of the energy as a functional of the density can correspond to different excited states. It will be important in the near future to develop, out of disparate research tracks, recognized/standardized density-based analysis

protocols for the analysis of bonding, reaction, and excitation mechanisms that can be used with OF-DFT much in the same way as standard approaches such as projected density of states (PDOS) or analysis of excitations between orbitals used with Kohn–Sham DFT. Novel density-derived quantities beyond those traditionally used in QTAIM, including nonscalar quantities such as those developed in NG-QTAIM, may be instrumental for this and offer promising avenues for future research.

Electron density-based analyses are also finding uses in materials informatics, for example, in the development of QTAIM-inspired similarity (machine learning) kernels proposed by von Lilienfeld and co-workers<sup>709,710</sup> used in the exploration of chemical spaces for the discovery of novel chemical species for applications ranging from drug development to renewable energy. While machine learning of molecular properties from descriptors of chemical composition and structure is becoming mainstream, machine learning from electron density-based descriptors is a current and exciting area of exploration.<sup>711</sup> QTAIM forms the theoretical foundation of quantum chemical topology force fields (QCTFF), also called FFLUX, a type of machine learning force field developed by Popelier and co-workers.<sup>712,713</sup> In it, the energy is partitioned into contributions from atoms, called “topological atoms”, defined by the Interacting Quantum Atoms (IQA) partitioning of the electron density, and a machine learning algorithm is trained to predict atomic energies and multipole moments (related to structure factors) in function of coordinates of atoms.<sup>714–719</sup> Machine learning is instrumental in handling the complexity of atomic environments. The QCTFF/FFLUX approach is essentially a hybrid between a force field and orbital-free DFT and is an example of a recent convergence of different fields of computational chemistry that had been evolving mostly independently. This diversity of applications including recently emerging applications and ongoing synergy of different types of methods guarantees that electron density analysis techniques and density-based methods will remain at the frontier of scientific developments in the foreseeable future.

## AUTHOR INFORMATION

### Corresponding Authors

**Michele Pavanello** — Department of Physics, Rutgers University, Newark, New Jersey 07102, United States; Department of Chemistry, Rutgers University, Newark, New Jersey 07102, United States;  [orcid.org/0000-0001-8294-7481](https://orcid.org/0000-0001-8294-7481); Email: [m.pavanello@rutgers.edu](mailto:m.pavanello@rutgers.edu)

**Chérif F. Matta** — Department of Chemistry and Physics, Mount Saint Vincent University, Halifax, Nova Scotia B3M 2J6, Canada;  [orcid.org/0000-0001-8397-5353](https://orcid.org/0000-0001-8397-5353); Email: [cherif.matta@msvu.ca](mailto:cherif.matta@msvu.ca)

**Samantha Jenkins** — College of Chemistry and Chemical Engineering, Hunan Normal University, Changsha, Hunan 410081, People's Republic of China;  [orcid.org/0000-4288-7653](https://orcid.org/0000-4288-7653); Email: [samanthajsuman@gmail.com](mailto:samanthajsuman@gmail.com)

**Sergei Manzhos** — School of Materials and Chemical Technology, Institute of Science Tokyo, Meguro-ku, Tokyo 152-8552, Japan;  [orcid.org/0000-0001-8172-7903](https://orcid.org/0000-0001-8172-7903); Email: [manzhos.s.aa@m.titech.ac.jp](mailto:manzhos.s.aa@m.titech.ac.jp)

### Authors

**Daniel Koch** — Centre Énergie Matériaux Télécommunications, Institut National de la Recherche

Scientifique, Varennes, Quebec J3X 1S2, Canada;

✉ orcid.org/0000-0003-4775-6879

Xuecheng Shao — Department of Chemistry, Rutgers University, Newark, New Jersey 07102, United States;  
✉ orcid.org/0000-0003-2215-0926

Manabu Ihara — School of Materials and Chemical Technology, Institute of Science Tokyo, Meguro-ku, Tokyo 152-8552, Japan

Paul W. Ayers — Department of Chemistry and Chemical Biology, McMaster University, Hamilton, Ontario L8S 4M1, Canada; ✉ orcid.org/0000-0003-2605-3883

Complete contact information is available at:  
<https://pubs.acs.org/10.1021/acs.chemrev.4c00297>

## Author Contributions

CRediT: Daniel Koch data curation, investigation, methodology, visualization, writing - original draft, writing - review & editing; Michele Pavanello formal analysis, funding acquisition, methodology, software, writing - original draft, writing - review & editing; Xuecheng Shao formal analysis, methodology, visualization, writing - review & editing; Manabu Ihara funding acquisition, resources, writing - review & editing; Paul Woodson Ayers conceptualization, writing - original draft, writing - review & editing; Chérif F. Matta funding acquisition, methodology, resources, software, visualization, writing - original draft, writing - review & editing; Samantha Jenkins formal analysis, funding acquisition, methodology, resources, software, visualization, writing - original draft, writing - review & editing; Sergei Manzhos conceptualization, formal analysis, methodology, project administration, supervision, writing - original draft, writing - review & editing.

## Notes

The authors declare no competing financial interest.

## Biographies

Daniel Koch did his undergraduate studies and obtained his M.Sc. degree in chemistry from Freie Universität Berlin in 2015 (group of Beate Paulus). He obtained his Ph.D. in 2020 from the National University of Singapore, department of Mechanical Engineering (under the supervision of Sergei Manzhos and Nhan Phan-Thien). From 2020–2023, he was a postdoctoral fellow at the Institut National de la Recherche Scientifique (INRS) in Quebec, Canada. His research interests are in electronic structure methods and in computational investigations of functional materials with a focus on materials for electrochemical power sources. In 2023, he joined the German Aerospace Center (DLR) as a Research Associate.

Michele Pavanello is a Professor of Chemistry and Physics in the Newark campus of Rutgers University. Michele graduated in 2010 with a Ph.D. in Chemistry from the University of Arizona working with Prof. Ludwik Adamowicz on describing few-particle Coulomb systems such as the H<sub>3</sub><sup>+</sup> molecular ion as accurately as possible. A Marie Curie fellowship took him to The Netherlands to work on density embedding and its formulations for describing charge-transfer reactions with Prof. Johannes Neugebauer (now at the University of Münster, Germany). Since 2012, Michele has been leading the Pavanello Research Group (PRG), focusing on electronic structure method development for material science problems, funded by NSF, DOE, and ACS-PRF grants. Michele received the ACS-COMP OpenEye junior faculty award in 2016, and in the same year he received the NSF CAREER award. In 2018 and 2020, Michele was awarded the Rutgers Board of Trustees Award for Excellence in

Research for recently promoted as well as for tenured faculty. In 2022, the Physical Chemistry division of ACS awarded him the ACS-PHYS Early Career Award in Theoretical Chemistry.

Xuecheng Shao is a postdoctoral fellow in the group of Michele Pavanello at Rutgers University, Newark, where he develops DFTpy, eDFTpy, and QEPy codes. He earned his Ph.D. in 2019 from Jilin University (Changchun, China) before joining the Pavanello group in 2019. In 2020, he won a MolSSI Software Fellow, a competitive postdoctoral fellowship from the MolSSI institute. He also received the Wiley Computers in Chemistry Outstanding Postdoc Award in 2020. His research interests are in the development of density-based electronic structure methods including orbital-free DFT.

Manabu Ihara is a Professor at the School of Chemistry and Chemical Technology, Tokyo Institute of Technology, where he is also Director of the Tokyo Tech Academy of Energy and Informatics and Head of the InfoSyEnergy Consortium. He obtained his Ph.D. in Chemical Engineering from The University of Tokyo in 1994. From 1994–1997, he was Assistant Professor at the Department of Chemical Systems Engineering, University of Tokyo, before joining the Tokyo Tech faculty in 2004. His research interests include experimental and computational studies of materials, devices, and systems for renewable energy technologies and materials informatics.

Paul W. Ayers earned his Ph.D. in chemistry in 2001 from the University of North Carolina, working under the direction of Robert G. Parr. After a postdoctoral fellowship with Weitao Yang (Duke University), he joined the faculty of McMaster University in 2002, where he is currently the Canada Research Chair for Theoretical Chemistry. Paul's research focuses on developing new qualitative and quantitative methods for describing molecular electronic structure and reactivity, focusing on the theory and applications of density (matrix) functional theory. He won various awards (including the Dirac Medal, the Rutherford Medal, the Steacie Prize, and the IAQMS medal) and is a Fellow of the Royal Society of Chemistry (UK) and a Member of the College of Young Scholars of the Royal Society of Canada. He cofounded the QC-Devs international software consortium for free and open-source software in the computational sciences.

Chérif F. Matta, B.Pharm.Sci. (Alexandria University), Dipl. (Sadat Academy), Ph.D. (McMaster University), HDR (Université de Lorraine), FRSA, FRSB, FInstP, FRSC, FAAS, FAAAS, is a Professor of Chemistry and Physics at Mount Saint Vincent University and Honorary Professor at Dalhousie, Laval, and Saint Mary's Universities (all in Canada). He is also a frequent Visiting Professor at the Zewail City for Science and Technology (Egypt). After completing his doctorate at McMaster under Professor Richard F. W. Bader, Dr. Matta was a postdoctoral researcher at the University of Toronto (with Nobel laureate Professor John C. Polanyi) and then an Izaak W. Killam postdoctoral researcher at Dalhousie University (with Professor Russell J. Boyd). His research stretches from theoretical and computational chemistry to theoretical biophysics. Matta has given more than 250 lectures in over 30 countries and has around 200 publications including four books. For this work, he received several national and international prizes and awards including elections as Fellow of the American Association for the Advancement of Science, of the African Academy of Sciences, of the Royal Society of Chemistry, of the Institute of Physics, of the Royal Society of Biology, and of the Royal Society of Arts. From 2021–2022, he chaired/headed the Canada Research Chairs (CRC) Interdisciplinary Adjudication Committee of the Tri-Council of Canada, and recently finished a term as Member of the Board of Directors of the Canadian Society for Chemistry. In the past, he served as a member of the multidisciplinary selection committee for the Tri-Council of Canada's

Canada Excellence Research Chairs (CERC) program. Chérif Matta is a member of the Commission on Quantum Crystallography of the International Union of Crystallography (IUCr) and of the Canadian National Committee on Crystallography (CNCC).

Samantha Jenkins is a Professor of Chemistry at Hunan Normal University, Changsha, China, where she joined in 2010 on the Hunan 100 Talents Project. She obtained her Ph.D. in physics from Salford University (United Kingdom) in 2000. She was a postdoctoral fellow in 2000 at the University of Sussex (UK) and at McMaster University (Ontario, Canada) from 2000–2002. From 2002–2010, she was Associate Professor (Docent Chemical Physics), Department of Computer Science, University West, Sweden. Her research interests are in developing the theory of atoms-in-molecules (QTAIM) to form Next Generation QTAIM that she pioneered. In 2013, she won a Chinese Government Friendship Award, and in 2021 she received the Hunan International Science and Technology Cooperation First Class Award.

Sergei Manzhos is an Associate Professor at the School of Chemistry and Chemical Technology, Tokyo Institute of Technology. He holds a master's degree in radio physics and electronics from Kharkiv National University, Ukraine (1999), and a Ph.D. in chemistry from Queen's University, Canada (2005). He was NSERC Postdoctoral Fellow at the University of Montreal, Canada, from 2005–2008. From 2008–2012, he was Project Assistant Professor at the University of Tokyo, and from 2012–2019 he was Assistant Professor and group leader at the Department of Mechanical Engineering, National University of Singapore. He was Associate Professor at the Centre Énergie Matériaux Télécommunications, Institut National de la Recherche Scientifique (INRS) in Quebec, Canada, before joining the Tokyo Institute of Technology in 2021. His research interests include modeling of materials for electrochemical power sources, computational spectroscopy, electron density-based methods, and machine learning. He investigates, in particular, the use of machine learning and data-based methods in electron density-based and atomistic modeling in general.

## ACKNOWLEDGMENTS

We thank the three anonymous reviewers of this paper for a thorough reading of the manuscript and insightful comments that has helped improve it. C.F.M. is indebted to Dr. Sonja Nikolić for helpful discussions. Financial support of this work was provided by the Natural Sciences and Engineering Research Council of Canada (NSERC), Canada Foundation for Innovation (CFI), and Mount Saint Vincent University. The Hunan Natural Science Foundation of China, project approval number 2022JJ30029, as well as the One Hundred Talents Foundation of Hunan Province are gratefully acknowledged for the support of S.J. and S.R.K. Steven R. Kirk is thanked for proof reading. S.J. would also like to thank Tianyu Xu, Alireza Azizi, Xiao Peng Mi, and Wenjing Yu, for assisting with the bibliography and figures. S.J. thanks The Japanese Society for the Promotion of Science (JSPS), Fellowship ID S2208. M.P. is supported by the National Science Foundation under grant nos. CHE-2154760, OAC-2321103, and OAC-2117429, and a grant by the DOE BES CTC program. S.M. and M.I. thank the JST Mirai program (grant no. JPMJMI22H1) for support. They also thank Yoshiaki Maeda and Daio Yoshioka for help with typesetting.

## ABBREVIATIONS

AIM	atoms-in-molecules
AO	atomic orbital

BCP	bond critical point
BCS	Bardeen–Cooper–Schrieffer
BLYP	Becke–Lee–Yang–Parr
CBED	using techniques such as convergent beam electron diffraction
CCP	cage critical point
CCW	counterclockwise
CDVR	charge distribution via reporters
CI	conical intersection
CIP	Cahn–Ingold–Prelog
CISD	configuration interaction singles and doubles
CP	critical point
CPU	central processing unit
CW	clockwise
DFT	density functional theory
DI	delocalization index
DKH2	Douglas–Kroll–Hess two-component
DOS	density of states
FOS	formal oxidation state
GBRV	Garrity–Bennett–Rabe–Vanderbilt
GGA	generalized gradient approximation
GPR	Gaussian process regression
IQA	interacting quantum atoms
IUPAC	International Union of Pure and Applied Chemistry
KED	kinetic energy density
KEF	kinetic energy functional
KRR	kernel ridge regression
KS	Kohn–Sham
LCAO	linear combination of atomic orbitals
LDA	local density approximation
LDM	localization–delocalization matrix
LI	localization index
MIB	metal ion battery
MO	molecular orbital
ML	machine learning
NAMD	nonadiabatic molecular dynamics
NG-QTAIM	next generation quantum theory of atoms-in-molecules
NN	neural network
NNM/NNA	non-nuclear maxima or non-nuclear attractor
OF-DFT	orbital-free
PARODI	parallel recording of dark-field images
PBE	Perdew–Burke–Ernzerhof
PCA	principal component analysis
PDOS	projected density of states
PES	potential energy surface
PP	pseudopotential
PPDOS	projected phonon density of states
QSAR	quantitative structure to activity relationships
QSPR	quantitative structure to property relationships
QTAIM	quantum theory of atoms-in-molecules
RCP	ring critical point
REG	relative energy gradient
sXAS	soft X-ray absorption spectroscopy
RIXS	resonant inelastic X-ray scattering
TD	time-dependent
TEM	transmission electron microscopy
TF	Thomas–Fermi
TM	transition metal
VSEPR	valence shell electron pair repulsion
vW	von Weizsäcker
WGC	Wang–Govind–Carter

WT	Wang–Teter
XC	exchange-correlation
XPS	X-ray photoelectron spectroscopy
XRD	X-ray diffraction

## REFERENCES

- (1) Bader, R. F. W. *Atoms in Molecules: A Quantum Theory*; International Series of Monographs on Chemistry; Oxford University Press: Oxford, NY, 1994.
- (2) Contreras-García, J.; Johnson, E. R.; Keinan, S.; Chaudret, R.; Piquemal, J.-P.; Beratan, D. N.; Yang, W. NCIPILOT: A Program for Plotting Noncovalent Interaction Regions. *J. Chem. Theory Comput.* **2011**, *7*, 625–632.
- (3) Hohenberg, P.; Kohn, W. Inhomogeneous Electron Gas. *Phys. Rev.* **1964**, *136*, B864–B871.
- (4) Levy, M. Universal Variational Functionals of Electron Densities, First-Order Density Matrices, and Natural Spin-Orbitals and Solution of the v-Representability Problem. *Proc. Natl. Acad. Sci. U. S. A.* **1979**, *76*, 6062–6065.
- (5) Burke, K. Perspective on Density Functional Theory. *J. Chem. Phys.* **2012**, *136*, 150901.
- (6) Yu, H. S.; Li, S. L.; Truhlar, D. G. Perspective: Kohn-Sham Density Functional Theory Descending a Staircase. *J. Chem. Phys.* **2016**, *145*, 130901.
- (7) Teale, A. M.; Helgaker, T.; Savin, A.; Adamo, C.; Aradi, B.; Arbuznikov, A. V.; Ayers, P. W.; Baerends, E. J.; Barone, V.; Calaminici, P.; et al. DFT Exchange: Sharing Perspectives on the Workhorse of Quantum Chemistry and Materials Science. *Phys. Chem. Chem. Phys.* **2022**, *24*, 28700–28781.
- (8) Lejaeghere, K.; Bihlmayer, G.; Björkman, T.; Blaha, P.; Blügel, S.; Blum, V.; Caliste, D.; Castelli, I. E.; Clark, S. J.; Dal Corso, A.; et al. Reproducibility in Density Functional Theory Calculations of Solids. *Science* **2016**, *351*, 1415.
- (9) Kohn, W.; Sham, L. J. Self-Consistent Equations Including Exchange and Correlation Effects. *Phys. Rev.* **1965**, *140*, A1133–A1138.
- (10) Baerends, E. J.; Gritsenko, O. V.; van Meer, R. The Kohn–Sham Gap, the Fundamental Gap and the Optical Gap: The Physical Meaning of Occupied and Virtual Kohn–Sham Orbital Energies. *Phys. Chem. Chem. Phys.* **2013**, *15*, 16408–16425.
- (11) van Meer, R.; Gritsenko, O. V.; Baerends, E. J. Physical Meaning of Virtual Kohn–Sham Orbitals and Orbital Energies: An Ideal Basis for the Description of Molecular Excitations. *J. Chem. Theory Comput.* **2014**, *10*, 4432–4441.
- (12) Baerends, E. J. From the Kohn–Sham Band Gap to the Fundamental Gap in Solids. An Integer Electron Approach. *Phys. Chem. Chem. Phys.* **2017**, *19*, 15639–15656.
- (13) Mei, Y.; Yang, W. Excited-State Potential Energy Surfaces, Conical Intersections, and Analytical Gradients from Ground-State Density Functional Theory. *J. Phys. Chem. Lett.* **2019**, *10*, 2538–2545.
- (14) Coropceanu, V.; Cornil, J.; da Silva Filho, D. A.; Olivier, Y.; Silbey, R.; Brédas, J.-L. Charge Transport in Organic Semiconductors. *Chem. Rev.* **2007**, *107*, 926–952.
- (15) Wen, S.-H.; Li, A.; Song, J.; Deng, W.-Q.; Han, K.-L.; Goddard, W. A. I. First-Principles Investigation of Anisotropic Hole Mobilities in Organic Semiconductors. *J. Phys. Chem. B* **2009**, *113*, 8813–8819.
- (16) Baumeier, B.; Kirkpatrick, J.; Andrienko, D. Density-Functional Based Determination of Intermolecular Charge Transfer Properties for Large-Scale Morphologies. *Phys. Chem. Chem. Phys.* **2010**, *12*, 11103–11113.
- (17) Newton, M. D. Quantum Chemical Probes of Electron-Transfer Kinetics: The Nature of Donor-Acceptor Interactions. *Chem. Rev.* **1991**, *91*, 767–792.
- (18) Senthilkumar, K.; Grozema, F. C.; Bickelhaupt, F. M.; Siebbeles, L. D. A. Charge Transport in Columnar Stacked Triphenylenes: Effects of Conformational Fluctuations on Charge Transfer Integrals and Site Energies. *J. Chem. Phys.* **2003**, *119*, 9809–9817.
- (19) Ramos, P.; Mankarious, M.; Pavanello, M. A Critical Look at Methods for Calculating Charge Transfer Couplings Fast and Accurately. In *Practical Aspects of Computational Chemistry IV*; Leszczynski, J., Shukla, M. K., Eds.; Springer: Boston, MA, 2016; pp 103–134.
- (20) Pavanello, M.; Van Voorhis, T.; Visscher, L.; Neugebauer, J. An Accurate and Linear-Scaling Method for Calculating Charge-Transfer Excitation Energies and Diabatic Couplings. *J. Chem. Phys.* **2013**, *138*, No. 054101.
- (21) Farazdel, A.; Dupuis, M.; Clementi, E.; Aviram, A. Electric-Field Induced Intramolecular Electron Transfer in Spiro.Pi.-Electron Systems and Their Suitability as Molecular Electronic Devices. A Theoretical Study. *J. Am. Chem. Soc.* **1990**, *112*, 4206–4214.
- (22) Marcus, R. A. Electron Transfer Reactions in Chemistry. Theory and Experiment. *Rev. Mod. Phys.* **1993**, *65*, 599–610.
- (23) Woiczikowski, P. B.; Kubář, T.; Gutiérrez, R.; Caetano, R. A.; Cuniberti, G.; Elstner, M. Combined Density Functional Theory and Landauer Approach for Hole Transfer in DNA along Classical Molecular Dynamics Trajectories. *J. Chem. Phys.* **2009**, *130*, 215104.
- (24) Vignale, G.; Di Ventra, M. Incompleteness of the Landauer Formula for Electronic Transport. *Phys. Rev. B* **2009**, *79*, No. 014201.
- (25) Feng, Y. P.; Shen, L.; Yang, M.; Wang, A.; Zeng, M.; Wu, Q.; Chintalapati, S.; Chang, C.-R. Prospects of Spintronics Based on 2D Materials. *WIREs Comput. Mol. Sci.* **2017**, *7*, No. e1313.
- (26) Rocha, A. R.; García-suárez, V. M.; Bailey, S. W.; Lambert, C. J.; Ferrer, J.; Sanvito, S. Towards Molecular Spintronics. *Nat. Mater.* **2005**, *4*, 335–339.
- (27) Cohen, A. J.; Tozer, D. J.; Handy, N. C. Evaluation of  $\langle \hat{S}^2 \rangle$  in Density Functional Theory. *J. Chem. Phys.* **2007**, *126*, 214104.
- (28) Ortiz, J. V. Dyson-Orbital Concepts for Description of Electrons in Molecules. *J. Chem. Phys.* **2020**, *153*, No. 070902.
- (29) Popelier, P. *Atoms in Molecules: An Introduction*; Prentice Hall: Harlow, 2000.
- (30) *The Quantum Theory of Atoms in Molecules: From Solid State to DNA and Drug Design*; Matta, C. F.; Boyd, R. J., Eds.; Wiley-VCH: Weinheim, 2007.
- (31) Koch, D.; Chaker, M.; Ihara, M.; Manzhos, S. Density-Based Descriptors of Redox Reactions Involving Transition Metal Compounds as a Reality-Anchored Framework: A Perspective. *Molecules* **2021**, *26*, 5541.
- (32) Koch, D.; Manzhos, S. On the Charge State of Titanium in Titanium Dioxide. *J. Phys. Chem. Lett.* **2017**, *8*, 1593–1598.
- (33) Fradera, X.; Austen, M. A.; Bader, R. F. W. The Lewis Model and Beyond. *J. Phys. Chem. A* **1999**, *103*, 304–314.
- (34) Bader, R. F. W.; Streitwieser, A.; Neuhaus, A.; Laidig, K. E.; Speers, P. Electron Delocalization and the Fermi Hole. *J. Am. Chem. Soc.* **1996**, *118*, 4959–4965.
- (35) Bader, R. F. W.; Johnson, S.; Tang, T.-H.; Popelier, P. L. A. The Electron Pair. *J. Phys. Chem.* **1996**, *100*, 15398–15415.
- (36) Cioslowski, J.; Liu, G. Electrostatic Interaction Energies from a Generalized Gaussian Quadrature. *Chem. Phys. Lett.* **1997**, *277*, 299–305.
- (37) Popelier, P. L. A.; Kosov, D. S. Atom–Atom Partitioning of Intramolecular and Intermolecular Coulomb Energy. *J. Chem. Phys.* **2001**, *114*, 6539–6547.
- (38) Blanco, M. A.; Martín Pendás, A.; Francisco, E. Interacting Quantum Atoms: A Correlated Energy Decomposition Scheme Based on the Quantum Theory of Atoms in Molecules. *J. Chem. Theory Comput.* **2005**, *1*, 1096–1109.
- (39) Martín Pendás, A.; Francisco, E.; Blanco, M. A. Binding Energies of First Row Diatomics in the Light of the Interacting Quantum Atoms Approach. *J. Phys. Chem. A* **2006**, *110*, 12864–12869.
- (40) Francisco, E.; Martín Pendás, A.; Blanco, M. A. A Molecular Energy Decomposition Scheme for Atoms in Molecules. *J. Chem. Theory Comput.* **2006**, *2*, 90–102.
- (41) Matta, C. F.; Ayers, P. W.; Cook, R. *Electron Localization-Delocalization Matrices*, Springer Nature: Switzerland, 2024.

- (42) Cook, R. L. Principal Components of Localization-Delocalization Matrices: New Descriptors for Modeling Biological Activities of Organic Compounds. Part I: Mosquito Insecticides and Repellents. *Struct. Chem.* **2017**, *28*, 1525–1535.
- (43) Sumar, I.; Cook, R.; Ayers, P. W.; Matta, C. F. Aromaticity of Rings-in-Molecules (RIMs) from Electron Localization–Delocalization Matrices (LDMs). *Phys. Scr.* **2016**, *91*, No. 013001.
- (44) Sumar, I.; Cook, R.; Ayers, P. W.; Matta, C. F. AIMLDLM: A Program to Generate and Analyze Electron Localization–Delocalization Matrices (LDMs). *Comput. Theor. Chem.* **2015**, *1070*, 55–67.
- (45) Sumar, I.; Ayers, P. W.; Matta, C. F. Electron Localization–Delocalization Matrices in the Prediction of pKa's and UV-Wavelengths of Maximum Absorbance of p-Benzoic Acids and the Definition of Super-Atoms in Molecules. *Chem. Phys. Lett.* **2014**, *612*, 190–197.
- (46) Timm, M. J.; Matta, C. F.; Massa, L.; Huang, L. The Localization–Delocalization Matrix and the Electron-Density-Weighted Connectivity Matrix of a Finite Graphene Nanoribbon Reconstructed from Kernel Fragments. *J. Phys. Chem. A* **2014**, *118*, 11304–11316.
- (47) Matta, C. F. Modeling Biophysical and Biological Properties from the Characteristics of the Molecular Electron Density, Electron Localization and Delocalization Matrices, and the Electrostatic Potential. *J. Comput. Chem.* **2014**, *35*, 1165–1198.
- (48) Jenkins, S.; Kirk, S. R. *Next Generation Quantum Theory of Atoms in Molecules: From Stereochemistry to Photochemistry and Molecular Devices*, 1st ed.; Lecture Notes in Chemistry; Springer Nature: Singapore, 2023.
- (49) Kirk, S. R.; Jenkins, S. Tools for Overcoming Reliance on Energy-Based Measures in Chemistry: A Tutorial Review. *Chem. Soc. Rev.* **2023**, *52*, 5861–5874.
- (50) Xu, T.; Li, J. H.; Momen, R.; Huang, W. J.; Kirk, S. R.; Shigeta, Y.; Jenkins, S. Chirality-Helicity Equivalence in the S and R Stereoisomers: A Theoretical Insight. *J. Am. Chem. Soc.* **2019**, *141*, 5497–5503.
- (51) Xu, T.; Kirk, S. R.; Jenkins, S. A Comparison of QTAIM and the Stress Tensor for Chirality-Helicity Equivalence in S and R Stereoisomers. *Chem. Phys. Lett.* **2020**, *738*, 136907.
- (52) Baerends, E. J.; Gritsenko, O. V.; van Meer, R. The Kohn–Sham Gap, the Fundamental Gap and the Optical Gap: The Physical Meaning of Occupied and Virtual Kohn–Sham Orbital Energies. *Phys. Chem. Chem. Phys.* **2013**, *15*, 16408–16425.
- (53) Xu, T.; Nie, X.; Li, S.; Yang, Y.; Frücht, H.; Mourik, T.; Kirk, S. R.; Paterson, M. J.; Shigeta, Y.; Jenkins, S. Chirality without Stereoisomers: Insight from the Helical Response of Bond Electrons. *ChemPhysChem* **2021**, *22*, 1989–1995.
- (54) Nie, X.; Yang, Y.; Xu, T.; Biczysko, M.; Kirk, S. R.; Jenkins, S. The Chirality of Isotopomers of Glycine Compared Using Next-Generation QTAIM. *Int. J. Quantum Chem.* **2022**, *122*, No. e26917.
- (55) Li, Z.; Nie, X.; Xu, T.; Li, S.; Yang, Y.; Frücht, H.; van Mourik, T.; Kirk, S. R.; Paterson, M. J.; Shigeta, Y.; et al. Control of Chirality, Bond Flexing and Anharmonicity in an Electric Field. *Int. J. Quantum Chem.* **2021**, *121*, No. e26793.
- (56) Yu, W.; Li, Z.; Peng, Y.; Feng, X.; Xu, T.; Frücht, H.; van Mourik, T.; Kirk, S. R.; Jenkins, S. Controlling Achiral and Chiral Properties with an Electric Field: A Next-Generation QTAIM Interpretation. *Symmetry* **2022**, *14*, 2075.
- (57) Li, Z.; Xu, T.; Frücht, H.; van Mourik, T.; Kirk, S. R.; Jenkins, S. Mixed Chiral and Achiral Character in Substituted Ethane: A next Generation QTAIM Perspective. *Chem. Phys. Lett.* **2022**, *803*, No. 139762.
- (58) Li, Z.; Xu, T.; Frücht, H.; van Mourik, T.; Kirk, S. R.; Jenkins, S. Chiral and Steric Effects in Ethane: A next Generation QTAIM Interpretation. *Chem. Phys. Lett.* **2022**, *800*, No. 139669.
- (59) Peng, Y.; Yu, W.; Feng, X.; Xu, T.; Frücht, H.; van Mourik, T.; Kirk, S. R.; Jenkins, S. The Cis-Effect Explained Using Next-Generation QTAIM. *Molecules* **2022**, *27*, 6099.
- (60) He, H.; Peng Mi, X.; Zhou, X.; Hong, G.; Xu, T.; Frücht, H.; van Mourik, T.; Paterson, M. J.; Kirk, S. R.; Jenkins, S. Ultra-Fast Laser Pulses as a Probe of Electron Dynamics: A next Generation QTAIM Perspective. *Chem. Phys. Lett.* **2024**, *835*, No. 141018.
- (61) Zhou, X.; He, H.; Hong, G.; Peng Mi, X.; Xu, T.; Frücht, H.; van Mourik, T.; Paterson, M. J.; Kirk, S. R.; Jenkins, S. Chirality Reversal with the Carrier-Envelope Phase: A next Generation QTAIM Interpretation. *Chem. Phys. Lett.* **2024**, *848*, No. 141391.
- (62) Xiao, D.; Chang, M.-C.; Niu, Q. Berry Phase Effects on Electronic Properties. *Rev. Mod. Phys.* **2010**, *82*, 1959–2007.
- (63) Hirsch, J. E. Superconducting Materials: Judge and Jury of BCS-Electron–Phonon Theory. *Appl. Phys. Lett.* **2022**, *121*, No. 080501.
- (64) Mi, W.; Luo, K.; Trickey, S. B.; Pavanello, M. Orbital-Free Density Functional Theory: An Attractive Electronic Structure Method for Large-Scale First-Principles Simulations. *Chem. Rev.* **2023**, *123*, 12039–12104.
- (65) Witt, W. C.; del Rio, B. G.; Dieterich, J. M.; Carter, E. A. Orbital-Free Density Functional Theory for Materials Research. *J. Mater. Res.* **2018**, *33*, 777–795.
- (66) Karasiev, V. V.; Trickey, S. B. Chapter Nine - Frank Discussion of the Status of Ground-State Orbital-Free DFT. In *Advances in Quantum Chemistry*; Sabin, J. R., Cabrera-Trujillo, R., Eds.; Concepts of Mathematical Physics in Chemistry: A Tribute to Frank E. Harris - Part A; Academic Press: New York, 2015; Vol. 71, pp 221–245.
- (67) Shao, X.; Jiang, K.; Mi, W.; Genova, A.; Pavanello, M. DFTpy: An Efficient and Object-Oriented Platform for Orbital-Free DFT Simulations. *WIREs Comput. Mol. Sci.* **2021**, *11*, No. e1482.
- (68) Golub, P.; Manzhos, S. CONUNDRUM: A Program for Orbital-Free Density Functional Theory Calculations. *Comput. Phys. Commun.* **2020**, *256*, No. 107365.
- (69) Mi, W.; Shao, X.; Su, C.; Zhou, Y.; Zhang, S.; Li, Q.; Wang, H.; Zhang, L.; Miao, M.; Wang, Y.; et al. ATLAS: A Real-Space Finite-Difference Implementation of Orbital-Free Density Functional Theory. *Comput. Phys. Commun.* **2016**, *200*, 87–95.
- (70) Chen, M.; Xia, J.; Huang, C.; Dieterich, J. M.; Hung, L.; Shin, I.; Carter, E. A. Introducing PROFESS 3.0: An Advanced Program for Orbital-Free Density Functional Theory Molecular Dynamics Simulations. *Comput. Phys. Commun.* **2015**, *190*, 228–230.
- (71) Tan, C. W.; Pickard, C. J.; Witt, W. C. Automatic Differentiation for Orbital-Free Density Functional Theory. *J. Chem. Phys.* **2023**, *158*, 124801.
- (72) Shao, X.; Mi, W.; Pavanello, M. Efficient DFT Solver for Nanoscale Simulations and Beyond. *J. Phys. Chem. Lett.* **2021**, *12*, 4134–4139.
- (73) Hung, L.; Carter, E. A. Accurate Simulations of Metals at the Mesoscale: Explicit Treatment of 1 Million Atoms with Quantum Mechanics. *Chem. Phys. Lett.* **2009**, *475*, 163–170.
- (74) Gavini, V.; Bhattacharya, K.; Ortiz, M. Quasi-Continuum Orbital-Free Density-Functional Theory: A Route to Multi-Million Atom Non-Periodic DFT Calculation. *J. Mech. Phys. Solids* **2007**, *55*, 697–718.
- (75) Gavini, V.; Knap, J.; Bhattacharya, K.; Ortiz, M. Non-Periodic Finite-Element Formulation of Orbital-Free Density Functional Theory. *J. Mech. Phys. Solids* **2007**, *55*, 669–696.
- (76) Radhakrishnan, B.; Gavini, V. Orbital-Free Density Functional Theory Study of the Energetics of Vacancy Clustering and Prismatic Dislocation Loop Nucleation in Aluminium. *Philos. Mag.* **2016**, *96*, 2468–2487.
- (77) Mi, W.; Pavanello, M. Orbital-Free Density Functional Theory Correctly Models Quantum Dots When Asymptotics, Nonlocality, and Nonhomogeneity Are Accounted For. *Phys. Rev. B* **2019**, *100*, No. 041105.
- (78) Shao, X.; Mi, W.; Pavanello, M. Revised Huang-Carter Nonlocal Kinetic Energy Functional for Semiconductors and Their Surfaces. *Phys. Rev. B* **2021**, *104*, No. 045118.
- (79) Huang, C.; Carter, E. A. Nonlocal Orbital-Free Kinetic Energy Density Functional for Semiconductors. *Phys. Rev. B* **2010**, *81*, No. 045206.
- (80) Constantin, L. A.; Fabiano, E.; Della Sala, F. Semilocal Pauli–Gaussian Kinetic Functionals for Orbital-Free Density Functional

- Theory Calculations of Solids. *J. Phys. Chem. Lett.* **2018**, *9*, 4385–4390.
- (81) Luo, K.; Karasiev, V. V.; Trickey, S. B. A Simple Generalized Gradient Approximation for the Noninteracting Kinetic Energy Density Functional. *Phys. Rev. B* **2018**, *98*, No. 041111.
- (82) Yao, K.; Parkhill, J. Kinetic Energy of Hydrocarbons as a Function of Electron Density and Convolutional Neural Networks. *J. Chem. Theory Comput.* **2016**, *12*, 1139–1147.
- (83) Seino, J.; Kageyama, R.; Fujinami, M.; Ikabata, Y.; Nakai, H. Semi-Local Machine-Learned Kinetic Energy Density Functional Demonstrating Smooth Potential Energy Curves. *Chem. Phys. Lett.* **2019**, *734*, No. 136732.
- (84) Imoto, F.; Imada, M.; Oshiyama, A. Order-N Orbital-Free Density-Functional Calculations with Machine Learning of Functional Derivatives for Semiconductors and Metals. *Phys. Rev. Res.* **2021**, *3*, No. 033198.
- (85) Snyder, J. C.; Rupp, M.; Hansen, K.; Blooston, L.; Müller, K.-R.; Burke, K. Orbital-Free Bond Breaking via Machine Learning. *J. Chem. Phys.* **2013**, *139*, 224104.
- (86) Golub, P.; Manzhos, S. Kinetic Energy Densities Based on the Fourth Order Gradient Expansion: Performance in Different Classes of Materials and Improvement via Machine Learning. *Phys. Chem. Chem. Phys.* **2019**, *21*, 378–395.
- (87) Manzhos, S.; Golub, P. Data-Driven Kinetic Energy Density Fitting for Orbital-Free DFT: Linear vs Gaussian Process Regression. *J. Chem. Phys.* **2020**, *153*, No. 074104.
- (88) Fujinami, M.; Kageyama, R.; Seino, J.; Ikabata, Y.; Nakai, H. Orbital-Free Density Functional Theory Calculation Applying Semi-Local Machine-Learned Kinetic Energy Density Functional and Kinetic Potential. *Chem. Phys. Lett.* **2020**, *748*, No. 137358.
- (89) Manzhos, S. Machine Learning for the Solution of the Schrödinger Equation. *Mach. Learn. Sci. Technol.* **2020**, *1*, No. 013002.
- (90) Kulik, H.; Hammerschmidt, T.; Schmidt, J.; Botti, S.; Marques, M. A. L.; Boley, M.; Scheffler, M.; Todorović, M.; Rinke, P.; Oses, C. Roadmap on Machine Learning in Electronic Structure. *Electron. Struct.* **2022**, *4*, 023004.
- (91) Brockherde, F.; Vogt, L.; Li, L.; Tuckerman, M. E.; Burke, K.; Müller, K.-R. Bypassing the Kohn-Sham Equations with Machine Learning. *Nat. Commun.* **2017**, *8*, 872.
- (92) Meyer, R.; Weichselbaum, M.; Hauser, A. W. Machine Learning Approaches toward Orbital-Free Density Functional Theory: Simultaneous Training on the Kinetic Energy Density Functional and Its Functional Derivative. *J. Chem. Theory Comput.* **2020**, *16*, 5685–5694.
- (93) Manzhos, S.; Lüder, J.; Ihara, M. Machine Learning of Kinetic Energy Densities with Target and Feature Smoothing: Better Results with Fewer Training Data. *J. Chem. Phys.* **2023**, *159*, 234115.
- (94) Jiang, K.; Shao, X.; Pavanello, M. Efficient Time-Dependent Orbital-Free Density Functional Theory: Semilocal Adiabatic Response. *Phys. Rev. B* **2022**, *106*, No. 115153.
- (95) Popelier, P. L. A. Quantum Chemical Topology. In *The Chemical Bond II: 100 Years Old and Getting Stronger*; Mingos, D. M. P., Ed.; Springer International Publishing: Cham, 2016; pp 71–117.
- (96) Popelier, P. L. A. On Topological Atoms and Bonds. *Intermolecular Interactions in Crystals: Fundamentals of Crystal Engineering*; Royal Society of Chemistry: London, United Kingdom, 2017.
- (97) Popelier, P. L. A. The QTAIM Perspective of Chemical Bonding. *The Chemical Bond*; John Wiley & Sons, Ltd.: New York, 2014; pp 271–308.
- (98) Popelier, P. L. A. On Quantum Chemical Topology. In *Applications of Topological Methods in Molecular Chemistry*; Chauvin, R., Lepetit, C., Silvi, B., Alikhani, E., Eds.; Springer International Publishing: Cham, 2016; pp 23–52.
- (99) Landeros-Rivera, B.; Gallegos, M.; Munarriz, J.; Laplaza, R.; Contreras-Garcia, J. New venues in electron density analysis. *Phys. Chem. Chem. Phys.* **2022**, *24*, 21538–21548.
- (100) Dirac, P. A. M. *The Principles of Quantum Mechanics*, 4th ed.; International Series of Monographs on Physics; Oxford University Press: Oxford, NY, 1981.
- (101) Bader, R. F. W.; Zou, P. F. An Atomic Population as the Expectation Value of a Quantum Observable. *Chem. Phys. Lett.* **1992**, *191*, 54–58.
- (102) Tsirelson, V. G.; Ozerov, R. P. *Electron Density and Bonding in Crystals: Principles, Theory and X-Ray Diffraction Experiments in Solid State Physics and Chemistry*; CRC Press: Boca Raton, FL, 2020.
- (103) Coppens, P. *X-Ray Charge Densities and Chemical Bonding*; International Union of Crystallography Texts on Crystallography; Oxford University Press: Oxford, NY, 1997.
- (104) Koritsanszky, T. S.; Coppens, P. Chemical Applications of X-Ray Charge-Density Analysis. *Chem. Rev.* **2001**, *101*, 1583–1628.
- (105) Bader, R. F. W.; Matta, C. F. Atomic Charges Are Measurable Quantum Expectation Values: A Rebuttal of Criticisms of QTAIM Charges. *J. Phys. Chem. A* **2004**, *108*, 8385–8394.
- (106) Coppens, P. Electron Density from X-Ray Diffraction. *Annu. Rev. Phys. Chem.* **1992**, *43*, 663–692.
- (107) Born, M.; Oppenheimer, R. Zur Quantentheorie Der Moleküle. *Ann. Phys.* **1927**, *389*, 457–484.
- (108) Bader, R. F. W.; Gillespie, R. J.; Martín, F. Core Distortions in Metal Atoms and the Use of Effective Core Potentials. *Chem. Phys. Lett.* **1998**, *290*, 488–494.
- (109) Hirshfeld, F. L. Bonded-Atom Fragments for Describing Molecular Charge Densities. *Theor. Chim. Acta* **1977**, *44*, 129–138.
- (110) Spackman, M. A.; Maslen, E. N. Chemical Properties from the Promolecule. *J. Phys. Chem.* **1986**, *90*, 2020–2027.
- (111) Stewart, R. F. V. One-Electron Density Functions and Many-Centered Finite Multipole Expansions. *Isr. J. Chem.* **1977**, *16*, 124–131.
- (112) Stewart, R. F. Generalized X-Ray Scattering Factors. *J. Chem. Phys.* **1969**, *51*, 4569–4577.
- (113) Stewart, R. F.; Bentley, J.; Goodman, B. Generalized X-ray Scattering Factors in Diatomic Molecules. *J. Chem. Phys.* **1975**, *63*, 3786–3793.
- (114) Hansen, N. K.; Coppens, P. Testing Aspherical Atom Refinements on Small-Molecule Data Sets. *Acta Crystallogr. A* **1978**, *34*, 909–921.
- (115) Bianchi, R.; Forni, A. VALTOPO: A Program for the Determination of Atomic and Molecular Properties from Experimental Electron Densities. *J. Appl. Crystallogr.* **2005**, *38*, 232–236.
- (116) Stash, A.; Tsirelson, V. WinXPRO: A Program for Calculating Crystal and Molecular Properties Using Multipole Parameters of the Electron Density. *J. Appl. Crystallogr.* **2002**, *35*, 371–373.
- (117) Petříček, V.; Dušek, M.; Palatinus, L. Crystallographic Computing System JANA2006: General features. *Z. Für Krist. - Cryst. Mater.* **2014**, *229*, 345–352.
- (118) Stash, A. I.; Tsirelson, V. G. WinXPRO, 3DPlot and TrajPlot Computer Software: New Options for Orbital-Free Quantum Crystallography Studies. *J. Appl. Crystallogr.* **2022**, *55*, 420–424.
- (119) Coppens, P.; Guru Row, T. N.; Leung, P.; Stevens, E. D.; Becker, P. J.; Yang, Y. W. Net Atomic Charges and Molecular Dipole Moments from Spherical-Atom X-Ray Refinements, and the Relation between Atomic Charge and Shape. *Acta Crystallogr. A* **1979**, *35*, 63–72.
- (120) Pearlman, D. A.; Kim, S.-H. Atomic Charges for DNA Constituents Derived from Single-Crystal X-Ray Diffraction Data. *J. Mol. Biol.* **1990**, *211*, 171–187.
- (121) Brown, A. S.; Spackman, M. A. A Model Study of the  $\kappa$ -Refinement Procedure for Fitting Valence Electron Densities. *Acta Crystallogr. A* **1991**, *47*, 21–29.
- (122) Li, N.; Su, Z.; Coppens, P.; Landrum, J. X-Ray Diffraction Study of the Electronic Ground State of (Mesotetraphenylporphinato)Iron(II). *J. Am. Chem. Soc.* **1990**, *112*, 7294–7298.
- (123) Modern Charge-Density Analysis; Gatti, C., Macchi, P., Eds.; Springer Netherlands: Dordrecht, 2012.

- (124) Jiang, B.; Zuo, J. M.; Jiang, N.; O'Keeffe, M.; Spence, J. C. H. Charge Density and Chemical Bonding in Rutile,  $TiO_2$ . *Acta Crystallogr. A* **2003**, *59*, 341–350.
- (125) Wahlberg, N.; Bindzus, N.; Bjerg, L.; Becker, J.; Christensen, S.; Dippel, A.-C.; Jørgensen, M. R. V.; Iversen, B. B. Powder X-Ray Diffraction Electron Density of Cubic Boron Nitride. *J. Phys. Chem. C* **2015**, *119*, 6164–6173.
- (126) Bindzus, N.; Straasø, T.; Wahlberg, N.; Becker, J.; Bjerg, L.; Lock, N.; Dippel, A.-C.; Iversen, B. B. Experimental Determination of Core Electron Deformation in Diamond. *Acta Crystallogr. Sect. Found. Adv.* **2014**, *70*, 39–48.
- (127) Fischer, A.; Tiana, D.; Scherer, W.; Batke, K.; Eickerling, G.; Svendsen, H.; Bindzus, N.; Iversen, B. B. Experimental and Theoretical Charge Density Studies at Subatomic Resolution. *J. Phys. Chem. A* **2011**, *115*, 13061–13071.
- (128) Elkaim, E.; Tanaka, K.; Coppens, P.; Scheidt, W. R. Low-Temperature Study of Bis(2-Methylimidazole)-(Octaethylporphyrinato)Iron(III) Perchlorate. *Acta Crystallogr. B* **1987**, *43*, 457–461.
- (129) Keith, T. A.; Frisch, M. J. Subshell Fitting of Relativistic Atomic Core Electron Densities for Use in QTAIM Analyses of ECP-Based Wave Functions. *J. Phys. Chem. A* **2011**, *115*, 12879–12894.
- (130) Jansen, G.; Hess, B. A. Revision of the Douglas-Kroll Transformation. *Phys. Rev. A* **1989**, *39*, 6016–6017.
- (131) Hess, B. A. Relativistic Electronic-Structure Calculations Employing a Two-Component No-Pair Formalism with External-Field Projection Operators. *Phys. Rev. A* **1986**, *33*, 3742–3748.
- (132) Hess, B. A. Applicability of the No-Pair Equation with Free-Particle Projection Operators to Atomic and Molecular Structure Calculations. *Phys. Rev. A* **1985**, *32*, 756–763.
- (133) Douglas, M.; Kroll, N. M. Quantum Electrodynamical Corrections to the Fine Structure of Helium. *Ann. Phys.* **1974**, *82*, 89–155.
- (134) Sadjadi, S.; Matta, C. F.; Lemke, K. H.; Hamilton, I. P. Relativistic-Consistent Electron Densities of the Coinage Metal Clusters  $M_2$ ,  $M_4$ ,  $M_{42-}$ , and  $M_4Na_2$  ( $M = Cu, Ag, Au$ ): A QTAIM Study. *J. Phys. Chem. A* **2011**, *115*, 13024–13035.
- (135) Sadjadi, S.; Matta, C. F.; Hamilton, I. P. Chemical Bonding in Groups 10, 11, and 12 Transition Metal Homodimers — An Electron Density Study. *Can. J. Chem.* **2013**, *91*, 583–590.
- (136) Bendeif, E.-E.; Matta, C. F.; Stradiotto, M.; Fertey, P.; Lecomte, C. Can a Formally Zwitterionic Rhodium(I) Complex Emulate the Charge Density of a Cationic Rhodium(I) Complex? A Combined Synchrotron X-Ray and Theoretical Charge-Density Study. *Inorg. Chem.* **2012**, *51*, 3754–3769.
- (137) Souhassou, M.; Lecomte, C.; Blessing, R. H.; Aubry, A.; Rohmer, M.-M.; Wiest, R.; Bénard, M.; Marraud, M. Electron Distributions in Peptides and Related Molecules. I. An Experimental and Theoretical Study of N-Acetyl-l-Tryptophan Methylamide. *Acta Crystallogr. B* **1991**, *47*, 253–266.
- (138) Zheng, J.-C.; Frenkel, A. I.; Wu, L.; Hanson, J.; Ku, W.; Božin, E. S.; Billinge, S. J. L.; Zhu, Y. Nanoscale Disorder and Local Electronic Properties of  $CaCu_3T_4O_{12}$ : An Integrated Study of Electron, Neutron, and x-Ray Diffraction, x-Ray Absorption Fine Structure, and First-Principles Calculations. *Phys. Rev. B* **2010**, *81*, No. 144203.
- (139) Bertaut, E. F. Electrostatic Potentials, Fields and Field Gradients. *J. Phys. Chem. Solids* **1978**, *39*, 97–102.
- (140) Schwarzenbach, D.; Thong, N. The Use of Electric Field Gradient Calculations in Charge Density Refinements. I. Hirshfeld-Type Deformation Functions and the Calculation of Electric Field Gradients by Fourier Series. *Acta Crystallogr. A* **1979**, *35*, 652–658.
- (141) Stewart, R. F. On the Mapping of Electrostatic Properties from Bragg Diffraction Data. *Chem. Phys. Lett.* **1979**, *65*, 335–342.
- (142) Sommer-Larsen, P.; Kadziola, A.; Gajhede, M. Determination of Electrostatic Potentials in Crystalline Compounds. The Application to Boric Acid. *Acta Crystallogr. A* **1990**, *46*, 343–351.
- (143) Zheng, J.-C.; Zhu, Y.; Wu, L.; Davenport, J. W. On the Sensitivity of Electron and X-Ray Scattering Factors to Valence Charge Distributions. *J. Appl. Crystallogr.* **2005**, *38*, 648–656.
- (144) Mott, N. F.; Massey, H. S. W. *The Theory of Atomic Collisions*, 3rd ed.; International series of monographs on physics (Oxford, England); Clarendon Press: Oxford, 1965.
- (145) Zuo, J. M. Automated Structure-Factor Refinement from Convergent-Beam Electron Diffraction Patterns. *Acta Crystallogr. A* **1993**, *49*, 429–435.
- (146) Zuo, J. M.; O'Keeffe, M.; Rez, P.; Spence, J. C. H. Charge Density of  $MgO$ : Implications of Precise New Measurements for Theory. *Phys. Rev. Lett.* **1997**, *78*, 4777–4780.
- (147) Zuo, J. M. Quantitative Convergent Beam Electron Diffraction. *Mater. Trans., JIM* **1998**, *39*, 938–946.
- (148) Taftø, J.; Zhu, Y.; Wu, L. A New Approach Towards Measuring Structure Factors and Valence-Electron Distribution in Crystals with Large Unit Cells. *Acta Crystallogr. A* **1998**, *54*, 532–542.
- (149) Zhu, Y.; Taftø, J. Measurement of Charge Transfer in  $YBa_2Cu_3O_7$  Using a Novel Electron Diffraction Method. *Philos. Mag. B* **1997**, *75*, 785–791.
- (150) Stout, G. H.; Jensen, L. H. *X-Ray Structure Determination: A Practical Guide*; Wiley-Interscience: New York, 1989.
- (151) Sands, D. E. *Introduction to Crystallography, Reprint*; Dover Publications: New York, 1994.
- (152) Rhodes, G. *Crystallography Made Crystal Clear: A Guide for Users of Macromolecular Models*; Elsevier, Inc. and Academic Press: San Diego, 2006.
- (153) Dunitz, J. D. *X-Ray Analysis and the Structure of Organic Molecules*; Verlag Helvetica Chimica Acta: Zürich, 1995.
- (154) Luger, P. *Modern X-Ray Analysis on Single Crystals: A Practical Guide*; De Gruyter: Hawthorne, NY, 2014.
- (155) Hauptman, H.; Karle, J. Crystal-Structure Determination by Means of a Statistical Distribution of Interatomic Vectors. *Acta Crystallogr.* **1952**, *S*, 48–59.
- (156) Karplus, P. A.; Diederichs, K. Linking Crystallographic Model and Data Quality. *Science* **2012**, *336*, 1030.
- (157) Brünger, A. T. Free R Value: Cross-Validation in Crystallography. *Methods in Enzymology; Macromolecular Crystallography Part B*; Academic Press: New York, 1997; Vol. 277, pp 366–396.
- (158) Stewart, R. F., III Total X-Ray Scattering and Two-Electron Density Functions. *Isr. J. Chem.* **1977**, *16*, 111–114.
- (159) Luzanov, A. V.; Prezhdo, O. V. Irreducible Charge Density Matrices for Analysis of Many-Electron Wave Functions. *Int. J. Quantum Chem.* **2005**, *102*, 582–601.
- (160) Density Matrices. In *Consistent Quantum Theory*; Griffiths, R. B., Ed.; Cambridge University Press: Cambridge, 2001; pp 202–215.
- (161) Matta, C. F.; Huang, L.; Massa, L. *Quantum Crystallography*; De Gruyter: Berlin, 2023.
- (162) Clinton, W. L.; Galli, A. J.; Massa, L. J. Direct Determination of Pure-State Density Matrices. II. Construction of Constrained Idempotent One-Body Densities. *Phys. Rev.* **1969**, *177*, 7–13.
- (163) Clinton, W. L.; Massa, L. J. Determination of the Electron Density Matrix from X-Ray Diffraction Data. *Phys. Rev. Lett.* **1972**, *29*, 1363–1366.
- (164) Clinton, W. L.; Frishberg, C. A.; Massa, L. J.; Oldfield, P. A. Methods for Obtaining an Electron-Density Matrix from X-Ray Diffraction Data. *Int. J. Quantum Chem.* **1973**, *7*, 505–514.
- (165) Massa, L.; Huang, L.; Karle, J. Quantum Crystallography and the Use of Kernel Projector Matrices. *Int. J. Quantum Chem.* **1995**, *56*, 371–384.
- (166) Huang, L.; Massa, L.; Karle, J. Quantum Kernels and Quantum Crystallography: Applications in Biochemistry. In *Quantum Biochemistry, Electronic Structure and Biological Activity (Vol. 1)*; Matta, C. F., Ed.; Wiley-VCH: Weinheim, 2010; Chapter 1, pp 1–60.
- (167) Huang, L.; Massa, L.; Karle, J. Quantum Crystallography. *J. Mol. Struct.* **1999**, *474*, 9–12.

- (168) Jayatilaka, D.; Grimwood, D. J. Wavefunctions Derived from Experiment. I. Motivation and Theory. *Acta Crystallogr. A* **2001**, *57*, 76–86.
- (169) Grimwood, D. J.; Jayatilaka, D. Wavefunctions Derived from Experiment. II. A Wavefunction for Oxalic Acid Dihydrate. *Acta Crystallogr. A* **2001**, *57*, 87–100.
- (170) Genoni, A.; Bučinský, L.; Claiser, N.; Contreras-García, J.; Dittrich, B.; Dominiak, P. M.; Espinosa, E.; Gatti, C.; Giannozzi, P.; Gillet, J.-M.; et al. Quantum Crystallography: Current Developments and Future Perspectives. *Chem. – Eur. J.* **2018**, *24*, 10881–10905.
- (171) Wu, L.; Zhu, Y.; Vogt, T.; Su, H.; Davenport, J. W.; Tafto, J. Valence-Electron Distribution in MgB<sub>2</sub> by Accurate Diffraction Measurements and First-Principles Calculations. *Phys. Rev. B* **2004**, *69*, No. 064501.
- (172) Eisenstein, M. Static Deformation Densities for Cytosine and Adenine. *Acta Crystallogr. B* **1988**, *44*, 412–426.
- (173) Cortés-Guzmán, F.; Bader, R. F. W. Complementarity of QTAIM and MO Theory in the Study of Bonding in Donor-Acceptor Complexes. *Coord. Chem. Rev.* **2005**, *249*, 633–662.
- (174) Cortés-Guzmán, F.; Bader, R. F. W. Transferability of Group Energies and Satisfaction of the Virial Theorem. *Chem. Phys. Lett.* **2003**, *379*, 183–192.
- (175) Bader, R. F. W.; Matta, C. F.; Cortés-Guzmán, F. Where to Draw the Line in Defining a Molecular Structure. *Organometallics* **2004**, *23*, 6253–6263.
- (176) Jara-Cortés, J.; Rocha-Rinza, T.; Hernández-Trujillo, J. Electron Density Analysis of Aromatic Complexes in Excited Electronic States: The Benzene and Naphthalene Excimers. *Comput. Theor. Chem.* **2015**, *1053*, 220–228.
- (177) Hernández-Trujillo, J.; Cortés-Guzmán, F.; Fang, D.-C.; Bader, R. F. W. Forces in Molecules. *Faraday Discuss.* **2007**, *135*, 79–95.
- (178) Bader, R. F. W. The Quantum Mechanical Basis of Conceptual Chemistry. *Monatshefte Für Chem. Chem. Mon.* **2005**, *136*, 819–854.
- (179) Matta, C. F. On the Connections between the Quantum Theory of Atoms in Molecules (QTAIM) and Density Functional Theory (DFT): A Letter from Richard F. W. Bader to Lou Massa. *Struct. Chem.* **2017**, *28*, 1591–1597.
- (180) Parr, R. G.; Weitao, Y. *Density-Functional Theory of Atoms and Molecules*; Oxford University Press: New York, 1994.
- (181) Kato, T. On the Eigenfunctions of Many-Particle Systems in Quantum Mechanics. *Commun. Pure Appl. Math.* **1957**, *10*, 151–177.
- (182) Harris, R. L. *Information Graphics: A Comprehensive Illustrated Reference*; Oxford University Press: New York, 1999.
- (183) Ray, S.; Lindsay, B. G. The Topography of Multivariate Normal Mixtures. *Ann. Stat.* **2005**, *33*, 2042–2065.
- (184) Matta, C. F. Applications of the Quantum Theory of Atoms in Molecules to Chemical and Biochemical Problems. Ph.D. Thesis, McMaster University, Hamilton ON, Canada, 2002; <https://macsphere.mcmaster.ca/handle/11375/14324> (accessed 2024-02-04).
- (185) Cao, W. L.; Gatti, C.; MacDougall, P. J.; Bader, R. F. W. On the Presence of Non-Nuclear Attractors in the Charge Distributions of Li and Na Clusters. *Chem. Phys. Lett.* **1987**, *141*, 380–385.
- (186) Cioslowski, J. Nonnuclear Attractors in the Lithium Dimeric Molecule. *J. Phys. Chem.* **1990**, *94*, 5496–5498.
- (187) Iversen, B. B.; Larsen, F. K.; Souhassou, M.; Takata, M. Experimental Evidence for the Existence of Non-Nuclear Maxima in the Electron-Density Distribution of Metallic Beryllium. A Comparative Study of the Maximum Entropy Method and the Multipole Refinement Method. *Acta Crystallogr. B* **1995**, *51*, 580–591.
- (188) Terrabuio, L. A.; Teodoro, T. Q.; Matta, C. F.; Haiduke, R. L. A. Nonnuclear Attractors in Heteronuclear Diatomic Systems. *J. Phys. Chem. A* **2016**, *120*, 1168–1174.
- (189) Platts, J. A.; Overgaard, J.; Jones, C.; Iversen, B. B.; Stasch, A. First Experimental Characterization of a Non-Nuclear Attractor in a Dimeric Magnesium(I) Compound. *J. Phys. Chem. A* **2011**, *115*, 194–200.
- (190) Bader, R. F. W.; Platts, J. A. Characterization of an F-center in an Alkali Halide Cluster. *J. Chem. Phys.* **1997**, *107*, 8545–8553.
- (191) Wu, L.-C.; Jones, C.; Stasch, A.; Platts, J. A.; Overgaard, J. Non-Nuclear Attractor in a Molecular Compound under External Pressure. *Eur. J. Inorg. Chem.* **2014**, *2014*, 5536–5540.
- (192) Azizi, A.; Momen, R.; Xu, T.; Kirk, S. R.; Jenkins, S. Non-Nuclear Attractors in Small Charged Lithium Clusters, Lim<sub>q</sub> (m = 2–5, q = ± 1), with QTAIM and the Ehrenfest Force Partitioning. *Phys. Chem. Chem. Phys.* **2018**, *20*, 24695–24707.
- (193) Taylor, A.; Matta, C. F.; Boyd, R. J. The Hydrated Electron as a Pseudo-Atom in Cavity-Bound Water Clusters. *J. Chem. Theory Comput.* **2007**, *3*, 1054–1063.
- (194) Timerghazin, Q. K.; Peslierbe, G. H. Non-Nuclear Attractor of Electron Density as a Manifestation of the Solvated Electron. *J. Chem. Phys.* **2007**, *127*, No. 064108.
- (195) Anderson, J. S. M.; Massa, L.; Matta, C. F. Non-Nuclear Maxima and the Universality of Bright Wilson's Justification of the First Hohenberg Kohn Theorem Revisited. *Chem. Phys. Lett.* **2021**, *780*, No. 138940.
- (196) Cohen, L. Representable Local Kinetic Energy. *J. Chem. Phys.* **1984**, *80*, 4277–4279.
- (197) Cohen, L. Local Kinetic Energy in Quantum Mechanics. *J. Chem. Phys.* **1979**, *70*, 788–789.
- (198) Anderson, J. S. M.; Ayers, P. W.; Hernandez, J. I. R. How Ambiguous Is the Local Kinetic Energy? *J. Phys. Chem. A* **2010**, *114*, 8884–8895.
- (199) Bader, R. F. W.; Beddall, P. M. The Spatial Partitioning and Transferability of Molecular Energies. *Chem. Phys. Lett.* **1971**, *8*, 29–36.
- (200) Bader, R. F. W.; Beddall, P. M. Virial Field Relationship for Molecular Charge Distributions and the Spatial Partitioning of Molecular Properties. *J. Chem. Phys.* **1972**, *56*, 3320–3329.
- (201) Bader, R. F. W.; Beddall, P. M.; Peslak, J., Jr. Theoretical Development of a Virial Relationship for Spatially Defined Fragments of Molecular Systems. *J. Chem. Phys.* **1973**, *58*, 557–566.
- (202) Srebrenik, S.; Bader, R. F. W. Towards the Development of the Quantum Mechanics of a Subspace. *J. Chem. Phys.* **1975**, *63*, 3945–3961.
- (203) Srebrenik, S.; Bader, R. F. W.; Nguyen-Dang, T. T. Subspace Quantum Mechanics and the Variational Principle. *J. Chem. Phys.* **1978**, *68*, 3667–3679.
- (204) Matta, C. F.; Sadjadi, S. A.; Braden, D. A.; Frenking, G. The Barrier to the Methyl Rotation in Cis-2-Butene and Its Isomerization Energy to Trans-2-Butene, Revisited. *J. Comput. Chem.* **2016**, *37*, 143–154.
- (205) Martín Pendás, A.; Blanco, M. A.; Francisco, E. The Nature of the Hydrogen Bond: A Synthesis from the Interacting Quantum Atoms Picture. *J. Chem. Phys.* **2006**, *125*, 184112.
- (206) Tiana, D.; Francisco, E.; Blanco, M. A.; Martín Pendás, M. Using Pseudopotentials within the Interacting Quantum Atoms Approach. *J. Phys. Chem. A* **2009**, *113*, 7963–7971.
- (207) Tiana, D.; Francisco, E.; Blanco, M. A.; Macchi, P.; Sironi, A.; Martín Pendás, A. Bonding in Classical and Nonclassical Transition Metal Carbonyls: The Interacting Quantum Atoms Perspective. *J. Chem. Theory Comput.* **2010**, *6*, 1064–1074.
- (208) Massa, L.; Keith, T.; Cheng, Y.; Matta, C. F. The Kernel Energy Method Applied to Quantum Theory of Atoms in Molecules – Energies of Interacting Quantum Atoms. *Chem. Phys. Lett.* **2019**, *734*, No. 136650.
- (209) Bader, R.; Martín, F. J. Interdeterminacy of Basin and Surface Properties of an Open System. *Can. J. Chem.* **1998**, *76*, 284–291.
- (210) Bader, R. F. W.; Keith, T. A. Properties of Atoms in Molecules: Magnetic Susceptibilities. *J. Chem. Phys.* **1993**, *99*, 3683–3693.
- (211) Bader, R. F. W.; Matta, C. F. Properties of Atoms in Crystals: Dielectric Polarization. *Int. J. Quantum Chem.* **2001**, *85*, 592–607.
- (212) Bader, R. F. W. Dielectric Polarization: A Problem in the Physics of an Open System. *Mol. Phys.* **2002**, *100*, 3333–3344.

- (213) Bader, R. F. W.; Bayles, D.; Heard, G. L. Properties of Atoms in Molecules: Transition Probabilities. *J. Chem. Phys.* **2000**, *112*, 10095–10105.
- (214) Popelier, P. L. A. A Fast Algorithm to Compute Atomic Charges Based on the Topology of the Electron Density. *Theor. Chem. Acc.* **2001**, *105*, 393–399.
- (215) Matta, C. F. FRAGDIP: Program to Calculate Functional Group Contributions to the Molecular Dipole Moment, 2001; <https://www.cmatta.ca/software/> (accessed 2024-02-21).
- (216) Keith, T. A. AIMAll, 2023; <https://aim.tkgristmill.com/> (accessed 2024-02-04).
- (217) Kohn, W. Density Functional and Density Matrix Method Scaling Linearly with the Number of Atoms. *Phys. Rev. Lett.* **1996**, *76*, 3168–3171.
- (218) Bader, R. F. W. Chemistry and the Near-Sighted Nature of the One-Electron Density Matrix. *Int. J. Quantum Chem.* **1995**, *56*, 409–419.
- (219) Prodan, E.; Kohn, W. Nearsightedness of Electronic Matter. *Proc. Natl. Acad. Sci. U. S. A.* **2005**, *102*, 11635–11638.
- (220) Benson, S. W.; Cruickshank, F. R.; Golden, D. M.; Haugen, G. R.; O'Neal, H. E.; Rodgers, A. S.; Shaw, R.; Walsh, R. Additivity Rules for the Estimation of Thermochemical Properties. *Chem. Rev.* **1969**, *69*, 279–324.
- (221) Cohen, N.; Benson, S. W. The Thermochemistry of Alkanes and Cycloalkanes. *Alkanes and Cycloalkanes* (1992); John Wiley & Sons, Ltd.: New York, 1992; pp 215–287.
- (222) Cohen, N.; Benson, S. W. Estimation of Heats of Formation of Organic Compounds by Additivity Methods. *Chem. Rev.* **1993**, *93*, 2419–2438.
- (223) Wiberg, K. B.; Bader, R. F. W.; Lau, C. D. H. Theoretical Analysis of Hydrocarbon Properties. 2. Additivity of Group Properties and the Origin of Strain Energy. *J. Am. Chem. Soc.* **1987**, *109*, 1001–1012.
- (224) Bader, R. F. W.; Keith, T. A.; Gough, K. M.; Laidig, K. E. Properties of Atoms in Molecules: Additivity and Transferability of Group Polarizabilities. *Mol. Phys.* **1992**, *75*, 1167–1189.
- (225) Bader, R. F. W.; Bayles, D. Properties of Atoms in Molecules: Group Additivity. *J. Phys. Chem. A* **2000**, *104*, 5579–5589.
- (226) Popper, K. R. In *The Logic of Scientific Discovery*; Group, H. P., Ed.; Routledge: New York, 1934.
- (227) Bader, R. F. W.; Matta, C. F. Bonding to Titanium. *Inorg. Chem.* **2001**, *40*, 5603–5611.
- (228) Tomaszewski, R.; Hyla-Kryspin, I.; Mayne, C. L.; Arif, A. M.; Gleiter, R.; Ernst, R. D. Shorter Nonbonded Than Bonded Contacts or Nonclassical Metal-to-Saturated Carbon Atom Interactions? *J. Am. Chem. Soc.* **1998**, *120*, 2959–2960.
- (229) Batsanov, S. S. Van der Waals Radii of Elements. *Inorg. Mater.* **2001**, *37*, 871–885.
- (230) Martín Pendás, A.; Francisco, E.; Blanco, M. A.; Gatti, C. Bond Paths as Privileged Exchange Channels. *Chem. – Eur. J.* **2007**, *13*, 9362–9371.
- (231) Popelier, P. L. A.; Logothetis, G. Characterization of an Agostic Bond on the Basis of the Electron Density. *J. Organomet. Chem.* **1998**, *555*, 101–111.
- (232) Tognetti, V.; Joubert, L.; Cortona, P.; Adamo, C. Toward a Combined DFT/QTAIM Description of Agostic Bonds: The Critical Case of a Nb(III) Complex. *J. Phys. Chem. A* **2009**, *113*, 12322–12327.
- (233) Tognetti, V.; Joubert, L.; Raucoles, R.; De Bruin, T.; Adamo, C. Characterizing Agosticity Using the Quantum Theory of Atoms in Molecules: Bond Critical Points and Their Local Properties. *J. Phys. Chem. A* **2012**, *116*, 5472–5479.
- (234) Matta, C. F.; Hernández-Trujillo, J.; Tang, T.-H.; Bader, R. F. W. Hydrogen–Hydrogen Bonding: A Stabilizing Interaction in Molecules and Crystals. *Chem. – Eur. J.* **2003**, *9*, 1940–1951.
- (235) Cioslowski, J.; Mixon, S. T. Universality among Topological Properties of Electron Density Associated with the Hydrogen–Hydrogen Nonbonding Interactions. *Can. J. Chem.* **1992**, *70*, 443–449.
- (236) Hernández-Trujillo, J.; Matta, C. F. Hydrogen–Hydrogen Bonding in Biphenyl Revisited. *Struct. Chem.* **2007**, *18*, 849–857.
- (237) García-Ramos, J. C.; Cortés-Guzmán, F.; Matta, C. F. On the Nature of Hydrogen–Hydrogen Bonding. In: *Intermolecular Interactions in Molecular Crystals: Fundamentals of Crystal Engineering*; Novoa, J. J., Ed.; Royal Society of Chemistry: London, UK, 2018; Chapter 16, pp 559–594.
- (238) Popelier, P. L. A.; Maxwell, P. I.; Thacker, J. C. R.; Alkorta, I. A Relative Energy Gradient (REG) Study of the Planar and Perpendicular Torsional Energy Barriers in Biphenyl. *Theor. Chem. Acc.* **2019**, *138*, 12.
- (239) Thacker, J. C. R.; Popelier, P. L. A. The ANANKE Relative Energy Gradient (REG) Method to Automate IQA Analysis over Configurational Change. *Theor. Chem. Acc.* **2017**, *136*, 86.
- (240) Bates, T. G.; de Lange, J. H.; Cukrowski, I. The CH···HC Interaction in Biphenyl Is a Delocalized, Molecular-Wide and Entirely Non-Classical Interaction: Results from FALDI Analysis. *J. Comput. Chem.* **2021**, *42*, 706–718.
- (241) De Lange, J. H.; van Niekerk, D. M. E.; Cukrowski, I. FALDI-Based Criterion for and the Origin of an Electron Density Bridge with an Associated (3,–1) Critical Point on Bader's Molecular Graph. *J. Comput. Chem.* **2018**, *39*, 2283–2299.
- (242) De Lange, J. H. Fundamental Nature of Chemical Bonding from the Novel Fragment Atom Localised Delocalised and Interatomic (FALDI) Electron Density Decomposition Scheme: A Theoretical Study. PhD Thesis, University of Pretoria, 2018; <https://repository.up.ac.za/handle/2263/70562> (accessed 2024-07-21).
- (243) De Lange, J. H. Theoretical Investigation of CH<sub>n</sub>HC Contacts and Other Intramolecular Interactions in 2,2'-Bipyridine and Itscomplexes with Metal Ions. M.Sc. thesis, University of Pretoria, 2013; <https://repository.up.ac.za/handle/2263/40364> (accessed 2024-07-21).
- (244) De Lange, J. H.; Cukrowski, I. Toward Deformation Densities for Intramolecular Interactions without Radical Reference States Using the Fragment, Atom, Localized, Delocalized, and Interatomic (FALDI) Charge Density Decomposition Scheme. *J. Comput. Chem.* **2017**, *38*, 981–997.
- (245) De Lange, J. H.; Cukrowski, I. Exact and Exclusive Electron Localization Indices within QTAIM Atomic Basins. *J. Comput. Chem.* **2018**, *39*, 1517–1530.
- (246) De Lange, J. H.; van Niekerk, D. M. E.; Cukrowski, I. FALDI-Based Decomposition of an Atomic Interaction Line Leads to 3D Representation of the Multicenter Nature of Interactions. *J. Comput. Chem.* **2018**, *39*, 973–985.
- (247) Cukrowski, I.; van Niekerk, D. M. E.; De Lange, J. H. Exploring Fundamental Differences between Red- and Blue-Shifted Intramolecular Hydrogen Bonds Using FAMSEC, FALDI, IQA and QTAIM. *Struct. Chem.* **2017**, *28*, 1429–1444.
- (248) Bader, R. F. W.; Gatti, C. A Green's Function for the Density. *Chem. Phys. Lett.* **1998**, *287*, 233–238.
- (249) Gatti, C.; Cargnani, F.; Bertini, L. Chemical Information from the Source Function. *J. Comput. Chem.* **2003**, *24*, 422–436.
- (250) Gatti, C. The Source Function Descriptor as a Tool to Extract Chemical Information from Theoretical and Experimental Electron Densities. In *Electron Density and Chemical Bonding II: Theoretical Charge Density Studies*; Stalke, D., Ed.; Structure and Bonding; Springer: Berlin, Heidelberg, 2012; pp 193–285.
- (251) Lo Presti, L.; Gatti, C. Using the Source Function Descriptor to Dampen the Multipole Model Bias in Charge Density Studies from X-Ray Structure Factors Refinements. *Chem. Phys. Lett.* **2009**, *476*, 308–316.
- (252) Monza, E.; Gatti, C.; Lo Presti, L.; Ortoleva, E. Revealing Electron Delocalization through the Source Function. *J. Phys. Chem. A* **2011**, *115*, 12864–12878.
- (253) Gatti, C. Challenging Chemical Concepts through Charge Density of Molecules and Crystals. *Phys. Scr.* **2013**, *87*, No. 048102.
- (254) Gatti, C.; Orlando, A. M.; Lo Presti, L. Insights on Spin Polarization through the Spin Density Source Function. *Chem. Sci.* **2015**, *6*, 3845–3852.

- (255) Gatti, C.; Saleh, G.; Lo Presti, L. Source Function Applied to Experimental Densities Reveals Subtle Electron-Delocalization Effects and Appraises Their Transferability Properties in Crystals. *Acta Crystallogr. Sect. B Struct. Sci. Cryst. Eng. Mater.* **2016**, *72*, 180–193.
- (256) Gatti, C.; Macetti, G.; Boyd, R. J.; Matta, C. F. An Electron Density Source-Function Study of DNA Base Pairs in Their Neutral and Ionized Ground States†. *J. Comput. Chem.* **2018**, *39*, 1112–1128.
- (257) Poater, J.; Visser, R.; Solà, M.; Bickelhaupt, F. M. Polycyclic Benzenoids: Why Kinked Is More Stable than Straight. *J. Org. Chem.* **2007**, *72*, 1134–1142.
- (258) Poater, J.; Solà, M.; Bickelhaupt, F. M. Hydrogen–Hydrogen Bonding in Planar Biphenyl, Predicted by Atoms-In-Molecules Theory, Does Not Exist. *Chem. – Eur. J.* **2006**, *12*, 2889–2895.
- (259) Poater, J.; Solà, M.; Bickelhaupt, F. M. A Model of the Chemical Bond Must Be Rooted in Quantum Mechanics, Provide Insight, and Possess Predictive Power. *Chem. – Eur. J.* **2006**, *12*, 2902–2905.
- (260) Bader, R. F. W. Definition of Molecular Structure: By Choice or by Appeal to Observation? *J. Phys. Chem. A* **2010**, *114*, 7431–7444.
- (261) Bader, R. F. W. Pauli Repulsions Exist Only in the Eye of the Beholder. *Chem. – Eur. J.* **2006**, *12*, 2896–2901.
- (262) Wolstenholme, D. J.; Matta, C. F.; Cameron, T. S. Experimental and Theoretical Electron Density Study of a Highly Twisted Polycyclic Aromatic Hydrocarbon: 4-Methyl-[4]Helicene. *J. Phys. Chem. A* **2007**, *111*, 8803–8813.
- (263) Wolstenholme, D. J.; Cameron, T. S. Comparative Study of Weak Interactions in Molecular Crystals: H–H Bonds vs Hydrogen Bonds. *J. Phys. Chem. A* **2006**, *110*, 8970–8978.
- (264) Robertson, K. N.; Knop, O.; Cameron, T. S. C–H...H–C Interactions in Organoammonium Tetraphenylborates: Another Look at Dihydrogen Bonds. *Can. J. Chem.* **2003**, *81*, 727–743.
- (265) Matta, C. F. Hydrogen–Hydrogen Bonding: The Non-Electrostatic Limit of Closed-Shell Interaction Between Two Hydrogen Atoms. A Critical Review. In *Hydrogen Bonding—New Insights*; Grabowski, S. J., Ed.; Springer Netherlands: Dordrecht, 2006; pp 337–375.
- (266) Cukrowski, I.; Matta, C. F. Hydrogen–Hydrogen Bonding: A Stabilizing Interaction in Strained Chelating Rings of Metal Complexes in Aqueous Phase. *Chem. Phys. Lett.* **2010**, *499*, 66–69.
- (267) Sabirov, D. Sh. A Correlation between the Mean Polarizability of the “Kinked” Polycyclic Aromatic Hydrocarbons and the Number of H...H Bond Critical Points Predicted by Atoms-in-Molecules Theory. *Comput. Theor. Chem.* **2014**, *1030*, 81–86.
- (268) Monteiro, N. K. V.; Firme, C. L. Hydrogen–Hydrogen Bonds in Highly Branched Alkanes and in Alkane Complexes: A DFT, Ab Initio, QTAIM, and ELF Study. *J. Phys. Chem. A* **2014**, *118*, 1730–1740.
- (269) Bakhmutov, V. I. *Dihydrogen Bond: Principles, Experiments, and Applications*; Wiley-Interscience: NJ, 2008.
- (270) Firme, C. L. *Introductory Organic Chemistry and Hydrocarbons: A Physical Chemistry Approach*; CRC Press: Boca Raton, FL, 2019.
- (271) Gupta, V. P. *Principles and Applications of Quantum Chemistry*; Academic Press: London, UK, 2015.
- (272) McWeeny, R. Some Recent Advances in Density Matrix Theory. *Rev. Mod. Phys.* **1960**, *32*, 335–369.
- (273) Coleman, A. J. Structure of Fermion Density Matrices. *Rev. Mod. Phys.* **1963**, *35*, 668–686.
- (274) McWeeny, R. *Methods of Molecular Quantum Mechanics*, 2nd ed.; Academic Press: London, 1992.
- (275) Davidson, E. R. *Reduced Density Matrices in Quantum Chemistry*; Academic Press: New York, 2012.
- (276) Yukalov, V. L.; Coleman, A. J. *Reduced Density Matrices: Coulson's Challenge*, 2000th ed.; Springer: Berlin; New York, 2008.
- (277) Wang, Y.-G.; Matta, C. F.; Werstiuk, N. H. Comparison of Localization and Delocalization Indices Obtained with Hartree–Fock and Conventional Correlated Methods: Effect of Coulomb Correlation. *J. Comput. Chem.* **2003**, *24*, 1720–1729.
- (278) Löwdin, P.-O. Scaling Problem, Virial Theorem, and Connected Relations in Quantum Mechanics. *J. Mol. Spectrosc.* **1959**, *3*, 46–66.
- (279) Magnoli, D. E.; Murdoch, J. R. Obtaining Self–Consistent Wave Functions Which Satisfy the Virial Theorem. *Int. J. Quantum Chem.* **1982**, *22*, 1249–1262.
- (280) Diudea, M. V.; Gutman, I.; Lorentz, J. *Molecular Topology*; Nova Science Pub Inc.: Hauppauge, NY, 2001.
- (281) Janežić, D.; Milicević, A.; Nikolić, S.; Trinajstić, N. *Graph-Theoretical Matrices in Chemistry*, 1st ed.; CRC Press: Boca Raton, FL; London; New York, 2015.
- (282) Balaban, A. T. Applications of Graph Theory in Chemistry. *J. Chem. Inf. Comput. Sci.* **1985**, *25*, 334–343.
- (283) Balaban, A. T. *Chemical Applications of Graph Theory*; Academic Press Inc.: London; New York, 1976.
- (284) Randić, M. Design of Molecules with Desired Properties: A Molecular Similarity Approach to Property Optimization. In *Concepts and Applications of Molecular Similarity*; Johnson, M. A., Maggiora, G. M., Eds.; John Wiley & Sons: New York, 1990.
- (285) Randić, M. Aromaticity of Polycyclic Conjugated Hydrocarbons. *Chem. Rev.* **2003**, *103*, 3449–3606.
- (286) Bonchev, D. *Chemical Graph Theory: Introduction and Fundamentals*; Routledge: London, 2020.
- (287) Kier, L. B.; Hall, L. H. *Molecular Connectivity in Chemistry and Drug Research*; Elsevier Science: New York, 1976.
- (288) Dmitriev, I. S. *Molecules Without Chemical Bonds*; Mir Publishers: Moscow, 1981.
- (289) Balasubramanian, K. Integration of Graph Theory and Quantum Chemistry for Structure-Activity Relationships. *SAR QSAR Environ. Res.* **1994**, *2*, 59–77.
- (290) Bader, R. F. W. The Physical Basis of the Lewis Electron Pair Model. In *Molecules in Physics, Chemistry, and Biology: Electronic Structure and Chemical Reactivity*; Maruani, J., Ed.; Topics in Molecular Organization and Engineering; Springer Netherlands: Dordrecht, 1989; pp 73–92.
- (291) Matta, C. F.; Hernández-Trujillo, J.; Bader, R. F. W. Proton Spin–Spin Coupling and Electron Delocalization. *J. Phys. Chem. A* **2002**, *106*, 7369–7375.
- (292) Carbó, R.; Leyda, L.; Arnaud, M. How Similar Is a Molecule to Another? An Electron Density Measure of Similarity between Two Molecular Structures. *Int. J. Quantum Chem.* **1980**, *17*, 1185–1189.
- (293) Carbó-Dorca, R.; Mezey, P. G. *Advances in Molecular Similarity*, 1st ed.; JAI Press: Greenwich, CT, 1996; Vol. 1.
- (294) Carbó-Dorca, R.; Mezey, P. G. *Advances in Molecular Similarity*; JAI Press Inc.: Greenwich, CT, 1999; Vol. 2.
- (295) Constans, P.; Amat, L.; Carbó-Dorca, R. Toward a Global Maximization of the Molecular Similarity Function: Superposition of Two Molecules. *J. Comput. Chem.* **1997**, *18*, 826–846.
- (296) Carbó-Dorca, R. *Molecular Quantum Similarity in QSAR and Drug Design*, Softcover reprint of the original first edition, 2000 ed.; Springer: Berlin; New York, 2013.
- (297) Popelier, P. L. A. Quantum Molecular Similarity. 1. BCP Space. *J. Phys. Chem. A* **1999**, *103*, 2883–2890.
- (298) O'Brien, S. E.; Popelier, P. L. Quantum Molecular Similarity. Part 2: The Relation between Properties in BCP Space and Bond Length. *Can. J. Chem.* **1999**, *77*, 28–36.
- (299) O'Brien, S. E.; Popelier, P. L. A. Quantum Molecular Similarity. 3. QTMS Descriptors. *J. Chem. Inf. Comput. Sci.* **2001**, *41*, 764–775.
- (300) O'Brien, S. E.; Popelier, P. L. A. Quantum Topological Molecular Similarity. Part 4. A QSAR Study of Cell Growth Inhibitory Properties of Substituted (E)-1-Phenylbut-1-En-3-Ones. *J. Chem. Soc., Perkin Trans. 2* (3), 478–483.
- (301) Popelier, P. L. A.; Chaudry, U. A.; Smith, P. J. Quantum Topological Molecular Similarity. Part 5. Further Development with an Application to the Toxicity of Polychlorinated Dibenz-p-Dioxins(PCDDs). *J. Chem. Soc., Perkin Trans. 2* (7), 1231–1237.

- (302) Popelier, P. L. A. Developing Quantum Topological Molecular Similarity (QTMS). In *Quantum Biochemistry: Electronic Structure and Biological Activity* (Vol. 2); Matta, C. F., Ed.; Wiley-VCH: Weinheim, 2010; pp 667–691.
- (303) Lide, D. R. *CRC Handbook of Chemistry and Physics*, 88th ed. CRC Press: New York, 2007–2008.
- (304) Jover, J.; Bosque, R.; Sales, J. QSPR Prediction of pKa for Benzoic Acids in Different Solvents. *QSAR Comb. Sci.* **2008**, *27*, 563–581.
- (305) Pavia, D. L.; Lampman, G. M.; Kriz, G. S.; Vyvyan, J. R. *Introduction to Spectroscopy*; Brooks/Cole: Pacific Grove, CA, 2009.
- (306) Guo, H.-B.; He, F.; Gu, B.; Liang, L.; Smith, J. C. Time-Dependent Density Functional Theory Assessment of UV Absorption of Benzoic Acid Derivatives. *J. Phys. Chem. A* **2012**, *116*, 11870–11879.
- (307) Kamath, B. V.; Mehta, J. D.; Bafna, S. L. Ultraviolet Absorption Spectra: Some Substituted Benzoic Acids. *J. Appl. Chem. Biotechnol.* **1975**, *25*, 743–751.
- (308) Macchi, P. *Quantum Crystallography: Expectations vs Reality*; Springer: Cham, 2022.
- (309) Macchi, P. The Connubium between Crystallography and Quantum Mechanics. *Crystallogr. Rev.* **2020**, *26*, 209–268.
- (310) Genoni, A.; Martín Pendás, Á. Critical Assessment of the X-Ray Restrained Wave Function Approach: Advantages, Drawbacks, and Perspectives for Density Functional Theory and Periodic Ab Initio Calculations. *J. Chem. Phys.* **2024**, *160*, 234108.
- (311) Shteingolts, S. A.; Stash, A. I.; Tsirelson, V. G.; Fayzullin, R. R. Orbital-Free Quantum Crystallographic View on Noncovalent Bonding: Insights into Hydrogen Bonds,  $\Pi\cdots\pi$  and Reverse Electron Lone Pair $\cdots\pi$  Interactions. *Chem. – Eur. J.* **2021**, *27*, 7789–7809.
- (312) Bartashevich, E.; Stash, A.; Yushina, I.; Minyaev, M.; Bol'shakov, O.; Rakitin, O.; Tsirelson, V. Bonding Features in Appel's Salt from the Orbital-Free Quantum Crystallographic Perspective. *Acta Crystallogr. Sect. B Struct. Sci. Cryst. Eng. Mater.* **2021**, *77*, 478–487.
- (313) Gatti, C. Chemical Bonding in Crystals: New Directions. *Z. Für Krist. - Cryst. Mater.* **2005**, *220*, 399–457.
- (314) Bertini, L.; Cargnoni, F.; Gatti, C. Chemical Insight into Electron Density and Wave Functions: Software Developments and Applications to Crystals, Molecular Complexes and Materials Science. *Theor. Chem. Acc.* **2007**, *117*, 847–884.
- (315) Otero-de-la-Roza, A. Finding Critical Points and Reconstruction of Electron Densities on Grids. *J. Chem. Phys.* **2022**, *156*, 224116.
- (316) Menéndez Crespo, D.; Wagner, F. R.; Francisco, E.; Martín Pendás, Á.; Grin, Y.; Kohout, M. Interacting Quantum Atoms Method for Crystalline Solids. *J. Phys. Chem. A* **2021**, *125*, 9011–9025.
- (317) Tsirelson, V. G.; Zhou, P. F.; Tang, T.-H.; Bader, R. F. W. Topological Definition of Crystal Structure: Determination of the Bonded Interactions in Solid Molecular Chlorine. *Acta Crystallogr. A* **1995**, *51*, 143–153.
- (318) Tsirelson, V. G.; Stash, A. I.; Tokatly, I. V. Bonding in Molecular Crystals from the Local Electronic Pressure Viewpoint\*. *Mol. Phys.* **2016**, *114*, 1260–1269.
- (319) Bartashevich, E.; Sobalev, S.; Matveychuk, Y.; Tsirelson, V. Variations of Quantum Electronic Pressure under the External Compression in Crystals with Halogen Bonds Assembled in Cl<sub>3</sub>-, Br<sub>3</sub>-, I<sub>3</sub>-Synthons. *Acta Crystallogr. Sect. B Struct. Sci. Cryst. Eng. Mater.* **2020**, *76*, 514–523.
- (320) Matveychuk, Y. V.; Sobalev, S. A.; Borisova, P. I.; Bartashevich, E. V.; Tsirelson, V. G. Negative Linear Compressibility of Formate Crystals from the Viewpoint of Quantum Electronic Pressure. *Crystals* **2023**, *13*, 1147.
- (321) Matveychuk, Y. V.; Bartashevich, E. V.; Skalyova, K. K.; Tsirelson, V. G. Quantum Electronic Pressure and Crystal Compressibility for Magnesium Diboride under Simulated Compression. *Mater. Today Commun.* **2021**, *26*, No. 101952.
- (322) Khainovsky, M. A.; Boldyreva, E.; Tsirelson, V. Elastic and Piezoelectric Properties of  $\beta$ -Glycine – a Quantum Crystallography View on Intermolecular Interactions and a High-Pressure Phase Transition. *Acta Crystallogr. Sect. B Struct. Sci. Cryst. Eng. Mater.* **2024**, *80*, 51–63.
- (323) Tsirelson, V. G.; Stash, A. I.; Tokatly, I. V. Quantum Pressure Focusing in Solids: A Reconstruction from Experimental Electron Density. *Acta Crystallogr. Sect. B Struct. Sci. Cryst. Eng. Mater.* **2019**, *75*, 201–209.
- (324) Stash, A. I.; Terekhova, E. O.; Ivanov, S. A.; Tsirelson, V. G. X-Ray Diffraction Study of the Atomic Interactions, Anharmonic Displacements and Inner-Crystal Field in Orthorhombic KNbO<sub>3</sub>. *Acta Crystallogr. Sect. B Struct. Sci. Cryst. Eng. Mater.* **2021**, *77*, 728–739.
- (325) Martín Pendás, A.; Costales, A.; Luña, V. Ions in Crystals: The Topology of the Electron Density in Ionic Materials. I. Fundamentals. *Phys. Rev. B* **1997**, *55*, 4275–4284.
- (326) Martín Pendás, A.; Costales, A.; Luña, V. Ions in Crystals: The Topology of the Electron Density in Ionic Materials. III. Geometry and Ionic Radii. *J. Phys. Chem. B* **1998**, *102*, 6937–6948.
- (327) Blanco, M. A.; Costales, A.; Martín Pendás, A.; Luña, V. Ions in Crystals: The Topology of the Electron Density in Ionic Materials. V. The B1-B2 Phase Transition in Alkali Halides. *Phys. Rev. B* **2000**, *62*, 12028–12039.
- (328) Luña, V.; Costales, A.; Martín Pendás, A. Ions in Crystals: The Topology of the Electron Density in Ionic Materials.II. The Cubic Alkali Halide Perovskites. *Phys. Rev. B* **1997**, *55*, 4285–4297.
- (329) Martín Pendás, A.; Costales, A.; Blanco, M. A.; Recio, J. M.; Luña, V. Local Compressibilities in Crystals. *Phys. Rev. B* **2000**, *62*, 13970–13978.
- (330) Luña, V.; Costales, A.; Mori-Sánchez, P.; Blanco, M. A.; Martín Pendás, A. Topological Properties of the Electron Density of Solids and Molecules. Recent Developments in Oviedo. *Acta Crystallogr. A* **2004**, *60*, 434–437.
- (331) Mori-Sánchez, P.; Martín Pendás, A.; Luña, V. A Classification of Covalent, Ionic, and Metallic Solids Based on the Electron Density. *J. Am. Chem. Soc.* **2002**, *124*, 14721–14723.
- (332) Jenkins, S. Direct Space Representation of Metallicity and Structural Stability in SiO Solids. *J. Phys.: Condens. Matter* **2002**, *14*, 10251.
- (333) Lazab, M.; Djebour, B.; Bouafia, H.; Bousmaha, M.; Sahli, B.; Boudia, K. Mechanical and Dynamical Stability, Electronic and Bonding Properties of a New Narrow-Gap Semiconductor YPdAs Half-Heusler: DFT and QTAIM Study. *Mater. Sci. Semicond. Process.* **2024**, *173*, No. 108160.
- (334) Jones, T. E.; Eberhart, M. E. The Bond Bundle in Open Systems. *Int. J. Quantum Chem.* **2010**, *110*, 1500–1505.
- (335) Jones, T. E.; Eberhart, M. E.; Imlay, S.; Mackey, C.; Olson, G. B. Better Alloys with Quantum Design. *Phys. Rev. Lett.* **2012**, *109*, No. 125506.
- (336) Aakeröy, C. B.; Seddon, K. R. The Hydrogen Bond and Crystal Engineering. *Chem. Soc. Rev.* **1993**, *22*, 397–407.
- (337) Zaworotko, M. J. Molecules to Crystals, Crystals to Molecules... and Back Again? *Cryst. Growth Des.* **2007**, *7*, 4–9.
- (338) Desiraju, G. R. Supramolecular Synthons in Crystal Engineering—A New Organic Synthesis. *Angew. Chem., Int. Ed. Engl.* **1995**, *34*, 2311–2327.
- (339) Iqbal, I.; Mahmood, A.; Noureen, S.; Lecomte, C.; Ahmed, M. Crystal Engineering, Electron Density Analysis, and in Situ Variable Temperature Studies on Co-Crystal between Nicotinic Acid and Gallic Acid Sesquihydrate. *CrystEngComm* **2023**, *25*, 770–784.
- (340) Gatti, C.; May, E.; Destro, R.; Cargnoni, F. Fundamental Properties and Nature of CH $\cdots$ O Interactions in Crystals on the Basis of Experimental and Theoretical Charge Densities. The Case of 3,4-Bis(Dimethylamino)-3-Cyclobutene-1,2-Dione (DMACB) Crystal. *J. Phys. Chem. A* **2002**, *106*, 2707–2720.
- (341) May, E.; Destro, R.; Gatti, C. The Unexpected and Large Enhancement of the Dipole Moment in the 3,4-Bis(Dimethylamino)-3-Cyclobutene-1,2-Dione (DMACB) Molecule upon Crystallization: A New Role of the Intermolecular CH $\cdots$ O Interactions. *J. Am. Chem. Soc.* **2001**, *123*, 12248–12254.

- (342) Robinson, I. K. X-Ray Crystallography of Surfaces and Interfaces. *Acta Crystallogr. A* **1998**, *54*, 772–778.
- (343) Duke, C. B. Semiconductor Surface Reconstruction: The Structural Chemistry of Two-Dimensional Surface Compounds. *Chem. Rev.* **1996**, *96*, 1237–1260.
- (344) Srivastava, G. P. Theory of Semiconductor Surface Reconstruction. *Rep. Prog. Phys.* **1997**, *60*, S61.
- (345) Cargnoni, F.; Gatti, C.; May, E.; Narducci, D. Geometrical Reconstructions and Electronic Relaxations of Silicon Surfaces. I. An Electron Density Topological Study of H-Covered and Clean Si(111) ( $1 \times 1$ ) Surfaces. *J. Chem. Phys.* **2000**, *112*, 887–899.
- (346) Bartashevich, E. V.; Levina, E. O.; Yushina, I. D.; Sozykin, S. A.; Tsirelson, V. G. Electron Delocalization in Defect-Containing Graphene and Its Influence on Tetrel Bond Formation. *Phys. Chem. Chem. Phys.* **2023**, *25*, 24342–24354.
- (347) Jenkins, S.; Kirk, S. R. *Next Generation Quantum Theory of Atoms in Molecules: From Stereochemistry to Photochemistry and Molecular Devices*, 1st ed.; Springer: Singapore, 2023.
- (348) *Advances in Quantum Chemical Topology Beyond QTAIM*; Rodríguez, J. I., Cortés-Guzmán, F., Anderson, J. S. M., Eds.; Elsevier: Amsterdam, 2023.
- (349) Nakatsuji, H. Common Nature of the Electron Cloud of a System Undergoing Change in Nuclear Configuration. *J. Am. Chem. Soc.* **1974**, *96*, 24–30.
- (350) Bone, R. G. A.; Bader, R. F. W. Identifying and Analyzing Intermolecular Bonding Interactions in van Der Waals Molecules. *J. Phys. Chem.* **1996**, *100*, 10892–10911.
- (351) Jenkins, S.; Heggie, M. I. Quantitative Analysis of Bonding in 90° Partial Dislocation in Diamond. *J. Phys.: Condens. Matter* **2000**, *12*, 10325–10333.
- (352) Ayers, P. W.; Jenkins, S. An Electron-Preceding Perspective on the Deformation of Materials. *J. Chem. Phys.* **2009**, *130*, 154104.
- (353) Jenkins, S.; Kirk, S. R.; Cote, A. S.; Ross, D. K.; Morrison, I. Dependence of the Normal Modes on the Electronic Structure of Various Phases of Ice as Calculated by Ab Initio Methods. *Can. J. Phys.* **2003**, *81*, 225–231.
- (354) Jenkins, S.; Blancafort, L.; Kirk, S. R.; Bearpark, M. J. The Response of the Electronic Structure to Electronic Excitation and Double Bond Torsion in Fulvene: A Combined QTAIM, Stress Tensor and MO Perspective. *Phys. Chem. Chem. Phys.* **2014**, *16*, 7115–7126.
- (355) Jenkins, S.; Maza, J. R.; Xu, T.; Jiajun, D.; Kirk, S. R. Biphenyl: A Stress Tensor and Vector-Based Perspective Explored within the Quantum Theory of Atoms in Molecules. *Int. J. Quantum Chem.* **2015**, *115*, 1678–1690.
- (356) Momen, R.; Azizi, A.; Wang, L. L.; Ping, Y.; Xu, T.; Kirk, S. R.; Li, W.; Manzhos, S.; Jenkins, S. Exploration of the Forbidden Regions of the Ramachandran Plot ( $\phi$ - $\psi$ ) with QTAIM. *Phys. Chem. Chem. Phys.* **2017**, *19*, 26423–26434.
- (357) Momen, R.; Azizi, A.; Wang, L.; Yang, P.; Xu, T.; Kirk, S. R.; Li, W.; Manzhos, S.; Jenkins, S. The Role of Weak Interactions in Characterizing Peptide Folding Preferences Using a QTAIM Interpretation of the Ramachandran Plot ( $\phi$ - $\psi$ ). *Int. J. Quantum Chem.* **2018**, *118*, No. e25456.
- (358) Guo, H.; Morales-Bayuelo, A.; Xu, T.; Momen, R.; Wang, L.; Yang, P.; Kirk, S. R.; Jenkins, S. Distinguishing and Quantifying the Torquoselectivity in Competitive Ring-Opening Reactions Using the Stress Tensor and QTAIM. *J. Comput. Chem.* **2016**, *37*, 2722–2733.
- (359) Jiajun, D.; Maza, J. R.; Xu, Y.; Xu, T.; Momen, R.; Kirk, S. R.; Jenkins, S. A Stress Tensor and QTAIM Perspective on the Substituent Effects of Biphenyl Subjected to Torsion. *J. Comput. Chem.* **2016**, *37*, 2508–2517.
- (360) Hu, M. X.; Xu, T.; Momen, R.; Huan, G.; Kirk, S. R.; Jenkins, S.; Filatov, M. A QTAIM and Stress Tensor Investigation of the Torsion Path of a Light-Driven Fluorene Molecular Rotary Motor. *J. Comput. Chem.* **2016**, *37*, 2588–2596.
- (361) Maza, J. R.; Jenkins, S.; Kirk, S. R. 11-Cis Retinal Torsion: A QTAIM and Stress Tensor Analysis of the S1 Excited State. *Chem. Phys. Lett.* **2016**, *652*, 112–116.
- (362) Tachibana, A. Electronic Energy Density in Chemical Reaction Systems. *J. Chem. Phys.* **2001**, *115*, 3497–3518.
- (363) Tachibana, A. Spindle Structure of the Stress Tensor of Chemical Bond. *Int. J. Quantum Chem.* **2004**, *100*, 981–993.
- (364) Tachibana, A. A New Visualization Scheme of Chemical Energy Density and Bonds in Molecules. *J. Mol. Model.* **2005**, *11*, 301–311.
- (365) Szarek, P.; Tachibana, A. The Field Theoretical Study of Chemical Interaction in Terms of the Rigged QED: New Reactivity Indices. *J. Mol. Model.* **2007**, *13*, 651–663.
- (366) Szarek, P.; Sueda, Y.; Tachibana, A. Electronic Stress Tensor Description of Chemical Bonds Using Nonclassical Bond Order Concept. *J. Chem. Phys.* **2008**, *129*, No. 094102.
- (367) Bader, R. F. W.; Laidig, K. E. The Prediction and Calculation of Properties of Atoms in Molecules. *J. Mol. Struct. THEOCHEM* **1991**, *234*, 75–80.
- (368) Bader, R. F. W.; Tal, Y.; Anderson, S. G.; Nguyen-Dang, T. T. Quantum Topology: Theory of Molecular Structure and Its Change. *Isr. J. Chem.* **1980**, *19*, 8–29.
- (369) Tal, Y.; Bader, R. F. W.; Nguyen-Dang, T. T.; Ojha, M.; Anderson, S. G. Quantum Topology. IV. Relation between the Topological and Energetic Stabilities of Molecular Structures. *J. Chem. Phys.* **1981**, *74*, 5162–5167.
- (370) Bader, R. F. W.; Anderson, S. G.; Duke, A. J. Quantum Topology of Molecular Charge Distributions. I. *J. Am. Chem. Soc.* **1979**, *101*, 1389–1395.
- (371) Bader, R. F. W.; Nguyen-Dang, T. T.; Tal, Y. Quantum Topology of Molecular Charge Distributions. II. Molecular Structure and Its Change. *J. Chem. Phys.* **1979**, *70*, 4316–4329.
- (372) Huang, W. J.; Momen, R.; Azizi, A.; Xu, T.; Kirk, S. R.; Filatov, M.; Jenkins, S. Next-Generation Quantum Theory of Atoms in Molecules for the Ground and Excited States of Fulvene. *Int. J. Quantum Chem.* **2018**, *118*, No. e25768.
- (373) Huang, W. J.; Xu, T.; Kirk, S. R.; Filatov, M.; Jenkins, S. QTAIM and Stress Tensor Bond-Path Framework Sets for the Ground and Excited States of Fulvene. *Chem. Phys. Lett.* **2018**, *713*, 125–131.
- (374) Huang, W. J.; Xu, T.; Kirk, S. R.; Jenkins, S. The 3-D Bonding Morphology of the Infra-Red Active Normal Modes of Benzene. *Chem. Phys. Lett.* **2018**, *710*, 31–38.
- (375) Li, J. H.; Huang, W. J.; Xu, T.; Kirk, S. R.; Jenkins, S. Stress Tensor Eigenvector Following with Next-Generation Quantum Theory of Atoms in Molecules. *Int. J. Quantum Chem.* **2019**, *119*, No. e25847.
- (376) Bin, X.; Azizi, A.; Xu, T.; Kirk, S. R.; Filatov, M.; Jenkins, S. Next-Generation Quantum Theory of Atoms in Molecules for the Photochemical Ring-Opening Reactions of Oxirane. *Int. J. Quantum Chem.* **2019**, *119*, No. e25957.
- (377) Bin, X.; Momen, R.; Xu, T.; Kirk, S. R.; Filatov, M.; Jenkins, S. A 3-D Bonding Perspective of the Factors Influencing the Relative Stability of the S1/S0 Conical Intersections of the Penta-2,4-Dieniminium Cation (PSB3). *Int. J. Quantum Chem.* **2019**, *119*, No. e25903.
- (378) Bin, X.; Xu, T.; Kirk, S. R.; Jenkins, S. The Directional Bonding of [1.1.1]Propellane with next Generation QTAIM. *Chem. Phys. Lett.* **2019**, *730*, 506–512.
- (379) Tian, T.; Xu, T.; Kirk, S. R.; Filatov, M.; Jenkins, S. Next-Generation Quantum Theory of Atoms in Molecules for the Ground and Excited State of DHCL. *Chem. Phys. Lett.* **2019**, *717*, 91–98.
- (380) Tian, T.; Xu, T.; Kirk, S. R.; Filatov, M.; Jenkins, S. Next-Generation Quantum Theory of Atoms in Molecules for the Ground and Excited State of the Ring-Opening of Cyclohexadiene (CHD). *Int. J. Quantum Chem.* **2019**, *119*, No. e25862.
- (381) Wang, L.; Azizi, A.; Xu, T.; Kirk, S. R.; Jenkins, S. Explanation of the Role of Hydrogen Bonding in the Structural Preferences of Small Molecule Conformers. *Chem. Phys. Lett.* **2019**, *730*, 206–212.
- (382) Malcolmson, T.; Azizi, A.; Momen, R.; Xu, T.; Kirk, S. R.; Paterson, M. J.; Jenkins, S. Stress Tensor Eigenvector Following with Next-Generation Quantum Theory of Atoms in Molecules: Excited

- State Photochemical Reaction Path from Benzene to Benzvalene. *J. Phys. Chem. A* **2019**, *123*, 8254–8264.
- (383) Li, S.; Xu, T.; van Mourik, T.; Frücht, H.; Kirk, S. R.; Jenkins, S. Halogen and Hydrogen Bonding in Halogenabenzene/NH<sub>3</sub> Complexes Compared Using Next-Generation QTAIM. *Molecules* **2019**, *24*, 2875.
- (384) Azizi, A.; Momen, R.; Kirk, S. R.; Jenkins, S. 3-D Bond-Paths of QTAIM and the Stress Tensor in Neutral Lithium Clusters, Lim ( $m = 2\text{--}5$ ), Presented on the Ehrenfest Force Molecular Graph. *Phys. Chem. Chem. Phys.* **2020**, *22*, 864–877.
- (385) Li, S.; Azizi, A.; Kirk, S. R.; Jenkins, S. An Explanation of the Unusual Strength of the hydrogen bond in Small Water Clusters. *Int. J. Quantum Chem.* **2020**, *120*, No. e26361.
- (386) Azizi, A.; Momen, R.; Frücht, H.; van Mourik, T.; Kirk, S. R.; Jenkins, S. Next-Generation QTAIM for Scoring Molecular Wires in E-Fields for Molecular Electronic Devices. *J. Comput. Chem.* **2020**, *41*, 913–921.
- (387) Xu, T.; Momen, R.; Azizi, A.; van Mourik, T.; Frücht, H.; Kirk, S. R.; Jenkins, S. The Destabilization of Hydrogen Bonds in an External E-Field for Improved Switch Performance. *J. Comput. Chem.* **2019**, *40*, 1881–1891.
- (388) Tian, T.; Xu, T.; van Mourik, T.; Frücht, H.; Kirk, S. R.; Jenkins, S. Next Generation QTAIM for the Design of Quinone-Based Switches. *Chem. Phys. Lett.* **2019**, *722*, 110–118.
- (389) Bader, R. F. W.; Nguyen-Dang, T. T. Quantum Theory of Atoms in Molecules—Dalton Revisited. In *Advances in Quantum Chemistry*; Löwdin, P.-O., Ed.; Advances in Quantum Chemistry; Academic Press: New York, 1981; Vol. 14, pp 63–124.
- (390) Bader, R. F. W. Quantum Topology of Molecular Charge Distributions. III. The Mechanics of an Atom in a Molecule. *J. Chem. Phys.* **1980**, *73*, 2871–2883.
- (391) Guevara-García, A.; Echegaray, E.; Toro-Labbe, A.; Jenkins, S.; Kirk, S. R.; Ayers, P. W. Pointing the Way to the Products? Comparison of the Stress Tensor and the Second-Derivative Tensor of the Electron Density. *J. Chem. Phys.* **2011**, *134*, 234106–234114.
- (392) Jenkins, S.; Kirk, S. R.; Guevara-García, A.; Ayers, P. W.; Echegaray, E.; Toro-Labbe, A. Electronic Stress as a Guiding Force for Chemical Bonding. In *Electronic Effects in Organic Chemistry*; Kirchner, R., Ed.; Topics in Current Chemistry; Springer Berlin Heidelberg: Berlin, 2011; pp 103–124.
- (393) Mahara, B.; Azizi, A.; Yang, Y.; Filatov, M.; Kirk, S. R.; Jenkins, S. Bond-Path-Rigidity and Bond-Path-Flexibility of the Ground State and First Excited State of Fulvene. *Chem. Phys. Lett.* **2021**, *766*, No. 138339.
- (394) Wang, L.; Azizi, A.; Xu, T.; Filatov, M.; Kirk, S. R.; Paterson, M. J.; Jenkins, S. The Role of the Natural Transition Orbital Density in the S0 → S1 and S0 → S2 Transitions of Fulvene with Next Generation QTAIM. *Chem. Phys. Lett.* **2020**, *751*, No. 137556.
- (395) Wang, L.; Azizi, A.; Momen, R.; Xu, T.; Kirk, S. R.; Filatov, M.; Jenkins, S. Next-Generation Quantum Theory of Atoms in Molecules for the S1/S0 Conical Intersections in Dynamics Trajectories of a Light-Driven Rotary Molecular Motor. *Int. J. Quantum Chem.* **2020**, *120*, No. e26062.
- (396) Yang, P.; Xu, T.; Momen, R.; Azizi, A.; Kirk, S. R.; Jenkins, S. Fatigue and Photochromism S1 Excited State Reactivity of Diarylethenes from QTAIM and the Stress Tensor. *Int. J. Quantum Chem.* **2018**, *118*, No. e25565.
- (397) Filatov, M.; Martínez, T. J.; Kim, K. S. Description of Ground and Excited Electronic States by Ensemble Density Functional Method with Extended Active Space. *J. Chem. Phys.* **2017**, *147*, No. 064104.
- (398) Mitra, S.; Chandra, A.; Gashnga, P.; Jenkins, S.; Kirk, S. Exploring Hydrogen Bond in the Excited State Leading toward Intramolecular Proton Transfer: Detailed Analysis of the Structure and Charge Density Topology along the Reaction Path Using QTAIM. *J. Mol. Model.* **2012**, *18*, 4225–4237.
- (399) Li, Z.; Yang, Y.; Xu, T.; Frücht, H.; van Mourik, T.; Paterson, M. J.; Shigeta, Y.; Kirk, S. R.; Jenkins, S. Next Generation QTAIM for the Design of Emitters Exhibiting Thermally-Activated Delayed Fluorescence (TADF) with Laser Irradiation. *J. Comput. Chem.* **2022**, *43*, 206–214.
- (400) Yang, Y.; Xu, T.; Kirk, S. R.; Jenkins, S. Bond Flexing, Twisting, Anharmonicity and Responsivity for the Infrared-Active Modes of Benzene. *Int. J. Quantum Chem.* **2021**, *121*, No. e26584.
- (401) Xing, H.; Yang, Y.; Nie, X.; Xu, T.; Kirk, S. R.; Jenkins, S. Understanding Chemical Coupling in Cyclic versus Compact Water Clusters with the Ehrenfest Force. *Chem. Phys. Lett.* **2021**, *781*, No. 138983.
- (402) *Effects of Electric Fields on Structure and Reactivity: New Horizons in Chemistry*, 1st ed.; Shaik, S., Stuyver, T., Eds.; Royal Society of Chemistry: Cambridge, 2021.
- (403) Kusalik, P. G.; Gracheva, M. E.; Shaik, S.; English, N. J. New Perspectives on Molecular Simulation of Chemistry and Physics in External Electric Fields. *Phys. Chem. Chem. Phys.* **2022**, *24*, 28660–28661.
- (404) Shaik, S.; Ramanan, R.; Danovich, D.; Mandal, D. Structure and Reactivity/Selectivity Control by Oriented-External Electric Fields. *Chem. Soc. Rev.* **2018**, *47*, 5125–5145.
- (405) Shaik, S.; Mandal, D.; Ramanan, R. Oriented Electric Fields as Future Smart Reagents in Chemistry. *Nat. Chem.* **2016**, *8*, 1091–1098.
- (406) Sowlati-Hashjin, S.; Matta, C. F. The Chemical Bond in External Electric Fields: Energies, Geometries, and Vibrational Stark Shifts of Diatomic Molecules. *J. Chem. Phys.* **2013**, *139*, 144101.
- (407) Huang, W. J.; Azizi, A.; Xu, T.; Kirk, S. R.; Jenkins, S. A Vector-Based Representation of the Chemical Bond for the Normal Modes of Benzene. *Int. J. Quantum Chem.* **2018**, *118*, No. e25698.
- (408) Xu, T.; Wang, L.; Ping, Y.; van Mourik, T.; Frücht, H.; Kirk, S. R.; Jenkins, S. Quinone-Based Switches for Candidate Building Blocks of Molecular Junctions with QTAIM and the Stress Tensor. *Int. J. Quantum Chem.* **2018**, *118*, No. e25676.
- (409) Maza, J. R.; Jenkins, S.; Kirk, S. R.; Anderson, J. S. M.; Ayers, P. W. The Ehrenfest Force Topology: A Physically Intuitive Approach for Analyzing Chemical Interactions. *Phys. Chem. Chem. Phys.* **2013**, *15*, 17823–17836.
- (410) Jenkins, S.; Morrison, I. The Chemical Character of the Intermolecular Bonds of Seven Phases of Ice as Revealed by Ab Initio Calculation of Electron Densities. *Chem. Phys. Lett.* **2000**, *317*, 97–102.
- (411) Isaacs, E. D.; Shukla, A.; Platzman, P. M.; Hamann, D. R.; Barbiellini, B.; Tulk, C. A. Covacency of the Hydrogen Bond in Ice: A Direct X-Ray Measurement. *Phys. Rev. Lett.* **1999**, *82*, 600–603.
- (412) Miliordos, E.; Xantheas, S. S. An Accurate and Efficient Computational Protocol for Obtaining the Complete Basis Set Limits of the Binding Energies of Water Clusters at the MP2 and CCSD(T) Levels of Theory: Application to (H<sub>2</sub>O)<sub>m</sub>, m = 2–6, 8, 11, 16, and 17. *J. Chem. Phys.* **2015**, *142*, 234303.
- (413) Tian, T.; Xu, T.; Kirk, S. R.; Rongde, I. T.; Tan, Y. B.; Manzhos, S.; Shigeta, Y.; Jenkins, S. Intramolecular Mode Coupling of the Isotopomers of Water: A Non-Scalar Charge Density-Derived Perspective. *Phys. Chem. Chem. Phys.* **2020**, *22*, 2509–2520.
- (414) Xing, H.; Azizi, A.; Momen, R.; Xu, T.; Kirk, S. R.; Jenkins, S. Chirality–Helicity of Cumulenes: A Non-Scalar Charge Density Derived Perspective. *Int. J. Quantum Chem.* **2022**, *122*, No. e26884.
- (415) Nie, X.; Filatov, M.; Kirk, S. R.; Jenkins, S. Photochemical Ring-Opening Reactions of Oxirane with the Ehrenfest Force Topology. *Chem. Phys. Lett.* **2021**, *769*, No. 138432.
- (416) Xu, T.; Bin, X.; Kirk, S. R.; Wales, D. J.; Jenkins, S. Flip Rearrangement in the Water Pentamer: Analysis of Electronic Structure. *Int. J. Quantum Chem.* **2020**, *120*, No. e26124.
- (417) Xu, T.; Farrell, J.; Momen, R.; Azizi, A.; Kirk, S. R.; Jenkins, S.; Wales, D. J. A Stress Tensor Eigenvector Projection Space for the (H<sub>2</sub>O)<sub>5</sub> Potential Energy Surface. *Chem. Phys. Lett.* **2017**, *667*, 25–31.
- (418) Hu, M. X.; Xu, T.; Momen, R.; Azizi, A.; Kirk, S. R.; Jenkins, S. The Normal Modes of Vibration of Benzene from the Trajectories of Stress Tensor Eigenvector Projection Space. *Chem. Phys. Lett.* **2017**, *677*, 156–161.

- (419) Azizi, A.; Momen, R.; Morales-Bayuelo, A.; Xu, T.; Kirk, S. R.; Jenkins, S. A Vector-Based Representation of the Chemical Bond for Predicting Competitive and Noncompetitive Torquoselectivity of Thermal Ring-Opening Reactions. *Int. J. Quantum Chem.* **2018**, *118*, No. e25707.
- (420) van Delden, R. A.; ter Wiel, M. K. J.; Feringa, B. L. A Chiroptical Molecular Switch with Perfect Stereocontrol. *Chem. Commun.* **2004**, No. 2, 200–201.
- (421) Nikiforov, A.; Gamez, J. A.; Thiel, W.; Filatov, M. Computational Design of a Family of Light-Driven Rotary Molecular Motors with Improved Quantum Efficiency. *J. Phys. Chem. Lett.* **2016**, *7*, 105–110.
- (422) Wang, L.; Huan, G.; Momen, R.; Azizi, A.; Xu, T.; Kirk, S. R.; Filatov, M.; Jenkins, S. QTAIM and Stress Tensor Characterization of Intramolecular Interactions Along Dynamics Trajectories of a Light-Driven Rotary Molecular Motor. *J. Phys. Chem. A* **2017**, *121*, 4778–4792.
- (423) Woodward, R. B.; Hoffmann, R. The Conservation of Orbital Symmetry. *Angew. Chem., Int. Ed. Engl.* **1969**, *8*, 781–853.
- (424) Fukui, K. The Role of Frontier Orbitals in Chemical Reactions (Nobel Lecture). *Angew. Chem., Int. Ed. Engl.* **1982**, *21*, 801–809.
- (425) Walker, M. J.; Hietbrink, B. N.; Thomas, B. E.; Nakamura, K.; Kallel, E. A.; Houk, K. N. Torquoselectivity Induced by Lone-Pair Conjugation in the Electrocyclic Reactions of 1-Azapolyenes. *J. Org. Chem.* **2001**, *66*, 6669–6672.
- (426) Cahn, R. S.; Ingold, C.; Prelog, V. Specification of Molecular Chirality. *Angew. Chem., Int. Ed. Engl.* **1966**, *5*, 385–415.
- (427) Prelog, V.; Helmchen, G. Basic Principles of the CIP-System and Proposals for a Revision. *Angew. Chem., Int. Ed. Engl.* **1982**, *21*, 567–583.
- (428) Hanson, R. M.; Musacchio, S.; Mayfield, J. W.; Vainio, M. J.; Yerin, A.; Redkin, D. Algorithmic Analysis of Cahn–Ingold–Prelog Rules of Stereochemistry: Proposals for Revised Rules and a Guide for Machine Implementation. *J. Chem. Inf. Model.* **2018**, *58*, 1755–1765.
- (429) Flack, H. Louis Pasteur's Discovery of Molecular Chirality and Spontaneous Resolution in 1848, Together with a Complete Review of His Crystallographic and Chemical Work. *Acta Crystallogr., Sect. A* **2009**, *65*, 371–389.
- (430) Fresnel, A. Mémoire Sur La Double Réfraction. *Mém. Académie Sci. Inst. Fr.* **1821**, *7*, 45–176.
- (431) Brewster, J. H. On the Helicity of Variously Twisted Chains of Atoms. *Stereochemistry I; Topics in Current Chemistry Fortschritte der Chemischen Forschung*; Springer Berlin Heidelberg: Berlin, Heidelberg, 1974; Vol. 47, pp 29–71.
- (432) Rosenfeld, L. Quantenmechanische Theorie der natürlichen optischen Aktivität von Flüssigkeiten und Gasen. *Z. Für Phys.* **1929**, *52*, 161–174.
- (433) Caldwell, D. J.; Eyring, H.; Chang, T. Y. The Theory of Optical Activity. *Phys. Today* **1972**, *25*, 53.
- (434) Tinoco, I.; Woody, R. W. Optical Rotation of Oriented Helices. IV. A Free Electron on a Helix. *J. Chem. Phys.* **1964**, *40*, 160–165.
- (435) Zhigang Wang, D. A Helix Theory for Molecular Chirality and Chiral Interaction. *Mendeleev Commun.* **2004**, *14*, 244–247.
- (436) Beaulieu, S.; Comby, A.; Descamps, D.; Fabre, B.; Garcia, G. A.; Géneaux, R.; Harvey, A. G.; Légaré, F.; Mašín, Z.; Nahon, L.; et al. Photoexcitation Circular Dichroism in Chiral Molecules. *Nat. Phys.* **2018**, *14*, 484–489.
- (437) Banerjee-Ghosh, K.; Ben Dor, O.; Tassinari, F.; Capua, E.; Yochelis, S.; Capua, A.; Yang, S.-H.; Parkin, S. S. P.; Sarkar, S.; Kronik, L.; et al. Separation of Enantiomers by Their Enantiospecific Interaction with Achiral Magnetic Substrates. *Science* **2018**, *360*, 1331–1334.
- (438) Harper, K. C.; Sigman, M. S. Three-Dimensional Correlation of Steric and Electronic Free Energy Relationships Guides Asymmetric Propargylation. *Science* **2011**, *333*, 1875–1878.
- (439) Garner, M. H.; Corminboeuf, C. Helical Electronic Transitions of Spiroconjugated Molecules. *Chem. Commun.* **2021**, *57*, 6408–6411.
- (440) Kondepudi, D. K.; Asakura, K. Chiral Autocatalysis, Spontaneous Symmetry Breaking, and Stochastic Behavior. *Acc. Chem. Res.* **2001**, *34*, 946–954.
- (441) Bickelhaupt, F. M.; Baerends, E. J. The Case for Steric Repulsion Causing the Staggered Conformation of Ethane. *Angew. Chem.* **2003**, *115*, 4315–4320.
- (442) Poplristic, V.; Goodman, L. Hyperconjugation Not Steric Repulsion Leads to the Staggered Structure of Ethane. *Nature* **2001**, *411*, 565–568.
- (443) Peng, M.; Dong, C.; Gao, R.; Xiao, D.; Liu, H.; Ma, D. Fully Exposed Cluster Catalyst (FECC): Toward Rich Surface Sites and Full Atom Utilization Efficiency. *ACS Cent. Sci.* **2021**, *7*, 262–273.
- (444) Chen, H.; Zou, X. Intermetallic Borides: Structures, Synthesis and Applications in Electrocatalysis. *Inorg. Chem. Front.* **2020**, *7*, 2248–2264.
- (445) Jakub, Z.; Hulva, J.; Meier, M.; Bliem, R.; Kraushofer, F.; Setvin, M.; Schmid, M.; Diebold, U.; Franchini, C.; Parkinson, G. S. Local Structure and Coordination Define Adsorption in a Model  $\text{Ir}_1/\text{Fe}_3\text{O}_4$  Single-Atom Catalyst. *Angew. Chem., Int. Ed.* **2019**, *58*, 13961–13968.
- (446) Huo, S.; Lu, J.; Wang, X. Recent Progress in Electrochemical Reduction of Carbon Dioxide on Metal Single-Atom Catalysts. *Energy Sci. Eng.* **2022**, *10*, 1584–1600.
- (447) Ladha, D. G. A Review on Density Functional Theory-Based Study on Two-Dimensional Materials Used in Batteries. *Mater. Today Chem.* **2019**, *11*, 94–111.
- (448) Liu, J.; Kan, W. H.; Ling, C. D. Insights into the High Voltage Layered Oxide Cathode Materials in Sodium-Ion Batteries: Structural Evolution and Anion Redox. *J. Power Sources* **2021**, *481*, No. 229139.
- (449) Maleki Kheimeh Sari, H.; Li, X. Controllable Cathode–Electrolyte Interface of  $\text{Li}[\text{Ni}_{0.8}\text{Co}_{0.1}\text{Mn}_{0.1}] \text{O}_2$  for Lithium Ion Batteries: A Review. *Adv. Energy Mater.* **2019**, *9*, No. 1901597.
- (450) Wang, Z.; Feng, X.; Bai, Y.; Yang, H.; Dong, R.; Wang, X.; Xu, H.; Wang, Q.; Li, H.; Gao, H.; et al. Probing the Energy Storage Mechanism of Quasi-Metallic Na in Hard Carbon for Sodium-Ion Batteries. *Adv. Energy Mater.* **2021**, *11*, No. 2003854.
- (451) Koga, H.; Croguennec, L.; Ménétrier, M.; Mannessiez, P.; Weill, F.; Delmas, C. Different Oxygen Redox Participation for Bulk and Surface: A Possible Global Explanation for the Cycling Mechanism of  $\text{Li}_{1.20}\text{Mn}_{0.54}\text{Co}_{0.13}\text{Ni}_{0.13}\text{O}_2$ . *J. Power Sources* **2013**, *236*, 250–258.
- (452) Koga, H.; Croguennec, L.; Ménétrier, M.; Douhil, K.; Belin, S.; Bourgeois, L.; Suard, E.; Weill, F.; Delmas, C. Reversible Oxygen Participation to the Redox Processes Revealed for  $\text{Li}_{1.20}\text{Mn}_{0.54}\text{Co}_{0.13}\text{Ni}_{0.13}\text{O}_2$ . *J. Electrochem. Soc.* **2013**, *160*, A786.
- (453) Zhu, Y.; Gao, T.; Fan, X.; Han, F.; Wang, C. Electrochemical Techniques for Intercalation Electrode Materials in Rechargeable Batteries. *Acc. Chem. Res.* **2017**, *50*, 1022–1031.
- (454) Goodenough, J. B.; Kim, Y. Challenges for Rechargeable Li Batteries. *Chem. Mater.* **2010**, *22*, 587–603.
- (455) Lyu, Y.; Wu, X.; Wang, K.; Feng, Z.; Cheng, T.; Liu, Y.; Wang, M.; Chen, R.; Xu, L.; Zhou, J.; et al. An Overview on the Advances of  $\text{LiCoO}_2$  Cathodes for Lithium-Ion Batteries. *Adv. Energy Mater.* **2021**, *11*, No. 2000982.
- (456) Pauling, L. The Principles Determining the Structure of Complex Ionic Crystals. *J. Am. Chem. Soc.* **1929**, *51*, 1010–1026.
- (457) Lee, G.-H.; Wu, J.; Kim, D.; Cho, K.; Cho, M.; Yang, W.; Kang, Y.-M. Reversible Anionic Redox Activities in Conventional  $\text{LiNi}_{1/3}\text{Co}_{1/3}\text{Mn}_{1/3}\text{O}_2$  Cathodes. *Angew. Chem., Int. Ed.* **2020**, *59*, 8681–8688.
- (458) Li, N.; Sallis, S.; Papp, J. K.; Wei, J.; McCloskey, B. D.; Yang, W.; Tong, W. Unraveling the Cationic and Anionic Redox Reactions in a Conventional Layered Oxide Cathode. *ACS Energy Lett.* **2019**, *4*, 2836–2842.
- (459) Ohzuku, T.; Ueda, A.; Nagayama, M. Electrochemistry and Structural Chemistry of  $\text{LiNiO}_2$  (R3m) for 4 V Secondary Lithium Cells. *J. Electrochem. Soc.* **1993**, *140*, 1862.
- (460) Yoon, W.-S.; Chung, K. Y.; McBreen, J.; Fischer, D. A.; Yang, X.-Q. Changes in Electronic Structure of the Electrochemically Li-Ion

- Deintercalated LiNiO<sub>2</sub> System Investigated by Soft X-Ray Absorption Spectroscopy. *J. Power Sources* **2006**, *163*, 234–237.
- (461) Zhang, Y.; Wu, M.; Ma, J.; Wei, G.; Ling, Y.; Zhang, R.; Huang, Y. Revisiting the Na<sub>2/3</sub>Ni<sub>1/3</sub>Mn<sub>2/3</sub>O<sub>2</sub> Cathode: Oxygen Redox Chemistry and Oxygen Release Suppression. *ACS Cent. Sci.* **2020**, *6*, 232–240.
- (462) Lu, Z.; Dahn, J. R. Understanding the Anomalous Capacity of Li/Li[Ni<sub>x</sub>Li<sub>(1/3-2x/3)</sub>Mn<sub>(2/3-x/3)</sub>]O<sub>2</sub> Cells Using In Situ X-Ray Diffraction and Electrochemical Studies. *J. Electrochem. Soc.* **2002**, *149*, A815.
- (463) Zhao, T.; Chen, S.; Li, L.; Zhang, X.; Chen, R.; Belharouak, I.; Wu, F.; Amine, K. Synthesis, Characterization, and Electrochemistry of Cathode Material Li[Li<sub>0.2</sub>Co<sub>0.13</sub>Ni<sub>0.13</sub>Mn<sub>0.54</sub>]O<sub>2</sub> Using Organic Chelating Agents for Lithium-Ion Batteries. *J. Power Sources* **2013**, *228*, 206–213.
- (464) Lim, J.-H.; Bang, H.; Lee, K.-S.; Amine, K.; Sun, Y.-K. Electrochemical Characterization of Li<sub>2</sub>MnO<sub>3</sub>–Li[Ni<sub>1/3</sub>Co<sub>1/3</sub>Mn<sub>1/3</sub>]O<sub>2</sub>–LiNiO<sub>2</sub> Cathode Synthesized via Co-Precipitation for Lithium Secondary Batteries. *J. Power Sources* **2009**, *189*, 571–575.
- (465) Zhou, F.; Zhao, X.; van Bommel, A.; Xia, X.; Dahn, J. R. Comparison of Li[Li<sub>1/2</sub>Ni<sub>1/3</sub>Mn<sub>5/9</sub>]O<sub>2</sub>, Li[Li<sub>1/5</sub>Ni<sub>1/5</sub>Mn<sub>3/5</sub>]O<sub>2</sub>, Li-Ni<sub>0.5</sub>Mn<sub>1.5</sub>O<sub>4</sub>, and LiNi<sub>2/3</sub>Mn<sub>1/3</sub>O<sub>2</sub> as High Voltage Positive Electrode Materials. *J. Electrochem. Soc.* **2011**, *158*, A187.
- (466) Barkhouse, D. A. R.; Dahn, J. R. A Novel Fabrication Technique for Producing Dense Li[Ni<sub>x</sub>Li<sub>(1/3-2x/3)</sub>Mn<sub>(2/3-x/3)</sub>]O<sub>2</sub>, 0 < x ≤ 1/2. *J. Electrochem. Soc.* **2005**, *152*, A746.
- (467) Kang, S.-H.; Johnson, C. S.; Vaughney, J. T.; Amine, K.; Thackeray, M. M. The Effects of Acid Treatment on the Electrochemical Properties of 0.5 Li<sub>2</sub>MnO<sub>3</sub> + 0.5 Li-Ni<sub>0.44</sub>Co<sub>0.25</sub>Mn<sub>0.31</sub>O<sub>2</sub> Electrodes in Lithium Cells. *J. Electrochem. Soc.* **2006**, *153*, A1186.
- (468) Kang, S.-H.; Sun, Y. K.; Amine, K. Electrochemical and Ex Situ X-Ray Study of Li(Li<sub>0.2</sub>Ni<sub>0.2</sub>Mn<sub>0.6</sub>)O<sub>2</sub> Cathode Material for Li Secondary Batteries. *Electrochim. Solid-State Lett.* **2003**, *6*, A183.
- (469) Chen, Z.; Sun, Y.-K.; Amine, K. Electrochemical Properties of Lithium-Rich Li<sub>1+x</sub>(Mn<sub>1/3</sub>Ni<sub>1/3</sub>Co<sub>1/3</sub>)<sub>1-x</sub>O<sub>2</sub> at High Potential. *J. Electrochem. Soc.* **2006**, *153*, A1818.
- (470) Sun, Y.-K.; Kim, M. G.; Kang, S.-H.; Amine, K. Electrochemical Performance of Layered Li[Li<sub>0.15</sub>Ni<sub>0.275</sub>–MgMn<sub>0.575</sub>]O<sub>2</sub> Cathode Materials for Lithium Secondary Batteries. *J. Mater. Chem.* **2003**, *13*, 319–322.
- (471) Dai, K.; Wu, J.; Zhuo, Z.; Li, Q.; Sallis, S.; Mao, J.; Ai, G.; Sun, C.; Li, Z.; Gent, W. E.; et al. High Reversibility of Lattice Oxygen Redox Quantified by Direct Bulk Probes of Both Anionic and Cationic Redox Reactions. *Joule* **2019**, *3*, 518–541.
- (472) House, R. A.; Maitra, U.; Jin, L.; Lozano, J. G.; Somerville, J. W.; Rees, N. H.; Naylor, A. J.; Duda, L. C.; Massel, F.; Chadwick, A. V.; et al. What Triggers Oxygen Loss in Oxygen Redox Cathode Materials? *Chem. Mater.* **2019**, *31*, 3293–3300.
- (473) Maitra, U.; House, R. A.; Somerville, J. W.; Tapia-Ruiz, N.; Lozano, J. G.; Guerrini, N.; Hao, R.; Luo, K.; Jin, L.; Pérez-Osorio, M. A.; et al. Oxygen Redox Chemistry without Excess Alkali-Metal Ions in Na<sub>2/3</sub>[Mg<sub>0.28</sub>Mn<sub>0.72</sub>]O<sub>2</sub>. *Nat. Chem.* **2018**, *10*, 288–295.
- (474) Wu, J.; Zhuo, Z.; Rong, X.; Dai, K.; Lebens-Higgins, Z.; Sallis, S.; Pan, F.; Piper, L. F. J.; Liu, G.; Chuang, Y. Dissociate Lattice Oxygen Redox Reactions from Capacity and Voltage Drops of Battery Electrodes. *Sci. Adv.* **2020**, *6*, No. eaaw3871.
- (475) Chen, R.; Ren, S.; Knapp, M.; Wang, D.; Witter, R.; Fichtner, M.; Hahn, H. Disordered Lithium-Rich Oxyfluoride as a Stable Host for Enhanced Li<sup>+</sup> Intercalation Storage. *Adv. Energy Mater.* **2015**, *5*, No. 1401814.
- (476) Clément, R. J.; Lun, Z.; Ceder, G. Cation-Disordered Rocksalt Transition Metal Oxides and Oxyfluorides for High Energy Lithium-Ion Cathodes. *Energy Environ. Sci.* **2020**, *13*, 345–373.
- (477) Freire, M.; Kosova, N. V.; Jordy, C.; Chateigner, D.; Lebedev, O. I.; Maignan, A.; Pralong, V. A New Active Li–Mn–O Compound for High Energy Density Li-Ion Batteries. *Nat. Mater.* **2016**, *15*, 173–177.
- (478) Lee, J.; Kitchev, D. A.; Kwon, D.-H.; Lee, C.-W.; Papp, J. K.; Liu, Y.-S.; Lun, Z.; Clément, R. J.; Shi, T.; McCloskey, B. D.; et al. Reversible Mn<sup>2+</sup>/Mn<sup>4+</sup> Double Redox in Lithium-Excess Cathode Materials. *Nature* **2018**, *556*, 185–190.
- (479) Li, X.; Qiao, Y.; Guo, S.; Jiang, K.; Ishida, M.; Zhou, H. A New Type of Li-Rich Rock-Salt Oxide Li<sub>2</sub>Ni<sub>1/3</sub>Ru<sub>2/3</sub>O<sub>3</sub> with Reversible Anionic Redox Chemistry. *Adv. Mater.* **2019**, *31*, No. 1807825.
- (480) Lun, Z.; Ouyang, B.; Kitchev, D. A.; Clément, R. J.; Papp, J. K.; Balasubramanian, M.; Tian, Y.; Lei, T.; Shi, T.; McCloskey, B. D.; et al. Improved Cycling Performance of Li-Excess Cation-Disordered Cathode Materials upon Fluorine Substitution. *Adv. Energy Mater.* **2019**, *9*, No. 1802959.
- (481) Yabuuchi, N.; Takeuchi, M.; Nakayama, M.; Shiiba, H.; Ogawa, M.; Nakayama, K.; Ohta, T.; Endo, D.; Ozaki, T.; Inamasu, T.; et al. High-Capacity Electrode Materials for Rechargeable Lithium Batteries: Li<sub>3</sub>NbO<sub>4</sub>-Based System with Cation-Disordered Rocksalt Structure. *Proc. Natl. Acad. Sci. U. S. A.* **2015**, *112*, 7650–7655.
- (482) Rahman, M. M.; Lin, F. Oxygen Redox Chemistry in Rechargeable Li-Ion and Na-Ion Batteries. *Matter* **2021**, *4*, 490–527.
- (483) Zhang, M.; Kitchev, D. A.; Levens-Higgins, Z.; Vinckeviciute, J.; Zuba, M.; Reeves, P. J.; Grey, C. P.; Whittingham, M. S.; Piper, L. F. J.; Van der Ven, A.; et al. Pushing the Limit of 3d Transition Metal-Based Layered Oxides That Use Both Cation and Anion Redox for Energy Storage. *Nat. Rev. Mater.* **2022**, *7*, 522–540.
- (484) Seo, D.-H.; Lee, J.; Urban, A.; Malik, R.; Kang, S.; Ceder, G. The Structural and Chemical Origin of the Oxygen Redox Activity in Layered and Cation-Disordered Li-Excess Cathode Materials. *Nat. Chem.* **2016**, *8*, 692–697.
- (485) Ben Yahia, M.; Vergnet, J.; Saubanère, M.; Doublet, M.-L. Unified Picture of Anionic Redox in Li/Na-Ion Batteries. *Nat. Mater.* **2019**, *18*, 496–502.
- (486) House, R. A.; Maitra, U.; Pérez-Osorio, M. A.; Lozano, J. G.; Jin, L.; Somerville, J. W.; Duda, L. C.; Nag, A.; Walters, A.; Zhou, K.-J.; et al. Superstructure Control of First-Cycle Voltage Hysteresis in Oxygen-Redox Cathodes. *Nature* **2020**, *577*, 502–508.
- (487) House, R. A.; Rees, G. J.; Pérez-Osorio, M. A.; Marie, J.-J.; Boivin, E.; Robertson, A. W.; Nag, A.; Garcia-Fernandez, M.; Zhou, K.-J.; Bruce, P. G. First-Cycle Voltage Hysteresis in Li-Rich 3d Cathodes Associated with Molecular O<sub>2</sub> Trapped in the Bulk. *Nat. Energy* **2020**, *5*, 777–785.
- (488) Li, X.; Qiao, Y.; Guo, S.; Xu, Z.; Zhu, H.; Zhang, X.; Yuan, Y.; He, P.; Ishida, M.; Zhou, H. Direct Visualization of the Reversible O<sup>2-</sup>/O<sup>-</sup> Redox Process in Li-Rich Cathode Materials. *Adv. Mater.* **2018**, *30*, No. 1705197.
- (489) McCalla, E.; Abakumov, A. M.; Saubanère, M.; Foix, D.; Berg, E. J.; Rousse, G.; Doublet, M.-L.; Gonbeau, D.; Novák, P.; Van Tendeloo, G.; et al. Visualization of O–O Peroxo-like Dimers in High-Capacity Layered Oxides for Li-Ion Batteries. *Science* **2015**, *350*, 1516–1521.
- (490) Sathiya, M.; Rousse, G.; Ramesha, K.; Laisa, C. P.; Vezin, H.; Sougrati, M. T.; Doublet, M.-L.; Foix, D.; Gonbeau, D.; Walker, W.; et al. Reversible Anionic Redox Chemistry in High-Capacity Layered-Oxide Electrodes. *Nat. Mater.* **2013**, *12*, 827–835.
- (491) Saubanère, M.; McCalla, E.; Tarascon, J.-M.; Doublet, M.-L. The Intriguing Question of Anionic Redox in High-Energy Density Cathodes for Li-Ion Batteries. *Energy Environ. Sci.* **2016**, *9*, 984–991.
- (492) Kitchev, D. A.; Vinckeviciute, J.; Van der Ven, A. Delocalized Metal–Oxygen π-Redox Is the Origin of Anomalous Nonhysteretic Capacity in Li-Ion and Na-Ion Cathode Materials. *J. Am. Chem. Soc.* **2021**, *143*, 1908–1916.
- (493) Assadi, M. H. N.; Okubo, M.; Yamada, A.; Tateyama, Y. Oxygen Redox in Hexagonal Layered Na<sub>x</sub>TMO<sub>3</sub> (TM = 4d Elements) for High Capacity Na Ion Batteries. *J. Mater. Chem. A* **2018**, *6*, 3747–3753.
- (494) Chen, Q.; Pei, Y.; Chen, H.; Song, Y.; Zhen, L.; Xu, C.-Y.; Xiao, P.; Henkelman, G. Highly Reversible Oxygen Redox in Layered Compounds Enabled by Surface Polyanions. *Nat. Commun.* **2020**, *11*, 3411.

- (495) Guo, Y.-J.; Wang, P.-F.; Niu, Y.-B.; Zhang, X.-D.; Li, Q.; Yu, X.; Fan, M.; Chen, W.-P.; Yu, Y.; Liu, X.; et al. Boron-Doped Sodium Layered Oxide for Reversible Oxygen Redox Reaction in Na-Ion Battery Cathodes. *Nat. Commun.* **2021**, *12*, 5267.
- (496) Koch, D.; Manzhos, S. Oxygen Redox Activity in Cathodes: A Common Phenomenon Calling for Density-Based Descriptors. *J. Phys. Chem. C* **2020**, *124*, 19962–19968.
- (497) Li, L.; Castro, F. C.; Park, J. S.; Li, H.; Lee, E.; Boyko, T. D.; Freeland, J. W.; Yao, Z.; Fister, T. T.; Vinson, J.; et al. Probing Electrochemically Induced Structural Evolution and Oxygen Redox Reactions in Layered Lithium Iridate. *Chem. Mater.* **2019**, *31*, 4341–4352.
- (498) Liu, X.; Xu, G.-L.; Kolluru, V. S. C.; Zhao, C.; Li, Q.; Zhou, X.; Liu, Y.; Yin, L.; Zhuo, Z.; Daali, A.; et al. Origin and Regulation of Oxygen Redox Instability in High-Voltage Battery Cathodes. *Nat. Energy* **2022**, *7*, 808–817.
- (499) Shang, T.; Xiao, D.; Meng, F.; Rong, X.; Gao, A.; Lin, T.; Tang, Z.; Liu, X.; Li, X.; Zhang, Q.; et al. Real-Space Measurement of Orbital Electron Populations for  $\text{Li}_{1-x}\text{CoO}_2$ . *Nat. Commun.* **2022**, *13*, 5810.
- (500) Vergnet, J.; Saubanère, M.; Doublet, M.-L.; Tarascon, J.-M. The Structural Stability of P2-Layered Na-Based Electrodes during Anionic Redox. *Joule* **2020**, *4*, 420–434.
- (501) Yang, L.; Liu, Z.; Liu, S.; Han, M.; Zhang, Q.; Gu, L.; Li, Q.; Hu, Z.; Wang, X.; Lin, H.-J.; et al. Superiority of Native Vacancies in Activating Anionic Redox in P2-Type  $\text{Na}_{2/3}[\text{Mn}_{7/9}\text{Mg}_{1/9}\square_{1/9}]\text{O}_2$ . *Nano Energy* **2020**, *78*, No. 105172.
- (502) Raebiger, H.; Lany, S.; Zunger, A. Charge Self-Regulation upon Changing the Oxidation State of Transition Metals in Insulators. *Nature* **2008**, *453*, 763–766.
- (503) Wolverton, C.; Zunger, A. First-Principles Prediction of Vacancy Order-Disorder and Intercalation Battery Voltages in  $\text{Li}_x\text{CoO}_2$ . *Phys. Rev. Lett.* **1998**, *81*, 606–609.
- (504) Zunger, A.; Lindefelt, U. Substitutional 3d Impurities in Silicon: A Self-Regulating System. *Solid State Commun.* **1983**, *45*, 343–346.
- (505) Zunger, A.; Lindefelt, U. Theory of Substitutional and Interstitial 3d Impurities in Silicon. *Phys. Rev. B* **1982**, *26*, 5989–5992.
- (506) Zunger, A. Electronic Structure of 3d Transition-Atom Impurities in Semiconductors. In *Solid State Physics*; Ehrenreich, H., Turnbull, D., Eds.; Academic Press: New York, 1986; Vol. 39, pp 275–464.
- (507) Haldane, F. D. M.; Anderson, P. W. Simple Model of Multiple Charge States of Transition-Metal Impurities in Semiconductors. *Phys. Rev. B* **1976**, *13*, 2553–2559.
- (508) Singh, V. A.; Zunger, A. Electronic Structure of Transition-Atom Impurities in GaP. *Phys. Rev. B* **1985**, *31*, 3729–3759.
- (509) Wolczanski, P. T. Flipping the Oxidation State Formalism: Charge Distribution in Organometallic Complexes As Reported by Carbon Monoxide. *Organometallics* **2017**, *36*, 622–631.
- (510) Lupinetti, A. J.; Strauss, S. H.; Frenking, G. Nonclassical Metal Carbonyls. *Prog. Inorg. Chem.* **2001**, *49*, 1–112.
- (511) Willner, H.; Aubke, F.  $\sigma$ -Bonded Metal Carbonyl Cations and Their Derivatives: Syntheses and Structural, Spectroscopic, and Bonding Principles. *Organometallics* **2003**, *22*, 3612–3633.
- (512) Koch, D.; Golub, P.; Manzhos, S. Stability of Charges in Titanium Compounds and Charge Transfer to Oxygen in Titanium Dioxide. *J. Phys. Conf. Ser.* **2018**, *1136*, No. 012017.
- (513) Koch, D.; Chen, Y.; Golub, P.; Manzhos, S. Revisiting  $\pi$  Backbonding: The Influence of d Orbitals on Metal–CO Bonds and Ligand Red Shifts. *Phys. Chem. Chem. Phys.* **2019**, *21*, 20814–20821.
- (514) Koch, D.; Manzhos, S. The Role of Solvent Charge Donation in the Stabilization of Metal Ions in Aqueous Solution. *MRS Commun.* **2018**, *8*, 1139–1144.
- (515) Lang, P. F.; Smith, B. C. Ionization Energies of Atoms and Atomic Ions. *J. Chem. Educ.* **2003**, *80*, 938.
- (516) Karen, P.; McArdle, P.; Takats, J. Comprehensive Definition of Oxidation State (IUPAC Recommendations 2016). *Pure Appl. Chem.* **2016**, *88*, 831–839.
- (517) Haaland, A. Covalent versus Dative Bonds to Main Group Metals, a Useful Distinction. *Angew. Chem., Int. Ed. Engl.* **1989**, *28*, 992–1007.
- (518) Chen, Z.; Yang, M.; Chen, G.; Tang, G.; Huang, Z.; Chu, M.; Qi, R.; Li, S.; Wang, R.; Wang, C.; et al. Triggering Anionic Redox Activity in Fe/Mn-Based Layered Oxide for High-Performance Sodium-Ion Batteries. *Nano Energy* **2022**, *94*, No. 106958.
- (519) Kim, D.; Cho, M.; Cho, K. Rational Design of  $\text{Na}(\text{Li}_{1/3}\text{Mn}_{2/3})\text{O}_2$  Operated by Anionic Redox Reactions for Advanced Sodium-Ion Batteries. *Adv. Mater.* **2017**, *29*, No. 1701788.
- (520) Li, Y.; Zhao, X.; Bao, Q.; Cui, M.; Qiu, W.; Liu, J. How Inactive D0 Transition Metal Controls Anionic Redox in Disordered Li-Rich Oxyfluoride Cathodes. *Energy Storage Mater.* **2020**, *32*, 253–260.
- (521) Zheng, M.; Bai, Z.; He, Y.-W.; Wu, S.; Yang, Y.; Zhu, Z.-Z. Anionic Redox Processes in Maricite- and Triphyllite- $\text{NaFePO}_4$  of Sodium-Ion Batteries. *ACS Omega* **2020**, *5*, 5192–5201.
- (522) Zheng, J.; Teng, G.; Yang, J.; Xu, M.; Yao, Q.; Zhuo, Z.; Yang, W.; Liu, Q.; Pan, F. Mechanism of Exact Transition between Cationic and Anionic Redox Activities in Cathode Material  $\text{Li}_2\text{FeSiO}_4$ . *J. Phys. Chem. Lett.* **2018**, *9*, 6262–6268.
- (523) Carroll, K. J.; Qian, D.; Fell, C.; Calvin, S.; Veith, G. M.; Chi, M.; Baggetto, L.; Meng, Y. S. Probing the Electrode/Electrolyte Interface in the Lithium Excess Layered Oxide  $\text{Li}_{1.2}\text{Ni}_{0.2}\text{Mn}_{0.6}\text{O}_2$ . *Phys. Chem. Chem. Phys.* **2013**, *15*, 11128–11138.
- (524) Assat, G.; Iadecola, A.; Foix, D.; Dedryvère, R.; Tarascon, J.-M. Direct Quantification of Anionic Redox over Long Cycling of Li-Rich NMC via Hard X-Ray Photoemission Spectroscopy. *ACS Energy Lett.* **2018**, *3*, 2721–2728.
- (525) Foix, D.; Sathiya, M.; McCalla, E.; Tarascon, J.-M.; Gonbeau, D. X-Ray Photoemission Spectroscopy Study of Cationic and Anionic Redox Processes in High-Capacity Li-Ion Battery Layered-Oxide Electrodes. *J. Phys. Chem. C* **2016**, *120*, 862–874.
- (526) Yang, W.; Devereaux, T. P. Anionic and Cationic Redox and Interfaces in Batteries: Advances from Soft X-Ray Absorption Spectroscopy to Resonant Inelastic Scattering. *J. Power Sources* **2018**, *389*, 188–197.
- (527) Frati, F.; Hunault, M. O. J. Y.; de Groot, F. M. F. Oxygen K-Edge X-Ray Absorption Spectra. *Chem. Rev.* **2020**, *120*, 4056–4110.
- (528) Wu, J.; Yang, Y.; Yang, W. Advances in Soft X-Ray RIXS for Studying Redox Reaction States in Batteries. *Dalton Trans.* **2020**, *49*, 13519–13527.
- (529) Leibens-Higgins, Z. W.; Chung, H.; Zuba, M. J.; Rana, J.; Li, Y.; Faenza, N. V.; Pereira, N.; McCloskey, B. D.; Rodolakis, F.; Yang, W.; et al. How Bulk Sensitive Is Hard X-Ray Photoelectron Spectroscopy: Accounting for the Cathode–Electrolyte Interface When Addressing Oxygen Redox. *J. Phys. Chem. Lett.* **2020**, *11*, 2106–2112.
- (530) Roychoudhury, S.; Qiao, R.; Zhuo, Z.; Li, Q.; Lyu, Y.; Kim, J.-H.; Liu, J.; Lee, E.; Polzin, B. J.; Guo, J.; et al. Deciphering the Oxygen Absorption Pre-Edge: A Caveat on Its Application for Probing Oxygen Redox Reactions in Batteries. *Energy Environ. Mater.* **2021**, *4*, 246–254.
- (531) Wu, J.; Li, Q.; Sallis, S.; Zhuo, Z.; Gent, W. E.; Chueh, W. C.; Yan, S.; Chuang, Y.; Yang, W. Fingerprint Oxygen Redox Reactions in Batteries through High-Efficiency Mapping of Resonant Inelastic X-Ray Scattering. *Condens. Matter* **2019**, *4*, 5.
- (532) Zhuo, Z.; Pemmaraju, C. D.; Vinson, J.; Jia, C.; Moritz, B.; Lee, I.; Sallis, S.; Li, Q.; Wu, J.; Dai, K.; et al. Spectroscopic Signature of Oxidized Oxygen States in Peroxides. *J. Phys. Chem. Lett.* **2018**, *9*, 6378–6384.
- (533) Walsh, A.; Sokol, A. A.; Buckeridge, J.; Scanlon, D. O.; Catlow, C. R. A. Oxidation States and Ionicity. *Nat. Mater.* **2018**, *17*, 958–964.
- (534) Karen, P.; McArdle, P.; Takats, J. Toward a Comprehensive Definition of Oxidation State (IUPAC Technical Report). *Pure Appl. Chem.* **2014**, *86*, 1017–1081.

- (535) International Union of Pure and Applied Chemistry. *IUPAC Compendium of Chemical Terminology - Gold Book*, Version 2.3.2, 2012.
- (536) Resta, R. Charge States in Transition. *Nature* **2008**, *453*, 735–735.
- (537) Jansen, M.; Wedig, U. A Piece of the Picture—Misunderstanding of Chemical Concepts. *Angew. Chem., Int. Ed.* **2008**, *47*, 10026–10029.
- (538) Raebiger, H.; Lany, S.; Resta, R.; Zunger, A. Oxidation Numbers as Social Security Numbers: Are They Predictive or Postdictive? *Nat. Preced.* **2009**; DOI: 10.1038/npre.2009.4012.1.
- (539) Walsh, A.; Sokol, A. A.; Buckeridge, J.; Scanlon, D. O.; Catlow, C. R. A. Electron Counting in Solids: Oxidation States, Partial Charges, and Ionicity. *J. Phys. Chem. Lett.* **2017**, *8*, 2074–2075.
- (540) Norman, N. C.; Pringle, P. G. In Defence of Oxidation States. *Dalton Trans.* **2022**, *51*, 400–410.
- (541) Zhao, L.; Pan, S.; Holzmann, N.; Schwerdtfeger, P.; Frenking, G. Chemical Bonding and Bonding Models of Main-Group Compounds. *Chem. Rev.* **2019**, *119*, 8781–8845.
- (542) Boys, S. F. Construction of Some Molecular Orbitals to Be Approximately Invariant for Changes from One Molecule to Another. *Rev. Mod. Phys.* **1960**, *32*, 296–299.
- (543) Pipek, J.; Mezey, P. G. Dependence of MO Shapes on a Continuous Measure of Delocalization. *Int. J. Quantum Chem.* **1988**, *34*, 1–13.
- (544) Pipek, J.; Mezey, P. G. A Fast Intrinsic Localization Procedure Applicable for Ab Initio and Semiempirical Linear Combination of Atomic Orbital Wave Functions. *J. Chem. Phys.* **1989**, *90*, 4916–4926.
- (545) Edmiston, C.; Ruedenberg, K. Localized Atomic and Molecular Orbitals. *Rev. Mod. Phys.* **1963**, *35*, 457–464.
- (546) Fleischer, H. Molecular “Floppyness” and the Lewis Acidity of Silanes: A Density Functional Theory Study. *Eur. J. Inorg. Chem.* **2001**, *2001*, 393–404.
- (547) Zhan, C.-G.; Zheng, F.; Xu, G.-X. Quantum Chemical Definition and Calculation of Oxidation Number. *J. Mol. Struct. THEOCHEM* **1994**, *309*, 309–314.
- (548) Thom, A. J. W.; Sundstrom, E. J.; Head-Gordon, M. LOBA: A Localized Orbital Bonding Analysis to Calculate Oxidation States, with Application to a Model Water Oxidation Catalyst. *Phys. Chem. Chem. Phys.* **2009**, *11*, 11297–11304.
- (549) Sit, P. H.-L.; Car, R.; Cohen, M. H.; Selloni, A. Simple, Unambiguous Theoretical Approach to Oxidation State Determination via First-Principles Calculations. *Inorg. Chem.* **2011**, *50*, 10259–10267.
- (550) Gimferrer, M.; Aldossary, A.; Salvador, P.; Head-Gordon, M. Oxidation State Localized Orbitals: A Method for Assigning Oxidation States Using Optimally Fragment-Localized Orbitals and a Fragment Orbital Localization Index. *J. Chem. Theory Comput.* **2022**, *18*, 309–322.
- (551) Kratzer, P.; Neugebauer, J. The Basics of Electronic Structure Theory for Periodic Systems. *Front. Chem.* **2019**, *7*, 106.
- (552) Schüler, M.; Peil, O. E.; Kraberger, G. J.; Pordzik, R.; Marsman, M.; Kresse, G.; Wehling, T. O.; Aichhorn, M. Charge Self-Consistent Many-Body Corrections Using Optimized Projected Localized Orbitals. *J. Phys.: Condens. Matter* **2018**, *30*, 475901.
- (553) Jensen, F. *Introduction to Computational Chemistry*, 2nd ed.; John Wiley & Sons, Ltd.: Chichester, 2007.
- (554) Tsirelson, V.; Stash, A. Orbital-Free Quantum Crystallography: View on Forces in Crystals. *Acta Crystallogr. Sect. B Struct. Sci. Cryst. Eng. Mater.* **2020**, *76*, 769–778.
- (555) Tsirelson, V.; Stash, A. Developing Orbital-Free Quantum Crystallography: The Local Potentials and Associated Partial Charge Densities. *Acta Crystallogr. Sect. B Struct. Sci. Cryst. Eng. Mater.* **2021**, *77*, 467–477.
- (556) Jiang, K.; Pavanello, M. Time-Dependent Orbital-Free Density Functional Theory: Background and Pauli Kernel Approximations. *Phys. Rev. B* **2021**, *103*, No. 245102.
- (557) Peverati, R.; Truhlar, D. G. Exchange–Correlation Functional with Good Accuracy for Both Structural and Energetic Properties While Depending Only on the Density and Its Gradient. *J. Chem. Theory Comput.* **2012**, *8*, 2310–2319.
- (558) Perdew, J. P.; Burke, K.; Ernzerhof, M. Generalized Gradient Approximation Made Simple. *Phys. Rev. Lett.* **1996**, *77*, 3865–3868.
- (559) Perdew, J. P.; Ruzsinszky, A.; Csonka, G. I.; Vydrov, O. A.; Scuseria, G. E.; Constantin, L. A.; Zhou, X.; Burke, K. Restoring the Density-Gradient Expansion for Exchange in Solids and Surfaces. *Phys. Rev. Lett.* **2008**, *100*, No. 136406.
- (560) Perdew, J. P.; Burke, K.; Wang, Y. Generalized Gradient Approximation for the Exchange-Correlation Hole of a Many-Electron System. *Phys. Rev. B* **1996**, *54*, 16533–16539.
- (561) Perdew, J. P.; Burke, K.; Ernzerhof, M. Generalized Gradient Approximation Made Simple [Phys. Rev. Lett. 77, 3865 (1996)]. *Phys. Rev. Lett.* **1997**, *78*, 1396–1396.
- (562) Bartlett, R. J.; Ranasinghe, D. S. The Power of Exact Conditions in Electronic Structure Theory. *Chem. Phys. Lett.* **2017**, *669*, 54–70.
- (563) Perdew, J. P.; Constantin, L. A. Laplacian-Level Density Functionals for the Kinetic Energy Density and Exchange-Correlation Energy. *Phys. Rev. B* **2007**, *75*, No. 155109.
- (564) Laricchia, S.; Constantin, L. A.; Fabiano, E.; Della Sala, F. Laplacian-Level Kinetic Energy Approximations Based on the Fourth-Order Gradient Expansion: Global Assessment and Application to the Subsystem Formulation of Density Functional Theory. *J. Chem. Theory Comput.* **2014**, *10*, 164–179.
- (565) Lehtomäki, J.; Lopez-Acevedo, O. Semilocal Kinetic Energy Functionals with Parameters from Neutral Atoms. *Phys. Rev. B* **2019**, *100*, No. 165111.
- (566) Seino, J.; Kageyama, R.; Fujinami, M.; Ikabata, Y.; Nakai, H. Semi-Local Machine-Learned Kinetic Energy Density Functional with Third-Order Gradients of Electron Density. *J. Chem. Phys.* **2018**, *148*, 241705.
- (567) Chacón, E.; Alvarellos, J. E.; Tarazona, P. Nonlocal Kinetic Energy Functional for Nonhomogeneous Electron Systems. *Phys. Rev. B* **1985**, *32*, 7868–7877.
- (568) Wang, Y. A.; Govind, N.; Carter, E. A. Orbital-Free Kinetic-Energy Functionals for the Nearly Free Electron Gas. *Phys. Rev. B* **1998**, *58*, 13465–13471.
- (569) Wang, L.-W.; Teter, M. P. Kinetic-Energy Functional of the Electron Density. *Phys. Rev. B* **1992**, *45*, 13196–13220.
- (570) García-González, P.; Alvarellos, J. E.; Chacón, E. Nonlocal Symmetrized Kinetic-Energy Density Functional: Application to Simple Surfaces. *Phys. Rev. B* **1998**, *57*, 4857–4862.
- (571) García-González, P.; Alvarellos, J. E.; Chacón, E. Nonlocal Kinetic-Energy-Density Functionals. *Phys. Rev. B* **1996**, *53*, 9509–9512.
- (572) Fermi, E. Eine statistische Methode zur Bestimmung einiger Eigenschaften des Atoms und ihre Anwendung auf die Theorie des periodischen Systems der Elemente. *Z. Für Phys.* **1928**, *48*, 73–79.
- (573) Weizsäcker, C. F. v. Zur Theorie der Kernmassen. *Z. Für Phys.* **1935**, *96*, 431–458.
- (574) Chen, M.; Jiang, X.-W.; Zhuang, H.; Wang, L.-W.; Carter, E. A. Petascale Orbital-Free Density Functional Theory Enabled by Small-Box Algorithms. *J. Chem. Theory Comput.* **2016**, *12*, 2950–2963.
- (575) González, D. J.; González, L. E. Structure and Motion at the Liquid-Vapor Interface of Some Interalkali Binary Alloys: An Orbital-Free Ab Initio Study. *J. Chem. Phys.* **2009**, *130*, 114703.
- (576) Carling, K. M.; Carter, E. A. Orbital-Free Density Functional Theory Calculations of the Properties of Al, Mg and Al–Mg Crystalline Phases. *Model. Simul. Mater. Sci. Eng.* **2003**, *11*, 339.
- (577) Legrain, F.; Manzhos, S. Highly Accurate Local Pseudopotentials of Li, Na, and Mg for Orbital Free Density Functional Theory. *Chem. Phys. Lett.* **2015**, *622*, 99–103.
- (578) Huang, C.; Carter, E. A. Transferable Local Pseudopotentials for Magnesium, Aluminum and Silicon. *Phys. Chem. Chem. Phys.* **2008**, *10*, 7109–7120.
- (579) Liu, Q.; Lu, D.; Chen, M. Structure and Dynamics of Warm Dense Aluminum: A Molecular Dynamics Study with Density

- Functional Theory and Deep Potential. *J. Phys.: Condens. Matter* **2020**, *32*, 144002.
- (580) Zhuang, H.; Chen, M.; Carter, E. A. Elastic and Thermodynamic Properties of Complex Mg-Al Intermetallic Compounds via Orbital-Free Density Functional Theory. *Phys. Rev. Appl.* **2016**, *5*, No. 064021.
- (581) Chai, J.-D.; Lignères, V. L.; Ho, G.; Carter, E. A.; Weeks, J. D. Orbital-Free Density Functional Theory: Linear Scaling Methods for Kinetic Potentials, and Applications to Solid Al and Si. *Chem. Phys. Lett.* **2009**, *473*, 263–267.
- (582) Xia, J.; Carter, E. A. Density-Decomposed Orbital-Free Density Functional Theory for Covalently Bonded Molecules and Materials. *Phys. Rev. B* **2012**, *86*, No. 235109.
- (583) Xia, J.; Huang, C.; Shin, I.; Carter, E. A. Can Orbital-Free Density Functional Theory Simulate Molecules? *J. Chem. Phys.* **2012**, *136*, No. 084102.
- (584) Zhou, B.; Carter, E. A. First Principles Local Pseudopotential for Silver: Towards Orbital-Free Density-Functional Theory for Transition Metals. *J. Chem. Phys.* **2005**, *122*, 184108.
- (585) Huang, C.; Carter, E. A. Toward an Orbital-Free Density Functional Theory of Transition Metals Based on an Electron Density Decomposition. *Phys. Rev. B* **2012**, *85*, No. 045126.
- (586) Finzel, K. Detailed Analysis of Deformation Potentials with Application in Orbital-Free Density Functional Theory. *Acta Crystallogr. Sect. B Struct. Sci. Cryst. Eng. Mater.* **2021**, *77*, 458–466.
- (587) Takahashi, H. Orbital-Free QM/MM Simulation Combined with a Theory of Solutions. *J. Chem. Phys.* **2023**, *159*, 124118.
- (588) Soler, J. M.; Artacho, E.; Gale, J. D.; García, A.; Junquera, J.; Ordejón, P.; Sánchez-Portal, D. The SIESTA Method for Ab Initio Order-N Materials Simulation. *J. Phys.: Condens. Matter* **2002**, *14*, 2745–2779.
- (589) Mohr, S.; Ratcliff, L. E.; Genovese, L.; Caliste, D.; Boulanger, P.; Goedecker, S.; Deutsch, T. Accurate and Efficient Linear Scaling DFT Calculations with Universal Applicability. *Phys. Chem. Chem. Phys.* **2015**, *17*, 31360–31370.
- (590) Nakata, A.; Baker, J. S.; Mujahed, S. Y.; Poulton, J. T. L.; Arapan, S.; Lin, J.; Raza, Z.; Yadav, S.; Truflandier, L.; Miyazaki, T.; et al. Large Scale and Linear Scaling DFT with the CONQUEST Code. *J. Chem. Phys.* **2020**, *152*, 164112.
- (591) Bowler, D. R.; Miyazaki, T. Calculations for Millions of Atoms with Density Functional Theory: Linear Scaling Shows Its Potential. *J. Phys.: Condens. Matter* **2010**, *22*, No. 074207.
- (592) Manzhos, S.; Giorgi, G.; Lüder, J.; Ihara, M. Modeling of Plasmonic Properties of Nanostructures for next Generation Solar Cells and Beyond. *Adv. Phys. X* **2021**, *6*, No. 1908848.
- (593) Manzhos, S.; Giorgi, G.; Lüder, J.; Ihara, M. Modeling Methods for Plasmonic Effects in Halide Perovskite Based Systems for Photonics Applications. *Halide Perovskites for Photonics*; AIP Publishing Books; AIP Publishing LLC: New York, 2021; pp 11–1–11–52.
- (594) Shin, I.; Carter, E. A. First-Principles Simulations of Plasticity in Body-Centered-Cubic Magnesium–Lithium Alloys. *Acta Mater.* **2014**, *64*, 198–207.
- (595) Shin, I.; Ramasubramaniam, A.; Huang, C.; Hung, L.; Carter, E. A. Orbital-Free Density Functional Theory Simulations of Dislocations in Aluminum. *Philos. Mag.* **2009**, *89*, 3195–3213.
- (596) Hayes, R. L.; Ho, G.; Ortiz, M.; Carter, E. A. Prediction of Dislocation Nucleation during Nanoindentation of Al<sub>3</sub>Mg by the Orbital-Free Density Functional Theory Local Quasicontinuum Method. *Philos. Mag.* **2006**, *86*, 2343–2358.
- (597) Hayes, R. L.; Fago, M.; Ortiz, M.; Carter, E. A. Prediction of Dislocation Nucleation During Nanoindentation by the Orbital-Free Density Functional Theory Local Quasi-Continuum Method. *Multiscale Model. Simul.* **2005**, *4*, 359–389.
- (598) Ho, G. S.; Huang, C.; Carter, E. A. Describing Metal Surfaces and Nanostructures with Orbital-Free Density Functional Theory. *Curr. Opin. Solid State Mater. Sci.* **2007**, *11*, 57–61.
- (599) Hung, L.; Carter, E. A. Orbital-Free DFT Simulations of Elastic Response and Tensile Yielding of Ultrathin [111] Al Nanowires. *J. Phys. Chem. C* **2011**, *115*, 6269–6276.
- (600) Chen, M.; Hung, L.; Huang, C.; Xia, J.; Carter, E. A. The Melting Point of Lithium: An Orbital-Free First-Principles Molecular Dynamics Study. *Mol. Phys.* **2013**, *111*, 3448–3456.
- (601) Das, S.; Iyer, M.; Gavini, V. Real-Space Formulation of Orbital-Free Density Functional Theory Using Finite-Element Discretization: The Case for Al, Mg, and Al-Mg Intermetallics. *Phys. Rev. B* **2015**, *92*, No. 014104.
- (602) Radhakrishnan, B. G.; Gavini, V. Electronic Structure Calculations at Macroscopic Scales Using Orbital-Free DFT. *Recent Progress in Orbital-free Density Functional Theory: Recent Advances in Computational Chemistry*; World Scientific: River Edge, NJ, 2012; Vol. 6, pp 147–163.
- (603) Radhakrishnan, B.; Gavini, V. Effect of Cell Size on the Energetics of Vacancies in Aluminum Studied via Orbital-Free Density Functional Theory. *Phys. Rev. B* **2010**, *82*, No. 094117.
- (604) Hung, L.; Carter, E. A. Ductile Processes at Aluminium Crack Tips: Comparison of Orbital-Free Density Functional Theory with Classical Potential Predictions. *Model. Simul. Mater. Sci. Eng.* **2011**, *19*, No. 045002.
- (605) Montavon, G.; Orr, G. B.; Mueller, K.-R. *Neural Networks: Tricks of the Trade*, 2nd ed.; Springer: Berlin Heidelberg, 2012.
- (606) Bishop, C. M. *Pattern Recognition and Machine Learning*; Information Science and Statistics; Springer: Singapore, 2006.
- (607) Rasmussen, C. E.; Williams, C. K. I. *Gaussian Processes for Machine Learning*; MIT Press: Cambridge, MA, 2006.
- (608) Manzhos, S.; Tsuda, S.; Ihara, M. Machine Learning in Computational Chemistry: Interplay between (Non)Linearity, Basis Sets, and Dimensionality. *Phys. Chem. Chem. Phys.* **2023**, *25*, 1546–1555.
- (609) Shao, X.; Paetow, L.; Tuckerman, M. E.; Pavanello, M. Machine Learning Electronic Structure Methods Based on the One-Electron Reduced Density Matrix. *Nat. Commun.* **2023**, *14*, 6281.
- (610) Bogojeski, M.; Vogt-Maranto, L.; Tuckerman, M. E.; Müller, K.-R.; Burke, K. Quantum Chemical Accuracy from Density Functional Approximations via Machine Learning. *Nat. Commun.* **2020**, *11*, 5223.
- (611) Remme, R.; Kaczun, T.; Scheurer, M.; Dreuw, A.; Hamprecht, F. A. KineticNet: Deep Learning a Transferable Kinetic Energy Functional for Orbital-Free Density Functional Theory. *J. Chem. Phys.* **2023**, *159*, 144113.
- (612) Sun, L.; Chen, M. Machine Learning Based Nonlocal Kinetic Energy Density Functional for Simple Metals and Alloys. *Phys. Rev. B* **2024**, *109*, No. 115135.
- (613) Ghasemi, S. A.; Kühne, T. D. Artificial Neural Networks for the Kinetic Energy Functional of Non-Interacting Fermions. *J. Chem. Phys.* **2021**, *154*, No. 074107.
- (614) de Silva, P.; Korchowiec, J.; Wesolowski, T. A. Revealing the Bonding Pattern from the Molecular Electron Density Using Single Exponential Decay Detector: An Orbital-Free Alternative to the Electron Localization Function. *ChemPhysChem* **2012**, *13*, 3462–3465.
- (615) de Silva, P.; Corminboeuf, C. Simultaneous Visualization of Covalent and Noncovalent Interactions Using Regions of Density Overlap. *J. Chem. Theory Comput.* **2014**, *10*, 3745–3756.
- (616) Hodges, C. H. Quantum Corrections to the Thomas–Fermi Approximation—The Kirzhnits Method. *Can. J. Phys.* **1973**, *51*, 1428–1437.
- (617) Tao, J.; Perdew, J. P.; Staroverov, V. N.; Scuseria, G. E. Climbing the Density Functional Ladder: Nonempirical Meta-Generalized Gradient Approximation Designed for Molecules and Solids. *Phys. Rev. Lett.* **2003**, *91*, No. 146401.
- (618) Deringer, V. L.; Bartók, A. P.; Bernstein, N.; Wilkins, D. M.; Ceriotti, M.; Csányi, G. Gaussian Process Regression for Materials and Molecules. *Chem. Rev.* **2021**, *121*, 10073–10141.
- (619) Luder, J.; Ihara, M.; Manzhos, S. A machine-learned kinetic energy model for light weight metals and compounds of group III–V elements. *Electr. Struct.* **2024**, DOI: 10.1088/2516-1075/ad7e8d.
- (620) Kanungo, B.; Kaplan, A. D.; Shahi, C.; Gavini, V.; Perdew, J. P. Unconventional Error Cancellation Explains the Success of

- Hartree-Fock Density Functional Theory for Barrier Heights. arXiv November 2, 2023.
- (621) Cohen, A. J.; Mori-Sánchez, P.; Yang, W. Insights into Current Limitations of Density Functional Theory. *Science* **2008**, *321*, 792–794.
- (622) Kulik, H.; Perspective, J. Treating Electron over-Delocalization with the DFT+U Method. *J. Chem. Phys.* **2015**, *142*, 240901.
- (623) Constantin, L. A.; Fabiano, E.; Della Sala, F. Performance of Semilocal Kinetic Energy Functionals for Orbital-Free Density Functional Theory. *J. Chem. Theory Comput.* **2019**, *15*, 3044–3055.
- (624) Medvedev, M. G.; Bushmarinov, I. S.; Sun, J.; Perdew, J. P.; Lyssenko, K. A. Density Functional Theory Is Straying from the Path toward the Exact Functional. *Science* **2017**, *355*, 49–52.
- (625) Wasserman, A.; Nafziger, J.; Jiang, K.; Kim, M.-C.; Sim, E.; Burke, K. The Importance of Being Inconsistent. *Annu. Rev. Phys. Chem.* **2017**, *68*, 555–581.
- (626) Sim, E.; Song, S.; Burke, K. Quantifying Density Errors in DFT. *J. Phys. Chem. Lett.* **2018**, *9*, 6385–6392.
- (627) Kohn, W.; Sham, L. J. Quantum Density Oscillations in an Inhomogeneous Electron Gas. *Phys. Rev.* **1965**, *137*, A1697–A1705.
- (628) Ballinger, R. A.; March, N. H. Extended Thomas-Fermi Methods. *Proc. Phys. Soc. Sect. A* **1954**, *67*, 378.
- (629) Yonei, K.; Tomishima, Y. On the Weizsäcker Correction to the Thomas-Fermi Theory of the Atom. *J. Phys. Soc. Jpn.* **1965**, *20*, 1051–1057.
- (630) Glazer, H.; Reiss, H. Calculation of the Dipole Moment of the Carbon-Hydrogen Bond in Methane by the Thomas-Fermi Method. *J. Chem. Phys.* **1955**, *23*, 937–941.
- (631) Teller, E. On the Stability of Molecules in the Thomas-Fermi Theory. *Rev. Mod. Phys.* **1962**, *34*, 627–631.
- (632) Yang, W.; Parr, R. G.; Lee, C. Various Functionals for the Kinetic Energy Density of an Atom or Molecule. *Phys. Rev. A* **1986**, *34*, 4586–4590.
- (633) Lembarki, A.; Chermette, H. Obtaining a Gradient-Corrected Kinetic-Energy Functional from the Perdew-Wang Exchange Functional. *Phys. Rev. A* **1994**, *50*, 5328–5331.
- (634) Yang, W. Gradient Correction in Thomas-Fermi Theory. *Phys. Rev. A* **1986**, *34*, 4575–4585.
- (635) Śmiga, S.; Fabiano, E.; Constantin, L. A.; Della Sala, F. Laplacian-Dependent Models of the Kinetic Energy Density: Applications in Subsystem Density Functional Theory with Meta-Generalized Gradient Approximation Functionals. *J. Chem. Phys.* **2017**, *146*, No. 064105.
- (636) Karasiev, V. V.; Jones, R. S.; Trickey, S. B.; Harris, F. E. Properties of Constraint-Based Single-Point Approximate Kinetic Energy Functionals. *Phys. Rev. B* **2009**, *80*, No. 245120.
- (637) Xia, J.; Carter, E. A. Single-Point Kinetic Energy Density Functionals: A Pointwise Kinetic Energy Density Analysis and Numerical Convergence Investigation. *Phys. Rev. B* **2015**, *91*, No. 045124.
- (638) Wang, Y. A.; Govind, N.; Carter, E. A. Orbital-Free Kinetic-Energy Density Functionals with a Density-Dependent Kernel. *Phys. Rev. B* **1999**, *60*, 16350–16358.
- (639) Smargiassi, E.; Madden, P. A. Orbital-Free Kinetic-Energy Functionals for First-Principles Molecular Dynamics. *Phys. Rev. B* **1994**, *49*, 5220–5226.
- (640) Frankcombe, T. J.; Kroes, G. J.; Choly, N. I.; Kaxiras, E. Orbital-Free Density Functional Theory Applied to NaAlH<sub>4</sub>. *J. Phys. Chem. B* **2005**, *109*, 16554–16562.
- (641) Xia, J.; Huang, C.; Shin, I.; Carter, E. A. Can Orbital-Free Density Functional Theory Simulate Molecules? *J. Chem. Phys.* **2012**, *136*, No. 084102.
- (642) Rios-Vargas, V.; Oyeniyi, E.; Okello, A.; Shao, X.; Pavanello, M. Pseudononlocal Pseudopotentials for Orbital-Free DFT. In preparation.
- (643) Garrity, K. F.; Bennett, J. W.; Rabe, K. M.; Vanderbilt, D. Pseudopotentials for High-Throughput DFT Calculations. *Comput. Mater. Sci.* **2014**, *81*, 446–452.
- (644) Perdew, J. P.; Zunger, A. Self-Interaction Correction to Density-Functional Approximations for Many-Electron Systems. *Phys. Rev. B* **1981**, *23*, 5048–5079.
- (645) Pucci, R.; Angilella, G. G. N. Density Functional Theory, Chemical Reactivity, and the Fukui Functions. *Found. Chem.* **2022**, *24*, 59–71.
- (646) Yang, W.; Parr, R. G.; Pucci, R. Electron Density, Kohn–Sham Frontier Orbitals, and Fukui Functions. *J. Chem. Phys.* **1984**, *81*, 2862–2863.
- (647) Mi, W.; Zhang, S.; Wang, Y.; Ma, Y.; Miao, M. First-Principle Optimal Local Pseudopotentials Construction via Optimized Effective Potential Method. *J. Chem. Phys.* **2016**, *144*, 134108.
- (648) Xu, Q.; Ma, C.; Mi, W.; Wang, Y.; Ma, Y. Nonlocal Pseudopotential Energy Density Functional for Orbital-Free Density Functional Theory. *Nat. Commun.* **2022**, *13*, 1385.
- (649) Zhou, B.; Alexander Wang, Y.; Carter, E. A. Transferable Local Pseudopotentials Derived via Inversion of the Kohn-Sham Equations in a Bulk Environment. *Phys. Rev. B* **2004**, *69*, No. 125109.
- (650) Neuhauser, D.; Pistinner, S.; Coomar, A.; Zhang, X.; Lu, G. Dynamic Kinetic Energy Potential for Orbital-Free Density Functional Theory. *J. Chem. Phys.* **2011**, *134*, 144101.
- (651) Moldabekov, Z. A.; Shao, X.; Pavanello, M.; Vorberger, J.; Graziani, F.; Dornheim, T. Imposing Correct Jellium Response Is Key to Predict the Density Response by Orbital-Free DFT. *Phys. Rev. B* **2023**, *108*, No. 235168.
- (652) Lindhard, J. On the Properties of a Gas of Charged Particles. *Kgl Dan. Vidensk. Selsk. Mat-Fys Medd* **1954**, *28*, 8.
- (653) Casida, M. E.; Jamorski, C.; Casida, K. C.; Salahub, D. R. Molecular Excitation Energies to High-Lying Bound States from Time-Dependent Density-Functional Response Theory: Characterization and Correction of the Time-Dependent Local Density Approximation Ionization Threshold. *J. Chem. Phys.* **1998**, *108*, 4439–4449.
- (654) Casida, M. E. Time-Dependent Density-Functional Theory for Molecules and Molecular Solids. *J. Mol. Struct. THEOCHEM* **2009**, *914*, 3–18.
- (655) Yabana, K.; Bertsch, G. F. Time-Dependent Local-Density Approximation in Real Time. *Phys. Rev. B* **1996**, *54*, 4484–4487.
- (656) Martin, R. L. Natural Transition Orbitals. *J. Chem. Phys.* **2003**, *118*, 4775–4777.
- (657) Herbert, J. M. Visualizing and Characterizing Excited States from Time-Dependent Density Functional Theory. *Phys. Chem. Chem. Phys.* **2024**, *26*, 3755–3794.
- (658) Furche, F. On the Density Matrix Based Approach to Time-Dependent Density Functional Response Theory. *J. Chem. Phys.* **2001**, *114*, 5982–5992.
- (659) Mewes, S. A.; Drew, A. Density-Based Descriptors and Exciton Analyses for Visualizing and Understanding the Electronic Structure of Excited States. *Phys. Chem. Chem. Phys.* **2019**, *21*, 2843–2856.
- (660) Perdew, J. P.; Levy, M. Extrema of the Density Functional for the Energy: Excited States from the Ground-State Theory. *Phys. Rev. B* **1985**, *31*, 6264–6272.
- (661) Yang, W.; Ayers, P. W. Foundation for the ΔSCF Approach in Density Functional Theory. arXiv March 7, 2024.
- (662) Ziegler, T.; Rauk, A.; Baerends, E. J. On the Calculation of Multiplet Energies by the Hartree-Fock-Slater Method. *Theor. Chim. Acta* **1977**, *43*, 261–271.
- (663) Zamani, A. Y.; Hratchian, H. P. Assessing the Performance of ΔSCF and the Diagonal Second-Order Self-Energy Approximation for Calculating Vertical Core Excitation Energies. *J. Chem. Phys.* **2022**, *157*, No. 084115.
- (664) Bourne Worster, S.; Feighan, O.; Manby, F. R. Reliable Transition Properties from Excited-State Mean-Field Calculations. *J. Chem. Phys.* **2021**, *154*, 124106.
- (665) Kaduk, B.; Kowalczyk, T.; Van Voorhis, T. Constrained Density Functional Theory. *Chem. Rev.* **2012**, *112*, 321–370.
- (666) Ramos, P.; Pavanello, M. Low-Lying Excited States by Constrained DFT. *J. Chem. Phys.* **2018**, *148*, 144103.

- (667) Barca, G. M. J.; Gilbert, A. T. B.; Gill, P. M. W. Communication: Hartree-Fock Description of Excited States of H<sub>2</sub>. *J. Chem. Phys.* **2014**, *141*, 111104.
- (668) Thom, A. J. W.; Head-Gordon, M. Hartree–Fock Solutions as a Quasidiabatic Basis for Nonorthogonal Configuration Interaction. *J. Chem. Phys.* **2009**, *131*, 124113.
- (669) Thom, A. J. W.; Head-Gordon, M. Locating Multiple Self-Consistent Field Solutions: An Approach Inspired by Metadynamics. *Phys. Rev. Lett.* **2008**, *101*, No. 193001.
- (670) Perdew, J. P.; Ruzsinszky, A.; Sun, J.; Nepal, N. K.; Kaplan, A. D. Interpretations of Ground-State Symmetry Breaking and Strong Correlation in Wavefunction and Density Functional Theories. *Proc. Natl. Acad. Sci. U. S. A.* **2021**, *118*, No. e2017850118.
- (671) Koch, D.; Manzhos, S.; Chaker, M. The Role of Local DFT+U Minima in the First-Principles Modeling of the Metal–Insulator Transition in Vanadium Dioxide. *J. Phys. Chem. A* **2022**, *126*, 3604–3611.
- (672) Morin, F. J. Oxides Which Show a Metal-to-Insulator Transition at the Neel Temperature. *Phys. Rev. Lett.* **1959**, *3*, 34–36.
- (673) Zheng, H.; Wagner, L. K. Computation of the Correlated Metal–Insulator Transition in Vanadium Dioxide from First Principles. *Phys. Rev. Lett.* **2015**, *114*, No. 176401.
- (674) Kylänpää, I.; Balachandran, J.; Ganesh, P.; Heinonen, O.; Kent, P. R. C.; Krogel, J. T. Accuracy of Ab Initio Electron Correlation and Electron Densities in Vanadium Dioxide. *Phys. Rev. Mater.* **2017**, *1*, No. 065408.
- (675) Zhang, Y.; Ke, D.; Wu, J.; Zhang, C.; Hou, L.; Lin, B.; Chen, Z.; Perdew, J. P.; Sun, J. Challenges for Density Functional Theory in Simulating Metal–Metal Singlet Bonding: A Case Study of Dimerized VO<sub>2</sub>. *J. Chem. Phys.* **2024**, *160*, 134101.
- (676) Cui, Y.; Ke, Y.; Liu, C.; Chen, Z.; Wang, N.; Zhang, L.; Zhou, Y.; Wang, S.; Gao, Y.; Long, Y. Thermochromic VO<sub>2</sub> for Energy-Efficient Smart Windows. *Joule* **2018**, *2*, 1707–1746.
- (677) Hu, B.; Ding, Y.; Chen, W.; Kulkarni, D.; Shen, Y.; Tsukruk, V. V.; Wang, Z. L. External-Strain Induced Insulating Phase Transition in VO<sub>2</sub> Nanobeam and Its Application as Flexible Strain Sensor. *Adv. Mater.* **2010**, *22*, 5134–5139.
- (678) Park, S.; Lee, C. W.; Kim, J.-C.; Song, H. J.; Shim, H.-W.; Lee, S.; Kim, D.-W. Heteroepitaxy-Induced Rutile VO<sub>2</sub> with Abundantly Exposed (002) Facets for High Lithium Electroactivity. *ACS Energy Lett.* **2016**, *1*, 216–224.
- (679) Strelcov, E.; Lilach, Y.; Kolmakov, A. Gas Sensor Based on Metal–Insulator Transition in VO<sub>2</sub> Nanowire Thermistor. *Nano Lett.* **2009**, *9*, 2322–2326.
- (680) Koch, D.; Manzhos, S. Ab Initio Modeling and Design of Vanadia-Based Electrode Materials for Post-Lithium Batteries. *J. Phys. Appl. Phys.* **2020**, *53*, No. 083001.
- (681) He, Z.; Millis, A. J. Photoinduced Phase Transitions in Narrow-Gap Mott Insulators: The Case of VO<sub>2</sub>. *Phys. Rev. B* **2016**, *93*, No. 115126.
- (682) Morrison, V. R.; Chatelain, Robert. P.; Tiwari, K. L.; Hendaoui, A.; Bruhács, A.; Chaker, M.; Siwick, B. J. A Photoinduced Metal-like Phase of Monoclinic VO<sub>2</sub> Revealed by Ultrafast Electron Diffraction. *Science* **2014**, *346*, 445–448.
- (683) González, L.; Escudero, D.; Serrano-Andrés, L. Progress and Challenges in the Calculation of Electronic Excited States. *ChemPhysChem* **2012**, *13*, 28–51.
- (684) Ang, S. T.; Pal, A.; Manzhos, S. Comparison of Optical Absorption Spectra of Organic Molecules and Aggregates Computed from Real Frequency Dependent Polarizability to TD-DFT and the Dipole Approximation. *J. Chem. Phys.* **2018**, *149*, No. 044114.
- (685) Legrain, F.; Manzhos, S. Understanding the Difference in Cohesive Energies between Alpha and Beta Tin in DFT Calculations. *AIP Adv.* **2016**, *6*, No. 045116.
- (686) Legrain, F.; Malyi, O. I.; Persson, C.; Manzhos, S. Comparison of Alpha and Beta Tin for Lithium, Sodium, and Magnesium Storage: An Ab Initio Study Including Phonon Contributions. *J. Chem. Phys.* **2015**, *143*, 204701.
- (687) Runge, E.; Gross, E. K. U. Density-Functional Theory for Time-Dependent Systems. *Phys. Rev. Lett.* **1984**, *52*, 997–1000.
- (688) Jiang, K.; Shao, X.; Pavanello, M. Nonlocal and Nonadiabatic Pauli Potential for Time-Dependent Orbital-Free Density Functional Theory. *Phys. Rev. B* **2021**, *104*, No. 235110.
- (689) White, A. J.; Certik, O.; Ding, Y. H.; Hu, S. X.; Collins, L. A. Time-Dependent Orbital-Free Density Functional Theory for Electronic Stopping Power: Comparison to the Mermitt-Kohn-Sham Theory at High Temperatures. *Phys. Rev. B* **2018**, *98*, No. 144302.
- (690) Baghramyan, H. M.; Della Sala, F.; Ciraci, C. Laplacian-Level Quantum Hydrodynamic Theory for Plasmonics. *Phys. Rev. X* **2021**, *11*, No. 011049.
- (691) Della Sala, F.; Pachter, R.; Sukharev, M. Advances in Modeling Plasmonic Systems. *J. Chem. Phys.* **2022**, *157*, 190401.
- (692) Della Sala, F. Orbital-Free Methods for Plasmonics: Linear Response. *J. Chem. Phys.* **2022**, *157*, 104101.
- (693) Bhan, L.; Covington, C. L.; Varga, K. Laser-Driven Petahertz Electron Ratchet Nanobubbles. *Nano Lett.* **2022**, *22*, 4240–4245.
- (694) Covington, C.; Malave, J.; Varga, K. Coupled Maxwell and Time-Dependent Orbital-Free Density Functional Calculations. *Phys. Rev. B* **2021**, *103*, No. 075119.
- (695) Casida, M. E. Time-Dependent Density Functional Response Theory for Molecules. *Recent Advances in Density Functional Methods; Recent Advances in Computational Chemistry*; World Scientific: River Edge, NJ, 1995; Vol. 1, pp 155–192.
- (696) Plasser, F.; Wormit, M.; Dreuw, A. New Tools for the Systematic Analysis and Visualization of Electronic Excitations. I. Formalism. *J. Chem. Phys.* **2014**, *141*, No. 024106.
- (697) Akimov, A. V.; Prezhdo, O. V. Large-Scale Computations in Chemistry: A Bird's Eye View of a Vibrant Field. *Chem. Rev.* **2015**, *115*, 5797–5890.
- (698) Shaik, S.; Danovich, D.; Hiberty, P. C. On the Nature of the Chemical Bond in Valence Bond Theory. *J. Chem. Phys.* **2022**, *157*, No. 090901.
- (699) Usharani, D.; Lai, W.; Li, C.; Chen, H.; Danovich, D.; Shaik, S. A Tutorial for Understanding Chemical Reactivity through the Valence Bond Approach. *Chem. Soc. Rev.* **2014**, *43*, 4968–4988.
- (700) Basic Valence Bond Theory. *A Chemist's Guide to Valence Bond Theory*; John Wiley & Sons, Ltd.: New York, 2007; pp 40–80.
- (701) Elstner, M.; Seifert, G. Density Functional Tight Binding. *Philos. Trans. R. Soc. Math. Phys. Eng. Sci.* **2014**, *372*, 20120483.
- (702) Elstner, M.; Porezag, D.; Jungnickel, G.; Elsner, J.; Haugk, M.; Frauenheim, Th.; Suhai, S.; Seifert, G. Self-Consistent-Charge Density-Functional Tight-Binding Method for Simulations of Complex Materials Properties. *Phys. Rev. B* **1998**, *58*, 7260–7268.
- (703) Dral, P. O.; Wu, X.; Spörkel, L.; Koslowski, A.; Weber, W.; Steiger, R.; Scholten, M.; Thiel, W. Semiempirical Quantum-Chemical Orthogonalization-Corrected Methods: Theory, Implementation, and Parameters. *J. Chem. Theory Comput.* **2016**, *12*, 1082–1096.
- (704) Anisimov, V. I.; Oganov, A. R.; Korotin, D. M.; Novoselov, D. Y.; Shorikov, A. O.; Belozerov, A. S. First-Principles Definition of Ionicity and Covalency in Molecules and Solids. *J. Chem. Phys.* **2024**, *160*, 144113.
- (705) Kirk, S. R.; Jenkins, S. QuantVec, 2021; [org/10.5281/zenodo.5553686](https://doi.org/10.5281/zenodo.5553686) (accessed 2021-10-07).
- (706) Mi, X. P.; Lu, H.; Xu, T.; Frücht, H.; van Mourik, T.; Paterson, M. J.; Kirk, S. R.; Jenkins, S. Response of the Mechanical and Chiral Character of Ethane to Ultra-Fast Laser Pulses. *J. Comput. Chem.* **2024**, *45*, 150–158.
- (707) Frenking, G. The Chemical Bond – an Entrance Door of Chemistry to the Neighboring Sciences and to Philosophy. *Isr. J. Chem.* **2022**, *62*, No. e202100070.
- (708) Schmidt, M. W.; Ivanic, J.; Ruedenberg, K. Covalent Bonds Are Created by the Drive of Electron Waves to Lower Their Kinetic Energy through Expansion. *J. Chem. Phys.* **2014**, *140*, 204104.
- (709) Huang, B.; von Lilienfeld, O. A. Quantum Machine Learning Using Atom-in-Molecule-Based Fragments Selected on the Fly. *Nat. Chem.* **2020**, *12*, 945–951.

- (710) Huang, B.; von Lilienfeld, O. A. Quantum Machine Learning Using Atom-in-Molecule-Based Fragments Selected on-the-Fly. arXiv:1707.04146. arXiv August 17, 2020.
- (711) Gallegos, M.; Vassilev-Galindo, V.; Poltavsky, I.; Martín Pendás, A.; Tkatchenko, A. Explainable Chemical Artificial Intelligence from Accurate Machine Learning of Real-Space Chemical Descriptors. *Nat. Commun.* **2024**, *15*, 4345.
- (712) Popelier, P. L. A Molecular Simulation by Knowledgeable Quantum Atoms. *Phys. Scr.* **2016**, *91*, No. 033007.
- (713) Symons, B. C. B.; Bane, M. K.; Popelier, P. L. A. DL\_FFLUX: A Parallel, Quantum Chemical Topology Force Field. *J. Chem. Theory Comput.* **2021**, *17*, 7043–7055.
- (714) Hughes, Z. E.; Thacker, J. C. R.; Wilson, A. L.; Popelier, P. L. A. Description of Potential Energy Surfaces of Molecules Using FFLUX Machine Learning Models. *J. Chem. Theory Comput.* **2019**, *15*, 116–126.
- (715) Thacker, J. C. R.; Wilson, A. L.; Hughes, Z. E.; Burn, M. J.; Maxwell, P. I.; Popelier, P. L. A. Towards the Simulation of Biomolecules: Optimisation of Peptide-Capped Glycine Using FFLUX. *Mol. Simul.* **2018**, *44*, 881–890.
- (716) Burn, M. J.; Popelier, P. L. A. Creating Gaussian Process Regression Models for Molecular Simulations Using Adaptive Sampling. *J. Chem. Phys.* **2020**, *153*, No. 054111.
- (717) Fletcher, T. L.; Popelier, P. L. A. Multipolar Electrostatic Energy Prediction for All 20 Natural Amino Acids Using Kriging Machine Learning. *J. Chem. Theory Comput.* **2016**, *12*, 2742–2751.
- (718) Hughes, Z. E.; Ren, E.; Thacker, J. C. R.; Symons, B. C. B.; Silva, A. F.; Popelier, P. L. A. A FFLUX Water Model: Flexible, Polarizable and with a Multipolar Description of Electrostatics. *J. Comput. Chem.* **2020**, *41*, 619–628.
- (719) Di Pasquale, N.; Davie, S. J.; Popelier, P. L. A. The Accuracy of Ab Initio Calculations without Ab Initio Calculations for Charged Systems: Kriging Predictions of Atomistic Properties for Ions in Aqueous Solutions. *J. Chem. Phys.* **2018**, *148*, 241724.